Institutional Repository - Research Portal
Dépôt Institutionnel - Portail de la Recherche
researchportal.unamur.be
University of Namur

THESIS / THÈSE

DOCTOR OF SCIENCES

Design of lithium-oxygen battery cathodes, a promising device for energy storage

Bizot, Quentin

Award date:
2021

Awarding institution:
University of Namur

Link to publication

General rights
Copyright and moral rights for the publications made accessible in the public portal are retained by the authors and/or other copyright owners and it is a condition of accessing publications that users recognise and abide by the legal requirements associated with these rights.

- Users may download and print one copy of any publication from the public portal for the purpose of private study or research.
- You may not further distribute the material or use it for any profit-making activity or commercial gain
- You may freely distribute the URL identifying the publication in the public portal ?

Take down policy
If you believe that this document breaches copyright please contact us providing details, and we will remove access to the work immediately and investigate your claim.

Download date: 04. May. 2023

Université de Namur

Faculté des Sciences
DEPARTEMENT DE CHIMIE
Laboratoire de Chimie des Matériaux Inorganiques

Design of lithium-oxygen battery cathodes, a promising device for energy storage

Dissertation présentée par
Quentin BIZOT

En vue de l'obtention du grade
De Docteur en Sciences

Composition du jury :

Prof.Vlad Alexandru (UCLouvain)
Prof.Garcia Yann (UCLouvain)
Dr.Fusaro Luca (UNamur)
Prof.Krief Alain (UNamur)
Prof.Berionni Guillaume (UNamur, président du jury)
Prof. Su Bao-Lian (UNamur, promoteur)

Août 2021

University of Namur
FACULTY OF SCIENCE
Rue de Bruxelles 61 – 5000 Namur
Phone : +32 (0)81 72 41 11

Design of lithium-oxygen battery cathodes, a promising device for energy storage

Quentin BIZOT

Abstract

For many years, humans have produced energy from fossil fuels such as oil, coal and natural gas. Combustion of these fuels produces a large amount of greenhouse gases that contribute to global warming. Other, more environmentally friendly sources of energy exist, such as sunlight and wind. However, the production of energy from these sources is intermittent and their development requires devices that allow significant storage during the production in order to release it at off-peak production times. The performance of the current lithium-ion battery systems does not allow optimum energy storage.

Lithium-oxygen (Li-O_2) batteries are one of the most promising energy storage and conversion technologies due to their ultra-high energy density (almost ten times higher than current Li-ion systems). Despite these promising characteristics, high efficiency Li-O_2 batteries development is still challenging. Some of these challenges include low round-trip efficiency, poor rechargeability, and high polarisation. One way to overcome these challenges is to focus on the cathode. This electrode is the site of the electrochemical reactions during cycles; therefore, it is essential to optimise it.

The objective of this work is to design cathodes for efficient lithium oxygen batteries. Two strategies have been used, the first consists of tuning the composition of the cathode in order to modulate the reaction kinetics and the second of creating a hierarchical structure in order to increase the diffusion within the electrode.

First, we designed a cathode structure with hierarchical micro/meso/macro porosity based on Murray's law. The hierarchically porous cathode is formed using a bottom-up, layer-by-layer evaporation-driven self-assembly process. This specific gradient porous cathode was tested in a non-aqueous lithium-oxygen battery and exhibited a higher discharge capacity compared with a slurry-based carbon powder cathode demonstrating the positive impact of this structure on the performances.

Then, a second study focused on the use of 3d transition metals as cathode material, and the relation between the electrochemical properties of the material on the performance of the battery was established.

Carbon being a source of degradation in Li-O_2 batteries, AB_2O_4 nanowire arrays carbon-free cathodes were synthetised and allowed good Li_2O_2 formation decomposition, resulting in improved performances.

Essay submitted for the degree of Doctor of Science
August 2021
Supervisor: Prof. Bao-Lian Su

Remerciements

Cette thèse a été réalisée au sein de l'équipe Chimie des Matériaux Inorganiques (CMI) de l'unité UCNano au sein de l'Université de Namur.

Mes premiers remerciements vont au Pr.Bao-Lian Su, Dr.Isabelle Ravet et au Dr.Diane Bailleul pour m'avoir accordé leur confiance pour le poste d'assistant.

Je souhaite remercier Alexandru Vlad et Yann Garcia, Professeurs à l'Université Catholique de Louvain, Alain Krief, Professeur à l'Université de Namur, et Luca Fusaro, Docteur et Logisticien de recherche à l'Université de Namur, de m'avoir fait l'honneur d'être les rapporteurs de ce travail. Toute ma gratitude s'adresse à Guillaume Berionni, Professeur à l'Université de Namur, d'avoir accepté de présider le jury de thèse.

Je tiens à remercier Mr.Su pour son investissement et notamment pour le temps passé lors des corrections du manuscrit de thèse. Je remercie également Isabelle et Valérie pour leur disponibilité et leur aide administrative que ce soit au niveau des commandes ou de la bureaucratie.

Le laboratoire CMI ne serait rien sans ses membres. Je remercie tout particulièrement Tom Lemaître avec qui nous avons initié ce projet ensemble, je le remercie également pour sa contribution sur les matériaux de Murray. Je remercie aussi Chao Li pour m'avoir expliqué le fonctionnement de tous les appareils relatifs aux batteries et Quentin Dry pour sa contribution sur les dépositions électrochimiques. Je tenais également à remercier Cyrille de m'avoir accueilli lors de mon arrivée et de m'avoir expliqué tous les rouages de l'université et Benjamin pour m'avoir fait découvrir l'histoire de la Belgique à travers de nombreuses histoires cocasses. Une pensée particulière me vient également pour les « Marie Curie » Diogo, Domenico et Silvia qui ont su apporter un vent de fraicheur au sein du laboratoire. Je remercie également tous les autres membres du laboratoire Li, Hongyan, Yanxin, Aizhong, Ming-Hui, Pengcheng, Yang, Thomas, Ivalina, Jamila, Dorothée, Lionel, Maxence, Maxime, Éloïse, Yingying, Tarek, Marvin, Myriam, et Yao.

L'unité CNano serait bien pâle sans sa seconde moitié le CMA. Je leur présente mes remerciements les plus chaleureux, pour leur bienveillance, aide et sympathie. Je garderai toujours en mémoire les accotés partagés avec eux, que ce soit aux diners de fin d'année ou bien autour d'une simple bière en fin de journée.

Je remercie l'ensemble de l'équipe pédagogique et en particulier Diane et Isabelle qui de par leur expertise et pédagogie ont su m'accompagner, me guider et me faire évoluer tout au long de cet assistanat.

Je remercie également tous les collègues assistants, Adrien, Coco, Céline, Loïc.C, Marine, Loïc.J, Sydney, Ali, Stéphane, Conrad, Pierre, Alban, François, Marie, Benoît, Paul, Denis, Cassandra avec qui nous avons eu de bons moments de franche camaraderie et surtout Jérémy avec qui nous avons partagé de longues heures de TP et quelques mêlées qui ferait pâlir une finale de HCup entre Toulouse et les Saracens (Couteau entre les dents !). Je remercie aussi Sarah qui arrive toujours à trouver des solutions tel MacGyver afin de nous dépatouiller de certaines situations.

D'une manière un peu plus formelle je remercie Alexandre pour les analyses XPS, Corry, Caroline et Jean-François pour la microscopie électronique, Nikolay pour la DRX et Sébastien pour les électrodépositions.

Je remercie également ma famille et en particulier mes parents et Alexandra ma compagne pour tout le soutien apporté tout au long de ces quatre années, parfois éprouvantes psychologiquement. Parce qu'à Namur il n'y a pas que l'université, je remercie aussi toutes les personnes ou groupe qui ont permis de m'épanouir dans cette ville : le cartel mexicain de Namur (Ayrton, Nacho), le rugby Namur XV, le groupe DPNM, la team punk, le groupe d'étude de la langue russe de l'UNamur, le groupe des pépites, la société ASEMES, le coffee and more, la brasserie de la Houppe, la fromagerie chez maître corbeau, et le cabinet kinésithérapique Libert et vous.

Table of contents

Part I – General introduction and objectives

Chapter 1 - Introduction

I) Battery technology in general 2
II) Lithium-oxygen batteries 7
II.1) Cathode 8
II.1.1) Textural properties 9
II.1.2) Chemical composition of the cathode 14
II.1.2.a) Carbon materials 15
II.1.2.b) Noble metals in carbon materials 27
II.1.2.c) Noble metal oxides in carbon material 32
II.1.2.d) Transition metal oxides in carbon material 35
II.1.2.e) Spinel in carbon material 43
II.1.2.f) Other materials in carbon material 51
II.1.2.g) Mixed materials in carbon material 58
II.1.3) Summary 64
II.2) Electrolyte 65
II.2.1) Solvent 66
II.2.2) Lithium salt 69
II.2.3) Additives 71
II.2.4) Summary 72
II.3) Conclusion 73
Bibliography 74
Figure table 79

Chapter 2: Objectives 84

Part II – Results and discussions

Chapter 3: Electrode design following Murray's law: towards a revolution in Li-O_2 batteries?

I) Introduction 87

II) Materials and Methods 88

II.1) Synthesis of metal oxide nanoparticles 88

II.2) Cathode electrode preparation 88

II.3) Electrochemical measurements 89

II.4) Materials characterisation 90

III) Results and discussions 91

III.1) Murray Material 91

III.2) ZnO nanoparticles synthesis 93

III.2) Zno synthesis 93

III.2.1) Effect of experimental conditions on the formation of microporous ZnO nanoparticles 93

III.2.1.a) Effect of reaction temperature during zinc hydroxide formation on zinc oxide nanoparticles 94

III.2.1.b) Effect of reaction time during zinc hydroxide formation on zinc oxide nanoparticles 96

III.2.1.c) Effect of reaction temperature during zinc hydroxide decomposition on zinc oxide nanoparticles 98

III.2.1.d) Effect of reaction time during zinc hydroxide decomposition on zinc oxide nanoparticles 100

III.2.1.e) Effect of an addition of a capping agent 102

III.2.1.f) Effect of zinc precursor concentration 105

III.3) Assembly of the hierarchically micro/meso/macroporous structure following Murray's law 111

III.3.1) Effect of the concentration of the suspension on the formation of the hierarchically micro/meso/macroporous structure 111

III.3.2) Effect of the relative humidity rate on the hierarchically micro/meso/macroporous structure. 114

IV) Electrochemical test 117

IV.1) Cathode with hierarchical micro/meso/macroporous structure 117

IV.1.1) Cathode based on zinc oxide nanoparticles 117

IV.1.2) Cathode based on carbon nanoparticles 118

IV.1.3) Cathode based on carbon nanotubes assembly 120

IV.1.4) Cathode based on zinc oxide/carbon assembly and slurry 121
Conclusion 124
Bibliography 125
Figure Table 126

Chapter 4: 3d metal oxides as cathode materials for Li-O_2 batteries

Introduction 129
Results and discussion 131
Electrochemical studies 137
Conclusion 149
Experimental 150
Synthesis of 3d metal oxide nanoparticles 150
Materials characterisation 151
Electrochemical measurements 152
Bibliography 153
Figure table 154
Supplementary Information 156

Chapter 5: Carbon free MCo_2O_4 (M = Mn, Ni, Zn) Nano-grass-like cathode: toward the Garden of Eden of the Li-O_2 battery?

Introduction 171
Results and Discussions 173
MCo_2O_4 (M=Ni, Mn, Zn) synthesis 173
Crystalline phase and morphology 173
Electrochemical studies 177
Conclusion 183
Experimental 184
MCo_2O_4 (M = Mn, Ni, Zn) electrodes synthesis 184
Materials characterisation 184
Electrochemical measurements 185
Bibliography 186
Figure Table 187
Supplementary Information 188

Part III – Conclusion and outlook

Chapter 6: General conclusion and outlook 192

Annexes

1) X-ray diffraction (XRD) 195
1.1) Principle 195
1.2) Measuring conditions 196
1.3) Data treatments 196
1.4) Size of the crystallites 197
2) Fourier Transform Infrared Spectroscopy (FTIR) 197
2.1) Principle 197
2.2) Measuring conditions 197
3) Transmission Electron Microscopy (TEM) 198
3.1) Principle 198
3.2) Samples Preparation and measuring conditions 199
4) Scanning Electron Microscopy (SEM) 199
4.1) Principle 199
4.2) Samples Preparation 200
5) X-ray Photoelectron spectroscopy (XPS) 201
5.1) Principle 201
5.2) Measuring conditions 202
6) Porosity measurement 203
6.1) Principle 203
6.2) Multi-point measurements 203
6.3) Single point measurement 204
6.4) Samples Preparation and measuring conditions 204
7) Accumulator design 206

Part I - General introduction and objectives

Chapter 1 - Introduction

I) Battery technology in general

The global need for energy, combined with a desire to be more environmentally friendly, leads to a significant increase in electricity consumption, with an average annual increase of 3.4%, 1.2 percentage higher than the average annual growth of total energy consumption.[1] As not all the electricity produced can be immediately used, the utilisation of specific devices to store unconsumed electricity becomes a key factor in resolving these energy issues.

Performances of the main devices currently used to store electricity are reported in Figure 1. Fuel cells can be defined as high-energy systems, whereas supercapacitors can be referred as high-power systems. Batteries offer the best compromise between power and energy density and attract intensive research interest.[2]

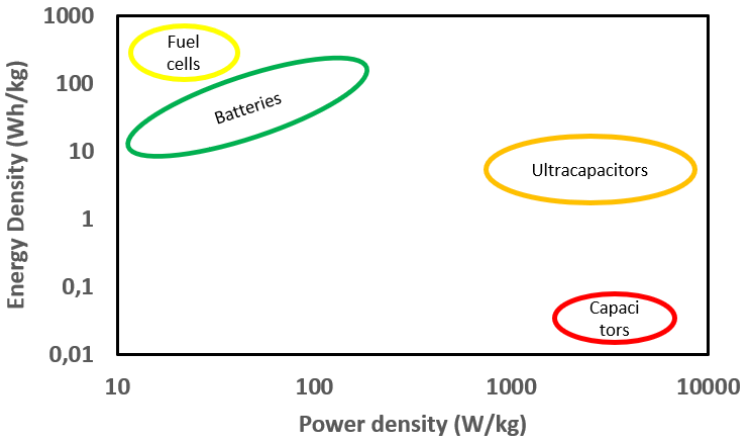

Figure 1: Power density and energy density obtained for fuel cells, batteries, capacitors, and ultracapacitors

A battery is made of two electrodes connected to a current collector. One of them is positively charged and called cathode while the other is negatively charged and called anode. Besides, an ionic conductor, called electrolyte, ensures the migration of ions between the electrodes. The reaction sites are located in the electrodes and once connected externally, chemical reactions take place simultaneously at both electrodes, releasing electrons and allowing the user to harvest the current. Chemical reactions are reversible and electrons can migrate in both directions depending on the external voltage applied. During charging the cathode oxidises, the anode reduces and the cations migrate to the anode. The electron current created will flow from the cathode to the anode. During discharge the anode oxidises, the cathode reduces and the cations migrate towards the anode. The electron flow will move from the cathode to the anode. Figure 2 resumes this phenomenon.

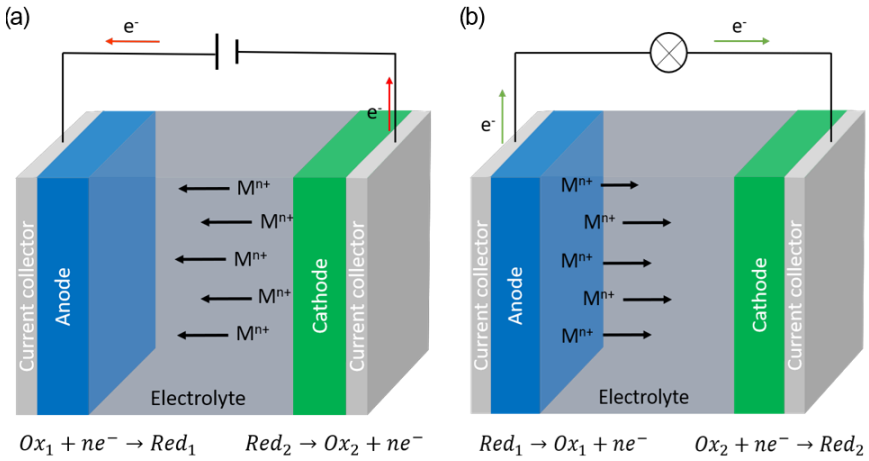

Figure 2: Illustration of charging (a) and discharging (b) process in batteries

Several kinds of batteries are commercially available. The most common among them are listed in Table 1 along with some of their characteristics.[3-4] It is evident from their properties that lithium batteries are the most promising devices. Indeed, their energy density, cycling rate, and voltage are much higher, which make them particularly interesting for application in portable devices.

Table 1: Characteristics of the main commercially available batteries

	Lead	NiCd	NiHM	Alcaline	Li-ion	LiPo
Cathode	PbO_2	NiOOH	NiOOH	MnO_2	$Li_{1-x}CoO_2$	$Li_{1-x}CoO_2$
Anode	Pb	Cd	HM	Zn	Li_xC_6	Li_xC_6
Energy density ($W.h.kg^{-1}$)	30-50	45-80	60-120	80	150-190	150-190
Voltage (V)	2	1.2	1.2	1.5	3.6	3.6
Cycling	200 to 300	1500	300 to 500	50	500 to 1000	300 to 500
Operating temperature (°C)	-20 to 60	-40 to 60	-20 to 60	0 to 65	-20 to 60	0 to 60
Self-discharge (%/month)	5	20	30	0.3	10	10

Lithium batteries are divided into several sub-categories: lithium-ion, lithium-sulphur, and lithium-oxygen. Li-ion batteries are widely marketed while Li-S, Li-O_2 are still in the development stage.

Due to their exceptional performance, lithium-ion batteries attract increasing attention and are extensively marketed. The main composition of this battery includes a graphite-type carbon anode and a $LiCoO_2$ cathode (Figure 3). In this system, the cathode is the main source of lithium.

Lead, NiCd, NiHM and alkaline batteries energy storage principle is based on metal oxidation and reduction reactions, while lithium-ion batteries energy storage process can be based on one of this three phenomena: conversion, capacitance, and intercalation.

The conversion is based on the breaking and creation of new chemical bonds during the insertion and extraction of lithium during the cycles. Two types of conversions are currently known and are

described in equations 1.1 and 1.2.[5] However this kind of battery also suffers from severe problems such as high hysteresis, low-rate capability and rapid capacity loss.

$$M'X_z + yLi \leftrightarrow M + zLi_{(y/z)}X \quad (1.1)$$

$$yLi + X' \leftrightarrow Li_yX \quad (1.2)$$

M' = transition metal ions, M = reduced transition metal ions, X = halogen or chalcogenide ions.

The energy storage of the capacitor is based on the storage of electrostatic charges at the electrode-electrolyte interface. The ions in the electrolyte are adsorbed and desorbed from the interface of the electrode, meaning that no charge transfer reaction occurs. The devices based on this phenomenon have a high-power density (10kW/kg) and lifetime, but suffer of a limited energy density (5Wh/kg).[6]

Energy storage of currently commercialised lithium-ion battery is based on lithium-cation intercalation. During charging, lithium cations are inserted in the graphite electrode, while in discharge, the lithium cations move from the graphite into the $LiCoO_2$ electrode. These phenomena are illustrated in Figure 3 and resumed in the following two equations:[7]

$$LiCoO_2 \leftrightarrow \frac{1}{2} Li^+ + \frac{1}{2} e^- + Li_{0.5}CoO_2 \quad (1.3)$$

$$C_6 + Li^+ + e^- \leftrightarrow LiC_6 \quad (1.4)$$

Charge/discharge processes are based on the reversible lithium intercalation in the electrodes. Charging leads to the oxidation and delithiation of $LiCoO_2$ and to the reduction and lithiation of graphite. The opposite reactions occur during discharge.[8] The lithiation of the graphite occurs in stages such as LiC_{24}, LiC_{27} and LiC_{12} via first-order phase transitions reactions.[9] Some metastable insoluble Li_xC_6 can be formed during cycling which can passivate the electrode, thus avoiding any further irreversible process.

The major drawback of this kind of battery comes from the phase transition of $LiCoO_2$ on discharge. The original hexagonal phase of $LiCoO_2$ is transformed into monoclinic $Li_{0.5}CoO_2$ and causes a c-axis expansion of 2.6% with negligible variation in the a-axis. The transformation of the lattice causes mechanical stresses leading to a decrease in the performance of the battery.[10] Other important challenges of Li-ion batteries is its low power density and low charging rate to meet the high energy requirements of modern renewable energy storage systems.

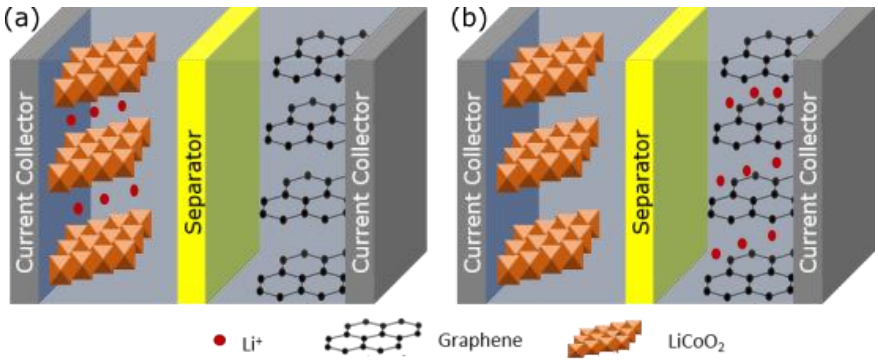

Figure 3: Representation of discharging (a) and charging (b) phenomenon in Li-ion batteries

The drawbacks of Li-ion batteries lead to the research of other kind of Li batteries, for example lithium sulphur (Li-S) cells. Their electrochemical process involves the transfer of two electrons per sulphur, giving a much higher theoretical energy density (3680 $mAh.g^{-1}$) compared to Li-ion batteries.[11] The main components of the battery as shown in Figure 4, comprise a lithium foil, a sulphur electrode, an electrolyte and a separator. The main reaction that occurs in the Li-S cell during charge/discharge processes is described in the following equation. During the discharge process Li_2S is formed via lithium intercalation in S_8 electrode while during charge process the lithium deintercalated to give back S_8.

$$S_8 + 16\,Li \leftrightarrow 8Li_2S \qquad (1.5)$$

Despite promising results, this kind of battery has several weaknesses. Sulphur and its various discharge products have low ionic and electrical conductivity which increase the internal resistance of the battery and reduce the energy efficiency of the battery. Moreover, the formation of an insoluble insulation layer made of Li_2S and Li_2S_2 on the surface of the sulphur particles during discharge contribute to the poor conductivity as it impedes sulphur reduction and limits its use. More importantly, lithium-sulphur battery suffers from the shuttle effect caused by polysulfides. Soluble polysulfides are produced at the cathode during redox processes and diffuse throughout the separator and can react with the anode to form an insoluble sulphide layer (Li_2S, Li_2S_2) retarding the fast access to Li, and leading to a rapid decrease in capacity.[12]

To resume, lithium-sulphur battery system is difficult to control due to the complex electrochemistry of sulphur. System instability leads to the formation of soluble polysulphide by products, resulting in inefficient charging process and battery death.[13]

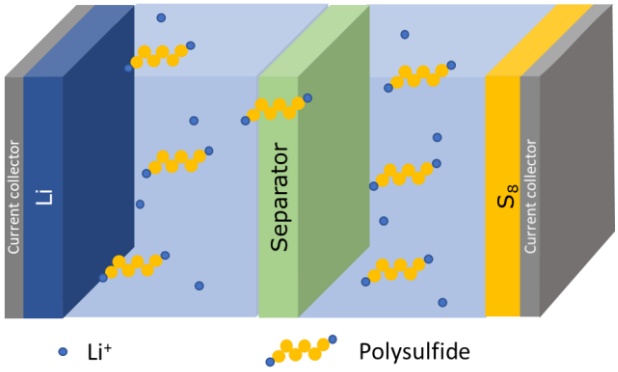

Figure 4: Representation of a traditional Li-S batteries

Lithium-oxygen battery attracts more and more attention. This battery is based on the reaction between lithium cation and oxygen.[14] Figure 5 reports the performances of most batteries, and show that lithium-oxygen batteries possess the highest energy density compared to other battery systems, which is close to that produced by a device based on gasoline combustion.

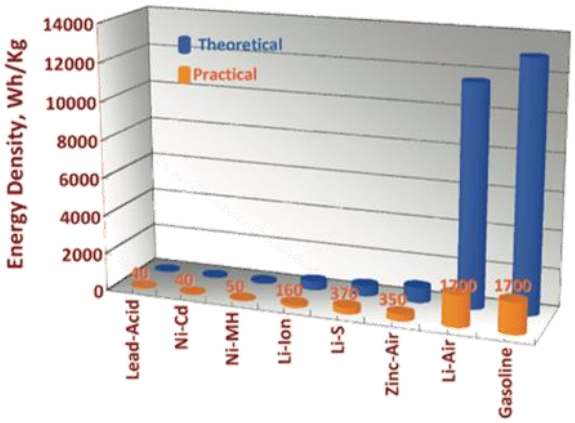

Figure 5: Graph representing the energy density (practical and theoretical) of different kinds of batteries compared to gasoline.[15]

Lithium-oxygen are thus considered as the best candidate for a high-efficient and future battery in terms of power density and energy density. Their high theoretical energy density increases by approximately 10 times compared to the actual performances of lithium-ion batteries.[15] This PhD will focus on the study of lithium-oxygen batteries and their optimisation via cathode design.

II) Lithium-oxygen batteries

Abraham and Jiang described the first lithium oxygen battery in 1996.[15] It was made of a lithium disc as anode associated with a porous carbon cathode. The connection between electrodes was ensured by a polymer electrolyte. Unfortunately, the low rechargeability of the system did not allow its immediate development. It was only 10 years later that Ogasawara et al. demonstrated the reversibility of this kind of battery.[16] Their system consisted of a lithium metal anode, a cathode composed of a mixture of porous carbon and MnO_2, and an organic solvent-based electrolyte.

Contrary to currently commercialised lithium-ion batteries, which operate through a mechanism of insertion and de-insertion of Li^+ ions into the electrodes, this new type of battery uses the reaction between Li^+ ions and oxygen to store energy. Oxygen is supplied from an external source. The system consists of a lithium anode, a non-aqueous electrolyte and a porous carbon cathode.

The fundamental chemistry of lithium-oxygen batteries involves lithium dissolution and deposition at the lithium anode and oxygen reduction reaction (ORR) and oxygen evolution reaction (OER) at the cathode. During the discharge, the reduction of oxygen leads to the formation of lithium superoxide LiO_2 through a one electron transfer (Equation 2.1). This superoxide can react with another lithium cation Li^+ and an electron (Equation 2.2) or undergo a dismutation reaction, to form lithium peroxide Li_2O_2 (Equation 2.3). The overall reaction is described in Equation 2.4.[17-18]

$$O_2 + Li^+ + e^- \rightarrow LiO_2 \quad (2.1)$$

$$LiO_2 + Li^+ + e^- \rightarrow Li_2O_2 \quad (2.2)$$

$$2LiO_2 \rightarrow Li_2O_2 + O_2 \quad (2.3)$$

$$2Li + O_2 \rightarrow Li_2O_2 \quad \Delta G° = -571{,}0\ kJ.mol^{-1} \quad (E° = 2.96\ V) \quad (2.4)$$

To be rechargeable, the Li_2O_2 previously formed during discharge must be able to be electrochemically decomposed into Li^+ and O_2 during charging. The decomposition of lithium superoxide is based on two main reactions involving a one or two-electron process. (Equation 2.5, 2.6, 2.7)

$$Li_2O_2 \rightarrow O_2 + 2Li^+ + 2e^- \quad (2.5)$$

$$Li_2O_2 \rightarrow LiO_2 + Li^+ + e^- \quad (2.6)$$

$$LiO_2 \rightarrow O_2 + Li^+ + e^- \quad (2.7)$$

Since Li_2O_2 is an insoluble solid, it is essential to decompose it completely as it could passivate the cathode and thus reduce the performance of the battery. Charging and discharging processes are summarised in Figure 6.

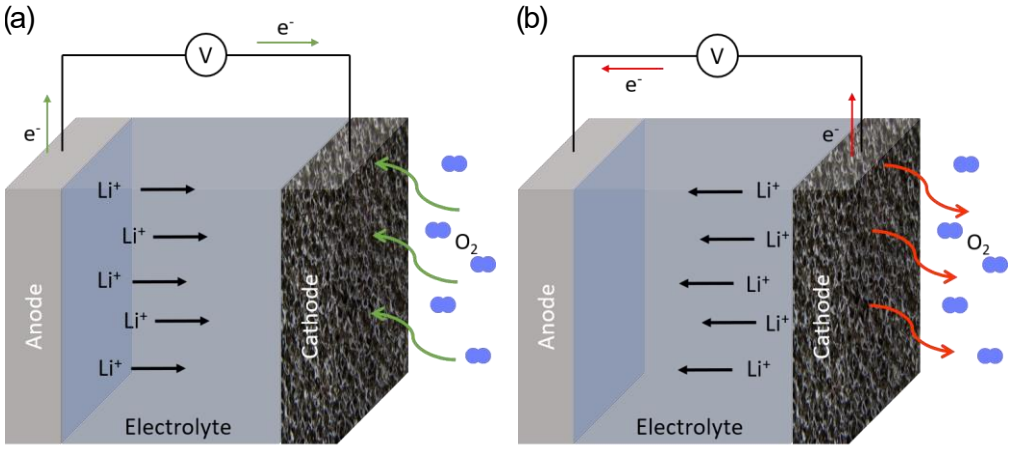

$$O_2 + Li^+ + e^- \rightarrow LiO_2$$

$$LiO_2 + Li^+ + e^- \rightarrow Li_2O_2 \qquad Li_2O_2 \rightarrow O_2 + 2Li^+ + 2e^-$$

$$2LiO_2 \rightarrow Li_2O_2 + O_2 \qquad Li_2O_2 \rightarrow LiO_2 + Li^+ + e^-$$

$$2Li + O_2 \rightarrow Li_2O_2 \qquad LiO_2 \rightarrow O_2 + Li^+ + e^-$$

Figure 6: Operating principle of a Li-O_2 battery during (a) discharge and (b) charge

In the following section, we present a review of research realised on each part of Li-O_2 battery. Firstly, we consider the recent developments concerning the cathode and discuss in detail the effects of textural properties and chemical composition of the cathode on battery performance. In the second part, we focus our attention on the electrolyte which plays a crucial role in Li-O_2 battery. Key parameters of the electrolyte like solvent, lithium salt and additives will be critically analysed and summarised. Some prospective electrolytes will be proposed.

II.1) Cathode

Cathode is the site of the oxygen reduction reaction (ORR) and oxygen evolution reaction (OER). These reactions are directly related to the performance of the battery. It is vital to optimise it in order to obtain the best characteristics such as high capacity, power density, high round-trip efficiency and high cycling stability. The two important parameters that need to be controlled are the textural properties and the chemical composition.

Cathode textural properties have a huge influence on the performances of the battery. In order to optimise the Li_2O_2 deposition, the oxygen-electrode must establish a close contact between the lithium ions, the electrolyte, and the electrons. Li_2O_2 nucleation is driven by the adsorption of O_2 and Li^+ on the cathode surface; the higher the adsorption, the higher the number of nucleation sites and the greater the Li_2O_2 formation. As a consequence, maximum oxygen diffusion and electrolyte

retention will increase the contact between Li^+ and O_2 and promote Li_2O_2 nucleation sites on the electrode.

Regarding the composition, the ideal material should have high conductivity, the ability to catalyse the OER/ORR, and should be inert to the electrolyte. Due to the high probability of generating insoluble side products in case of battery instability, it is of prime importance to carefully select the right materials to increase this stability and consequently battery performance.

The aim of this section will be to evaluate the influence of the textural properties and the chemical composition of the cathode on the performance of the battery.

II.1.1) Textural properties

Textural properties play a crucial role in maximising the deposition of lithium peroxide. The solid Li_2O_2 formed during discharge will cover the electrode surface and occupy the surrounding space. To obtain more reaction sites to maximise Li_2O_2 deposition, a high surface area is required.

Kim et al.[19] tried to understand the role of porosity in a carbon electrode by studying the influence of micro and meso porosity. They synthetized two materials via carbonization using a triazine-based covalent organic polymer (TCOP). The first material was carbonised for two hours under a nitrogen atmosphere at 800°C (C-800), and the second one was physically activated via a carbonisation under carbon dioxide at 950°C for one hour (AC-950). The morphology of the obtained particles was analysed by scanning electronic microscopy (SEM) and the textural properties by nitrogen physisorption. A commercial hexagonally ordered mesoporous carbon (CMK-3) was also used for comparison and the results are shown in Figure 7.

C-800 material contained 96% micro-porosity with a pore size distribution from 0.5 to 1 nm and a specific surface area of 1022 $m^2.g^{-1}$. AC-950 material possessed both micro (0.5-0.6 nm) and mesoporosity (2-9 nm) with a micro/meso ratio of 55:45 and a specific surface area of 2003 $m^2.g^{-1}$. The commercial mesoporous carbon (5-6 nm) CMK-3 had a specific surface area of 789 $m^2.g^{-1}$ (Figure 7b-f). The difference of porosity between C-800 and AC-950 resulted from the carbonization. The distinctive pore-size structure of AC-950 was attributed to the destruction and collapse of the carbon structure during the physical activation process.

The effect of the pore size of carbon electrodes on the Li-O_2 cell was investigated by monitoring the formation of the discharge products at several capacities. Li_2O_2 discharge products were found to be distributed along pore channels that are well-accommodated within the porous cathode. More specifically, the discharge products in the AC-950 electrode were distributed in all the porous area, while the CMK-3 electrode had a denser distribution of Li_2O_2 in the porous channels. These observations were consistent with the electrochemical tests. The cell discharge capacity was 6003, 8433, and 9968 $mAh.g^{-1}$ for C-800, AC950, and CMK-3 respectively at a current density of 200 $mA.g^{-1}$ (Figure 7g).

This study highlights the importance of modulating the pore size with respect to lithium peroxide formation. Mesopores provide a higher lithium peroxide formation compared to micropores, thus increasing the performance of the battery.

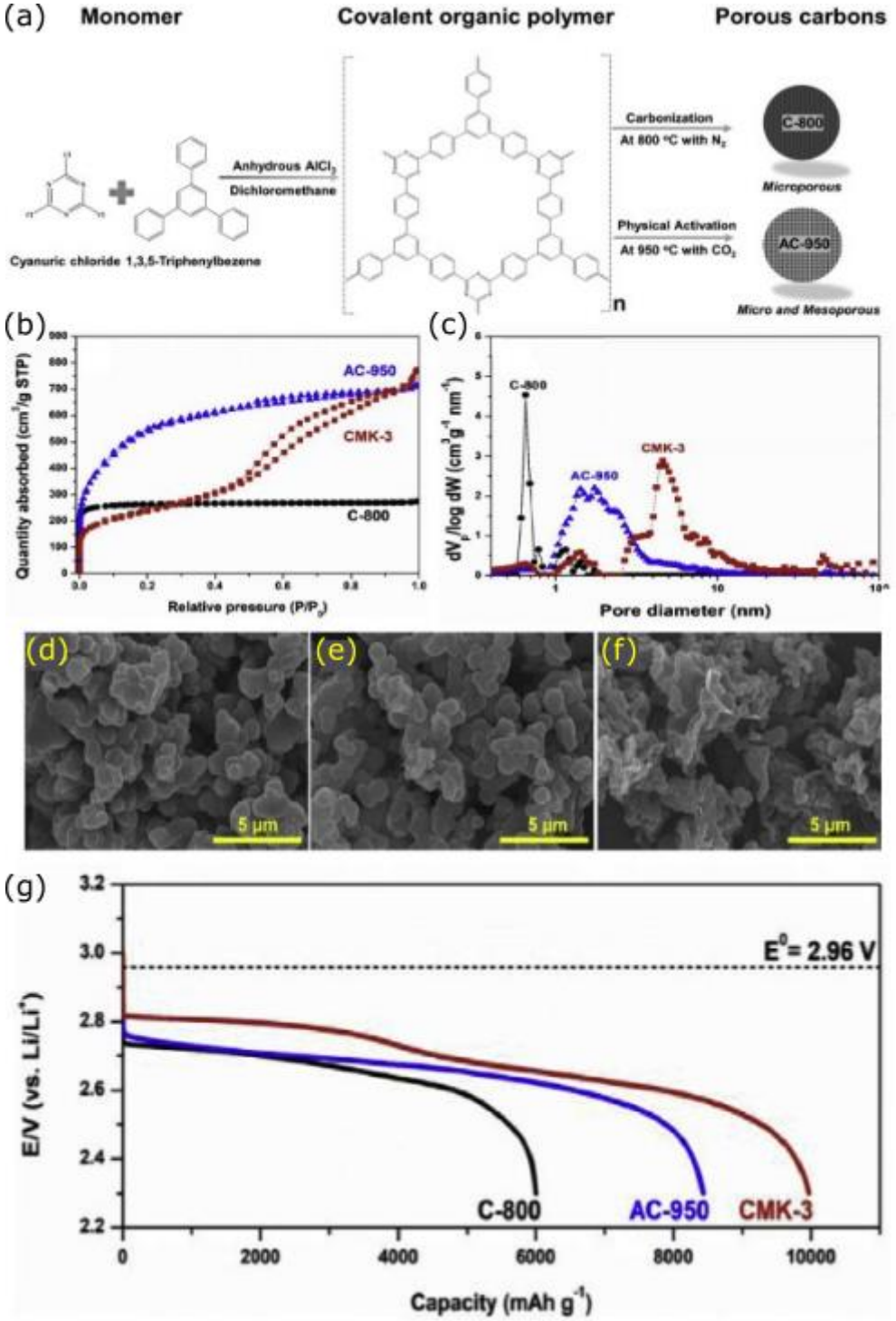

Figure 7: (a) Illustration of the fabrication of different porous carbon cathodes derived from a triazine-based covalent organic polymer (TCOP); (b) N_2 adsorption-desorption isotherms and (c) pore size distributions of C-800, AC-950, and CMK- 3; SEM microphotographs of (d) C-800, (e) AC-950, and (f) CMK-3; (f) 1st discharge-charge curves of Li-O_2 cells with the C-800, AC-950, and CMK-3 electrodes at a current density of 200 mA.g^{-1}. [19]

Doo et al.[20] studied the influence of porosity by comparing three different types of carbon: YP-50F, CEP21S and an aerogel. Their properties as determined in their study are described in Table 2.

Table 2: Results obtained for Doo et al. study, comparison and link between porosity and battery performances. [20]

	Pore Volume ($cm^3.g^{-1}$)	BET surface area ($m^2.g^{-1}$)	Pore diameter (nm)	Discharge Capacity ($mAh.g^{-1}$)	Volume ratio of Li_2O_2 in carbon pores
Aerogel	2.53	688	25-40	4155	0.61
YP-50F	0.55	1908	< 2	264	0.18
CEP21S	0.85	1195	< 2	124	0.05

The results show that the discharge capacity decreases with increase in specific surface area. Since the formation of lithium peroxide is a surface phenomenon, more lithium peroxide should be formed with increase in surface area of electrode, which should result in higher performance of the battery. However, this study presented the opposite and showed that the most important parameter is not the specific surface area but the size of the pores. Mesopores allowed to optimise the volume ratio of Li_2O_2 in carbon pores compared to the micropores. This ratio increased from 5% for the microporous CEP21S to 61% for the mesoporous aerogel, resulting in an increase in capacity from 124 to 4155 $mAh.g^{-1}$.

In order to properly assess the impact of cathode porosity on battery performance it is important to evaluate the homogeneity of lithium peroxide formation throughout the electrode. Zhang et al. [21] studied the formation of lithium peroxide on single-wall carbon nanotube SWNT/CNT buckypapers of different thicknesses (19.7 µm, 65.5 µm, 219.2 µm) and the results are shown in figure 8.

The specific surface area and the pore size distribution of the SWNT/CNT buckypapers were determined by N_2 physisorption and the specific surface area was determined to be 173 $m^2.g^{-1}$ with an average pore size of 9nm. The porosity of the SWNT/CNT buckypapers was estimated at 77% and the pore size distribution showed a maximum at 3.4 nm and indicated the presence of mesopores of all diameters between 2 and 20 nm. (Figure 8a)

The relation between the discharge capacity and the thickness of the electrode is shown in Figure 8 b. Capacity of 2550, 1580 and 350 $mAh.g^{-1}$ were achieved for 19.7, 65.5, and 219.2 µm electrodes respectively. It was observed that the capacity decreased with increase in thickness. This difference in performance as a function of cathode thickness was explained by the presence of an oxygen concentration gradient. The oxygen concentration was found to be non-uniform inside the O_2 electrode which resulted in a nonuniform deposition of the Li_2O_2 discharge product. More specifically, the porosity near the oxygen side decreased faster than that close to the membrane. The correlation between the specific capacitance and the thickness of the electrode can be translated into the fact that the discharge product is deposited near the electrode/oxygen interface and in the oxygen diffusion road. When the thickness of the O_2 electrode is greater than the oxygen diffusion length, most of the pore volume is not filled by the discharge medium, therefore the specific capacitance decreases. The SEM micrographs of two different surfaces of a cathode of 65.5 µm thickness after discharge (fig. 8 d,e) presented a clear difference of surface morphologies. The surface of the oxygen side was fully covered by the discharge product while the membrane side still had a high porosity. This

experiment confirmed that it is necessary to create a specific architecture for the cathode in order to create an optimal pathway for the oxygen.

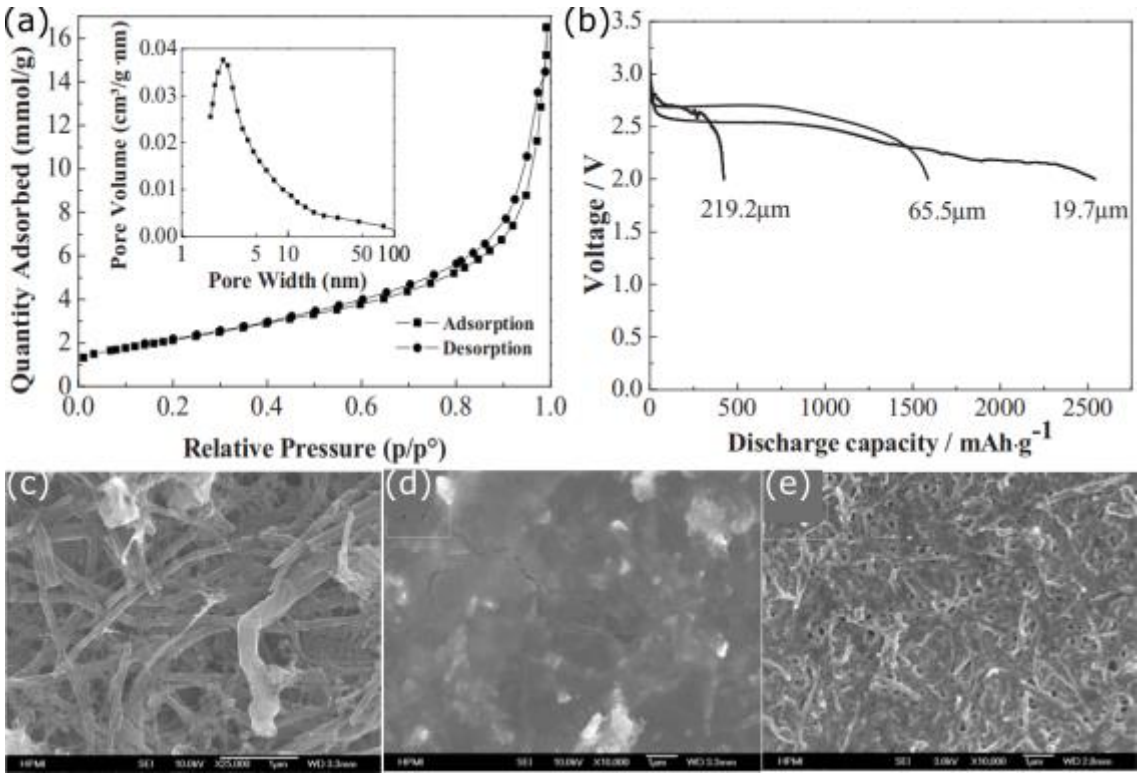

Figure 8: (a) N_2 isotherm and pore size distribution measured on buckypaper, (b) discharge curves from Li-O_2 cells made with different electrode thicknesses, (c) SEM image of the buckypaper, SEM images of the oxygen electrode surfaces at (d) separator and (e) oxygen sides after discharge. [21]

In order to evaluate the oxygen pathway through the electrode Tan et al.[22] designed a gradient porous cathode and discussed its impact on the performances of the Li-O_2 battery. The gradient porous cathode was formed by binding three carbon layers with different pore sizes. The first layer had the largest pores (500 nm) and was located on the oxygen side, the layer with the smallest pores (100 nm) was on the membrane side and between these two layers there was an intermediate layer with pores of 300 nm. The morphology of this electrode as observed by SEM is shown in Figure 9 a-d.

The galvanostatic discharge obtained from the layered electrode is shown in Figure 9 e. In order to compare the influence of the porosity gradient, two other cathodes with pores of 100 and 500 nm respectively were used for comparison. The discharge capacity obtained with the gradient porous cathode was found to be the highest (2120 $mAh.g^{-1}$) followed by the 100 nm porous film (1713 $mAh.g^{-1}$) and the 500 nm porous film (375 $mAh.g^{-1}$). This result demonstrated that a porosity gradient can increase the performance of the battery. Once the discharge was completed, the electrodes were analysed by SEM to verify the homogeneity of the product formation on the electrodes (fig. 9 f,g) The uniform porous cathode exhibited toroid like products on both side of the electrode. However, the particle sizes were observed to be larger at the separator side. The increase in size resulted from a lower current density. The current density is directly related to the oxygen concentration.[23] The lower

the oxygen concentration, the lower the current and the larger the particles. The gradient porous cathode showed toroidal like products on the oxygen side surface, like those obtained with the uniform porous cathode, while at the separator side the particles were smaller. This decrease in size revealed the presence of higher oxygen concentration, indicating a more efficient oxygen transport provided by the porous gradient. With this study, sufficient evidence was provided to justify that creating a pathway for oxygen within the cathode can improve the formation of discharge products and increase the performance of the battery.

It has been shown that the textural properties are essential for the improvement of battery performances. It is interesting to note that it is the pore size but not the specific surface area that is favourable for lithium peroxide depositions and for increased battery performance. However, porosity alone cannot ensure an efficient cathode. It must be controlled in order to exploit the entire cathode volume. Pores that are too small can clog the cathode on the oxygen side and prevent its full volume from being used. It is important to create a pathway through the electrode in order to increase the oxygen concentration on the separator side. This pathway will allow the full volume of the cathode to be used and increase the performance of the battery.

The first chapter of the thesis will thus focus on the design of a structure with hierarchical micro-meso-macroporosity following Murray's law to optimise the oxygen pathway in the cathode. The optimisation of the diffusion of oxygen will maximise the formation of the discharge products and thus increase the performance of the battery.

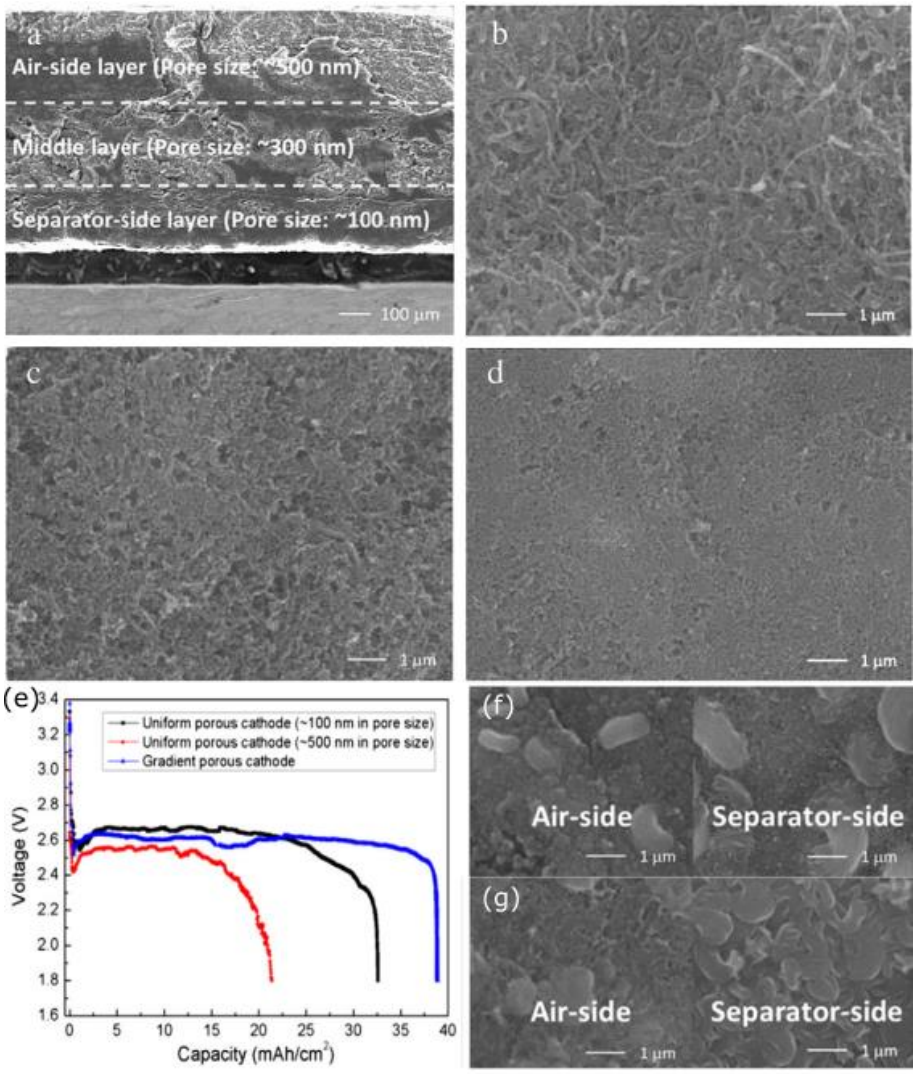

Figure 9: SEM image of (a) the cross section of the gradient porous cathode (b) the oxygen-side, (c) middle, and (d) separator-side layer, (e) Galvanostatic discharge curves at 0.1 mA/cm², SEM image of the cathode after discharge (f) uniform porous cathode (g) and gradient porous cathode. [22]

II.1.2) Chemical composition of the cathode

As previously stated, the oxidation and reduction of oxygen leading to the formation and dissolution of lithium peroxide occurs in the cathode. The selection of the cathode material is therefore of prime importance. The ideal material should possess a high electrolyte wettability to limit the ionic transfer resistance, to exhibit good electrical conductivity, and to have the ability to accelerate the kinetics of both ORR and OER processes. Several classes of materials identified in the literature will be discussed in this section.

II.1.2.a) Carbon materials

Carbon had been widely used as an electrode material in various batteries because of their availability, low cost, light and good electrical conductivity. Carbon can be found in different forms in the cathode of lithium-oxygen batteries. It can be classified into three main categories: commercial carbon, carbon with a specific shape and finally nitrogen-doped carbon. All categories will be discussed in detail in the following subsections.

Commercial carbons are among the widely used materials in lithium oxygen batteries. The most employed are the Super P, the Ketjen Black and the CMK-3.[16,29,31-32]. Gasteiger et al.[33] compared 7 carbon types which are listed in Table 3 along with their characteristics. The external specific surface area was calculated by subtracting the volume of the micropores from the total volume.

Table3: Surface area analysis data of cathodes coated on Al foil.[33]

Carbon type	Graphitized (yes/no)	Total Specific surface area ($m^2.g^{-1}$)	External Specific surface area ($m^2.g^{-1}$)
Timcal Super C65 (C)	No	50	50
Tanaka Va-type (VA)	Yes	82	82
Tanaka EA-type (EA)	Yes	128	128
Tanaka V-type (V)	No	152	137
Tanaka BA-type (BA)	Yes	193	193
Tanaka E-type (E)	No	533	432
Tanaka B-type (B)	No	1123	513

Firstly, discharge profiles of batteries made with those electrodes, as presented in Figure 10, show that the nature of the carbon does not significantly affect battery performance. The difference in capacity comes from the textural properties. The higher the specific surface area, the higher the capacity. However, there is a limitation to this study as it only took into account the volume of micropores but did not clearly state their sizes. As previously mentioned, pore size has a major impact on the performance of the battery.

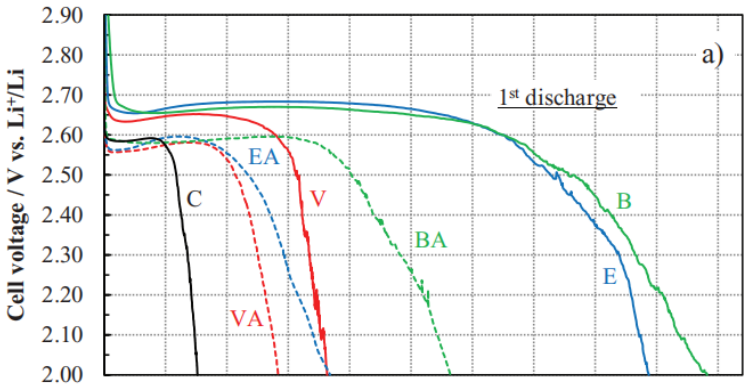

Figure 10: First Galvanostatic discharge curves for all carbon. [33]

Mao et al.[34] compared activated carbon SY TC-03 (AC), Ketjen black, Super P and Vulcan-XC72. Their characteristics are listed in Table 4.

Table 4: The discharge capacity of various carbon type and their related physical parameters.[34]

Carbon type	Discharge Capacity ($mAh.g^{-1}$)	Carbon Loading ($mg.cm^{-3}$)	Specific surface area ($m^2.g^{-1}$)	Average pore diameter (nm)	Pore Volume ($cm^3.g^{-1}$)
Super P	4255	3.03	259	12.8	10.6
XC 72	1706	3.54	200	10.9	10.3
AC	2311	3.28	1759	4.1	10.2
KB	3374	3.76	1724	6.5	11.7

Several hypotheses can be made from the data in Table 4. Firstly, Super P carbon, which has the largest pores, was found to have the highest capacity. These results are in agreement with the previous statements. Carbon KB has smaller pores than Carbon XC 72 but was observed to have a higher capacity. This increase in capacity is due to the larger number of pores in Carbon KB compared to XC 72. Indeed, when comparing the pore volumes, the carbon KB has a higher pore volume which indicates the presence of more pores in its structure and therefore a higher capacity. Activated carbon (AC) has the smallest pores. However, for the same pore volume, its capacity was found to be higher than that of the XC 72 carbon which has larger pores. This increase in capacity may be due to the activation process that the AC carbon underwent. During this activation the structure was partly destroyed and allowed micropores to be connected to the mesopores allowing better diffusion of oxygen within the electrode resulting a higher capacity.

The textural properties are the most important parameter for this kind of cathode. In this context, several carbon forms have emerged in order to achieve the best characteristics. The properties of graphene as cathode were investigated. This specific structure possesses a high electron transfer rate, large surface area (≈ 2630 $m^2.g^{-1}$), high conductivity, and high thermal and chemical stability.

Sun et al.[35] used a graphene nanosheet as cathode material and showed improved electrochemical performance with a capacity of 8705.9 $mAh.g^{-1}$ compared to 1053.8 $mAh.g^{-1}$ obtained with a Vulcan XC-72 carbon electrode (Figure 11). These results can be explained by the structure of the graphene nanosheet which forms an ideal three-phase 3D electrochemical zone that increases the diffusion channels of the electrolyte and oxygen, and leads to an increase in the efficiency of the catalytic reaction (Figure 12). Moreover, the active edge sites contribute significantly to the higher electrocatalytic activity towards ORR. The hypothesis that could explain this reactivity is the presence of dangling bonds that are highly reactive towards oxygen. Therefore, the ORR activity will be higher.

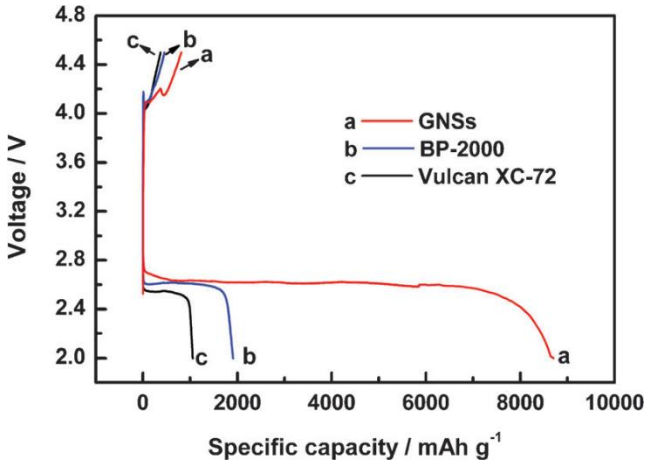

Figure 11: Discharge–charge performance of lithium-oxygen batteries with Graphene nanosheet, BP-2000, and Vulcan XC-72 cathodes at a current density of 75 mA.g^{-1}.[35]

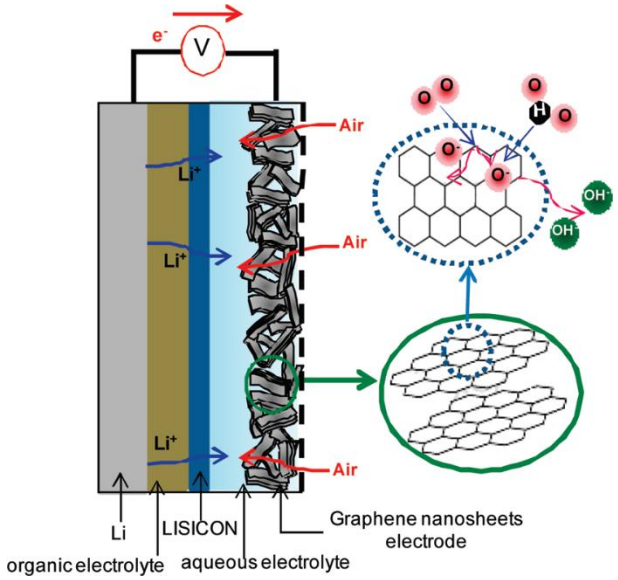

Figure 12: Structure of the rechargeable Li-oxygen battery based on graphene nanosheet as an O_2 electrode (hybrid electrolyte). [36]

Zhou et al.[36] confirmed that graphene possesses good catalytic performances with regard to ORR. The low overpotential comes from both the presence of dangling σ-bonds from sp^3 carbon atoms at the edges and defects of graphene nanosheet.

Carbon nanotubes (CNTs) have high chemical and thermal stability, high conductivity, high tensile strength and large surface area and could be a good candidate for cathode material.[37-38] Dong et al.[39] synthesized a highly ordered and ultra-long carbon nanotube array (vertically aligned carbon nanotube VACNT-Ta) by thermal chemical vapour deposition (TCVD) which showed a larger specific surface area (206 $m^2.g^{-1}$) and fewer surface defects than powder CNTs or commercial VACNTs (80 $m^2.g^{-1}$) (Figure 13 a).

First discharge-charge profiles as reported are presented in Figure 13 b. VACNTs-Ta showed a larger discharge capacity, better rate capability and cycling stability compared to commercial VACNTs. These

electrochemical results were explained by the promotion of ORR and OER reactions due to enhancement of the transport of ionic species, electrons and gas. The large surface area of the nanotubes led to an increase in the number of active sites and was favourable for the reaction between the soluble catalysts in the liquid electrolyte and the formation of Li_2O_2 on its surface (Figure 13 c). Therefore, it considerably reduced charging overpotential and improved energy efficiency. Lee et al.[40] synthesized a highly oriented CNT sheets that provided an electrical conductivity of 389 $S.cm^{-1}$ and a mesoporous structure with a specific surface area of 171 $m^2.g^{-1}$. This CNT sheet achieved a maximum discharging capacity of 1810 $mAh.g^{-1}$ which was found to be better than that of CNT bucky paper (300 $mAh.g^{-1}$) and vertically aligned multiwall CNT cathode electrode (~1000 $mAh.g^{-1}$), thereby showing the importance of the organisation of nanotubes.

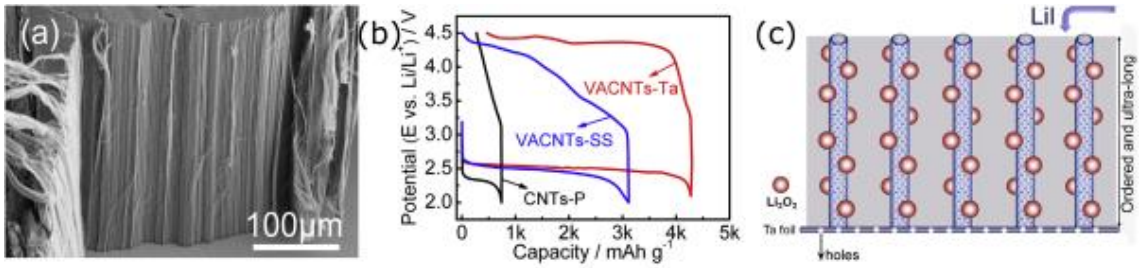

Figure 13: (a) SEM images of the VACNTs-Ta, (b) First discharge-charge profiles of VACNTs-Ta, VACNTs-SS and CNT-P, (c) Scheme of the Li_2O_2 formation toward the VACNTs-TA .[39]

Nanofibers are another widely used form of carbon (CNFs). Lü et al.[41] investigated the electrochemical performance of the CNF-grafted cathodes that displayed a maximum discharge capacity of 20000 $mAh.g^{-1}$ under the current density of 937 $mA.g^{-1}$. This cathode was able to reach 200 cycles under a 0.06 $mA.cm^{-2}$ current density. It is important to note that the current density used is very low to get a good cycling performance. In order to increase the performances, Song et al.[42] prepared graphitic carbon nanofiber web by varying the pyrolysis temperature. Their electrochemical tests, as presented in Figure 14, showed that an increase in the degree of graphitization coupled with a decrease in surface defects leads to a decrease in polarization and an improvement in cyclability compared to low graphitized nanofibers with many surface defects.

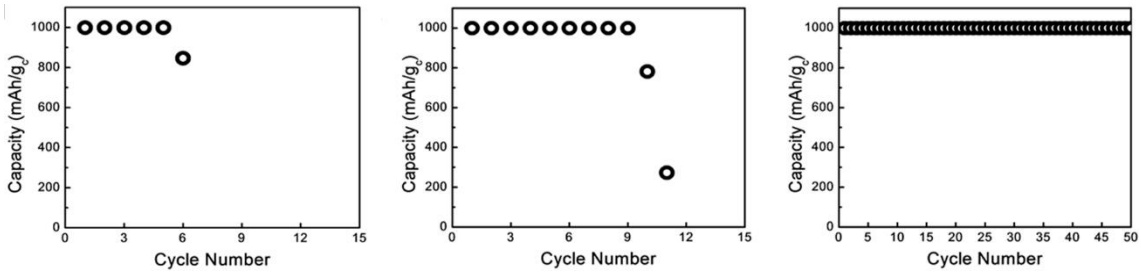

Figure 14: Cycling performances of CNF electrodes pyrolyzed at several temperature (a) CNF 1000, (b) CNF 1200 and (c) CNF 1400.[42]

Jung et al.[43] used carbon sphere as cathode material (triple hierarchical porous carbon spheres THPC). The fabrication process, the SEM micrographs, and the N_2 physisorption isotherms are presented in Figure 15 a-d. In order to evaluate its electrochemical performance, a comparison with super P carbon was carried out and showed an increase in energy efficiency from 63% to 70%. Discharge capacities,

as depicted in Figure 15 e, showed an increase for THPC cathode from 2427 mAh.g^{-1} to 3891 mAh.g^{-1} compared to Super P electrode. Moreover, the end potential of the carbon sphere during charge was observed to be 4.15 V, which is 0.33V lower than that of Super P, illustrating a system stabilization. This improvement in performance came from the ordered porous carbon structure, optimising the diffusion of the oxygen flow as well as the immersion of the electrolyte, while simultaneously offering an efficient space for the deposition of Li_2O_2.

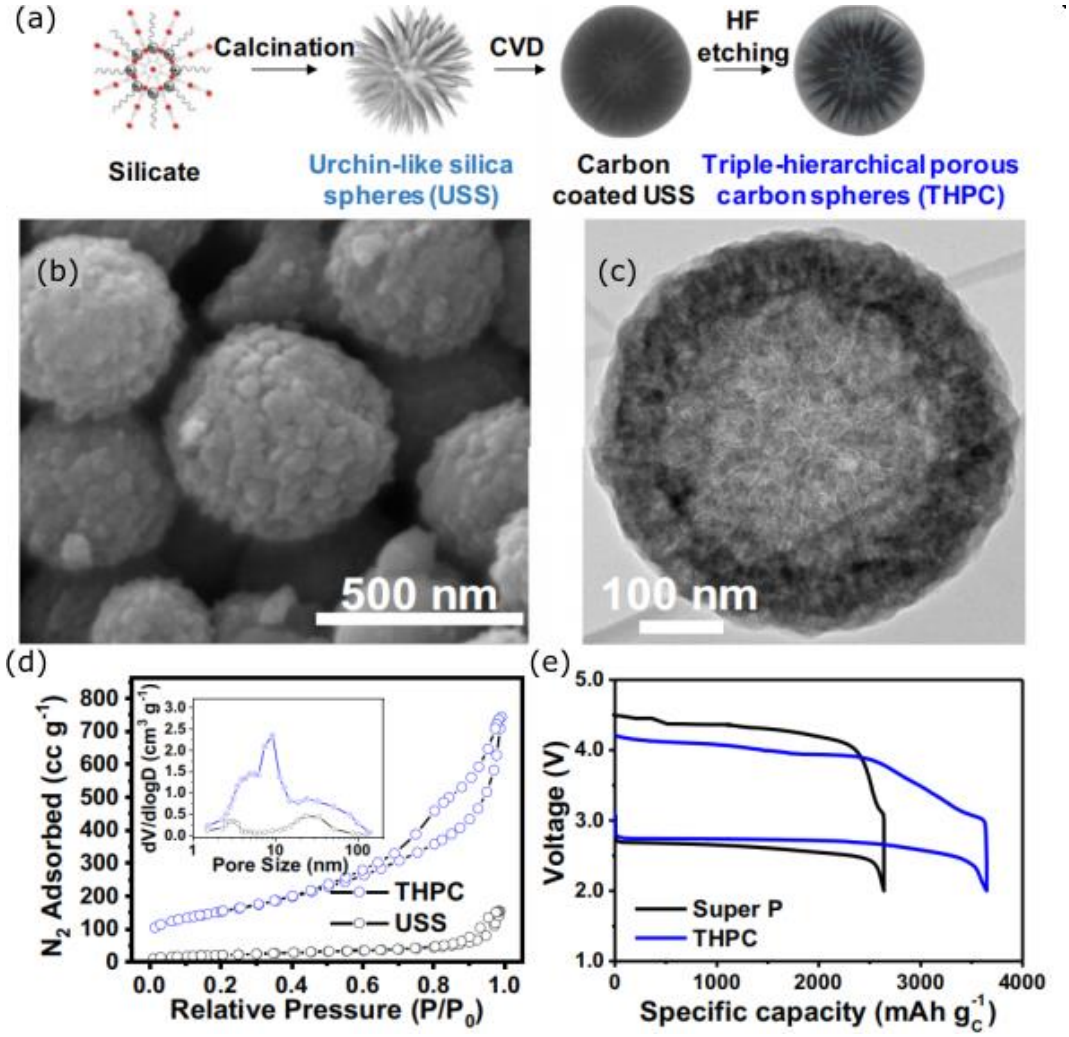

Figure 15: (a) Schematic illustration for fabrication process of triple hierarchical porous carbon spheres (THPC) (b) SEM and (c) corresponding TEM images of THPC, (d) , N2 adsorption–desorption isotherms with pore size distribution curve for the USS and THPC in the inset (e) Discharge and charge profile at 100 mA.g^{-1} with a voltage window of 2.0–5.0 V for Super P and THPC carbon material.[43]

Nitrogen doping of carbon materials leads to a modification of the surface and electronic properties, and improves the oxygen reduction reaction catalytic activity of the carbon.[44] O_2 molecule prefers to adsorb on the graphene surface with the two O atoms close to two C atoms along the diagonal of the C_6 ring. The adsorption of O_2 molecules is based on the charge transfer occurring between them and the graphene sheet. N atom has one electron more than C atom. As the adsorption is based on the charge transfer, nitrogen doping will enhance this phenomenon. For the adsorption of a single O atom

on the graphene surface, N-doping increases the adsorption energies, thus promoting interactions with oxygen (Figure 16).

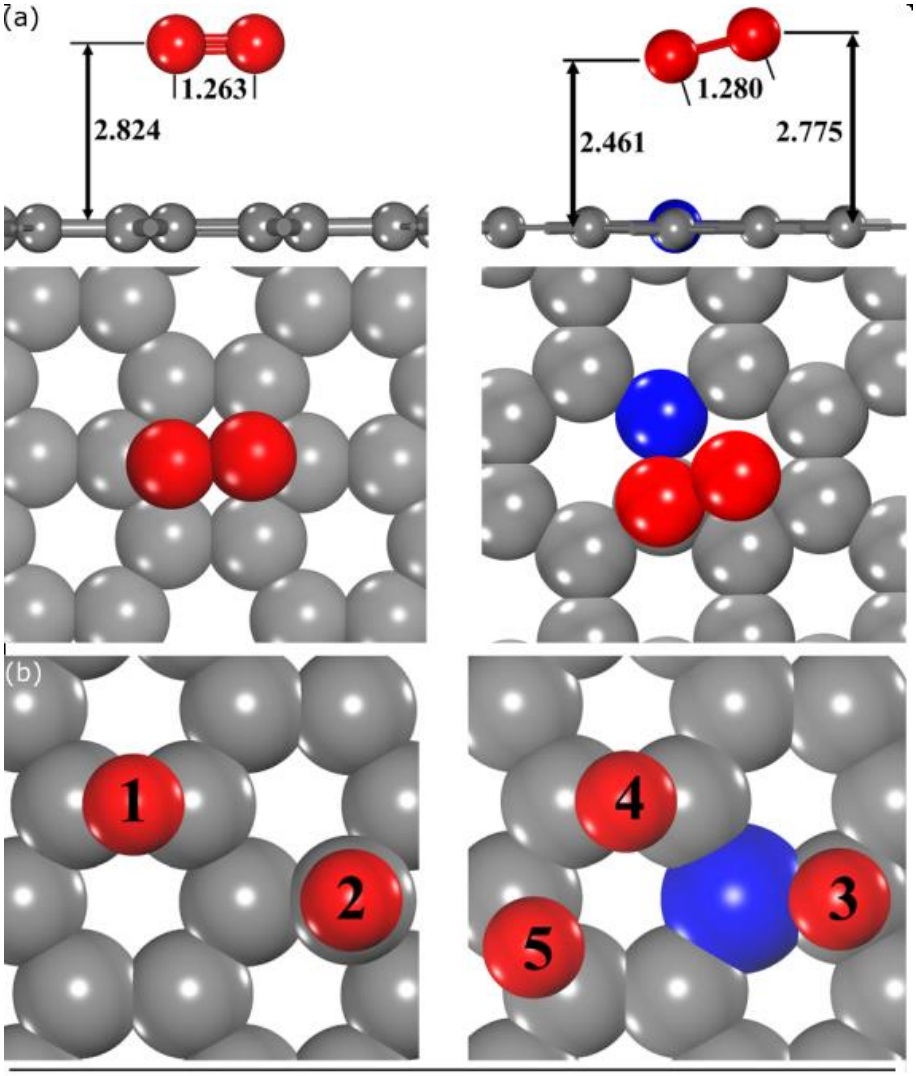

	Graphene		N-doped graphene		
Adsorption sites	1 (bridge)	2 (top)	3 (top)	4 (bridge)	5 (edge)
E_{ad} (eV)	3.97	3.25	4.68	4.47	4.08
C-O bond length (Å)	1.472	1.418	1.323	1.443	1.493
	1.472			1.536	1.499
Distortion, *h* (Å)	0.340	0.398	0.544	0.336	0.321
	0.340			0.299	0.329

Figure 16: (a) The atomic geometry of O_2 molecule physically adsorbed on graphene (left) and N-doped graphene (right). The grey, red, and blue spheres are C, O, and N atoms, respectively. The numbers are the corresponding marked distances in angstrom, (b) Schematic view of O atom adsorbed on graphene (left) and N-doped graphene (right) with the local atomic distortions and adsorption energies of O atoms at different sites. [44]

Xu et al.[45] synthesised a hierarchical porous nitrogen doped three-dimensional graphene (N-3DG) by combining hydrothermal self-assembly and annealing process (Figure 17 a,b and c) with a surface area of 137 $m^2.g^{-1}$ and two pore size distributions in the range of 1-80 nm and 80-180 nm (Figure 17 d,e). This material exhibited a higher specific capacity and better cycle stability than its undoped counterpart. Figure 17 f,g present the cycling performances obtained at a fixed capacity of 500 $mAh.g^{-1}$ with a current density of 100 mA g^{-1} for the nitrogen-doped material and its pure carbon counterpart. The N-doped cathode reached 21 cycles with a stable reversible capacity. The initial round-trip, which is the percentage of electricity put into storage that is later retrieved, was around 66%. The discharge and charge plateaus were about 2.5V and 4.6 V respectively, and after 21 cycles they remained at the same potential. The charge voltage plateau corresponds to the OER process and the discharge plateau to the ORR process. The theoretical potential for the formation and decomposition of Li_2O_2 was about 3V. Experimentally, the higher the charge plateau and the lower the discharge plateau, the more degradation will occur in the battery, such as electrolyte decomposition. The difference between the two plateaus is called the overpotential and indicates the polarisation of the battery. The non-nitrogen-doped cathode only cycles 8 times with an initial round trip of 61% and a charge plateau of 4.4V. The overpotential increases considerably over cycles. After 8 cycles, the discharge plateau reaches 2.3V and the charge plateau 5 V, revealing the high polarization of the battery. A high polarization leads to some degradations in the battery and to a progressive passivation of the cathode, reducing the surface area and therefore the performance of the battery. This study confirms that carbon-nitrogen doping increases battery performance through improved ORR catalytic activities. This improvement in ORR is reflected in the stabilisation of the charge plateau over the cycles.

Meng et al.[47] synthesised several carbon-based materials with different percentages of nitrogen doping (1%, 4%, 6%, 12%). Figure 18 presents their morphology, textural and electrochemical properties (Figure 18 a-e). The highest efficiency was observed in the case of the electrode containing 6% of nitrogen. The cell reached 71 cycles over 420h and possessed a first discharge capacity of 7250 $mAh.g^{-1}$ at a 200$mA.g^{-1}$ current density. The addition of 6% nitrogen improved the OER and ORR catalytic activities of the battery, which was reflected in the decrease in overvoltage (Figure 18 g) and in the higher cycling stability (Figure 18 h). However, a 12% nitrogen doping led to a high number of active sites that can react with the oxygen of the solvent (Tetraethylene glycol dimethyl ether (TEGDME)) and decompose it to form an isolated Li_2CO_3 film. This hypothesis was confirmed via scanning linear sweep voltammetry (LSV) where a specific peak appeared at 4.02 V which corresponded to the decomposition of the electrolyte. The study confirmed that adding nitrogen to carbon materials can stabilise the system and improve battery performance. However, it was noted that the doping should be limited in order to avoid the decomposition of the electrolyte.

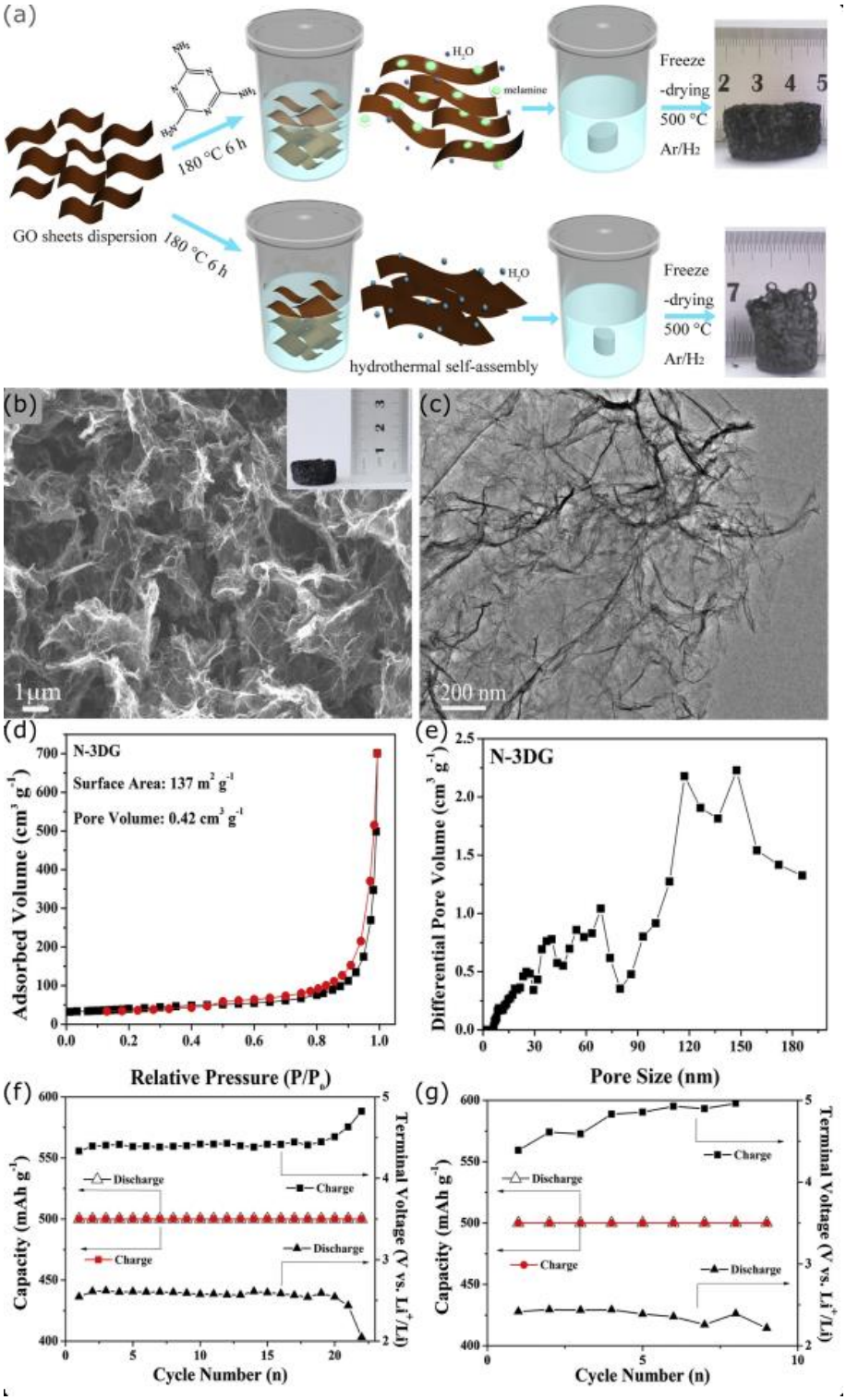

Figure 17: (a) Schematic illustration of the preparation processes of N-3DG and 3DG, (b) SEM and (c) TEM images of N-3DG, (d), N_2 adsorption-desorption isotherms and (e) the corresponding pore size distribution curve of N-3DG,and Cycling performances of Li-O_2 batteries with (f) N-dopes and (g) pure carbon electrodes at a current density of 100 mA g^{-1} and cut-off capacity of 500 mAh g^{-1} .[45]

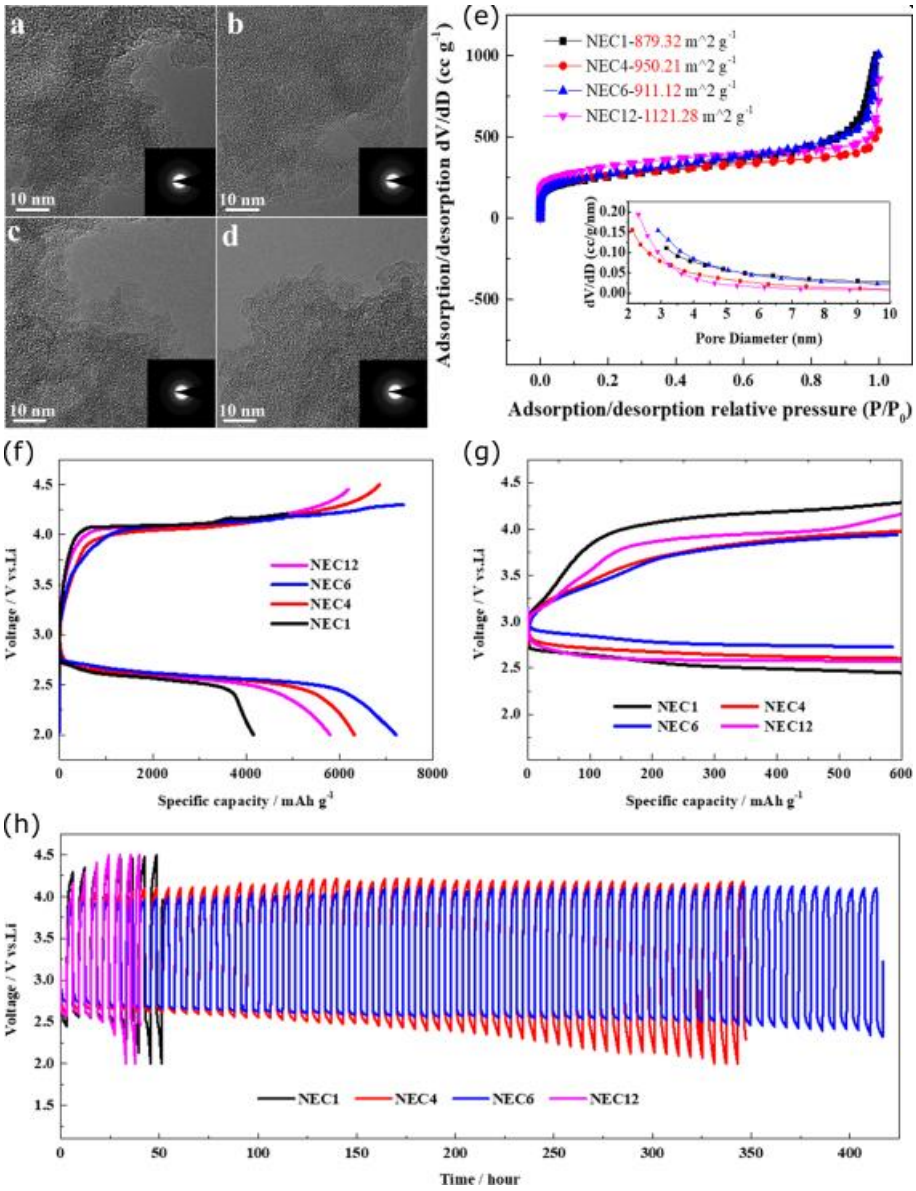

Figure 18: SEM images of the nitrogen doped carbon (a) NEC1; (b) NEC4; (c) NEC6; (d)NEC12 with insets of selected area electron diffraction (SAED) patterns respectively, (e) N_2adsorption/desorption isotherms with corresponding pore size distribution (inset) of the carbon materials (f) Capacity obtained with the different percentage N-doping electrode at a 200mA.g^{-1} current density and a 2.0-4.5V window, (g) Initial discharge-charge curves at a 200mA.g^{-1} current density for a 600 mAh.g^{-1} specific capacity, (h) Cyclic performances of the different N-doped cathodes at a 200mA.g^{-1} current density for a 600 mAh.g^{-1} specific capacity.[47]

It is obvious that carbon materials had been widely used as cathode materials due to their conductivity, surface area, and catalytic activity towards oxygen. All the carbon-based cathodes used for Li-O_2 batteries in research reports are summarised in Table 5. However, the major drawback that limits the applications of these cathodes is the reactivity of carbon with lithium peroxide that gives insoluble lithium carbonate (Equations (1.7) and (1.8)).

Table 5: Capacity reached, morphology and textural properties of the principal carbon-based cathodes for Li-O_2 batteries applications

Carbon type	Morphology	Discharge Capacity ($mAh.g^{-1}$)	Specific surface area ($m^2.g^{-1}$)	Average pore diameter (nm)	Pore Volume ($cm^3.g^{-1}$)	Reference
Super P	nanoparticle	4255	259	12.807	10.6	[34]
XC 72	nanoparticle	1706	200	10.942	10.3	[34]
AC	nanoparticle	2311	1759	4.132	10.2	[34]
KB	nanoparticle	3374	1724	6.538	11.7	[34]
GNS	graphene	15000	186	18	0.83	[36]
VACNT-TA	nanotube	4300	206	-	-	[39]
CNF	nanofiber	20000	-	-	-	[41]
THPC	nanosphere	3891	-	7	-	[43]
N doped carbon						
N-3DG	graphene	7300	137	-	0.42	[46]
NEC1	nanoparticle	4200	879	-	-	[47]
NEC4	nanoparticle	6200	950	-	-	[47]
NEC6	nanoparticle	7250	911	-	-	[47]
NEC12	nanoparticle	5800	1121	-	-	[47]
CA	spherical particle cluster	16600	754	3.67	-	[48]

$$Li_2O_2 + C + \frac{1}{2}\,O_2 \rightarrow Li_2CO_3 \quad (1.7)$$

$$2\,Li_2O_2 + C \rightarrow Li_2CO_3 + Li_2O \quad (1.8)$$

Yashina et al.[50] investigated the reactivity of carbon as cathode material in lithium-oxygen batteries, and showed via in-situ ambient pressure XPS experiments that superoxide radicals formed by oxygen reduction favour nucleophilic addition or electron transfer leading to the creation of epoxy groups on carbon surface which are then transformed into carbonates. They also demonstrated that carbon double bonds or aromatic systems activated by the oxygen superoxide and associated defects promote carbonate formation. Figure 19 resumes these phenomena.

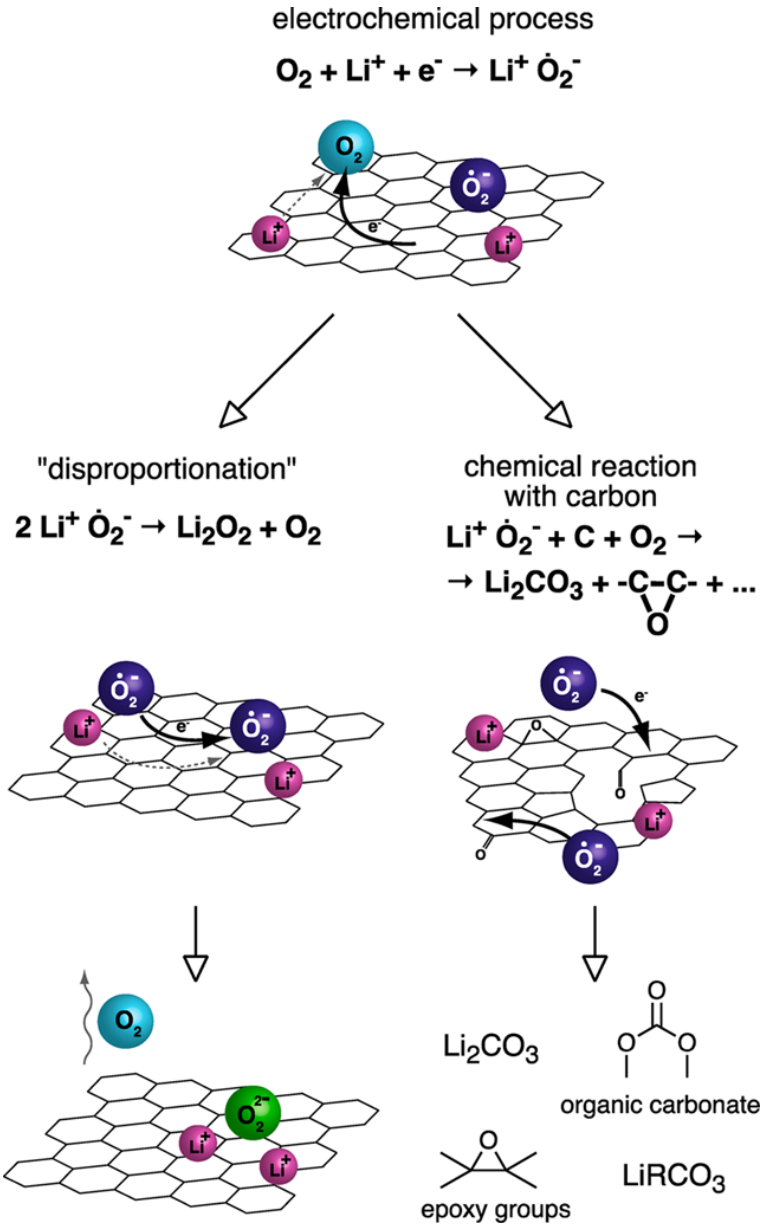

Figure 19: Chemical transformations of superoxide species. The scheme illustrates chemical processes that are being initiated right after ORR [50]

The lithium carbonate formed during the discharge is insoluble and cannot be totally removed during the charge. Li_2CO_3 will accumulate during the cycles and clog the cathode. The consequences on the battery performances will be, a reduction by ten to one hundred times of the current density, and an increase of the overpotential.[31] According to Bruce et al.[49], carbon electrodes are stable up to a potential of 3.5V; beyond this voltage, the carbon will react with Li_2O_2 to form Li_2CO_3 which limits their applications.

Another source of degradation is the reaction between carbon and highly reactive singlet oxygen produced during cycling.[51] The formation of $^1O_2$ at charging is possible at potential exceeding 3.5 to 3.9V vs Li/Li^+. However, most of $^1O_2$ comes from the superoxide disproportionation with a $^1O_2$ yield of ~3% in a standard Li-O_2 cell.[52] The disproportionation of superoxide goes through $Li(O_2)_2Li$ dimers. The

energetic pathway to $^3O_2$ and $^1O_2$ will depend on the cations. The lower the Lewis acidity of the cation, the weaker the O_2^- - cation interaction, the more the intermediate will be destabilised. The different energy pathways for the formation of lithium peroxide from superoxide are summarised in Figure 20.

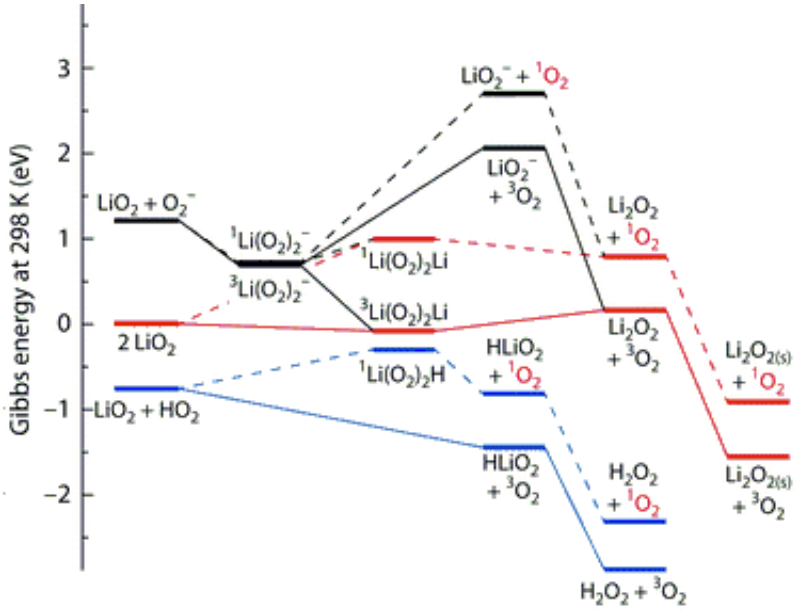

Figure 20: Reaction free energy profiles for superoxide disproportionation LiO_2 disproportionation with itself, O_2^- or HO_2 to Li_2O_2 and molecular oxygen. [52]

Regarding LiO_2 (red pathway). The dimer ($^3Li_2(O_2)_2Li$ is slightly stabilised compared to the two monomers (LiO_2, Li_2O_2). The formation of Li_2O_2 and the release of $^3O_2$ is slightly endergonic and the precipitation of Li_2O_2 is illustrated by a strong decrease in energy level. The formation of the ($^1Li_2(O_2)_2Li$ dimer is higher in energy and will therefore be disfavoured. The energy of this pathway (~1eV) creates a higher thermodynamic barrier. The formation of $^1O_2$ remains possible but is slower explaining the low $^1O_2$ yield observed experimentally.

The most common strategy to limit these degradations is the deactivation of $^1O_2$ to $^3O_2$. Deactivation can be achieved via chemical or physical quenching.[53]

Chemical quenching involves a reaction between singlet oxygen and a quencher R to form RO_2. The most famous chemical quencher is 9,10-dimethylanthracene (DMA) which forms, after reaction with oxygen endoperoxide (DMA-O_2). However, the DMA is quickly completely consumed and cannot regulate the entire flow of $^1O_2$. Moreover, the possible formation of insulating intermediate species can clog the cathode, leading to a decrease of capacity.

Physical quenching is preferred since the quencher is not consumed and no insulating products are formed. This quenching is based on two mechanisms: energy transfer and charge transfer. In electrochemical systems quenchers based on change transfer are the most efficient. The electron deficient $^1O_2$ molecule will interact with an electron donor quencher to form a charge transfer complex. The detail of the formation and the charge transfer mechanism can be described as follow. Firstly $^1O_2$ and R, the quencher, form a singlet complex $^1(R^1\Delta)_{EC}$, in which electronic charge is partially transferred to the oxygen to form $^1(R\Delta^1)_{CT.}$ Energy is then released during the intersystem crossing (isc) to the triplet complex which dissociates it and gives R and $^3O_2$ (Equation 1.9).[54]

$$R + {}^1O_2 \leftrightarrow {}^1(R^1\Delta)_{EC} \leftrightarrow {}^1(R^1\Delta)_{CT} \rightarrow {}^3(R^3\Delta\Sigma)_{CT} \leftrightarrow R + {}^3O_2 \quad (1.9)$$

Currently azide and amine molecules are used as physical quencher.[54-55] More recently, Petit et al.[54] used DABCOnium as singlet oxygen quencher for metal-oxygen cells. This molecule possesses a high voltage stability and could be suitable for non-aqueous lithium oxygen battery system. However, this research area is still in the early stage of development and it is necessary to carry out an in-depth study which will clarify the main requirements and characteristics of these molecules and their action mechanisms.

We have seen that carbon-based cathodes are widely used in lithium oxygen batteries. However, we believe that it is possible to optimise these cathodes to improve the performance of the battery. Two main areas of improvement are being envisaged. The first, as discussed in the previous section, is to use one or several forms of carbon to create an optimal pathway for the oxygen. The second is to use catalysts that will be integrated into the structure. The nature of these catalysts is multiple and their characteristics will be described in the following sections.

II.1.2.b) Noble metals in carbon materials

As mentioned above, superoxide radicals formed during oxygen reduction process lead to the formation of insoluble and non-conductive carbonate species, which greatly influence the overpotential and thus battery performance. In order to enhance OER/ORR process, to reduce the overpotential, and thus to prevent degradation and the formation of carbonate species, some catalysts can be added to the carbon matrices. In this section, the performance of precious metals such as Pt, Pd, Ru, Au, and Ir will be investigated as catalysts for lithium oxygen batteries.

Shao-Horn et al.[56] studied the catalytic activity of Ru, Au, Pt and Pd on the oxygen reduction reaction and proposed two mechanisms depending on the strength of the M-O bond (Figure 21).

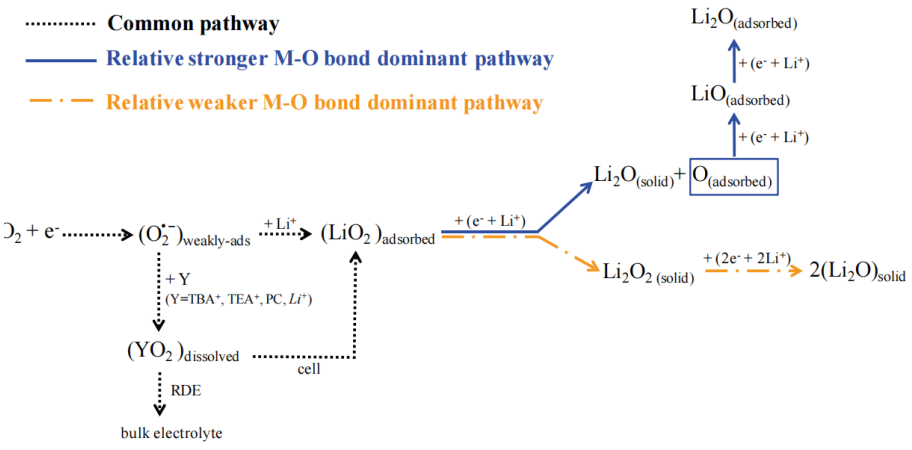

Figure 21: ORR mechanism for Li^+ containing nonaqueous solvents [56]

The activities between Li^+ and the ORR process on the surface correlates to oxygen adsorption energy formed a "volcanic-type" trend (Figure 22 a). The activity increased from graphitic carbon (GC) to Pd as the oxygen adsorption energy increased. A further increase in the oxygen adsorption energy on Ru resulted in a decrease in the activity. This volcano shape confirmed that the strength of oxygen bonding on the catalyst influences the ORR activity. In order to assess catalyst activity, the initial discharge voltage profiles were compared in Figure 22 b, and confirmed that the catalytic activity decreased in the order: Pd > Pt > Ru ≈ Au > C. The authors explained these observations by proposing a two-step electron reduction mechanism where the catalyst would influence the kinetics of the second reduction to form Li_2O + O adsorbed.

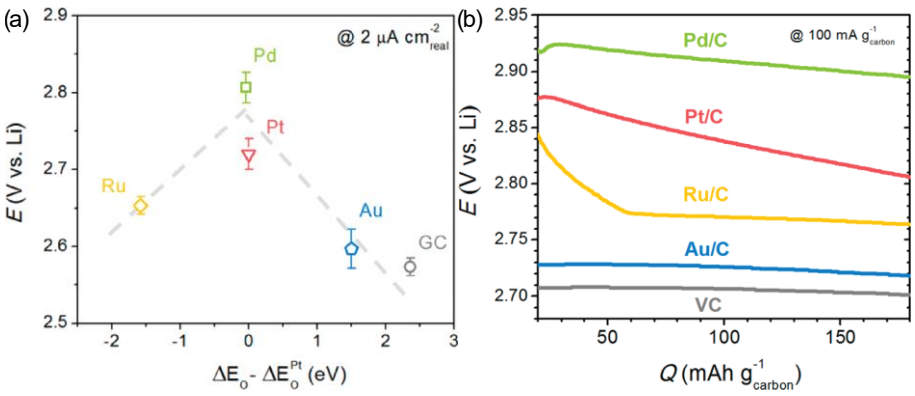

Figure 22: (a) Potentials at 2 µA.cm^{-2} real as a function of calculated oxygen adsorption energy, ΔE_O relative to that of Pt. (b) Initial discharge profiles of Pd/C, Pt/C, Ru/C, Au/C, and VC at 100 mAh.g^{-1}.[56]

Huguenin et al.[57] investigated the role of platinum nanoparticles in the kinetic mechanism of oxygen reduction reaction and showed that Pt-nanoparticles influenced the ORR and the OER process. The use of Pt-nanoparticles allowed a higher onset potential of the ORR compared to bulk Pt and carbon materials and a lower OER potential than carbon. Pt-nanoparticles electrodes produced more Li_2O_2 leading to a higher capacity. From a kinetic point of view, the limiting step on discharge is the first transfer of electrons to form LiO_2. They suggested that for each elemental step, 1.6 electrons per reduced oxygen are transferred for Li_2O_2 formation when a Pt catalyst is used instead of 1 electron without a catalyst, indicating a higher energy density (because more electrons can be transferred per oxygen molecule) compared to the chemical disproportionation reaction ($2LiO_2 \rightarrow Li_2O_2 + O_2$)

Wang et al.[58] synthesized a porous nitrogen doped carbon nanofiber-supported palladium composite (Pd/PNCNF-2) (Figure 23 a). This material presented favourable catalytic activity towards both the ORR and the OER (Figure 23 b-d). The catalytic activity was determined by Linear Sweep Voltammetry (LSV) (Figure 23 e,f). For ORR, Pd/PNCNF-2 had the lowest current density at the onset potential, and for the OER it had the highest. The increase in current density implied an increase in the number of electrons transferred per oxygen molecule and allowed an increase in reaction kinetics. Discharge/charge capacities of 10080/9405 mAh.g^{-1} were reached at a current density of 100 mA.g^{-1} with a round-trip efficiency of 64 %, while its palladium-free counterpart achieved only 2533/1976 mAh.g^{-1} with a 59 % round-trip efficiency. The consequences of Pd on overpotential was tested at a fixed capacity of 1000 mAh.g^{-1} with a current density of 100 mA.g^{-1}, and revealed a 22.7 % decrease and 6.8 % increase of the initial discharge/charge terminal voltages, respectively.

Noble metals have proved their good catalytic property on the OER and ORR processes. Considering their individual performances, combination of noble metals could lead to better results. Lee et al.[59] deposited some AuPt nanoparticles into hollow mesoporous nitrogen-doped carbon microspheres (AuPt/HMCMS). The morphology and textural properties studied by TEM, SEM and N_2 physisorption (Figure 24 a-e) revealed that the material was a meso/macroporous hollow microspheres. The results of the electrochemical tests performed at a current density of 100 $mA.g^{-1}$ with a 2.2-4.4 V window voltage, are presented Figure 24 f. The AuPt/HMCMS cathode displayed the highest specific capacity and the smallest charge–discharge overpotential. Capacity reached 6028 mA h g^{-1}, which was 168% and 244% higher than that of the AuPt NPs and HMCMS electrode, respectively. Regarding overpotential at 2000 $mAh.g^{-1}$, AuPt/HMCMS electrode possessed a 1.28 V gap, which was 1.41 V and 1.88 V lower than that of AuPt NPs and HMCMS respectively. This decrease of overpotential reflected the good catalytic efficiency of AuPt/HMCMS electrode. Moreover, Li-O_2 cells made of AuPt/HMCMS cathode performed 75 cycles at a discharge capacity of 1000 $mAh.g^{-1}$ without a cut-off charge voltage (voltage level at which the charge controller disconnects the load from the battery) exceeding 4.4 V, while with the HMCMS cathode, the batteries performed only 9 cycles with cut-off charge voltage up to 5.0 V. The good electrochemical performance of the AuPt/HMCMS cathode was explained by the duality between the meso/macro porosity and the ORR/OER activities of AuPt nanoparticles (higher ORR voltage plateaus and lower OER voltage plateaus).

A possible way of improving these catalysts is to create a coating, by Chemical Vapor Deposition (CVD), on ultra-porous carbons in order to maximise catalyst deposits and enhance the electrochemical performance of batteries.

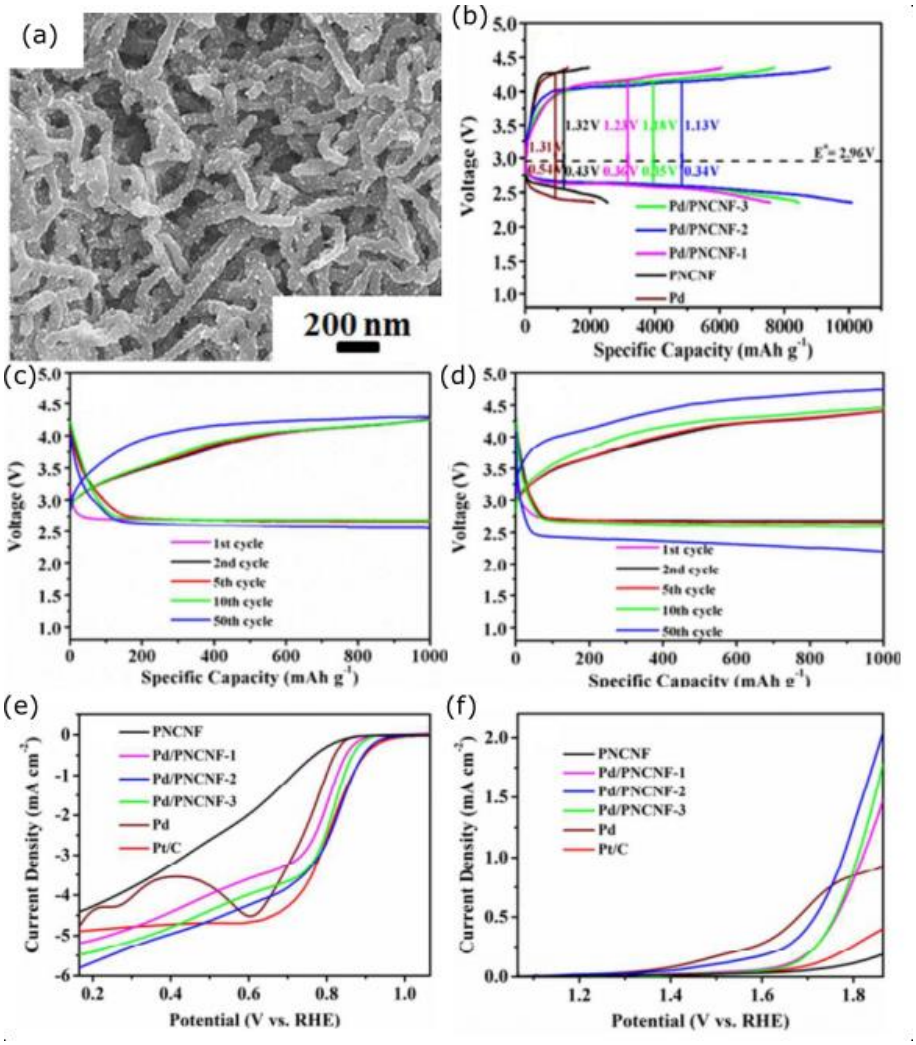

Figure 23: (a) SEM micrograph of the Pd/PNCNF-2, (b) Comparison of the initial discharge/charge profiles of the Li-O_2 batteries from 2.35 to 4.35 V for (a) the pure Pd, the pure PNCNF, and the Pd/PNCNF cathodes at 100 mA g^{-1}, (c, d), and the corresponding typical discharge/charge profiles. (e) ORR LSV profiles for the samples at a rotation speed of 1600 rpm and (f) OER LSV profiles of the different samples. [58]

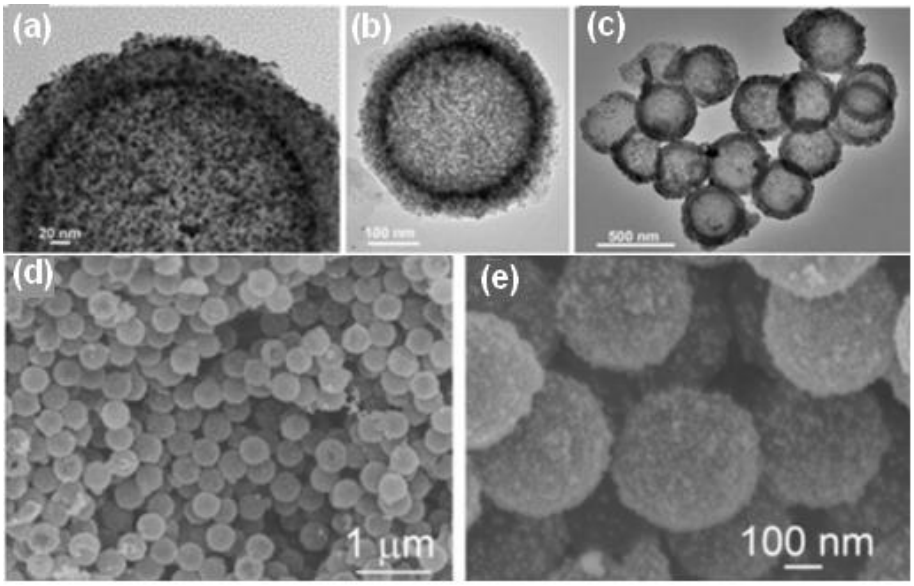

Specific surface area $m^2.g^{-1}$	Pore volume $cm^3.g^{-1}$
74,2	0,11

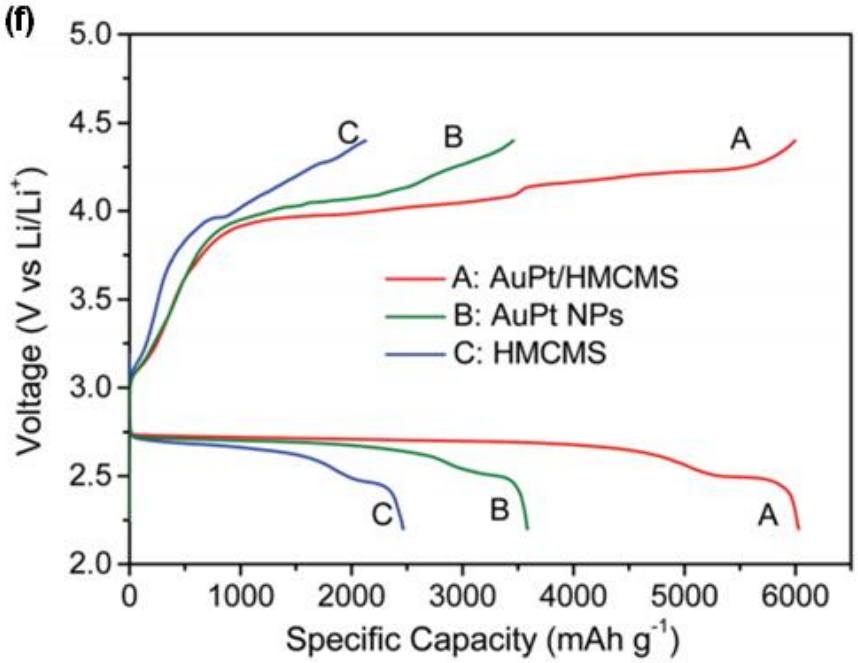

Figure 24: (a-c) High resolution TEM images of AuPt/ HMCMS composite, (d,e) High resolution SEM images of AuPt/ HMCMS composite an their textural properties (f) First cycle discharge/charge profile obtained with AuPt/HMCMS, AuPt NPs and HMCMS electrodes.[59]

II.1.2.c) Noble metal oxides in carbon material

The efficiency of noble metal oxides as a catalyst was also investigated. The most researched were iridium oxide (IrO_2) and ruthenium oxide (RuO_2). Yang et al.[60] evaluated the performance of a thin layer of iridium oxide on carbon nanoparticles (KB) and compared it with KB mixed with IrO_2 nanoparticles and KB only.

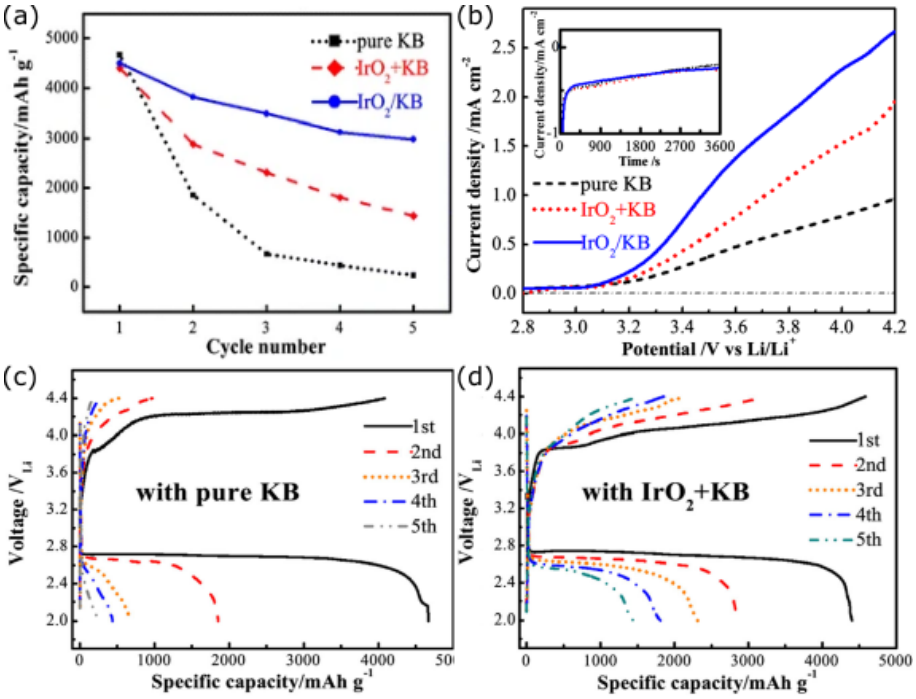

Figure 25: (a) Comparison of discharge capacity for 5 cycles of Li–O_2 batteries with pure KB, IrO_2+KB, and IrO_2/KB at 0.1 mA.cm^{-2}, (b) OER LSV profiles of the different samples, and discharge–charge profiles at different cycles of the Li–O_2 batteries with (c) pure KB, and (d) IrO_2/KB, with a limited capacity of 500 mAh.g^{-1} at 0.1 mA.cm^{-2}. [60]

The discharge capacities of the first five cycles obtained with pure KB, IrO_2+KB mixture, and IrO_2/KB electrodes at 0.1 mA.cm^{-2} are presented in Figure 25 a. The decrease of the capacity was observed to be important and abrupt for the pure carbon electrode. After only five cycles it tended towards zero reflecting its poor performance. The addition of iridium oxide within the carbon matrices allowed damping in the decrease of the capacity. After 5 cycles, the capacity reached 1400 mAh.g^{-1} showing an increase in stability provided by IrO_2. KB coated with IrO_2 reached a discharge capacity of 3400 mAh.g^{-1} after 5 cycles confirming the stabilising effect of IrO_2 on the system. The enhancement of the cyclability was attributed to the high activity of IrO_2 regarding the OER process, which accelerated the decomposition of discharge products, thus improving the rechargeability. The catalytic activity towards the OER was determined by Linear Sweep Voltammetry (LSV) and the obtained results are shown in Figure 25 b. IrO_2-based cathode exhibited the highest current density at the onset potential. The increase in current density implied an increase in the number of electrons transferred per oxygen molecule that allowed an increase in reaction kinetics. Overpotential was been determined by a test at a fixed capacity of 500 mAh.g^{-1} at a current density of 0.1 mA.cm^{-2}. Results obtained for KB and IrO_2/KB electrodes (Figure 25 c,d), showed an overpotential of 1.24V for KB cathode, 0.97V for the

mixed IrO_2 + carbon and 0.81V for the IrO_2 coated KB electrode. The increase of overpotentials after the first cycle for IrO_2/KB cathode was explained by the partial coverage by Li_2O_2 and other undesired additional reaction products such as Li_2CO_3. Regarding cycling stability, iridium oxide coating on the KB electrode allowed the battery to achieve an additional 40 cycles. These results confirmed the good OER catalytic activity of IrO_2 and explained the improvement of the electrochemical performances.

The performance of ruthenium oxide deposited on vertically aligned carbon nanotubes (RuO_2/VACNT) were studied by Tan et al.[61] In this study, CNT, VACNT (Figure 26 a and c) and RuO_2/VACNT (Figure 26 b and d) cathode materials were compared to evaluate their respective impact on performance. The morphology and the electrochemical properties of the cathodes are presented in Figure 26.

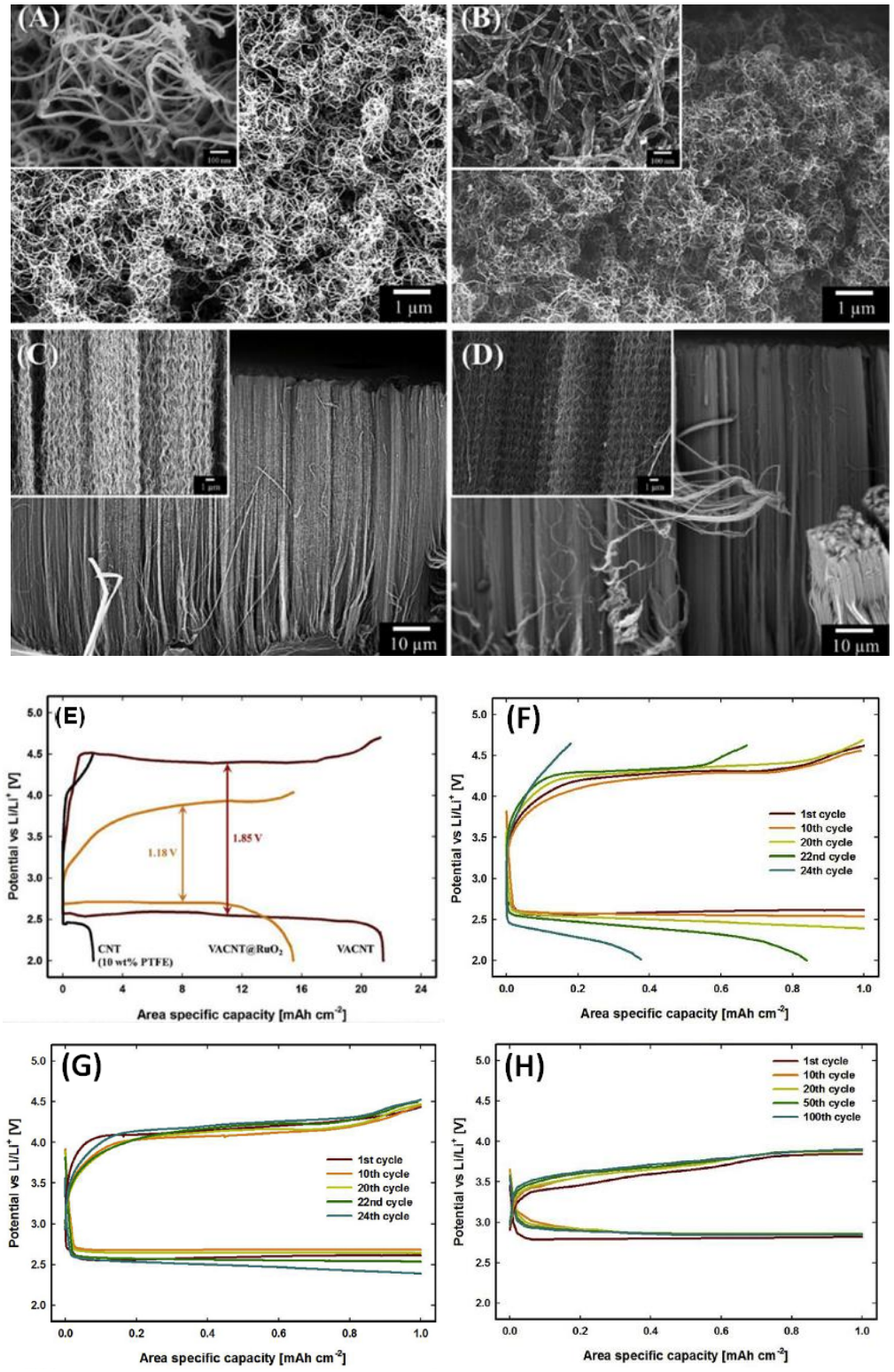

Figure 26: SEM images of (A) the VACNT cathode and (B) the VACNT@RuO_2 cathode. SEM images on the cross-sectional surfaces of (C) the VACNT cathode and (D) the VACNT@RuO_2 cathode. The insets show high-resolution SEM images. (E) Comparison of the discharge-charge characteristics at 0.5 mA.cm^{-2} after fully discharged and charged. Comparison of the cycling stability at 0.5 mA cm^{-2}with a fixed capacity of 1.0 mAh.cm^{-2}. (F) CNT, (G) VACNT, and (H) VACNT@RuO2cathode.[61]

The battery built with CNT cathode exhibited a capacity of 1.99 mAh.cm^{-2} at a current density of 0.5 mA.cm^{-2}, and a 1.85 V overpotential. VACNT cell reached a 21.4 mAh.cm^{-2} capacity, and a 1.72 V overpotential. The performance improvement over the CNT cathode was attributed to the increase in surface area and pore volume caused by the hierarchical organisation of the nanotubes. The addition of RuO_2 on VACNT, reduced the overpotential to 1.18 V and also reduced the capacity to 15.4 mAh.cm^{-2} (Figure 26 e). The authors justified the lower capacity of RuO_2/VACNT compared to VACNT by the different crystallinity and morphology of Li_2O_2 induced by the oxygen adsorption properties of RuO_2. RuO_2 has a high adsorption of O_2 and promotes the growth of thin film defective Li_2O_2 on the cathode surface. The thin film contained Li and O vacancies that were beneficial for the transport of lithium and oxygen. The cycling stability of the CNT (Figure 26 f), VACNT (Figure 26 g) and RuO_2/VACNT (Figure 26 h) cathodes was evaluated at 0.5 mA.cm^{-2} with a fixed capacity of 1.0 mAh.cm^{-2}. After 10 cycles, overpotential increased for the CNT and VACNT, causing the decomposition of both electrolyte and electrode on charge. As a consequence, poor cyclability was obtained, 21 cycles for the CNT and 26 for the VACNT electrode. On the contrary, RuO_2/VACNT cathode maintained a low overpotential, with a charge plateau lower than 4V. Moreover, it reached 100 cycles without any reduction in cycling performance. The decrease in overpotential and the increase in cyclability reflect the excellent catalytic activities of RuO_2 both for ORR and OER.

In conclusion, noble metals and their oxides have been widely used in lithium-oxygen batteries. Their utilisation has been justified by their good catalytic properties for the OER and ORR processes, reducing overpotential and increasing performance during cycling. However, the price of these materials remains high, limiting their large-scale use.

One of the ways to improve these cathodes would be to use a wet ball milling process using porous carbon nanoparticles and catalyst precursor salts. The resulting product can be calcined in order to obtain the Noble metal oxide/carbon catalyst. This protocol can result in a homogeneous distribution of the catalyst on the carbon support and thus can enhance battery performance.

II.1.2.d) Transition metal oxides *in carbon material*

Metal oxides have a good catalytic activity for the oxygen evolution and reduction reactions. In contrast to noble metals, metal oxides are reasonably priced and can be exploited on a larger scale.

Zhao et. al. evaluated the catalytic activity of metal oxides such as NiO-RuO_2, NiO and RuO_2 by mixing them with Ketjen Black (KB).[62] Their textural properties and results from electrochemical tests are shown in Figure 27. The capacity achieved was found to be related to the pore volume. The larger the pore volume, the better the diffusion of lithium and oxygen and the higher the capacity. For RuO_2 catalyst, the higher discharge voltage and lower charge voltage resulted from the high electrocatalytic activity for the oxygen reduction and evolution reactions. Linear Sweep Voltammetry showed the active oxidation potential with respect to the decomposition of side product (Figure 27 b). The onset potential of the electrode made of NiO/KB was 3.56 V, and that of NiO-RuO_2/KB was 3.55 V. These values were consistent with the onset potential of Li_2CO_3 decomposition and proved that NiO can promote the decomposition of side products.[24]

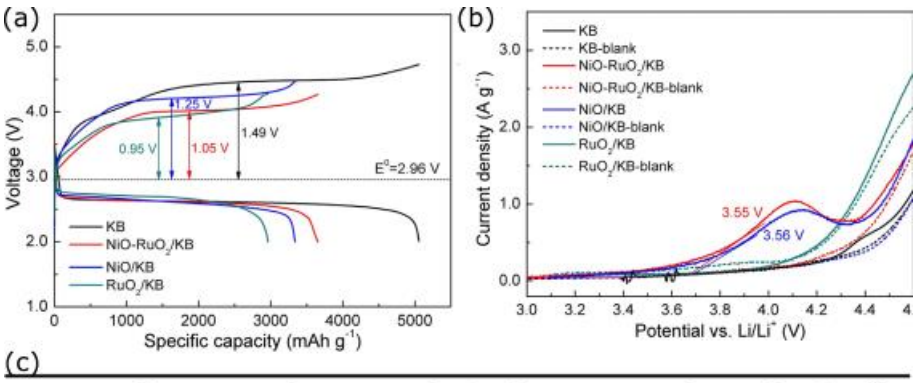

(c)

Sample	Surface area ($m^2.g^{-1}$)	Pore Volume ($cm^3.g^{-1}$)
KB	133,5	2,42
NiO-RuO2/KB	799,6	1,8
NiO/KB	894,4	1,49
RuO2/KB	729,1	1,49

Figure 27: (a) Li-O_2 charging-discharging profile with different cathodes: Ketjen Black (KB), NiO-RuO_2/KB, NiO/KB and RuO_2/KB, (b) LSV curves of Ketjen Black (KB), NiO-RuO_2/KB, NiO/KB and RuO_2/KB cathodes with side products and (c) Surface area and pore volume of: Ketjen Black (KB), NiO-RuO_2/KB, NiO/KB and RuO_2/KB.[62]

Iron, cobalt, manganese, titanium and nickel oxides are the most common catalysts used in Li-O_2 battery. The objective of this section will be to evaluate their performance as cathode material.

Yang et al.[63] investigated the performances of NiO via a layered nanosphere structure. SEM/TEM (Figure 28 a-g) confirmed the layered nature of the nanosphere and nitrogen physisorption, (Figure 28 h) the specific surface area of the NiO was estimated to be 27 $m^2.g^{-1}$ and the pore size distribution supported the mesoporous and macroporous characteristics of the product. The catalytic activity of NiO was studied by LSV and showed considerable activity on the OER compared to a Pt/C electrode (Figure 28 i). To estimate battery stability, a test with a limited capacity of 800 $mAh.g^{-1}$ was performed (Figure 28 j,k). Li–O_2 batteries made with NiO electrode were able to run for 50 cycles while the one with the KB reached only 15 cycles. This improvement in performance was explained not only by the OER catalytic activity of NiO but also by its morphology. Li-O_2 battery made with the of NiO layered nanosphere catalyst showed an increase in capacity from 2600 $mAh.g^{-1}$ to 3040 $mAh.g^{-1}$ compared with pure KB cathode (Figure 28 l). In the first cycle, the reduction in overpotential led to an efficiency of 98.3% which is considerably higher than that of the KB electrode at 54.8%. The catalytic reaction mechanism of the layered nanosphere NiO electrocatalyst is illustrated in Figure 28 m.

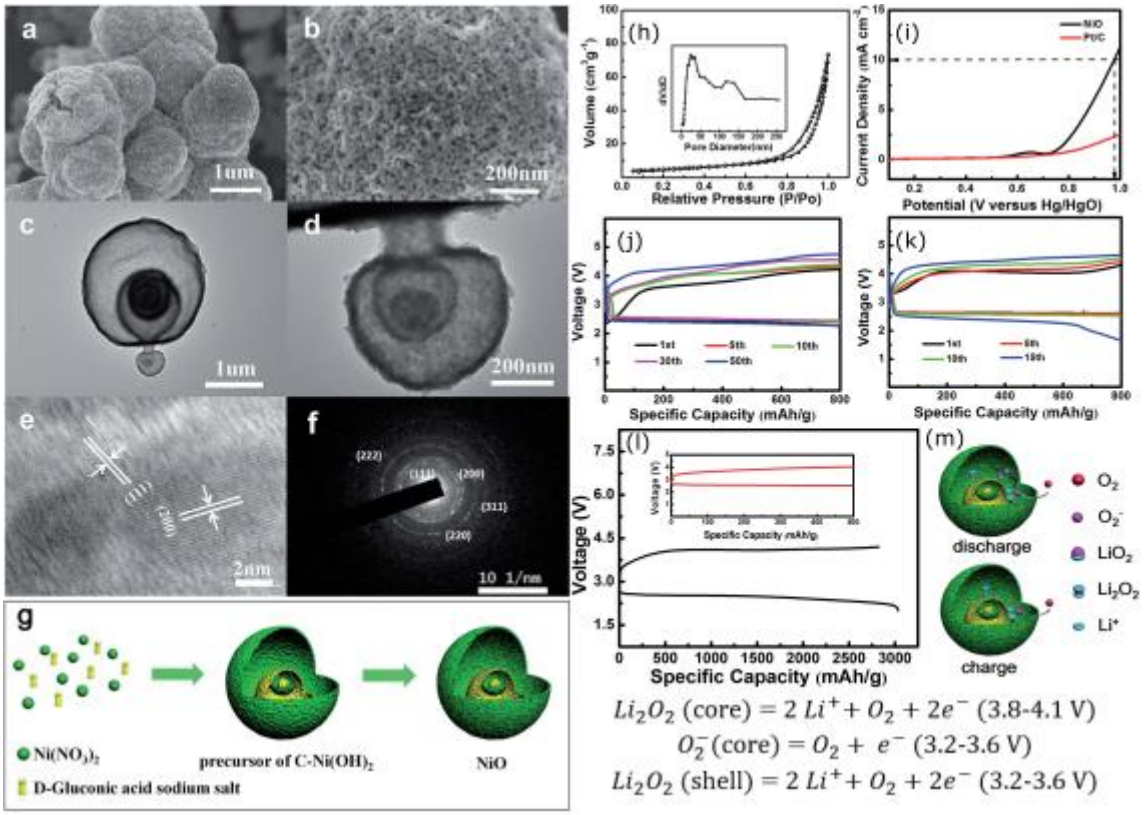

Figure 28: (a) SEM image of NiO. (b) FESEM, (c) TEM and (d) HRTEM images of the layered nanosphere NiO, (e) lattice fringes and (f) hysteretic loop. (g) Schematic illustration of the synthesis process of NiO, (h) nitrogen adsorption/desorption isotherms and pore-size distribution of NiO, (i) Oxygen evolution reaction curves of NiO and Pt/C at a rotation rate of 1600 rpm with a scanning rate of 10 mV s^{-1} discharge–charge profiles of the Li–O_2 batteries with (j) NiO catalyst, and (k) KB only, with a limited capacity of 800 mAh.g^{-1} at 0.1 mA.cm^{-2} within a 2.0 - 4.2 V voltage range, (l) Galvanostatic discharge/charge curves of Li–O2 batteries with a NiO catalyst at a current density of 0.1 mA cm^{-2} in the voltage range of 2.0–4.2 V vs. Li^+/Li. (m) Illustration of the catalytic reaction mechanism for the layered nanosphere NiO in Li–O_2 batteries [63]

Porous titanium dioxide microspheres were synthetized, mixed with carbon nanotubes and tested as cathode in Li-O_2 batteries.[64] Textural properties of the carbon nanotubes and the titanium dioxide microsphere are presented in Figure 29 a-d. TiO_2 microspheres exhibited a surface area of 55.3 $m^2.g^{-1}$ with a majority of mesopores ranging from 4 to 30 nm and the carbon nanotube possessed a surface area of 202.4 $m^2.g^{-1}$ with an average pore size of 5nm. The first discharge capacity was 6590 mAh.g^{-1} for the TiO_2 cathode and 1794 mAh.g^{-1} for the pure carbon nanotubes cathode. A test at limited capacity of 500 mAh.g^{-1} was performed to investigate the catalytic effect of TiO_2 microspheres on the OER/ORR process (Figure 29 e). The discharge potential plateau increased by 50 mV and the charge potential plateau decreased by 250 mV compared to pure CNT electrodes. Li-O_2 battery based on TiO_2 microspheres was able to operate without loss of voltage or capacity for 75 cycles, while the one based on CNT could operate only for 10 cycles under the same conditions, which revealed the good stability provided by titanium oxide. This stability is assumed to come from the specific structure of the microsphere coupled with an increase in the number of electrons transferred per oxygen molecule.

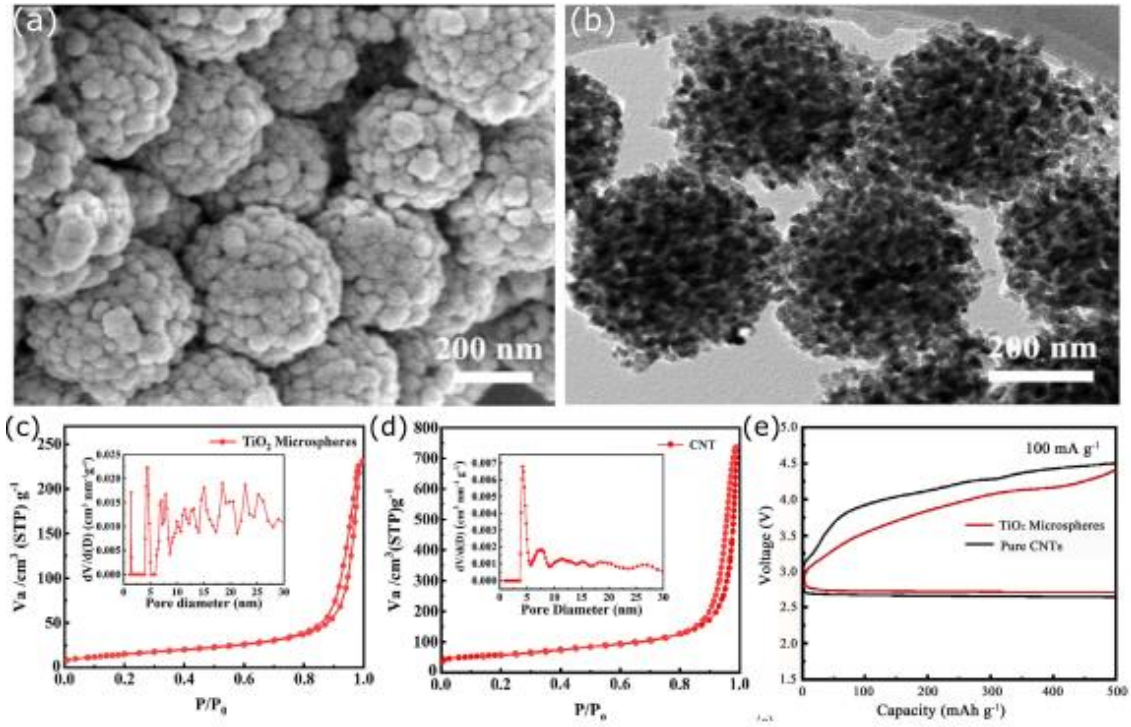

Figure 29: (a) SEM and (b) TEM images of TiO_2 microspheres, nitrogen adsorption–desorption isotherm of (c) TiO_2 microspheres and (d) CNTs (e) The initial discharge/charge profiles of TiO2 microspheres and pure CNT electrodes under the capacity limit of 500 mAh g^{-1} at 100 mA g^{-1}. [64]

Zhu et al.[65] studied the effects of Fe_2O_3 nanoparticles, by mixing them with Vulcan XC-72 carbon. Their results showed that the first discharge capacity and discharge plateau achieved for the XC-72 cathode was equal to that of the Fe_2O_3/XC electrode. When charging, the addition of Fe_2O_3 reduced the plateau by 0.43V, indicating the improvement of the OER induced by the catalytic properties of the oxide. The electrocatalytic activity of Fe_2O_3 toward OER was evaluated by linear sweep voltammetry (LSV) (Figure 30 a). The cathode containing Fe_2O_3 exhibited a larger OER current density and lower onset potential compared with that of the pure XC cathode, demonstrating that Fe_2O_3 is an effective OER catalyst. The cycling performance of batteries using Fe_2O_3/XC cathode and its oxide-free counterpart was evaluated by testing at a fixed capacity of 500 mAh.g^{-1} at a current of 200 mA.g^{-1}. Their results are presented in Figure 30 b,c. The discharge voltage plateau of XC cathode was 2.6 V and the charge plateau was 4.4 V, while Fe_2O_3/XC cathode presented a charge voltage plateau of 4.0 V, 0.4 V less than that of XC-72 electrode, but had an equivalent discharge plateau of 2.6 V. Regarding cycling performance, Li-O_2 batteries made of XC-72 cathode reached 15 cycles while the one based on Fe_2O_3/XC performed 39 cycles reflecting the stability provided by the oxide. It should be noted that the cycles beyond 39 were obtained after a battery refresh and cannot be taken into account in a rigorous methodology. This study showed that, owing to their activity on the OER process, Fe_2O_3 nanoparticles enable a reduction in overpotential leading to the preservation of the electrolyte, limiting the formation of side products and thus increasing the battery's performance.

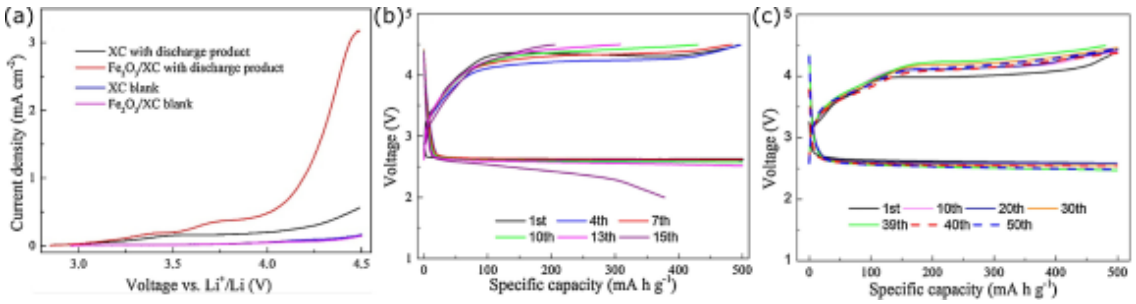

Figure 30: (a) Linear sweep voltammograms of OER in non-aqueous lithium-oxygen batteries with XC and Fe_2O_3/XC cathodes of 1 mVs^{-1} with and without initial discharge product and Discharge/charge curves in lithium–oxygen battery with (b) XC and (c) Fe_2O_3/XC cathode at 200 $mA.g^{-1}$ with a fixed capacity. [65]

MnO_2 is another metal oxide widely used as a cathode material in lithium-oxygen batteries. Zhang et al. synthetised manganese nanoparticles to decorate multi-walled carbon nanotubes (MnO_2/MWCNTs) (Figure 31 a,b).[67]

The ORR and OER activities on MnO_2/MWCNTs cathode were examined by Cyclic Voltammetry (CV) (Figure 31 c). The MnO_2/MWCNT cathode exhibited an ORR onset voltage of 3.12 V, about 270 mV higher than that of the pure MWCNTs electrode, indicating higher ORR kinetics. MnO_2/ MWCNTs cathode also provided a lower OER onset potential and larger OER peak current, revealing a better ORR and OER activity induced by MnO_2. The first discharge capacity was evaluated at 100 $mA.g^{-1}$, and gave a capacity of 8643 $mAh{\cdot}g^{-1}$ for the MnO_2/MWCNTs cathode, which was twice as high as that obtained with the pure MWCNTs electrode (4.512 $mAh{\cdot}g^{-1}$) (Figure 31 d). The cycling stability was evaluated at a capacity of 1000 $mAh{\cdot}g^{-1}$ under a current density of 200 $mA{\cdot}g^{-1}$. The charge/discharge potentials of the MnO_2/MWCNTs cathode (Figure 31 e,f) were 2.69 and 4.10 V respectively (compared to Li/Li^+) giving a 65.6% round-trip efficiency. Concerning MWCNTs cathode, the charge/discharge potentials were 2.69 and 4.25 V respectively, leading to a 63.3% round-trip efficiency (Figure 31 g,h). Regarding cycling stability, battery built with MnO_2/MWCNTs cathode reached 90 cycles while the MWCNTs electrode reached 28 cycles. The performance improvement was justified not only by the electrode structure but also by the enhancement of the catalytic activity by MnO_2 which improved the OER process and reduced the polarisation, thus accelerating the kinetics of the electrochemical reactions.

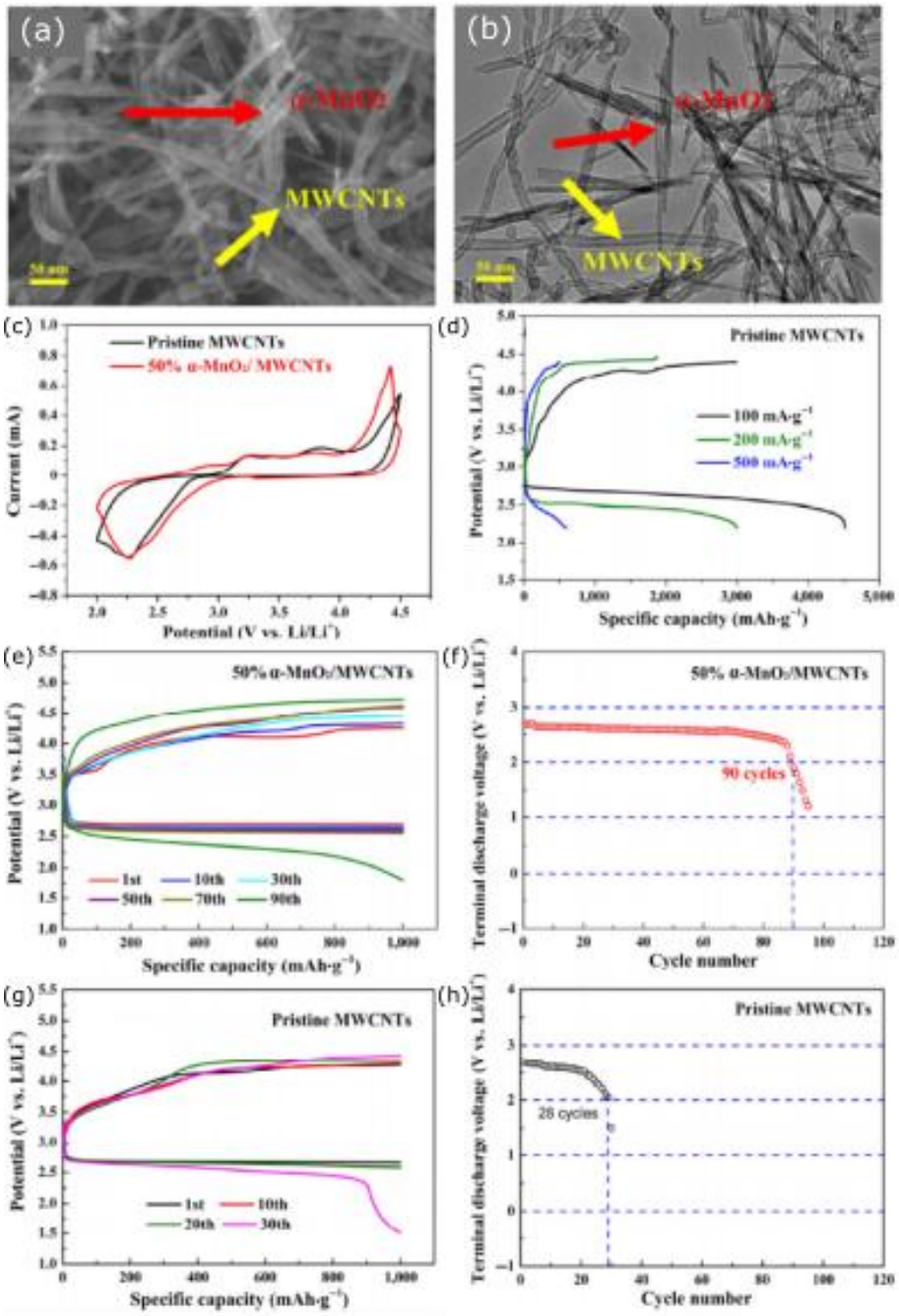

Figure 31: (a) Representative SEM images of 50% α-MnO_2/MWCNTs nanocomposite, (b) TEM image of the 50% α-MnO_2/MWCNT nanocomposite, discharge-charge voltage curves of different cycles for the (c) 3D 50% α-MnO_2/MWCNTs cathode (e) and pristine MWCNTs cathode. Variation of the terminal discharge voltage with the cycle number for (d) the 3D 50% α-MnO_2/MWCNTs hybrid cathode (f) and pristine MWCNTs cathode, (g) CV curves of pure MWCNTs and 50% α-MnO_2/ MWCNT electrodes between 2.0 and 4.5 V at 0.5 mV·s^{-1}.[67]

Cobalt oxide is also widely used as catalyst for Li-O_2 cathode batteries.[69-71] The performance of Co_3O_4 nanoparticles (Figure 32 a) was investigated by Yan et al. by mixing it with carbon black.[69] The first charge-discharge profile was performed at 100 mA.g^{-1} within a 2.0 – 4.3 V voltage window and showed a discharge capacity of 2050 mAh.g^{-1} and 1750 mAh.g^{-1} for the cell with a pure KB electrode (Figure 32 b) and that with the Co_3O_4/KB cathode (Figure 32 c), respectively. To evaluate the cycling stability, the

capacity was set at 500 mAh.g^{-1} at a current density of 100mA.g^{-1}. The cell made with Co_3O_4/KB cathode reached 33 cycles, twice that of the pure carbon electrode which performed only 17 cycles. Cyclic voltammetry (CV) confirmed the catalytic activity of Co_3O_4 (Figure 32 d,e). The initial reduction peak of Co_3O_4/KB and KB cathode were located at the same position, but sharper shape and larger peak areas were observed for Co_3O_4/KB, meaning that a faster ORR kinetics occurred during first discharge. For the oxidation peak, a higher oxidation current was noted, which indicated higher catalytic activity on OER. The increase of current peaks revealed a higher number of electrons transferred per oxygen molecule supplied by the addition of the Co_3O_4.

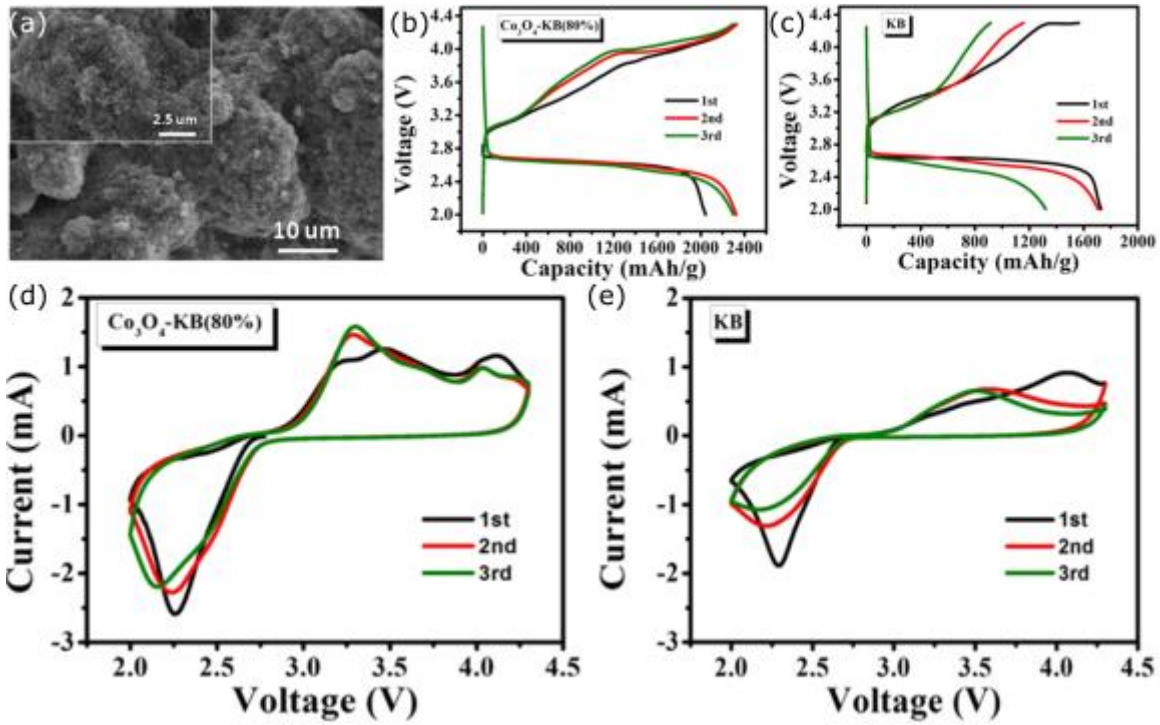

Figure 32: (a) SEM micrograph of as-deposited electrodes Co_3O_4/KB (80%), Charge and discharge profiles of (c) Co3O4/KB (80%), (d) pure KB electrodes, CV curve results of initial 3 cycles of (e) Co_3O_4/KB (80%), (f) KB electrodes at a constant scan rate at 0.5 mV s^{-1} from 2.0 to 4.3 V. [69]

Cerium oxide can also be used as a catalyst in Li-O_2 batteries. Chen et al.[72] designed a cerium oxide embedded on mesoporous carbon nanosheets (CeO_2/MC-600) (Figure 33 a-f) that showed a decrease in the overpotential by 0.11V and an increase of the capacity at the first discharge from 5261 to 12753 mAh.g^{-1} compared with the catalyst-free electrode (Figure 33 g). Moreover, Li-O_2 cells made of cerium oxide cathode performed 55 cycles at 1000 mAh.g^{-1} (Figure 33 h) which was five times more than their pure carbon counterpart (Figure 33i). The improvement in battery performance was related to the morphology of the Li_2O_2. Batteries with CeO_x/MC-600 cathode formed a large amount of Li_2O_2 uniformly accumulated in the form of fine nanoparticles whereas pure MC cathodes formed large nano-islands of Li_2O_2. This difference in morphology was explained by the presence of CeO_2 which facilitated oxygen redox reactions and regulated the nucleation of Li_2O_2 to form a uniform and fine distribution on the catalyst surface. The irregular deposition of Li_2O_2, passivated the surface of the MC electrode and obstructed the electron and mass transfer pathways, which increased the polarisation

and the irreversibility of electrochemical reactions. A schematic diagram for the improvement mechanism of CeO_x/MC-600 for Li-O_2 batteries is demonstrated in Figure 33 l.

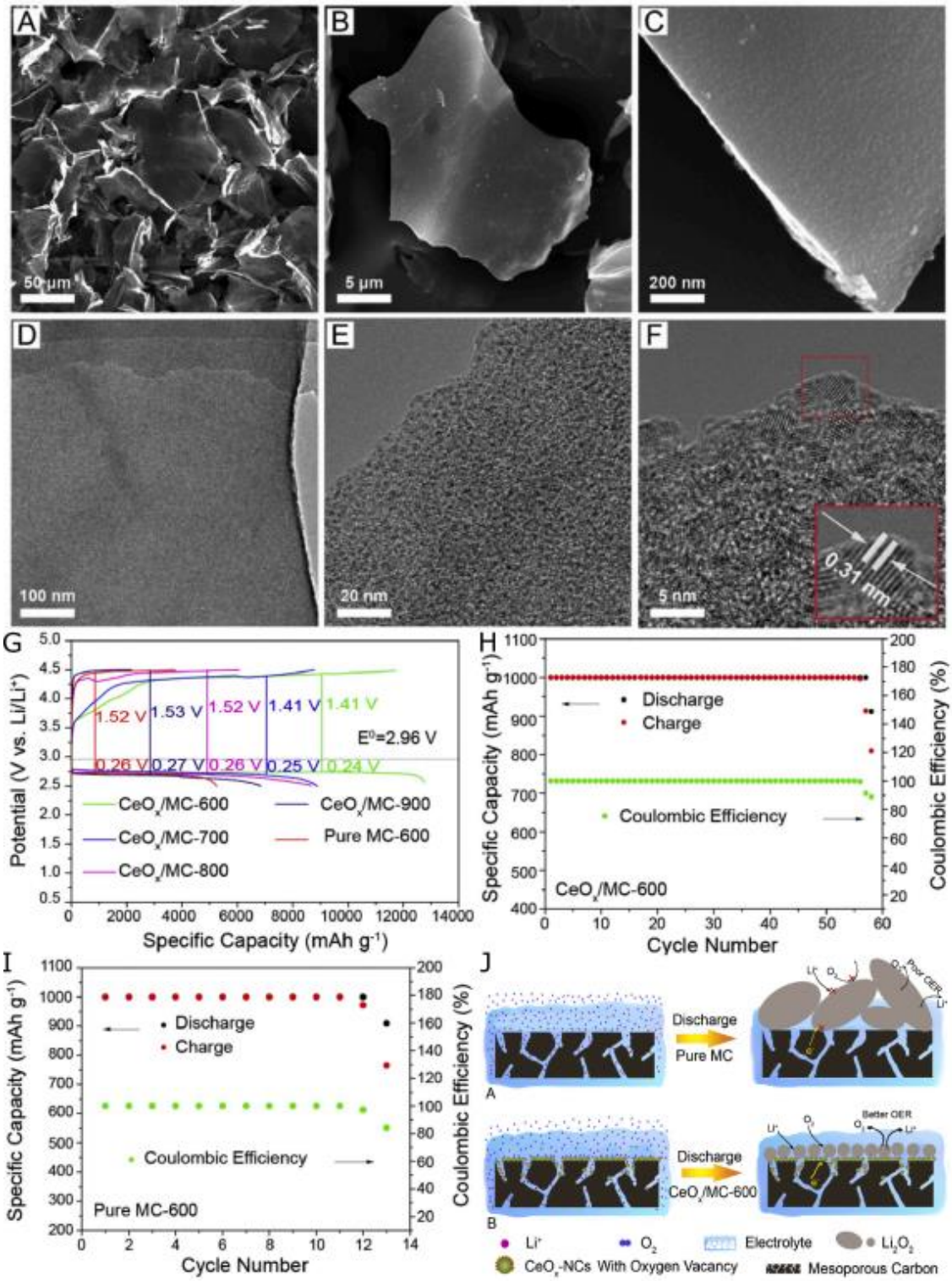

Figure 33: (a-c) SEM and (d-e) TEM images of CeO_x/MC-600 under different magnifications, and (f) TEM micrograph of pure MC, (g) first charge/discharge profile tested at 100 mA g^{-1} for all cathodes, long term cycling performance of (h) CeO_x/MC- 600 and (i) Pure MC, (j) Schematic diagram for the improvement mechanism of CeO_x/MC-600.[72]

All the metal oxide-based cathodes for Li-O_2 batteries along with their main characteristics are summarised in Table 6.

Tableau 6: Capacity reached, metal oxide and carbon morphology, and decrease in overpotential compared to pure carbon-based cathodes for Li-O_2 batteries applications.

Metal Oxide	Morphology	Carbon type	Discharge Capacity ($mAh.g^{-1}$)	Δ Overpotential (V)	Reference
RuO_2	nanoparticle	KB	3000	0.54	[60]
NiO	nanoparticle	KB	3300	0.44	[60]
NiO	nanosphere	KB	3040	0.025	[61]
TiO_2	microsphere	CNT	6590	0.3	[62]
Fe_2O_3	nanoparticle	XC-72	2000	0.43	[63]
Fe_2O_3	nanoparticle	CNT	-	0.47	[64]
MnO_2	nanoparticle	MWCNT	8643	0.15	[65]
MnO_2	nanosheet	XC-72	1976	0.34	[66]
MnO_2	coating	Hierarchically porous	9200	0.33	[67]
MnO_2	nanoflake	graphene	3218	0.07	[68]
Co_3O_4	nanoparticle	KB	2050	0.4	[69]
Co_3O_4	mesoporous nanocristal	paper	8.2 ($mAh.cm^{-2}$)	0.4	[70]
Co_3O_4	Inverse opal	KB	6959	0.28	[71]
CeO	nanoparticle	microporous	12753	0.11	[72]

Metal oxides have been widely used as catalysts for carbon-based cathode due to their high catalytic activity toward OER/ORR, reasonable price, and their ability to be easily synthesised into various morphologies. Although metal oxides have outstanding catalytic properties on OER/ORR, their various morphologies, test conditions, and carbon sources used in the experiments make comparisons between studies impossible. It will therefore be essential to compare the metal oxides under the same conditions in order to really estimate their properties on battery performance. As this study had never been carried out, we propose to carry it out in this work by initially focussing on the 3d metals and extending it to 4d metals.

II.1.2.e) Spinel in carbon material

As in the case of noble metals, 3d mixed metal oxides were tested in order to optimise their catalytic properties. These combined oxides often possess spinel structure AB_2O_4. The objective of this section is to evaluate their catalytic properties for OER/ORR and their influence on battery performance.

$NiCo_2O_4$ nanotubes consisting of nanoflakes were synthesized through hydrothermal method (Figure 34 a,b) by Yu et al.[73] Such nanotube exhibited a type II isotherms with a surface area of 129.0 $m^2.g^{-1}$ and pore sizes inferior to 5 nm. (Figure 34 c,d). Battery made with this cathode showed an initial discharge capacity of 1979.4 $mAh.g^{-1}$ which was better than its pure carbon counterpart which reached 1100 $mAh.g^{-1}$ (Figure 34 e). $NiCo_2O_4$ reduced the charge voltage from 4.14 to 3.92 V revealing its high catalytic activity toward the OER. The cyclability of the battery was evaluated when

discharging at a 2.0 V cut off voltage. It showed that the battery using nickel cobaltite was more stable and reached 44 cycles while its pure carbon counterpart reached only 20 cycles (Figure 34 f).

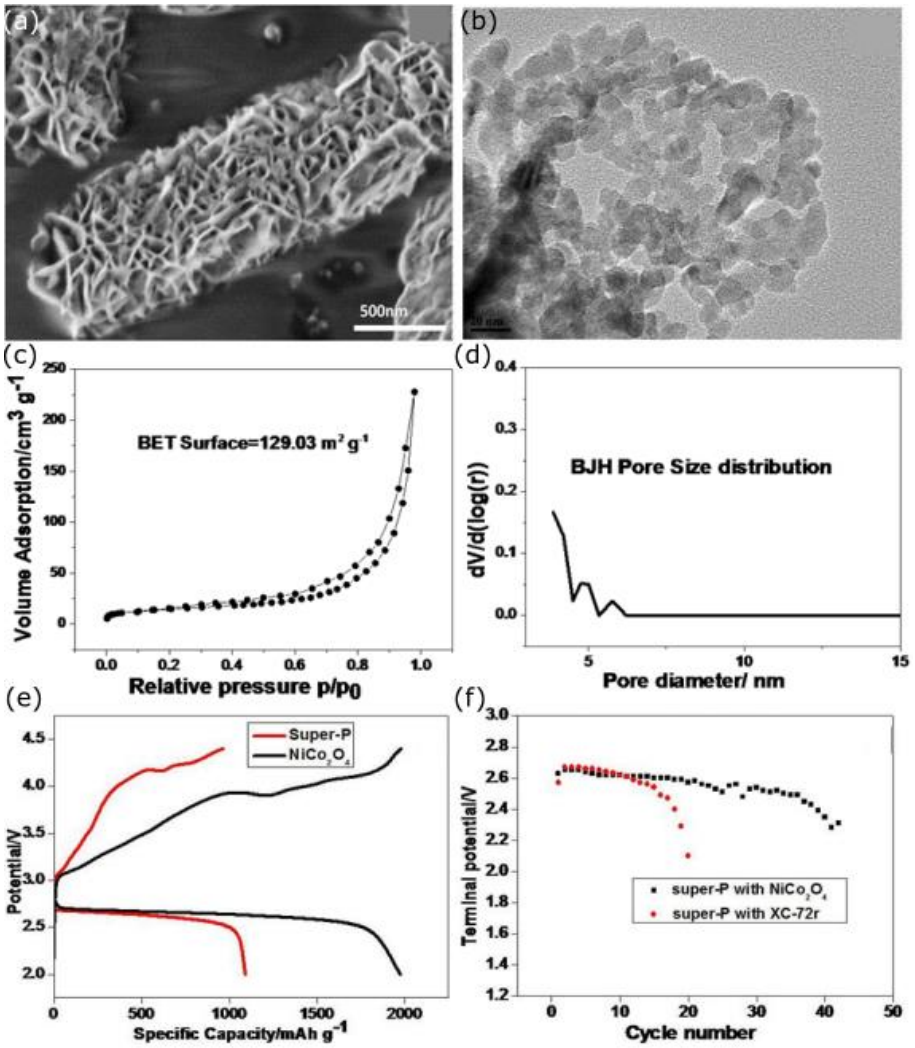

Figure 34: (a) SEM images, (b) TEM micrograph, (c) N_2 adsorption-desorption isotherms (d) and pore size distribution of $NiCo_2O_4$ (e) First discharge-charge profiles, 0.05 mA.cm^{-2} current density, of the Li-O_2 cell with $NiCo_2O_4$ and Super P electrodes. (f) Cycling stability of the Li-O_2 cell with the $NiCo_2O_4$ and pure carbon cathodes.[73]

Sun et al.[76] compared the performance of a KB electrode with a $CuCo_2O_4$/KB cathode (Figure 35 a,b). Textural properties of $CuCo_2O_4$ were examined by N_2 physisorption and their results are presented in Figure 35 c,d. The specific surface area of the mesoporous metal oxides was 97.1 $m^2.g^{-1}$ and the pore size distributions showed a narrow distribution centred at 3.4 nm. The electro activity of the $CuCO_2O_4$/KB electrode was investigated via cyclic voltammetry (CV) (Figure 35 e). The $CuCo_2O_4$/KB electrode presented a higher cathodic peak voltage, a lower anodic onset potential, and a larger cathodic and anodic currents demonstrating the catalytic efficiency of the cathode for the OER and ORR processes. The porous structure of $CuCo_2O_4$ allowed high diffusion of lithium and oxygen within it and high catalytic activity on the OER/ORR, that led to excellent battery performance. Figure 35 shows its cycling performance of $CuCo_2O_4$ and KB cathodes at a current density of 100 mA.g^{-1} with a capacity of 500 mAh.g^{-1}. For the first cycle (Figure 35 f), the electrode made with the catalyst showed a decrease of the overpotential of 0.61V reflecting its good activity with regard to the OER process.

Furthermore, $CuCo_2O_4$ electrode was found to be stable for 25 cycles with a terminal voltage above 2.0 V, unlike the KB cathode which performed 7 cycles under the same conditions (Figure 35 g). To conclude, the improvement in performance was largely explained by the catalytic activity (OER/ORR) and morphology of copper cobaltite.

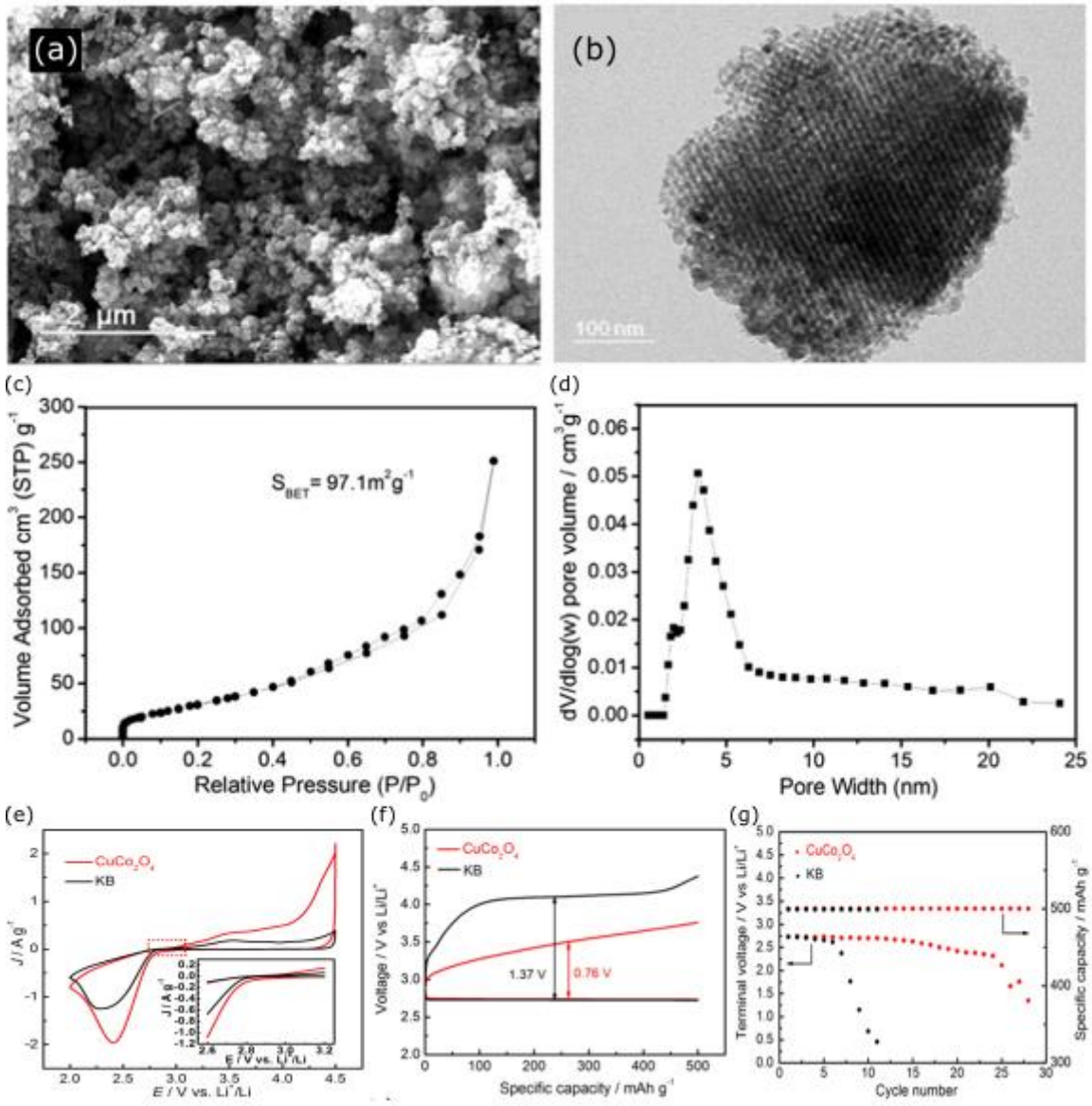

Figure 35: (a) SEM, (b) TEM, (c) Nitrogen adsorption and desorption isotherms and (d) the corresponding pore size distributions of the mesoporous $CuCo_2O_4$ (e) CV curves of $CuCo_2O_4$/KB and KB carbon-only electrode at a scan rate of 0.1 mV s−1 (f) First discharge/charge profiles of Li-O_2 cells with the $CuCo_2O_4$/KB and KB electrodes with a restricting capacity of 500 mAh.g^{-1} at a constant current density of 100 mA.g^{-1} (g) and their cycling stability.[76]

Another widely used cobaltite is manganese cobaltite $MnCo_2O_4$. Jian et al.[77] synthetised mesoporous nanospheres with a specific surface area of 14.4 m².g^{-1} and a pore volume of 0.05 cm^3.g^{-1} (Figure 36 a,b). A cyclic voltammetry test was performed to investigate the catalytic activity toward ORR and OER (Figure 36 c). The peak potential of the $MnCo_2O_4$/KB electrode was 75 mV higher than that of the pure KB for the ORR. To estimate the activity for OER, Linear sweep voltammetry (LSV) test was carried out (Figure 36 d). It presented an onset potential of 3.2 V for $MnCo_2O_4$/KB and 3.4 V for pure KB electrode. These two tests confirmed the catalytic activity of $MnCo_2O_4$ for OER/ORR processes. The

full discharge–charge cycle performance of the Li-O_2 batteries made of $MnCo_2O_4$/KB and pure KB cathode were studied for the first 3 cycles at 100 mA.g^{-1} within a voltage range of 2.2–4.5 V. As shown in Figure 36 e,f, in the first discharge, the $MnCo_2O_4$/KB electrode achieved a capacity of 8518 mAh.g^{-1} while the KB cathode reached only 6403 mAh.g^{-1}. At the second cycle, the retention capacity was observed to be 21.3% higher for the cobaltite electrode. However, the capacity decreased rapidly with each cycle. This reduction was explained by the accumulation of insulated product Li_2O_2 collected through the cycle. Figure 36 g presents the first discharge/charge profiles obtained with $MnCo_2O_4$/KB and pure KB cathode at a current density of 100 mA.g^{-1} at a capacity of 1000 mAh.g^{-1}, and shows an increase in the discharge plateau from 2.75 to 2.86 V, and a clear decrease in the charge plateau reflecting the catalytic activity of manganese cobaltite with respect to OER and ORR.

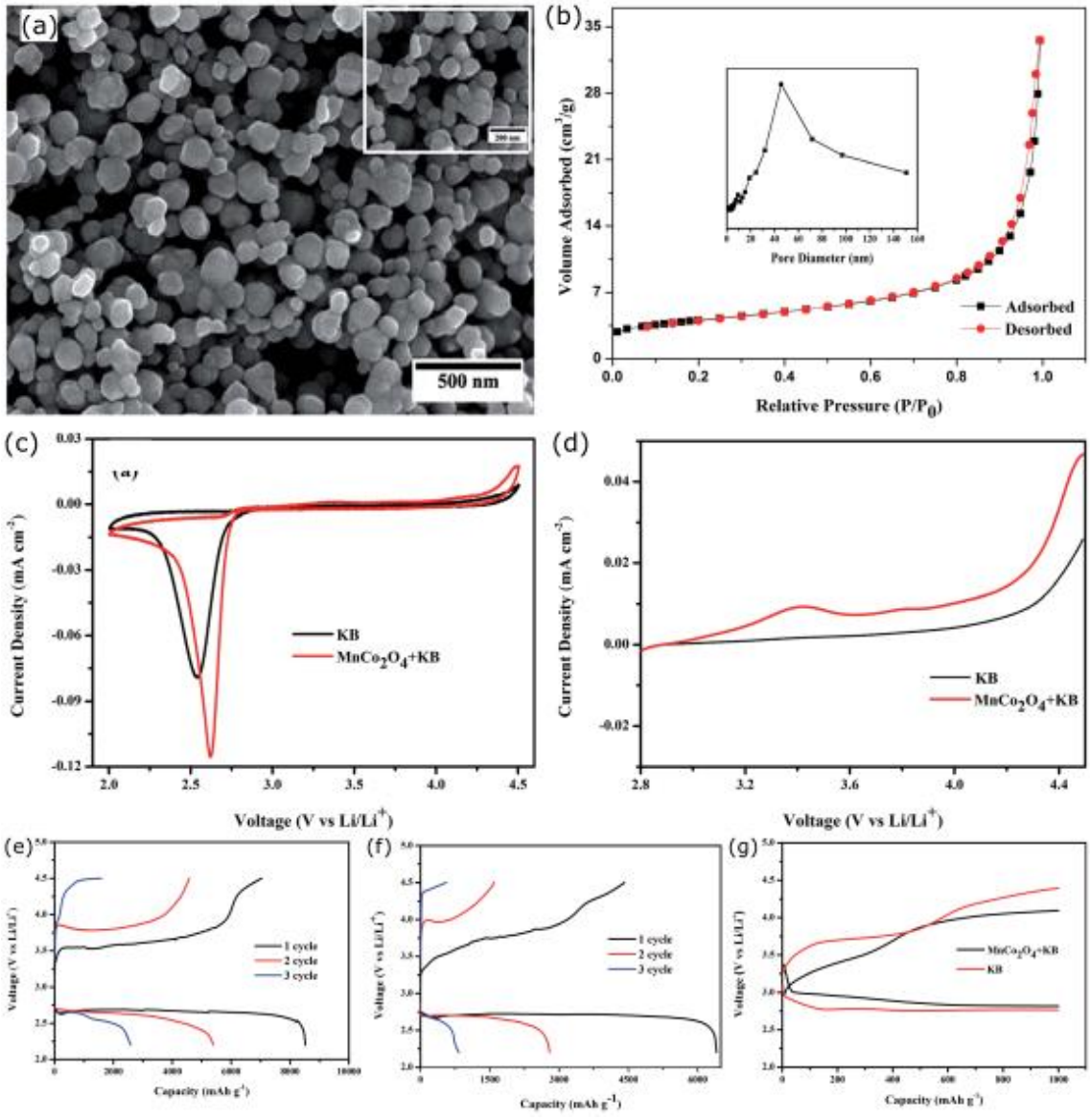

Figure 36: (a) SEM of $MnCo_2O_4$ nanospheres, (b) Nitrogen adsorption–desorption isotherms of MnCo2O4 nanospheres and the pore size distribution (inset), (c) CV curves of $MnCo_2O_4$/KB and pure KB (d) and linear scanning voltammograms. First three cycles of Li-O_2 batteries made with (e) $MnCo_2O_4$/KB and (f) pure KB as cathode at the current density of 100 mA.g^{-1} within a 2.2–4.5 V voltage windows, and (g) first cycle with a limited capacity of 1000 mAh.g^{-1} at the current density of 100 mA.g^{-1} for both electrodes.[77]

The last type of cobaltite to be discussed in this section is zinc cobaltite. Liu et al. [78] synthetised mesoporous $ZnCo_2O_4$ nanoflakes with a specific surface area of 34 $m^2.g^{-1}$, and an average pore diameter of 10 nm, and tested it as catalyst in Li-O_2 batteries (Figure 37 a,b). LSV (Figure 37 c,d) and CV (Figure 37 e) tests were performed to investigate the catalytic activity towards ORR and OER of $ZnCo_2O_4$. The LSV curves of $ZnCo_2O_4$ exhibited a higher OER onset potential and a lower ORR onset potential compared to the Pt/C reference which confirmed the catalytic activity of $ZnCo_2O_4$ for OER/ORR processes. Regarding electrochemical performances of the battery, the use of $ZnCo_2O_4$ as a cathode material increased capacity in the first cycle from 996 $mAh.g^{-1}$ to 1322 $mAh.g^{-1}$ compared to its pure carbon counterpart. Tested at a fixed capacity of 500 $mAh.g^{-1}$ the charge and discharge potentials reached the values of 2.6V and 4V respectively, representing a round-trip efficiency of 65 %. Regarding cyclability, this battery performed 30 cycles (Figure 37 f). Another study by Sun et al. [79] confirmed that $ZnCo_2O_4$ reduced the overpotential by 220 mV at the first cycle at a 500 $mAh.g^{-1}$ capacity.

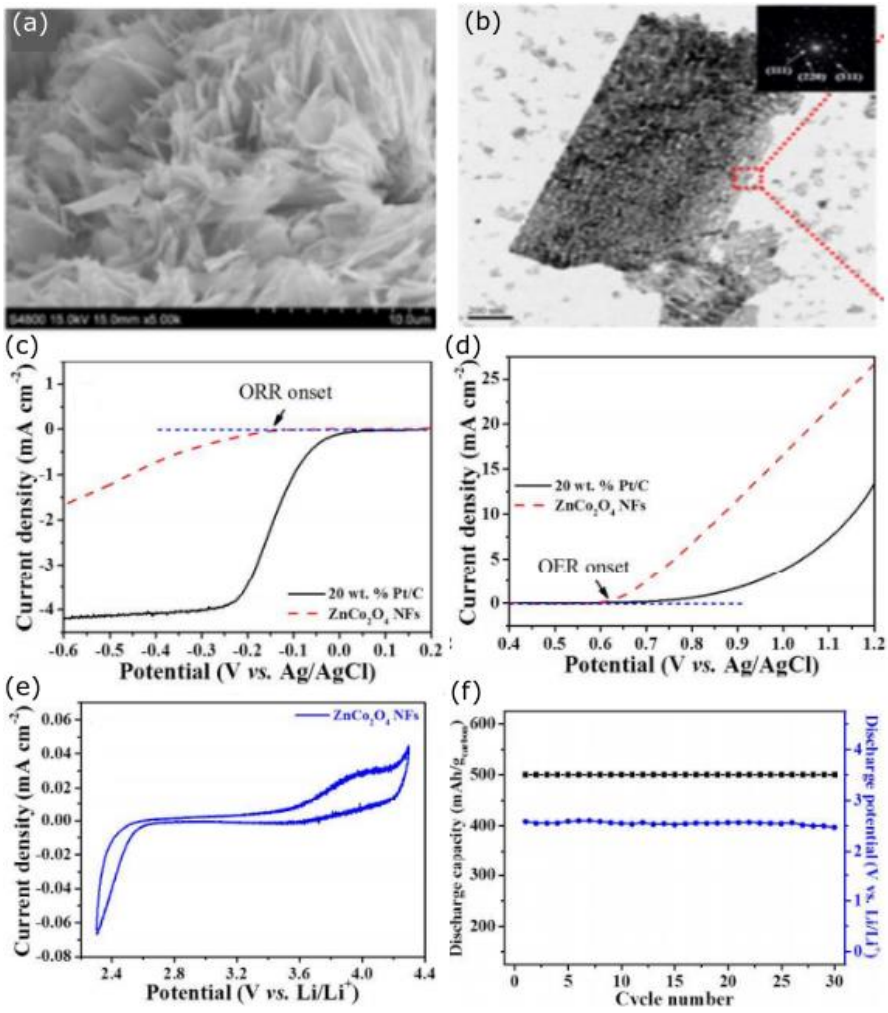

Figure 37: (a) SEM and (b) TEM micrographs, LSV profiles of (c) ORR and (d) OER profiles, (e) CV curve of the mesoporous $ZnCo_2O_4$ and (f) Discharging capacities and corresponding potentials as a function of cycle numbers of the aprotic Li-O_2 battery with mesoporous $ZnCo_2O_4$ based cathode.[78]

Kim et al.[80] synthetised and studied the performance of 3D microporous cobalt ferrite (3DOM CFO) as cathode in lithium oxygen batteries. The overall fabrication process of the bifunctional 3DOM CFO

catalyst and a conceptual description of the discharging process of the electrode are resumed in Figure 38 a-d. The morphology of the materials is presented in the figure 38 e-f. The textural properties tested by N_2 physisorption indicated specific surface areas of 58.1 $m^2.g^{-1}$ and 41.3 $m^2.g^{-1}$ for 3DOM CFO@140 and 3DOM CFO @60, respectively (@140 and @60 refer to the size of polystyrene sphere used during the synthesis and consequently to the size of the pores in the final materials). In this structure, Li^+ and O_2 could migrate easily into the channels of the 3DOM CFO material and optimise the deposition of Li_2O_2 on the surface of the structure. Electrochemical tests were performed over the first five cycles at a current density of 200 $mAh.g^{-1}$ in a 2.3 – 4.5 V voltage window. $CoFe_2O_4$ electrodes properties were compared with a KB cathode. The results, as presented in Figure 38 g, show that the addition of cobalt ferrite resulted in a stabilization of the battery leading to an increase in capacity. The improvement in capacity of the cobalt ferrites was attributed to their specific structure. The larger the pore size, the higher the capacity, reflecting a better accessibility to the active sites for the Li^+ and the O_2. Results from tests at a capacity of 500 $mAh.g^{-1}$ with a current density of 200$mA.g^{-1}$ are shown in Figure 38 h-j. The overpotential was determined at the first cycle and showed values of 1.56 V, 1.51 V, 1.37 V, and 1.13 V for KB, Cobalt ferrite (CFO) nanoparticle, CFO@60, and CFO@140 electrodes respectively, proving the catalytic activity of cobalt ferrites. The lower the overvoltage, the more the catalyst was able to improve the kinetics of the OER/ORR. The catalytic activity of cobalt ferrites was also reflected in the efficiency. At the first cycle, the efficiency reached 70.5% for the CFO@140 electrode, and decreased to 65.9%, 63.6%, and 62.8% for the CFO@60, nanoparticle CFO, and KB cathodes. Furthermore, with regard to the total number of cycles performed, CFO@140 electrode reached 47 cycles, 10 cycles more than that of the CFO@60 cathode and 20 more than that of the KB electrode. In summary, this material improved the electrochemical performance of the battery by combining a hierarchically ordered structure with catalytic activity on the OER/ORR, optimising Li_2O_2 formation/dissociation during discharge/charge processes.

The last spinel structure that will be discussed in this part is $CuCr_2O_4$ (CCO).[82] Batteries using $CuCr_2O_4$ (Figure 39 a,b) were tested at a 1000 $mAh.g^{-1}$ limited capacity and under a 200 $mA.g^{-1}$ current density and it showed that batteries based on $CuCr_2O_4$ cathode can charge and discharge for 80 cycles and reach 100 cycles while using RGO instead of KB (Figure 39 c). The authors explained this increase in performance by the advantages of the spinel structure, and by the synergetic effect between the between CCO nanoparticles and reduced graphene oxide (rGO).

All the spinel-based cathodes for Li-O_2 batteries with their main characteristics are summarised in Table 7.

Table 7: Capacity reached, spinel and carbon morphology, and decrease in overpotential compared to pure carbon-based cathodes for Li-O2 batteries applications.

Spinel	Morphology	Carbon type	Discharge Capacity ($mAh.g^{-1}$)	Δ Overpotential (V)	Reference
$NiCo_2O_4$	Nanotube/nanoflake	Super P	1979	0.22	[73]
$NiCo_2O_4$	coating	N-rGO	6716	0.26	[74]
$CuCo_2O_4$	Mesoporous nanoparticles	Super P	5288	0.55	[75]
$CuCo_2O_4$	Mesoporous nanoparticles	KB	-	0.61	[76]
$MnCo_2O_4$	Mesoporous nanospheres	KB	8518	0.11	[77]
$ZnCo_2O_4$	nanoflakes	CNT	1322	-	[78]
$ZnCo_2O_4$	Mesoporous nanoparticles	KB	6024	0.22	[79]
$CoFe_2O_4$	3D microporous particles	KB	9200	0.43	[80]
$CoFe_2O_4$	nanorod	CNT	1355	0.40	[81]
$CuCr_2O_4$	nanoparticles	rGO	-	-	[82]

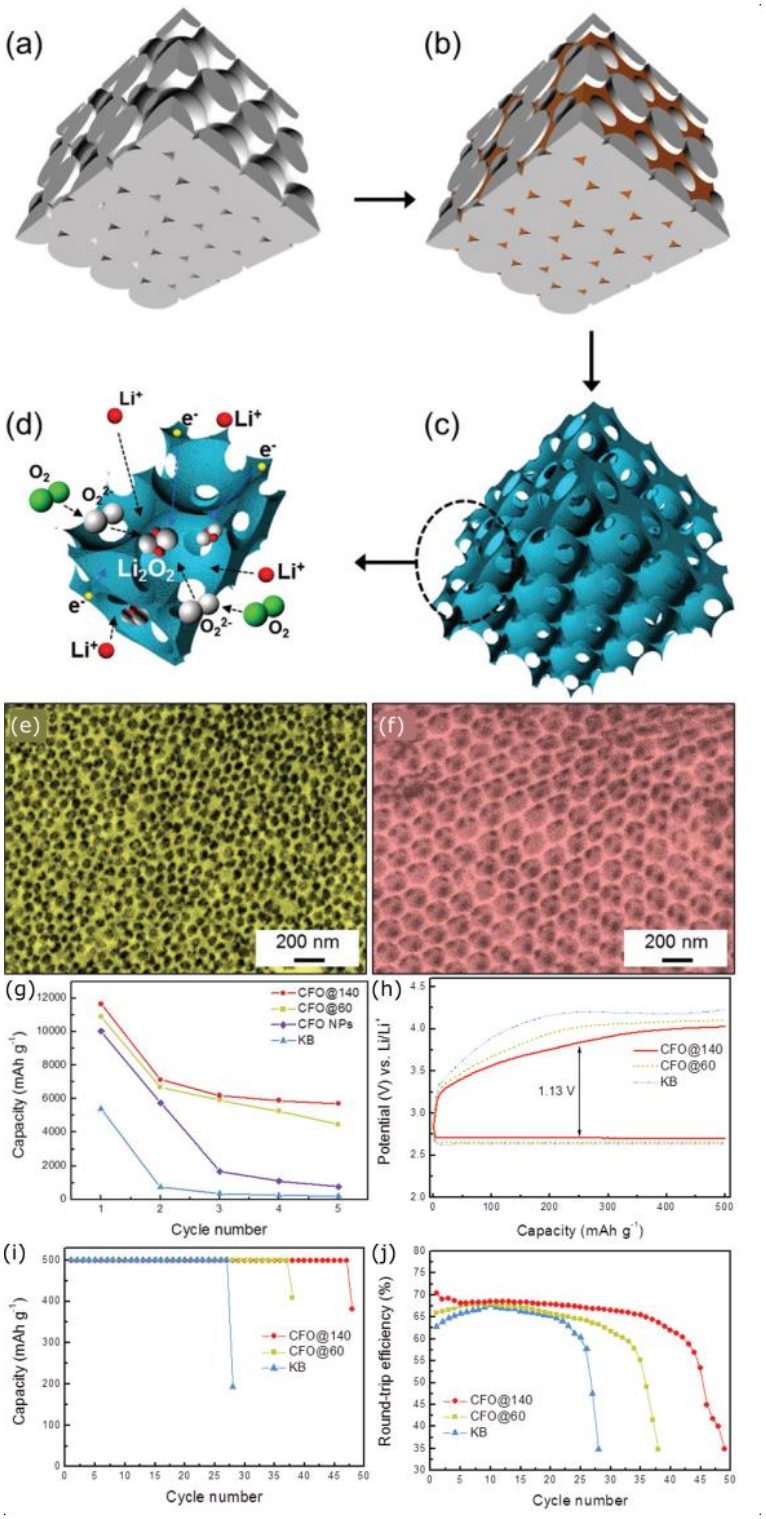

Figure 38: Illustration of the overall fabrication process for the 3DOM CFO catalysts; (a) PS, (b) cobalt–iron precursor impregnated PS, (c) 3DOM CFO. (d) Schematic description of the discharging process of the as-fabricated 3DOM CFO catalyst, SEM images of (e) 3DOM CFO@60, and (f) 3DOM CFO@140, (g) Cycling performance of Li–O_2 cells with KB, CFO NPs, CFO@60, and CFO@140 catalysts for first five cycles at a current rate of 200 mA g^{-1} with a limited voltage window of 2.3 and 4.5 V, (h) discharge–charge curves of Li–O_2 cells with KB, CFO@60, and CFO@140 catalysts at a current rate of 200 mA g^{-1} with a limited capacity depth of 500 mAh.g^{-1} for the first cycle, (i) cyclability of the Li–O_2 cells and (j) round-trip efficiency with KB, CFO@60, and CFO@140 catalysts under a limited capacity of 500 mAh.g^{-1} at a current rate of 200 mA g^{-1}. [80]

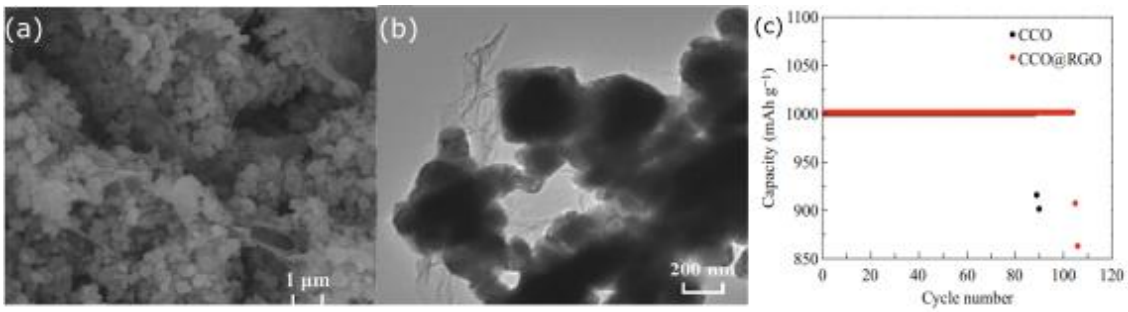

Figure 39: (a) SEM micrograph, (b) TEM micrograph of CCO@rGO nanocomposites, and (c) Cyclic stability of the LOBs with CCO@rGO and CCO cathodes [82]

In this section we have seen that spinel structures have several advantages to be used as cathodes in lithium oxygen batteries. Their structure allows them to combine two metals which can improve their properties. They have a good activity on the OER/ORR which allowed an increase in performance of the batteries. They are cost-effective and their synthesis can be easily scaled up to industrial scale. Their morphologies are easily adjustable allowing optimised cathode designs. All these properties make spinel a serious candidate to be considered as a catalyst for Li-O_2 batteries. In this manuscript, we will use cobaltite spinel that will be directly grown onto the support in order to design carbon-free electrodes.

II.1.2.f) Other materials in carbon material

The previous subsections highlighted the main cathode materials used for lithium-oxygen batteries. Other structures such as perovskites were also tested. Hierarchical mesoporous/macroporous perovskite $La_{0.5}Sr_{0.5}CoO_{3-x}$ nanotubes (HPNLSC) are used as an example.[83] The morphology and the textural properties of HPNLSC were investigated by electronic microscopy and nitrogen physisorption. Results showed a meso/macroporous nanotube with a specific surface area of 17.2 $m^2.g^{-1}$ (Figure 40 a-c). The catalytic activity on ORR/OER processes was investigated by CV, which showed that compared to a pure KB electrode the HPNLSC/KB cathode exhibited higher onset potential and larger peak current density confirming its catalytic activity (Figure 40 d). Figures 40 e,f show the data collected over the first five cycles with the HPNLSC and HPNLSC/KB electrodes within a voltage window between 2.20 and 4.35 V and at a current density of 0.025 $mA.cm^{-2}$. At the first cycle, the discharge plateau obtained with HPNLSC/KB was 0.06 V higher than that obtained with KB only. This difference increased to 0.33 V with regard to charge potential. As a result, the overpotential decreased from 1.53 to 1.14 V. The decrease in overpotential confirmed the catalytic activity of HPNLSC previously observed by CV. The capacity reached by the HPNLSC/KB electrode was 5799 $mAh.g^{-1}$ which is much higher than the 4041 $mAh.g^{-1}$ obtained with the KB cathode. The cycling performances of Li−O_2 batteries at a capacity of 500 $mAh.g^{-1}$ are shown in Figure 40.g.h. The results showed greater stability for the battery made with HPNLSC/KB electrode; the latter was able to perform 50 cycles instead of 13 in the case its pure KB counterpart. The improvement of the Li−O_2 batteries performance was attributed to the synergistic effect of the high catalytic activity and the stable hierarchical

mesoporous/macroporous nanotubular structure of the HPNLSC allowing a higher diffusion of Li^+ and O_2 and consequently optimising Li_2O_2 formation.

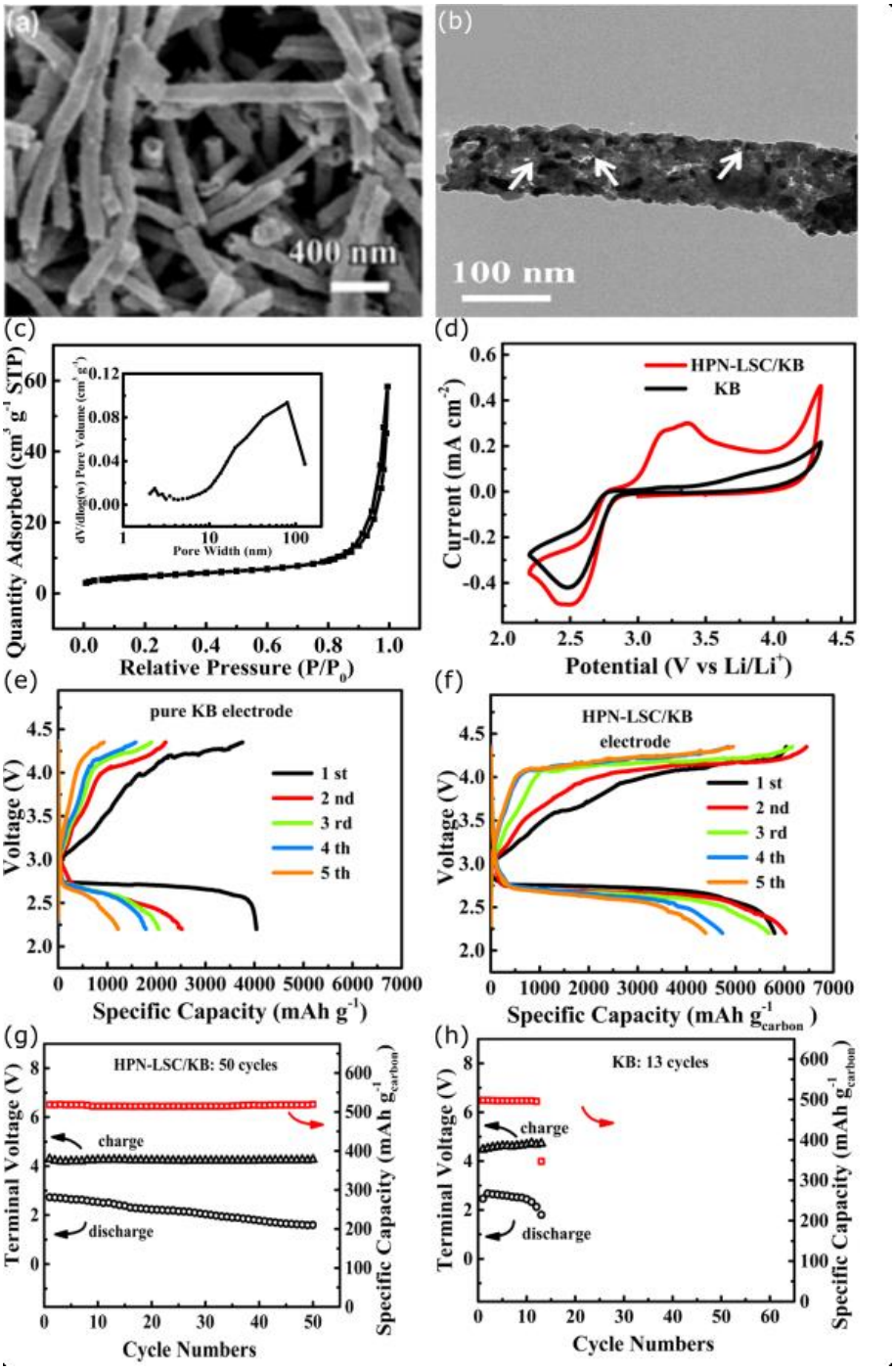

Figure 40: (a) SEM micrograph, (b) TEM micrograph, (c) Nitrogen adsorption−desorption isotherms and pore size distribution of HPNLSC, (d) CV curves of HPNLSC/KB and KB electrodes between 2.20 and 4.35 V at 0.1 mV s^{-1}, First five discharge–charge curves of Li–O_2 cells obtained within a voltage window between 2.20 and 4.35 V, at a current density of 0.025 mA.cm^{-2} and with (e) pure KB (f) HPNLSC/KB electrodes. Cyclic performance of Li–O_2 batteries at a current density of 0.1 mA.cm^{-2} with a limit capacity of 500 mAh.g^{-1} with (g) KB and (h) HPN-LSC/KB electrodes.[83]

Carbides were also used as cathode material in lithium-oxygen batteries. The most commonly employed was molybdenum carbide. A study involving MoC-Mo_2C nanorod grafted on N-doped

carbon nanotube (MoC–Mo_2C/NCNT) is chosen in this analysis as an illustration.[84] The morphology of MoC–Mo_2C/NCNT can be observed in Figure 41 a,b. Performances of MoC–Mo_2C/NCNT electrode were compared with that of Mo_2C mixed with carbon graphite (Mo_2C@GC) and that of Mo_2c grafted on carbon nanotubes doped with nitrogen (Mo_2C/NCNTs). The specific surface area of these materials was found to be 58.1, 112.9, and 79.9 m^2g^{-1} for Mo_2C@GC, Mo_2C/NCNT and MoC–Mo_2C/NCNT, respectively. The reaction kinetics were examined by CV between 2.0 and 4.35 V at the scan rate of 0.1 $mV.s^{-1}$ (Figure 41 c). The MoC–Mo_2C/NCNT catalyst displayed more favourable ORR and OER onset potentials and higher ORR and OER peak current density compared to Mo_2C@GC and Mo_2C/NCNTs electrodes. The presence of two cathodic peaks indicated a two-step discharge product formation reaction. The cathodic peak at ~ 3.0 V was attributed to the formation of lithium superoxide and the other peak observed at around 2.5 V corresponded to the formation of Li_2O_2. Nyquist plots showed lower semicircle (assigned to the charge-transfer resistance) for the MoC-Mo_2C/NCNTs electrode, indicating a better conductivity of the material. The electrochemical performances were studied via a 2.0 – 4.35 V voltage windows, at a current density of 200 $mA.g^{-1}$ (Figure 41 d). Capacities obtained were 34862, 26385, and 12148 $mAh.g^{-1}$ for MoC-Mo_2C/NCNTs, Mo_2C/NCNTs, and Mo_2C@GC electrodes respectively. This increase in capacity was attributed to the higher specific surface area of the nanotubes and also to the improved catalytic activity induced by MoC. Tests at a capacity of 500 $mAh.g^{-1}$ at a current density of 200 $mA.g^{-1}$, were done and the results are shown in Figure 41 e,f. The Li–O_2 cell made of MoC–Mo_2C/NCNTs electrode exhibited the best initial discharge and charge voltage plateaus. The discharge potential of the Li–O_2 battery with the MoC–Mo_2C/NCNT catalyst was lower than that of Mo_2C/NCNTs by 0.03 V and higher than that of Mo_2C@GC by 0.05 V. This difference in potential is not significant. The charge potential plateau of MoC–Mo_2C/NCNTs was reduced by 0.13 V and by 0.17 V compared with Mo_2C/NCNTs and Mo_2C@GC, resulting in a decrease in polarization and thus promoting the reversible reaction. In terms of cycling stability, the battery made with the MoC-Mo_2C/NCNT electrode achieved 164 cycles, which was 72 and 122 cycles more than that of Mo_2C/NCNTs and Mo_2C@GC cathodes showing the great stability provided by the electrochemical and textural properties of MoC-Mo_2C/NCNT material.

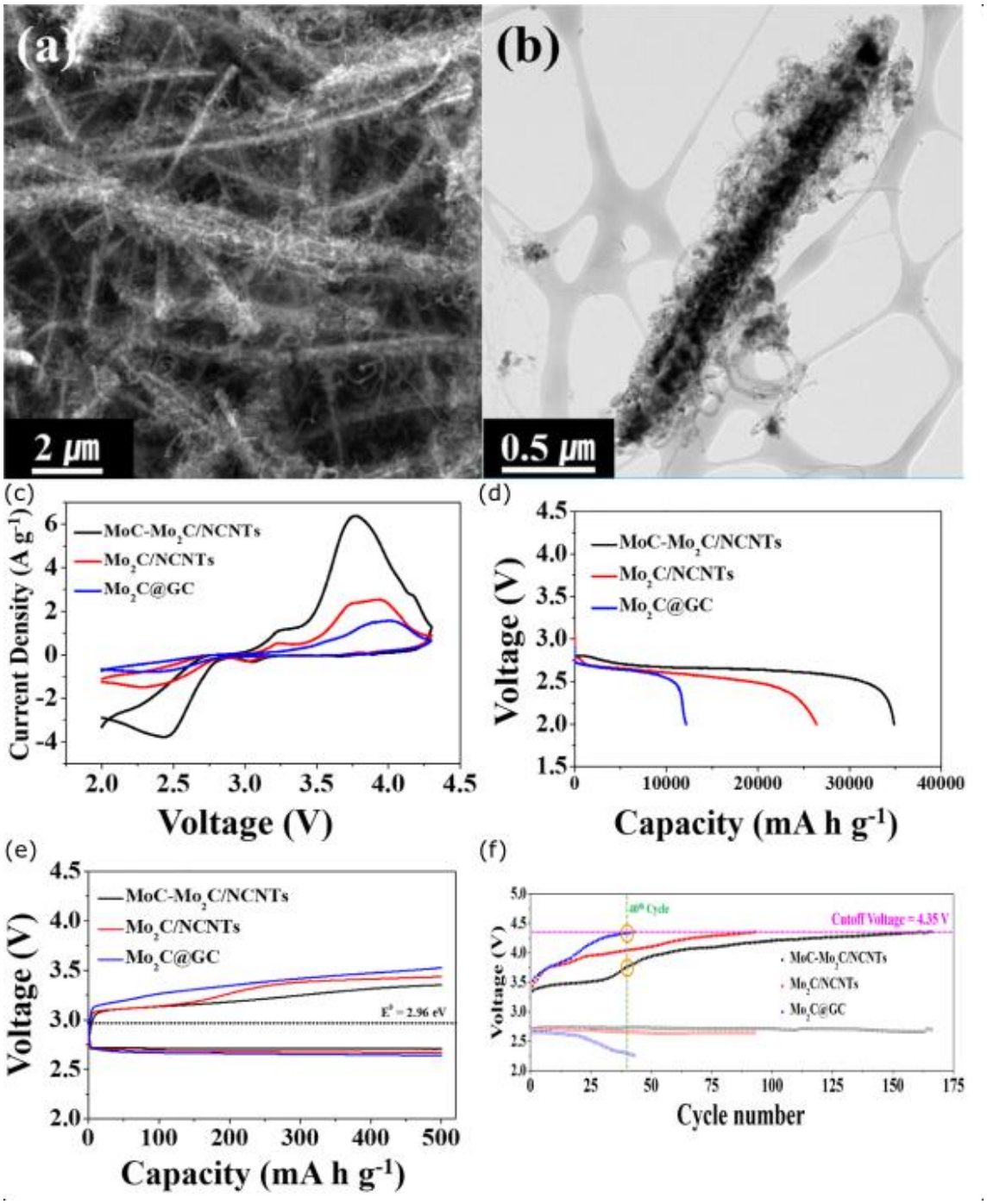

Figure 41: (a) SEM and (b) TEM micrographs of the as-synthetised MoC–Mo_2C/NCNT, (c) CV curves recorded between 2.0 and 4.35 V at the scan rate of 0.1 mV.s^{-1} and (d) Initial charge discharge profile obtained within a 2.0 – 4.35 V voltage windows, at a current density of 200 mA.g^{-1} for Li-O_2 battery based on Mo_2C/NCNTs, Mo_2C/NCNTs, and Mo_2C@GC electrodes (e) First charge discharge profile and (f) cycling stability obtained with Mo_2C/NCNTs, Mo_2C/NCNTs, and Mo_2C@GC electrodes within Li-O_2 cells and performed at 500 mAh.g^{-1} with a current density of 200 mA.g^{-1}.[84]

The final class of materials that will be discussed in this section is metal hydroxide. Fellinger et al.[85] used vertically aligned carbon nanosheets grafted with metal hydroxide as electrode material. The hydroxides involved are: cobalt (II) hydroxide, and iron (III) hydroxide (Figure 42 a,b). The first full discharge/charge profiles were performed at a current density of 75 mA.g^{-1} (Figure 42 c,e). $Co(OH)_2$@CNS achieved the highest capacity 5403 mAh.g^{-1}, followed by $Fe(OH)_3$@CNS which reached

3762 mAh.g^{-1} and pure CNS 1248 mAh.g^{-1}. Testing at a fixed capacity of 1000 mAh.g^{-1} showed a decrease in the charge potential plateau of 0.37 V for $Co(OH)_2$@CNS electrode and 0.51 V for $Fe(OH)_3$@CNS compared to the pure CNS electrode. This reduction of charge potentials, reduced side reactions and improved cycling stability. Regarding discharge potential, it increased by 0.29 V for $Co(OH)_2$@CNS and 0.33 V for $Fe(OH)_3$@CNS compared with CNS . These results reflected the higher catalytic activity of the iron and cobalt hydroxides to the oxygen reduction reaction. Moreover, hydroxides facilitated the crystallisation of the lithium peroxide through hydrogen bonds that improved the OER.

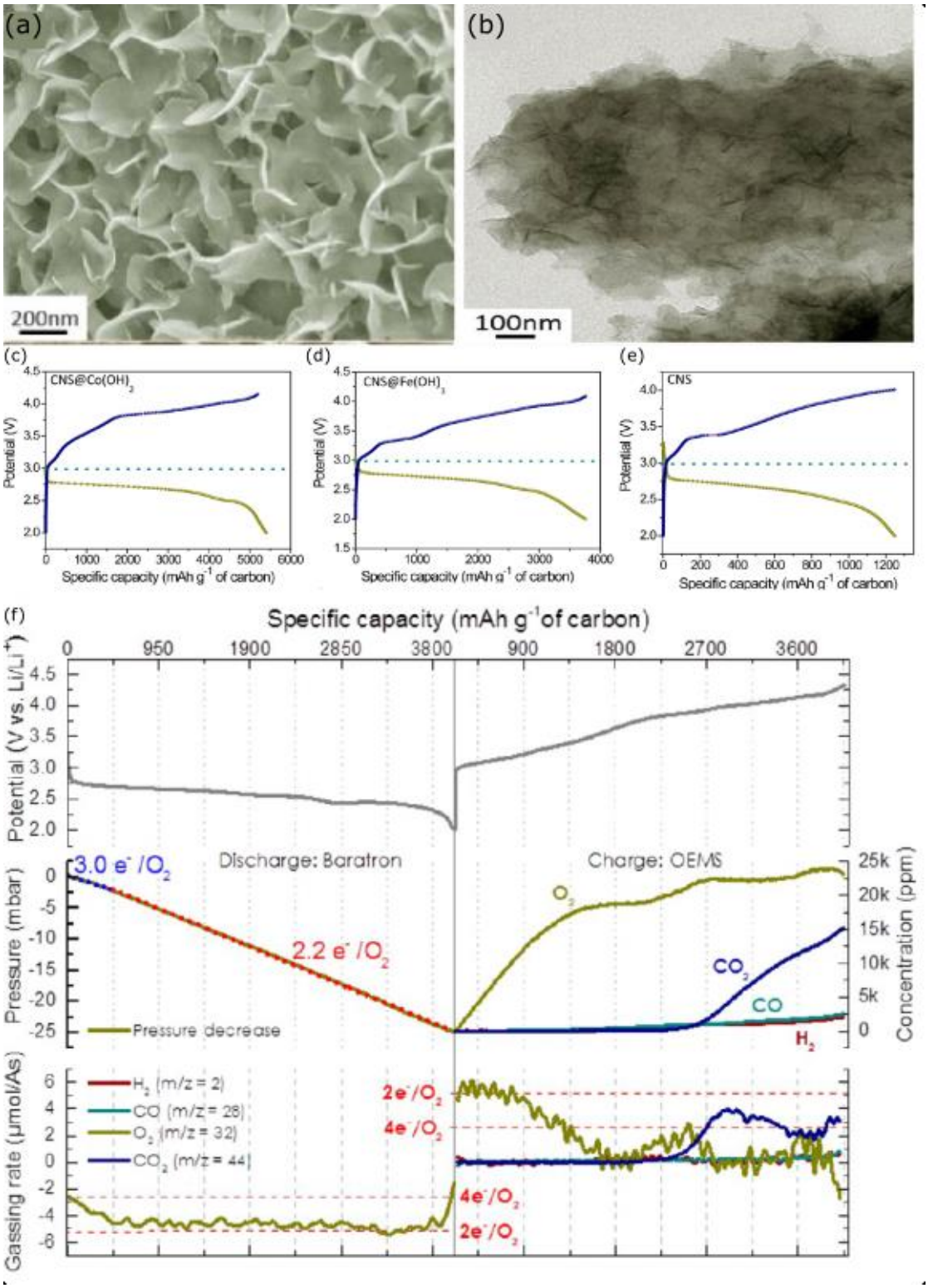

Figure 42: (a) SEM micrograph and (b) TEM micrograph of typical $M(OH)_2$@CNS (M = Co,Fe), First charge discharge profile of Li-O_2 cells with (c) CNS@$Co(OH)_2$, (d) CNS@$Fe(OH)_3$, and (e) pure CNS electrode and (f) gas analysis of first discharge and charge of $Co(OH)_2$@CNS at 175 mA.g−1 by combined approach using a Baratron pressure transducer to investigate gas consumption during discharge and OEMS to analyse gas evolution during charge. Upper panel shows potential profile, middle panel absolute gas consumption/evolution, and lower panels gas consumption/evolution rates. Dashed lines indicate respective values for $2e^-/O_2$ and $4\ e^-/O_2$.[85]

The cycle stability has only been studied for the $Co(OH)_2$@CNS electrode. It was found to reach 40 cycles at a capacity of 715 $mAh.g^{-1}$ at a current density of 150 $mA.g^{-1}$. The gas evolution during charge and discharge was monitored with a Baratron pressure transducer for the $Co(OH)_2$@CNS electrode, as shown in Figure 42 f. During discharge, 25 mbar (≈23 µmol) of O_2 was consumed in two regimes implying a 3.0 electrons per O_2 (average of a 2 and a 4 electron per O_2 process) and a 2.2 electrons per O_2 revealing that Li_2O_2 is the main discharge product formed. During charge, most of the O_2 was released before 3.9 V, via a two-electron-per-oxygen process corresponding to the oxidation of Li_2O_2 formed during discharge. However, when the voltage exceeded 3.9 V, CO and CO_2 resulted from the oxidation of the electrolyte. The OER/ORR ratio was calculated for the first cycle on the basis of the O_2 concentration at the end of the charge (23000 ppm ≈ 9 µmol) and that which was consumed during the discharge, this ratio reaches 40% illustrating the use of oxygen in parasitic reactions, such as the formation of lithium carbonate, for example. Nevertheless, the author pointed out that all of the discharge products (Li_2O_2/Li_2O) might not be fully obtained during charging. To conclude, the use of metal hydroxides made it possible to reduce the overpotential. To optimize the performance of this battery, a maximum voltage of 3.9 V was necessary to be applied in order to preserve degradation.

The cathodes based on perovskite, metal carbide, and metal hydroxides used for Li-O_2 batteries with their main characteristics are summarised in Table 8.

Table 8: Capacity reached, material nature, carbon morphology, and decrease in overpotential compared to pure carbon-based cathodes for Li-O_2 batteries applications.

Material	Morphology	Carbon type	Discharge Capacity ($mAh.g^{-1}$)	Δ Overpotential (V)	Reference
Perovskite					
$La_{0.5}Sr_{0.5C}oO_{3-x}$	Nanotube	KB	5799	0.39	[83]
Carbide					
MoC-Mo_2C	Nanorod	N-CNT	34862	0.17	[84]
MoC-Mo_2C	Nanorod	Graphite	26385	0.04	[84]
Metal hydroxide					
$Co(OH)_2$	Coating	Nanosheet	5403	0.37	[85]
$Fe(OH)_3$	Coating	Nanosheet	3762	0.51	[85]

This sub-section highlighted several materials that have been used as catalysts within cathodes for applications in Li-O_2 batteries. These materials increase the performance of the battery through their catalytic activity on the OER and ORR and could be promising. However, their synthesis remains rather complicated, and a possible way of optimisation could be to find simpler synthesis methods in order to be able to use these materials on a larger scale.

II.1.2.g) Mixed materials in carbon material

The previous sections have described the main categories of cathode materials in lithium-oxygen batteries. In this section, some mixed materials combining the previous materials will be introduced and their performance evaluated.

The first mixed materials that are to be discussed in this section are noble and transition metal-based alloys such as MPt and MPd. Metin et al. studied these alloys by designing two RGO-MPd (M = Co, Cu, Ni)[86] and RGO-MPt (M = Co, Cu, Ni)[87] electrodes (Figure 43 a-c).

A test at a fixed capacity of 0.5 $mAh.cm^{-2}$, at a current density of 0.05 $mA.cm^{-2}$ was conducted with a MPt cathode (Figure 43 d). The overpotential of the MPt catalysts was determined at the second cycle. All catalysts displayed a similar 2.8 V discharge plateau. The rGO-CoPt, rGO-CuP and rGO-NiPt charge overpotentials were 0.7 V, 0.9 V and 1.2 V respectively. The charging overpotential is defined as the voltage gap between the observed charging potential and thermodynamic potential (E_{rev} Li_2O_2 = 2.96V). The decrease in charge overpotential was explained by the effect of alloying which increased the 5d vacancies of the Pt surface, resulting in an increase of O_2 adsorption and a weakening of the O-O bond. It was also related to the absorption of LiO_2. A lower charge overpotential meant that the LiO_2 adsorption strength surface increased as the adsorption strength towards LiO_2 decreased. Regarding the different cathodes, the lower charge overpotential of the CoPt alloy was attributed to the lower electronegativity of Co with respect to Pt resulting in impairment of the metal-oxygen bond due to the increased electron density of Pt. In terms of cycling stability, CoPt and CuPt performed 40 cycles, but NiPt reached only 25 (Figure 43 e). The full discharge and charge capacity test for the three catalysts were performed under a current density of 0.05 $mA.cm^{-2}$ and showed maximum values of 9876 $mAh.g^{-1}$, 9714 $mAh.g^{-1}$, and 9898 $mAh.g^{-1}$ for NiPt, CuPt, and CoPt respectively. These electrochemical results were in agreement with the previous observations.

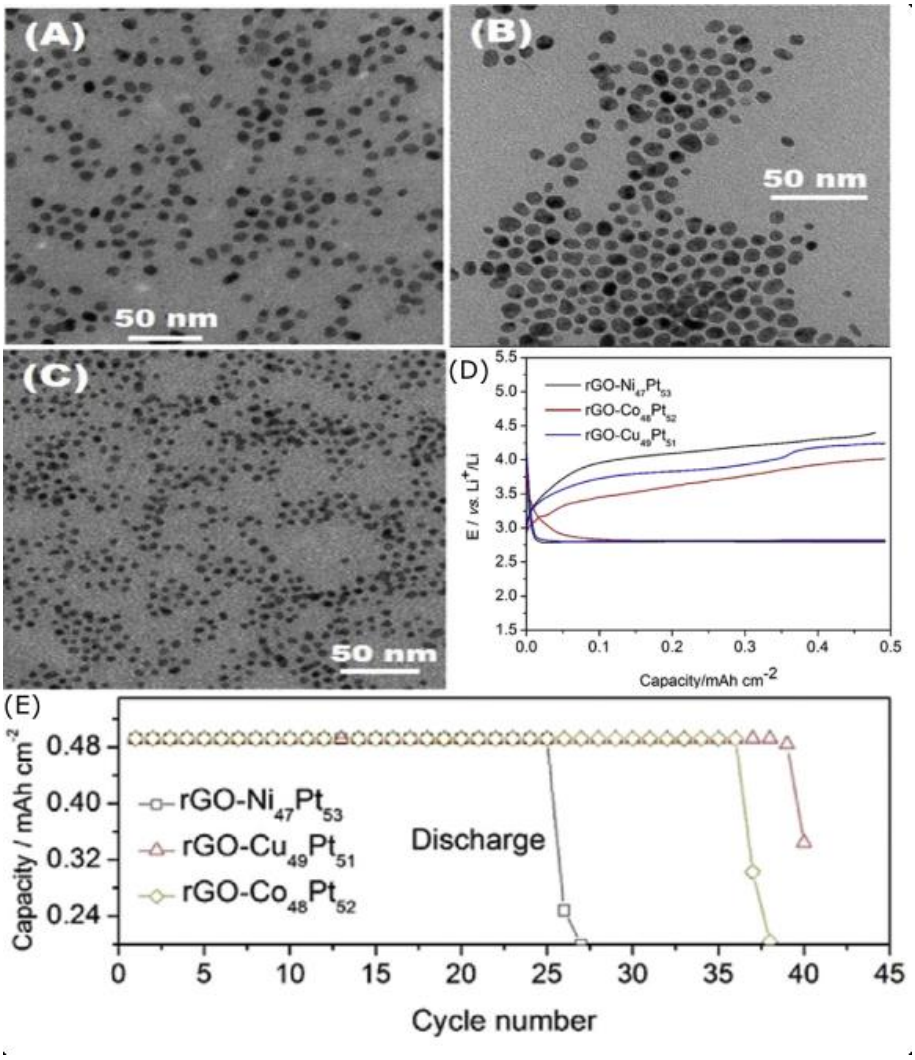

Figure 43: TEM micrographs of (A) CoPt, (B) NiPt and (C) CuPt alloy NPs; Galvanostatic discharge tests at the limited capacity of 0.5 mAh cm^{-2} , (D) Capacity vs. cell voltage profiles for (A) at the 2nd cycle for the three cathodes (E) Capacity vs. number of cycles for the three cathodes. [87]

The next mixed materials that will be discussed in this section are a combination of metal oxides and noble metals. Palladium nanoparticles supported onto manganese oxide nanorod (Pd/αMnO_2) was synthetised and tested as cathode in Li-O_2 battery. For comparison purposes, batteries made with αMnO_2 nanorod only and pure KB cathodes were tested under the same conditions. Textural properties and morphology of the material are presented in Figure 44 a,b. Pd deposited on αMnO_2 nanorods possessed higher surface area and pore size than αMnO_2 nanorod only. Catalytic performances of the materials were determined by LSV and the results are resumed in Figure 44 c. The increase of current peaks revealed a higher amount of electron transferred per oxygen molecule: 3.9, 3.8 and 3.3 electrons for Pt/C, Pd/αMnO_2 and MnO_2, respectively. The oxidation of Li_2O is a one-step direct four-electron transfer mechanism ($2Li_2O \rightarrow 4Li^+ + O_2 + 4e^-$). The transfer of 3.8 electrons with the Pd/αMnO_2 cathode is close to the required 4 electrons and could explain the good electrocatalytic activity of this material. Pd/αMnO_2 material was tested as cathode at a current density of 0.1 mA.cm^{-2} in the potential range of 2.0 – 4.3 V.[88] The first charge discharge profile is shown in Figure 44 d. The capacity of the battery containing the Pd/α-MnO_2 nanorod electrode was found to be 8526 mAh.g^{-1}, which was much higher than that obtained with the palladium-free cathode (3997

$mAh.g^{-1}$), and the pure carbon electrode (2000 $mAh.g^{-1}$). The lowest overpotential was displayed by Pd/α-MnO_2 electrode while the highest was that by pure KB cathode. This decrease in overpotential confirmed the catalytic effect on the OER and the ORR of the catalyst. The increase in catalytic effects, described previously, explains the improved performance during cycles. In order to evaluate the stability of the battery built with the Pd/α-MnO_2 cathode, a test at 500 $mAh.g^{-1}$ capacity was carried out, at a current density of 0.1 $mA.cm^{-2}$. The results, as presented in Figure 44 e, show that the battery was able to reach 35 cycles. However, it should be noted that the battery remained table only for the first 20 cycles, after which the potential increased drastically.

The next mixed material to be discussed is carbon/titanium oxide grafted with bimetallic platinum/iridium (Figure 45 a-d).[90] Electrochemical data obtained from LSV are resumed in Figure 45 e. The calculated electron transfer numbers were 3.9, 3.7, and 3.8 for Pt/C–TiO_2, Ir/C–TiO_2, and Pt–Ir/C–TiO_2, respectively. These catalysts allowed the transfer of almost four electrons, enabling the complete oxidation of Li_2O. These electrochemical properties of the catalyst can lead to efficient battery performances. The first charge discharge profile was obtained at a current density of 0.1 mA in a 2.0–4.3 V potential window, and confirmed that the hybrid Pt-Ir/C-TiO_2 reached the highest capacity (4375 $mAh.g^{-1}$) compared to Pt/C-TiO_2 (3856 $mAh.g^{-1}$), Ir/C-TiO_2 (3600 $mAh.g^{-1}$), and KB electrodes (2150 $mAh.g^{-1}$) (Figure 45 f). The overpotential of the electrodes containing the hybrids was observed to be lower than that of the carbon electrode affirming their catalytic properties on the OER/ORR. Battery stability was tested at a fixed capacity of 500 $mAh.g^{-1}$ (Figure 45 g-i). Li-O_2 batteries with Pt-Ir/C-TiO_2 cathode achieved the highest number of cycles with 35 cycles, 2 cycles more than the Ir/C-TiO_2 cathode and 5 more than those of the Pt/C-TiO_2 cathode.

Kang et al.[91] studied the properties of a noble metal/spinel mix as cathode material using $NiCo_2O_4$ nanosheets impregnated with Pd on porous carbon (Figure 46 a). The addition of Pd to the surface of the spinel structure created oxygen vacancies which provided interesting electrochemical properties for OER/ORR. Electrochemical tests were performed at 200 $mA.g^{-1}$ between 2.0 and 4.5 V (Figure 46 b) and showed an initial discharge capacity of 4000 $mAh.g^{-1}$ for Pd@$NiCo_2O_4$ which was higher than that of $NiCo_2O_4$ only (3000 $mAh.g^{-1}$). The discharge voltage plateau was similar for both cathodes at 2.3 V. At charge, $NiCo_2O_4$ reached 4.2 V while Pd@$NiCo_2O_4$ reached 4.0 V indicating better catalytic activity for the OER for Pd@$NiCo_2O_4$. However, the round-trip efficiency was significantly higher for the batteries made with $NiCo_2O_4$ electrodes. A test at 1000 $mAh.g^{-1}$ and at a current density of 200 $mA.g^{-1}$ revealed that the Li-O_2 cell made with Pd@$NiCo_2O_4$ cathode achieved 100 cycles while with $NiCo_2O_4$ electrode it reaches only 10 cycles. The stabilisation was explained by the reduction of the overpotential, which helped prevent the degradation within the battery. The stable cycle life and voltage of Pd@$NiCo_2O_4$ during ORR and OER demonstrated that the surface oxygen vacancy generated by Pd decoration facilitated uniform nucleation and growth of Li_2O_2 around the Pd@$NiCo_2O_4$ surface during discharge. The Li_2O_2 formed on the oxygen vacancy of Pd@$NiCo_2O_4$ was easily decomposed during the charge with a much lower overpotential. A schematic illustration for the surface atomic arrangement of Pd@$NiCo_2O_4$ is presented in Figure 46 c.

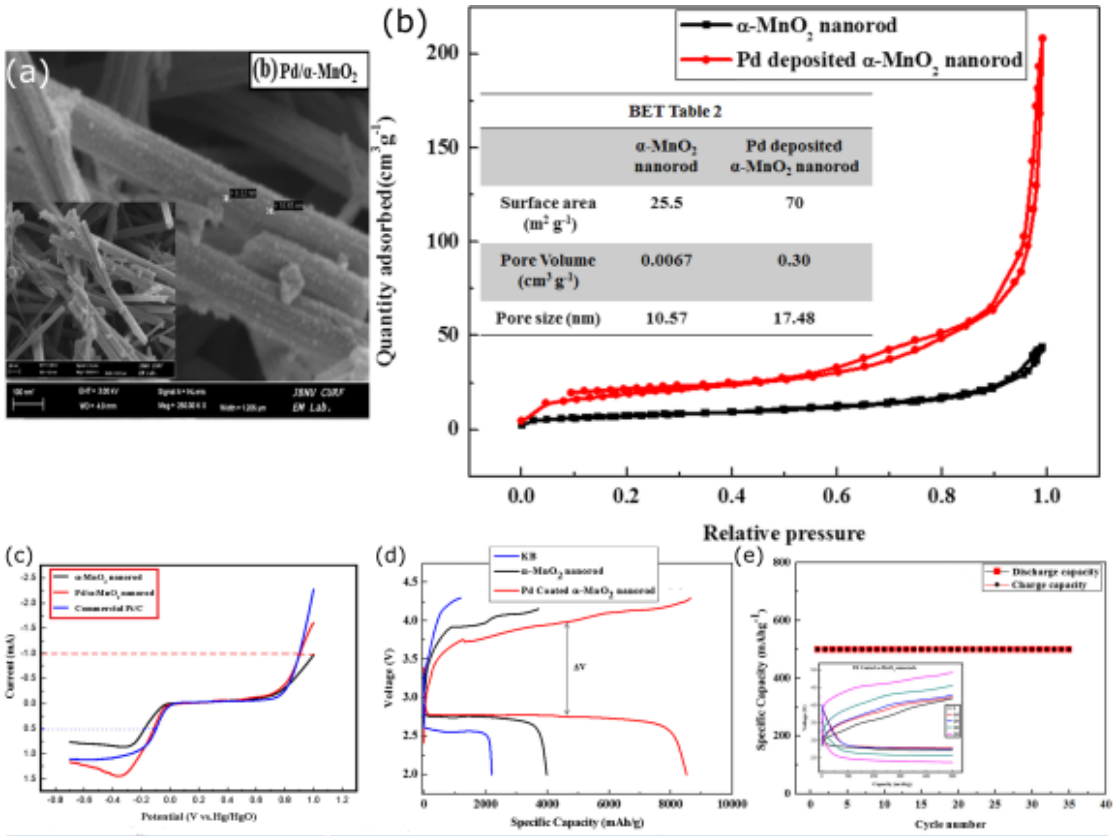

Table 3 ORR characteristics derived from Figure 4					Electrochemical properties of the catalysts		
S.NO	Sample	Onset Potential V	Mass activity mA/mg	Electron transfer number	ORR *E* (V) at *I* = 0.5 mA	OER *E* (V) at *I* = -1.0 mA	Oxygen Electrode Δ (OER - ORR) *E* (V)
1	α–MnO_2	-0.005	22	3.3	-0.18	1.00	1.18
2	Pd /α–MnO_2	-0.003	57	3.8	-0.11	0.89	1.00
3	Commercial Pt/C	-0.003	93	3.9	-0.09	0.89	0.98

Figure 44 : (a) SEM images of Pd-deposited α-MnO_2 nanorods, (b) N_2 adsorption/desorption isotherm of Pd-deposited α-MnO_2 nanorod-catalysed Li–O_2 battery in comparison with α-MnO_2 nanorod, (c) LSV curves recorded in the oxygen-saturated 0.1 M KOH solution at a scan rate of 5 mV s−1 with a disk rotation rate of 1600 rpm. The ORR and OER polarization curves were obtained in the potential ranges of 0.3∼−0.8 and 0.3∼1.0 V, respectively (d) First charge discharge profile of Li-O_2 with Pd/α-MnO_2 nanorod, α-MnO_2 nanorod, and pure KB electrodes and (e) cycling performances of Li-O_2 cells made with Pd/α-MnO_2 nanorod electrodes at limited capacity of 500 mAh.g^{-1}.[88]

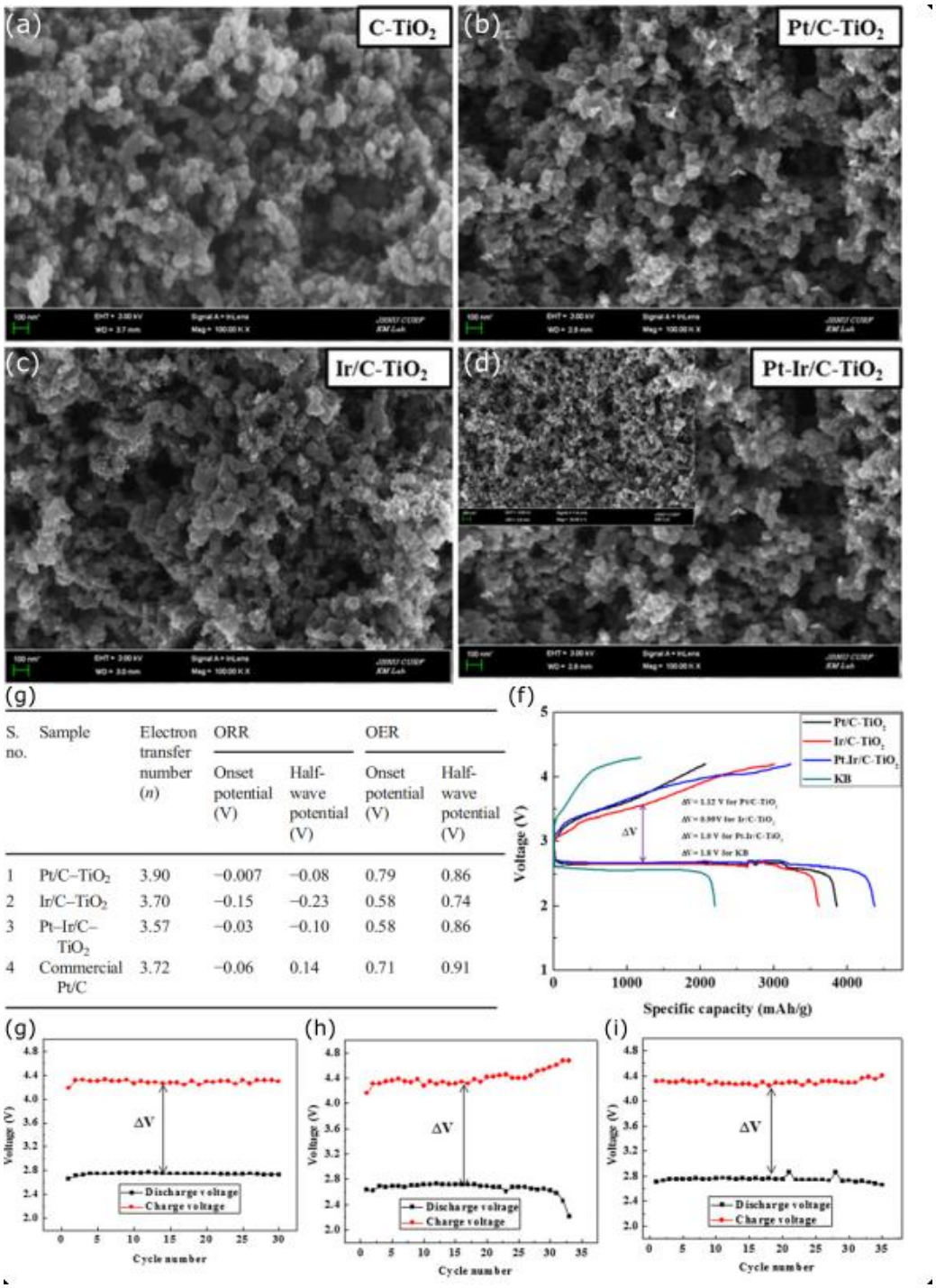

Figure 45: SEM micrographs of (a) C– TiO_2 (b) Pt, (c) Ir, and (d) Pt/Ir nanocomposites supported on C– TiO_2, (e) Electrochemical data obtained from the LSV curves, (f) The first discharge capacity of Pt, Ir, and Pt–Ir/C–TiO_2 catalysts in comparison with the KB cathode, cycling performance of the (g) Pt/C–TiO_2, (h) Ir/C–TiO_2, (i) Pt–Ir/C–TiO_2-catalyzed Li–O_2 battery limited to 500 mAh g^{-1}. [90]

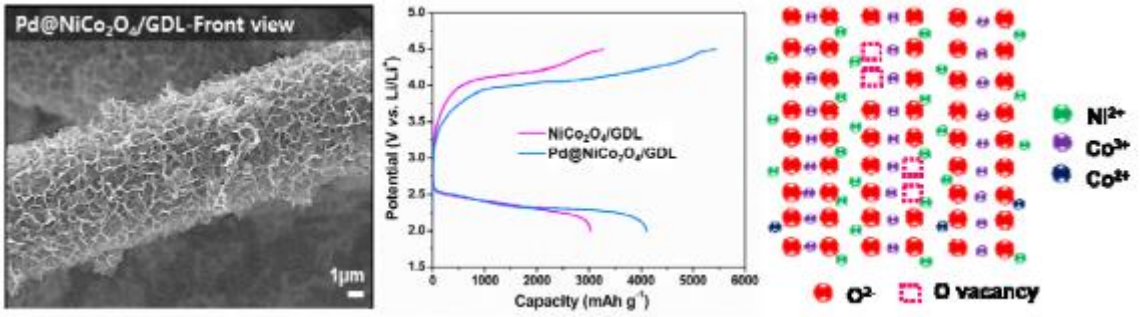

Figure 46: (a) SEM micrograph of $Pd@NiCo_2O_4$ on carbon foam, (b) Initial deep discharge-charge curve of $Pd@NiCo_2O_4$, (c) Schematic illustration for the surface atomic arrangement of $Pd@NiCo_2O_4$.[91]

To put it in a nutshell, many materials were used as cathodes in lithium-oxygen batteries. These materials differ not only in their intrinsic properties such as conductivity, catalytic activity with respect to OER/ORR processes, morphology or textural properties, but also in their extrinsic properties such as price or availability. The main advantages and disadvantages are resumed in Table 9 below.

Table 9: Advantages and inconvenient of all the reported cathode materials for lithium-oxygen batteries

Material	Advantage	Inconvenient	Reference
Noble metals	Catalytic activity / Conductivity	Price / Availability	51-58
Carbon	Conductivity / Availability / Price	High potential needed leading to degradations	16,29,31-50
Metal oxides	Catalytic activity / Availability / Price	Conductivity	60-72
Perovskite	Catalytic activity	Conductivity	83
Carbide	Catalytic activity	Conductivity	84
Metal hydroxide	Catalytic activity	Limited voltage	85

II.1.3) Summary

To summarise this section, the cathode is an essential component of lithium oxygen batteries. It is the site of the electrochemical reactions that allows the formation and decomposition of lithium peroxide during the charge/discharge cycles. This reaction conditions the performance of the battery, which makes it important to create an electrode that allows its optimisation. To this end, two ways of improvement have been proposed. The first is based on the design of the electrode to allow optimal deposition of lithium peroxide on the surface of the cathode. The second is the use of catalytically active materials to the OER/ORR process to increase the reaction kinetics of lithium peroxide formation and decomposition and thus reduce degradation within the battery.

In the first part, several examples of high porosity cathodes were discussed and showed that battery performance cannot be judged only on the specific surface area of the electrode. The porosity and architecture of the cathode must be taken into account. In order to optimise the design of the cathode several factors need to be considered. The electrochemically accessible surface is much lower than the physical surface area and is dependent on the size and structure of the porosity. For the reaction to take place, lithium ions and oxygen must be able to meet on the surface of the cathode. The physical nature of these two compounds being different (liquid, gas) it is important that the cathode is accessible to both forms and that it does not block the reaction flow. The formation of products during the discharge in the cathode pores must not block the diffusion of the reagents. It has been shown that pores that are too small, micropores for example, are not suitable for cycling. In order to improve upon this, we propose to create a cathode with a hierarchical micro-meso/macro porosity according to Murray's law which could allow an optimal diffusion of species within the electrode and thus improve the performance of the battery.

Regarding cathode materials, we have seen that carbon has been widely used because it has good conductivity and catalytic activity on oxygen. Moreover, carbon has several morphologies (nanotube, nanosheet, nanoparticles, ...) allowing the modulation of specific surface of the cathode and the creation of a multitude of diffusion pathways for oxygen and lithium cation. However, carbon is unstable in Li-O_2 batteries and leads to the formation of side products that can passivate the cathode and block the diffusion of species within the electrode. One of the solutions to increase carbon stability is to add a catalyst for OER/ORR. The purpose of the catalyst is to reduce the cathode overpotential during charge/discharge cycles. Many catalysts have been used, the most common being noble metals and metal oxides. These catalysts reduced the overvoltage and improved the performance of the battery. Developing highly active and stable catalytic materials such as bi-functional catalysts towards both ORR and OER is still challenging. The catalysts shouldn’t decompose the electrolyte. However, before looking for new catalysts it would be interesting to have a better understanding of how current catalysts work. Fundamental understanding of the reaction mechanisms of Li-oxygen batteries is required especially for the mechanisms related to ORR and OER. Based on this fundamental knowledge, catalysts could be selected and optimised to increase the performance of the battery.

However, no studies have been undertaken so far to compare the catalysts under the same conditions and to determine their electrochemical properties. In this manuscript we will focus on the study of 3d transition metals. The aim will be to relate the electrochemical properties of the catalysts to the

performance of the battery. This study could be a good basis for understanding the properties of metal oxides as catalysts in oxygen batteries and could provide information on how the catalysts work. As mentioned earlier, carbon leads to degradation within the Li-O_2 battery. Another way to improve battery performances would be to create carbon-free cathodes. In this work, the synthesis, characterisation and testing of a carbon-free cathode will be reported and discussed.

II.2) Electrolyte

The main role of an electrolyte is to ensure the transport of lithium ions between the cathode and the anode according to the charge and discharge cycles. In its simplest form, it consists of a solvent and a lithium salt. Additives can be added to modify the properties according to requirements needed. There are four different types of electrolytes: aqueous, non-aqueous, solid and hybrid. It should be noted that the internal structure of the batteries will change depending on the electrolyte selected. These configurations are shown in Figure 47.

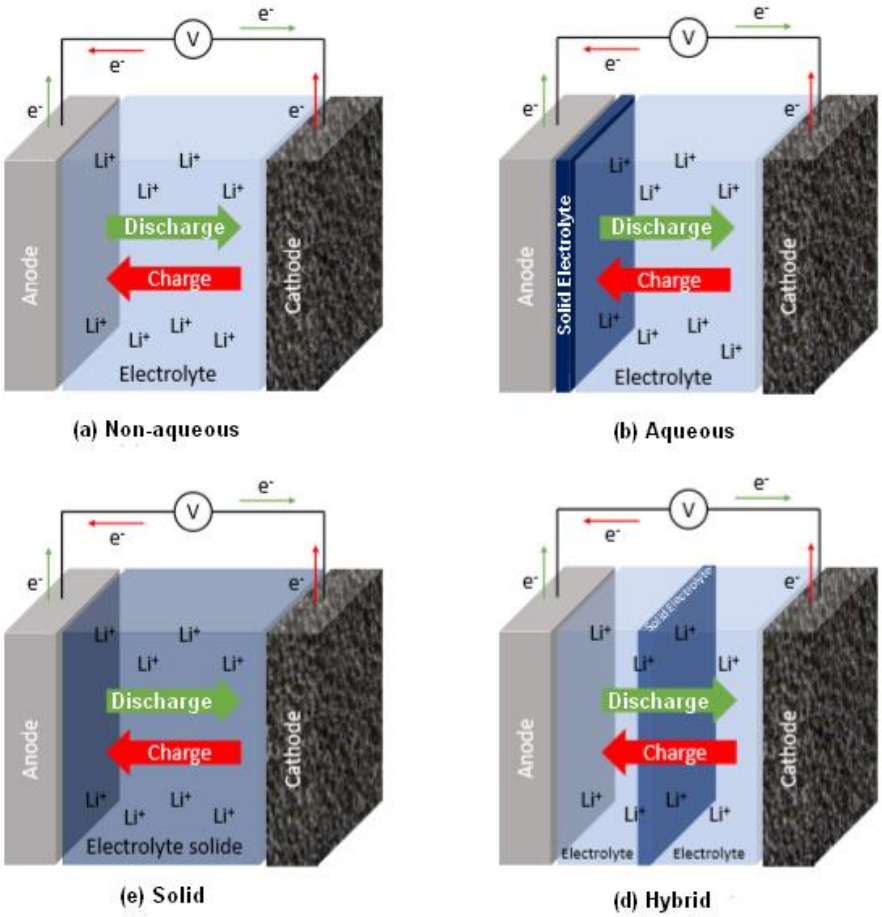

Figure 47: Composition of batteries related to the electrolytes.[18]

Changing the electrolyte will not only influence the composition of the battery but also the electrochemical processes taking place in the battery. The reactions, advantages and disadvantages

for each electrolyte are listed in Table 10. In this project, we selected a non-aqueous electrolyte because it has the advantages of having a high density of thermal energy and a high-recharging capacity. However, the main disadvantage of this type of electrolyte is the production of insoluble products caused by instability problems, that which is relatively easier to address compared to those encountered with other electrolytes.

Table 10: Comparison of batteries regarding electrolytes types.

Electrolyte	Reaction	Advantages	Inconvenients	Reference
Aprotic	$O_2 + 2e^- + 2Li^+ \Rightarrow Li_2O_2$ $O_2 + 4e^- + 4Li^+ \Rightarrow 2Li_2O$	High theoretical energy density Good recharging ability	Insoluble product created during discharge Stability problem.	15,16,94
Aqueous	$4Li + O_2 + 2H_2O = 4\ LiOH$ (alkaline electrolyte) $4Li + O_2 + 4H^+ = 4Li^+ + 2H_2O$ (acid electrolyte)	Soluble products created during discharge	Lack of a conductive Li-ion membrane. Unknown behaviour during charging.	95-97
Hybrid	$4Li + O_2 + 2H_2O = 4\ LiOH$ (alkaline electrolyte) $4Li + O_2 + 4H^+ = 4Li^+ + 2H_2O$ (acid electrolyte)	Soluble products created during discharge. Natural SEI on Li while using an aprotic electrolyte.	Lack of a conductive Li-ion membrane. Unknown behaviour during charging.	36,98
Solid	$O_2 + 2e^- + 2Li^+ \Rightarrow Li_2O_2$	Good stability and recharging capacity. No lithium dendrite formation.	Low conduction of Li^+ ions. Undesirable capacity and energy density.	99,100

II.2.1) Solvent

The choice of organic solvents has a great impact on the performance and life of the battery.[101] First of all, these solvents must have good ionic conductivity, a high capacity for solubilization of lithium salts and oxygen, and a window of electrochemical stability consistent with the applications envisaged. Carbonate-based solvents such as propylene carbonate (PC) and ethylene carbonate (EC), were the first solvents used in non-aqueous lithium-oxygen batteries. The cycling performance was poor and the main discharge products were lithium carbonate and alkylcarbonate, not Li_2O_2. Freunberger et al. propose a possible reaction path to explain the wild range of product formed (Figure 48). [102] The formation of lithium carbonate comes from the reaction between the solvent and the superoxide $O_2^{\cdot -}$. The reduction of the dioxygen involves the formation of superoxide, which is a strong reducing agent that decomposes the carbonated based solvent. Lithium carbonate is an insoluble and insulating compound. It can passivate the cathode preventing electron transfer and inhibiting electrochemical reactions. These products are responsible for the poor reversibility. Regarding electrochemical performance, the cycle performance is associated with the decomposition of solvents rather than the reversible formation and decomposition of Li_2O_2, resulting in a poor cycling life. [102]

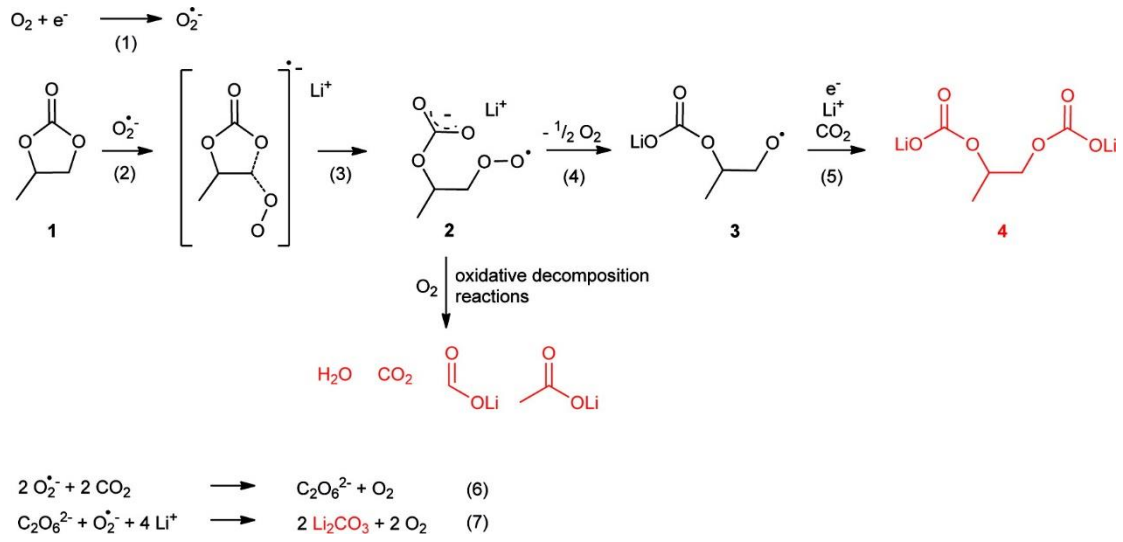

Figure 48: Scheme of discharge reaction explaining the formation of side products: Li Propyl Dicarbonate, Li Formate, Li Acetate, Li_2CO_3, CO_2, and H_2O. [102]

The instability of carbonate-based solvents led to the search for and use of other solvents. Ether-based solvents were tested due to their high stability with respect to superoxide radicals and oxidation potentials. The two most commonly used ethers are dimethoxyethane (DME) and tetraethylene glycol dimethyl ether (TEGDME). The dominant discharge product in ether-based solvent is Li_2O_2 and not Li_2CO_3, which leads to improved cycling life compared to carbonate-based solvent. [103] However, upon discharge, the ether-based solvents are oxidised at high potential by Li_2O_2. [104] Although ethers are relatively stable against nucleophilic attack, they are prone to autoxidation by oxygen radicals to be converted to unstable peroxide species (Figure 49). In addition, some solvents such as TEGDME are unstable at high potential (≈4.5V) [105]

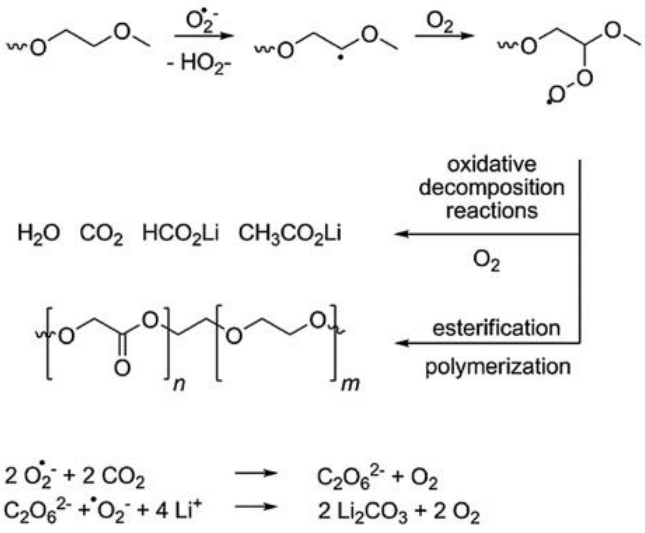

Figure 49: Mechanism of side reactions occurring with ether-based electrolytes during Li–air cell discharge. [105]

Another promising solvent is dimethyl sulfoxide (DMSO), which is relatively stable in the superoxide environment.[105] However, during the oxygen reduction on carbon electrodes, the solvent undergoes oxidation with reactive oxygen species and lithium oxides to form side-products such as LiOH, dimethyl sulfone, Li_2SO_3 and Li_2SO_4 (Figure 50).[107] In addition, the chemical reaction between DMSO and Li_2O_2 could decompose DMSO to $DMSO_2$ and form LiOH.

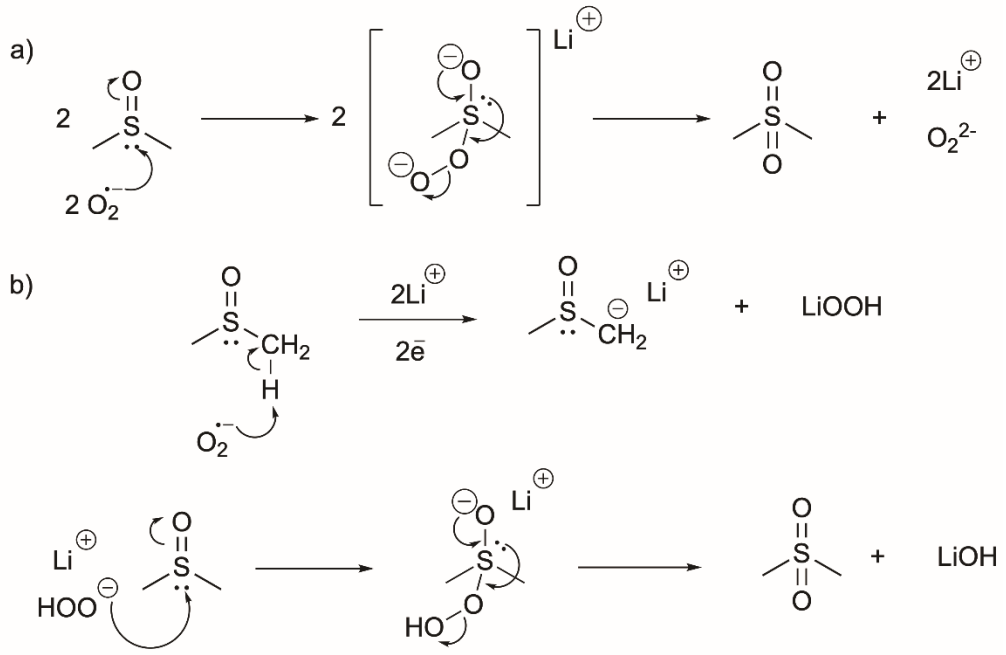

Figure 50: Possible degradation Mechanism of DMSO during discharge via either (a) nucleophilic attack by superoxide or (b) proton abstraction by superoxide ions followed by the formation of DMSO2 and LiOH [107]

Room temperature ionic liquids (RTILs) have various advantages over conventional non-aqueous solvents. They possess a wide electrochemical window and high thermal stability, making them promising stable candidates for non-aqueous lithium-air batteries. [110] However, the high viscosity of RTILs is a big issue, and leads to large transport resistance. Moreover, RTILs have low lithium salt solubility and low conductivity, limiting the discharge current density. [108]

The most commonly used solvents are listed in the following Table 11 with their advantages and disadvantages. According to the information available in the Table 11, ether-based solvents were chosen for this project and more specifically the DME. The DME was preferred to the TEGDME because it has a lower viscosity. However, the vapor pressure is higher but since the system is closed, solvent evaporation will be limited.

From a more general point of view, the selection of the solvent is one of the essential means towards for improving the electrochemical performance of the nonaqueous Li-O_2 battery. The electrolyte must

meet certain stability requirements. It must be inactive towards lithium metal and more importantly it must be stable in the presence of superoxide radicals. It should also have high oxygen solubility, and high diffusivity. Currently, none of the above solvents could meet all of the requirements. Electrolyte degradation is mainly caused by superoxide O_2^-. Therefore, novel nonaqueous electrolytes need to be designed to be stable against nucleophilic attack by the intermediate. This instability could lead to safety issues and is a big problem for potential industrialisation. It is important to stabilise these solvents. Several ways to improve these solvents can be proposed. The first would be to compose mixtures of solvents. The second would be to use redox mediators or soluble catalysts to reduce the overpotential and stabilise the electrolyte. The third would be to substitute labile hydrogens, which are the starting point for solvent decomposition, with methyl or methoxy groups.

Table 11: Main solvents used for non-aqueous electrolyte with their advantages and inconvenient

Solvent	Advantages	Inconvenients	Examples	Reference
Carbonates	High ionic conductivity Good viscosity High boiling temperature	Unstable against superoxide Inflammable	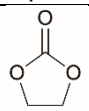	102
Ether	Stable to lithium Stable at more than 4.5V vs. Li^+	Some are volatile Inflammable	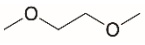	109
Ionic liquid	Large stability window Stable with respect to formed products	High viscosity	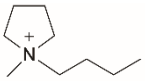	110
Sulfones	High ionic conductivity	Unstable against superoxide	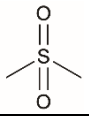	106,107

II.2.2) Lithium salt

The lithium salt, like the solvent, plays a key role in the electrolyte as it ensures ionic conductivity. A lithium salt should be selected following two criteria: it should have a high solubility in solvent and its anion must be inert with respect to the solvent and other battery components.[18,111,112] In addition, the lithium salt influences the solubility of oxygen in the electrolyte.[112,113] The most frequently used salts are shown in Figure 51.

(a)

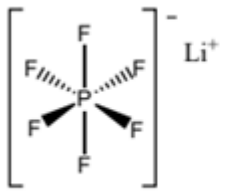

Lithium hexafluorophosphate ($LiPF_6$)

(b)

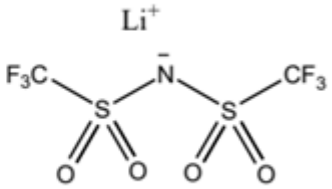

Lithium bis(trifluoromethanesulfonyl)imide (LiTFSI)

(c)

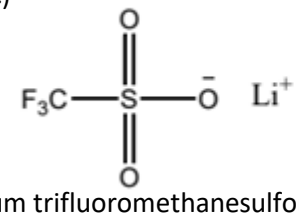

Lithium trifluoromethanesulfonate (LiTf)

(d)

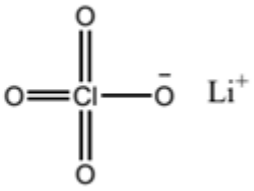

Lithium perchlorate ($LiClO_4$)

Figure 51: Most frequently used lithium salts in Li-O_2 batteries

$LiPF_6$ (Figure 51 a) was the first lithium salt to be used in Li-O_2 batteries.[114] However, it decomposes when used in Li-O_2 batteries, and produces LixPFyOz, POF_3 and mainly insoluble LiF, which passivates the cathode and reduces performance.[115-118] Moreover, the production of HF degrades the other components of the battery. The degradation of the $LiPF_6$ salt has two origins: the first is from parasitic reactions with superoxide [116] and the second is from reactions with traces of water.[117] The degradation of $LiPF_6$ leads to the utilisation of other Li-salts. LiTFSI (Figure 51 b) has been widely used in Li-O_2 cells, but the TFSI anion is unstable vs. ORR and OER in ether and sulfone-based electrolyte solvents.[118,119] LiTf (Figure 51 c) utilisation can lead to high rechargeability battery.[120] LiTf possesses a high donor number (DN; describing the electron donating properties) of the Tf anion compared to other anions and could be favourable for Li-O_2 cells as it increases the solubility of LiO_2.[121,122] The degradation of both LiTFSI and LiTf result in the formation of LiF and -CF3. [118,119] LiF always forms when any of the fluorinated Li-salts are used. To avoid this degradation, a fluorine-free anion could be used to improve the performance. Nasybulin et al.[112] evaluated the stability of different lithium salts in TEGDME. They analysed the products generated during discharge and showed that each salt decomposes but at different levels. $LiClO_4$ (Figure 51 d) exhibits the highest stability, but has lower performance than LiTFSI. However, perchlorate is an oxidizer and its use presents severe safety issues. In case of malfunction, it can lead to an explosion.

A key step in the improvement of lithium-oxygen batteries is to design Li-salts which are electrochemically stable in presence of oxygen superoxides and peroxides. Once mixed with solvent, the electrolyte should provide sufficient ionic conductivity, oxygen solubility, and anodic stability at cathode. Fluorinated salts have the best characteristics. LiTf could be a good option as Li-salt once coupled with high DN solvents. However, stability of fluorinated salts in long-term cycling as well as its compatibility with Li-metal anode are major problems. One of the solutions is to synthetise a fluorine-free anion possessing a high DN property.

II.2.3) Additives

As mentioned above, most of the degradation takes place during discharge and comes from the reaction between superoxide and battery components such as the solvent or the lithium salt. These reactions lead to the formation of side products and drastically reduce the performance of the battery. During charge, the electrochemical oxidation of Li_2O_2 to $2Li^+$ and O_2 is a slow process, and could lead to a large overpotential and low energy efficiency.[123] Additives can be added to the electrolyte to accelerate the kinetics of the reaction, thus increasing the capacity and lifetime of the battery.[124,125] The main additives used are redox mediators, which can be divided into two categories: charge and discharge redox mediators.

Charge redox mediators are the most commonly used additives in lithium-oxygen batteries because they facilitate the oxidation of Li_2O_2. Their oxidation potentials are higher than that of lithium peroxide and could be directly oxidise on the electrode. Once oxidised, they will oxidise the lithium peroxide. Moreover, charge redox mediators could accelerate the decomposition of Li_2O_2 by moving into the cathode and facilitating the transport of electrons between the lithium peroxide and the cathode.

The reactions between the redox mediator (RM) and the Li_2O_2 are illustrated below:

$$2RM \rightarrow 2RM^+ + 2e^- \quad (1.9)$$

$$Li_2O_2 + 2RM^+ \rightarrow 2Li^+ + O_2 + 2RM \quad (1.10)$$

The addition of a mediator reduces the overvoltage during charging. The slow charge transfer between the peroxide and the electrode is replaced by the diffusion of the mediator between the electrode and Li_2O_2.[123] Chen et al. were able to reduce the charge potential of the battery using tetrathiafulvalene (TFF), thereby allowing to keep a constant capacity for 100 cycles.[126] During the charging process, TTF is oxidized to TTF^+ at the surface of the cathode, and during discharging, TTF^+ oxidized Li_2O_2, and reformed TTF. It was found that TTF acts as a molecular electron–hole transfer agent, which allows efficient oxidation of insoluble Li_2O_2. Lim et al. were able to increase the number of cycles from 90 to 900 while maintaining a charge potential below 3.5 V using LiI[127]. Iodine could be oxidized to I_3^- or I_2 on the surface of the electrode and then react with Li_2O_2 to form Li^+ and O_2 gas with the regeneration of I^- ions. The charging overpotential is considerably decreased and leads to an increase of cycling stability. However, the reaction mechanism of iodide mediator is still unclear. LiBr has been also used and demonstrated that it could suppress the parasitic reaction even with water contaminations. However, highly corrosive and reactive Br_2 is produced during discharge and could be a problem. [128]

Discharge redox mediator could also have significant impact on the capacity and cycling stability of the battery. In low DN solvents, the electrochemistry on the cathode surface consists of the reduction of redox mediators rather than the generation of Li_2O_2. Ideally, the redox mediator could promote reactions in solution and suppress Li_2O_2 formation on cathode surface, preventing the creation of an

insulating layer and increasing the capacity of the battery. The most widely used discharge redox mediator is 2,2,6,6-tetramethyl-1-piperidinyloxy (TEMPO). Bergner et al. [129] used the addition of 10 mM TEMPO in the electrolyte. The charging potentials had a distinct reduction of 500 mV, and the cycle life of the battery was doubled from 25 to 50 cycles at the fixed capacity of 1000 mah.g_{carbon}^{-1}. However, undesirable reactions accompanied were noticed, a parasitic shuttle to lithium anode occurred, resulting in a poor cycle life.

The main RM are resumed in Table 12 along with their redox reactions and oxidation potentials.

Table 12: RM formula with their redox reaction and potentials

Name	Structural Formula	Redox Reaction	Oxidation potential	Reference
Tetramethylpiperidinyloxyl (TEMPO)	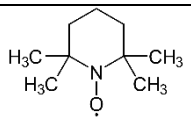	$TEMPO^- \rightarrow TEMPO + e^-$ $TEMPO \rightarrow TEMPO^+ + e^-$	E = 2.92 V E = 3.76 V	[129,130]
Tetrathiafulvalene (TTF)	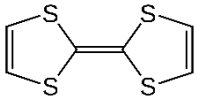	$TTF \rightarrow TTF^+ + e^-$ $TTF^+ \rightarrow TTF^{2+} + e^-$	E = 3.44 V E = 3.75 V	[129,132]
Dimethylphenazine (DMPZ)	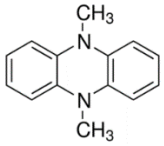	$DMPZ \rightarrow DMPZ^+ + e^-$ $DMPZ^+ \rightarrow DMPZ^{2+} + e^-$	E = 3.28 V E = 3.95 V	[133,134]
Lithium bromide (LiBr)	LiBr	$Br^- \rightarrow \frac{1}{3} Br_3^- + \frac{2}{3} e^-$ $\frac{1}{3} Br_3^- \rightarrow \frac{1}{2} Br_2 + \frac{1}{3} e^-$	E = 3.57 V E = 4.05 V	[128,135]
Lithium iodide (LiI)	LiI	$I^- \rightarrow \frac{1}{3} I_3^- + \frac{2}{3} e^-$ $\frac{1}{3} I_3^- \rightarrow \frac{1}{2} I_2 + \frac{1}{3} e^-$	E = 3.17 V E = 3.73 V	[136,137]

Redox mediators are key molecules for obtaining a stable battery. RM's have the potential reduce the overpotential and prevent electrolyte degradation. However, RM's are quite unstable in Li-O_2 batteries. The search for new stable RM may be an interesting line of research and more specifically, Organometallic RMs, in which the red-ox active center is a transition metal cation, and is surrounded by cyclic organic ligands, may be more stable in Li-O_2 cells.

II.2.4) Summary

To conclude, the selection of the electrolyte is essential for improving electrochemical performance of nonaqueous Li-O_2 system. The main drawback of this type of battery is the presence of superoxide that degrades solvent and lithium salts. In order to obtain an ideal non-aqueous electrolyte for the Li-O_2 battery system, it is necessary that the electrolyte has excellent physicochemical and electrochemical stability, especially in the presence of superoxide radicals (O_2^-), high oxygen and lithium salts solubility, and high diffusivity. The main challenges at the current stage are the search for stable solvents and lithium salts. Currently, none of the above electrolytes could meet all the

requirements for highly stable Li-O_2 batteries. Therefore, novel non-aqueous electrolytes need to be synthetised to be stable against nucleophilic attack by the superoxide. In addition, some binary or even ternary solvent mixtures could be developed. Also, new sustainable redox mediators or soluble catalysts could be explored to reduce the overpotential and stabilize the electrolyte

II.3) Conclusion

To conclude this chapter, we have seen that lithium oxygen batteries are promising devices for energy storage. Their high theoretical energy density makes them a prime candidate to become the battery of the future. However, these batteries face stability problems that hamper their commercialisation. In order to increase the stability of the battery, it is necessary to optimise the different components of the battery. The two main components that can improve the Li-O_2 battery performances are the cathode and the electrolyte.

The cathode is the site of electrochemical reactions in the battery. These reactions lead to the formation and decomposition of lithium peroxide during the charge/discharge cycles and determine the performance of the battery. Two approaches have been considered to optimise the cathode. The first consists of creating a hierarchical structure to optimise the flow of reagent to maximise the formation of Li_2O_2 and the second is to use catalysts capable of increasing the kinetics of lithium peroxide formation and decomposition during the cycles.

The electrolyte allows the transport of ions and oxygen during cycling. It is important that the electrolyte is stable and has good conductivity to be efficient. The main problem with current electrolytes is their instability with respect to superoxide radicals (O_2^-). The search for an electrolyte that is stable with respect to this superoxide is essential. Possible ways of improvement would be to create some binary or even ternary solvent mixtures, new sustainable redox mediators or soluble catalysts. Unfortunately, due to time constraints, this work will only focus on the optimisation of the cathode.

Bibliography

1. Liu.Z, *Global Energy Interconnection*, 2015.
2. Brodd.R, *Chem. Rev*, 2004, **104**, 4245−4269.
3. Iclodean.C, Varga.B, Burnete.N, Cimerdean.D, Jurchis.B, *IOP Conf. Ser.: Mater. Sci. Eng,* 2017, **252,** 012058.
4. Schwarz.V, Gindroz.B, Le Stockage Électrochimique, ADEME, 2005.
5. Wu.F, Yushin.G, *Energy Environ. Sci*, 2017,**10**, 435-459
6. Soltani.M, Hamidreza Beheshti.S, *Journal of Energy Storage*, 2021, **34**, 102019
7. Etacheri.V, Marom.R, Elazari.R, Salitra.G, Aurbach.D, *Energy Environ. Sci,* 2011, **4**, 3243-3262.
8. Whitingham.S, *Chem Rev,* 2004, **104**, 4271.
9. Kamali.A.R, Fray.D.J, *J.New Mater, Electrochem.Syst,* 2010, **13**, 147.
10. Cho.J, Kim.Y.J, Kim.T.J, Park.B, *Angewandte Chemie Intenational Edition,* 2001, **40**, 1272.
11. Walu´s.S, Offer.G, Hunt.I, Patel.Y, Stockley.T, Williams.J, Purkayastha.R, Energy Storage Materials 2018, **10**, 233–245.
12. Yin.Y.X, Xin.S, Guo.Y.G, Wan.L.J, *Angewandte Chemie Intenational Edition,* 2013, **52**, 13186-13200.
13. Yin.Y.X et al, *Chinese Phys. B*, 2016, **25**, 018801.
14. Bruce.P.G, Freunberger.S.A, Hardwick.L.J and Tarascon.J.M, *Nat. Mater*, 2012, **11**, 19–29.
15. Abraham.K.M and Jiang.Z, *J. Electrochem. Soc*, 1996, **143**,1.
16. Ogasawara.T, Débart.A, Holzapfel.M, Novàk.P, Bruce.P.G, *J Am Chem Soc*, 2006**, 128**, 1390–1393.
17. Black.R, Adams.B, Nazar.L.F, *Adv. Energy Mater*, 2012, **2**, 801–815.
18. Tan.P, Jiang.H.R, Zhu.X.B, An.L, Jung.C.Y, Wu.M.C, Shi.L, Shyy.W, Zhao.T.S, *Appl. Energ*, 2017, **204**, 780–806.
19. Kim.M, Yoo.E, Ahn.W.S, Shim.S.E, *Journal of Power Sources*, 2018, **389**, 20–27.
20. Ma.S.B, Lee.D.J, Roev.V, Im.D, Doo.S.G, *Journal of Power Sources*, 2013, **244**, 494– 498.
21. Zhang.G. Q. et al, *J. Electrochem. Soc*, 2010, **157**, A953.
22. Tan.P et al, *Electrochemistry Communications*, 2014, **46**, 111–114.
23. Adams.B.D, Radtke.C, Black.R, Trudeau.M.L, Zaghib.K, Nazar.L.F, *Energy Environ. Sci*, 2013, **6**, 1772-1778
24. Wang.R et al*., Journal of Power Sources,* 2012, **18**, 113–118.
25. Cui.Y, Wen.Z, Liu.Y, *Energy Environ Sci*, 2011, **4**, 4727-34.
26. Oakes.L, Muralidharan.N, Cohn.A.P, Pint.C.L, *Nanotechnology*, 2016, **27**, 495404.
27. Johnson.L, Li.C, Liu.Z et al, *Nature Chem,* 2014*,* **6**, 1091–1099.
28. Adams.B.D, Radtke.C, Black.R, Trudeau.M.L, Zaghib.K, Nazar.L.F, *Energy Environ. Sci*, 2013**,** 6, 1772-1778.
29. Song.M, Du.X, Chen.Y, Zhang.L, Zhu.D, Chen.Y, *Materials Reasearch Bulletin*, 2015, **68**, 75-79.
30. Sharon.D, Hirsberg.D, Salama.M, Afri.M, Frimer.A.A, Noked.M, Kwak.W, Sun.Y.K, Aurbach.D, *ACS Appl. Mater. Interfaces,* 2016, 8, **8**, 5300-5307.

31. McCloskey.B.D, Speidel.A, Scheffler.R, Miller.D.C, Viswanathan.V, Hummelshøj.J.S, Nørskov.J.K, Luntz.A.C, *J. Phys. Chem. Lett*, 2012, **3**, 997.
32. Kim.J.H, Woo.H.S, Kim.W.K, Ryu.K.H, Kim.D.W, *ACS Appl. Mater. Inter*, 2016, **8**, 32300–32306.
33. Meini.S, Piana.M, Beyer.H, Schwämmlein.J and Gasteiger.H.A, *J. Electrochem. Soc*, 2012, **159**, A2135-A2142.
34. Gao.Y, Wang.C, Pu.W, Liu.Z, Deng.C, Zhang.P and Mao.Z, *Int. J. Hydrogen Energ*, 2012, **37**, 12725-12730.
35. Li.Y, Wang.J, Li.X, Geng.D, LI.R, Sun.X, *Chem. Commun*, 2011, **47**, 9438-9440.
36. Yoo.E and Zhou.H, *ACS Nano*, 2011, **5**, 3020-3026.
37. Nomura.A, Ito.K, Kubo.Y, *Sci. Rep UK*, 2017, **7**, 1–8.
38. Ryu.W.H, Gittleson.F.S, Thomsen.J.M, Li.J, Schwab.M.J, Brudvig.G.W, Taylor.A.D, *Nat. Com,* 2016, 7.
39. Yu.R, Fan.W, Guo.X, Dong.S, *Journal of Power Sources*, 2016, **306**, 402– 407.
40. Ryu.S, Kim.B.G, Choi.J.W, Lee.H, *J. Nanosci. Nanotechnol*, 2015, **15**, 10.
41. Zhu.X, Wu.Y, Wan.W, Yan.Y, Wang.Y, He.X, Lü.Z, *International Journal Of Hydrogen Energy*, 2018, **43**, 739-747.
42. Han.H, Jeon.Y, Liu.Z, Song.T, *Appl. Sci*, 2018, **8,** 209.
43. Jeong.M.G, Kwak.W.J, Islam.M, Park.J, Byon.H.R, Jang.M, Sun.Y.K, Jung.H.G, *Journal of The Electrochemical Society*, 2019, 166, **4**, A455-A463.
44. Yan.H.J, Xu.B, Shi.S.Q, Ouyang.C.Y*, J.Appl.Phys*, 2012, 112, 104316.
45. He.M, Zhang.P, Liu.L, Liu.B, Xu.S, *Electrochimica Acta*, 2016, **191**, 90-97.
46. Shu.C, Li.B, Rhang.B, Su.D, *ChemSusChem*, 2015, **8**, 3973 – 3976.
47. Lin.Z, Liang.G, Wu.Y, Huang.G, Li.J, Zhang.H, Chen.J, Xie.F, Jin.Y, Meng.H, *Journal of Catalysis*, 2020, **383**, 199-205.
48. Li.S, Wang.M, Yao.Y, Zhao.T, Yang.L, Wu.F, *ACS Appl. Mater. Interfaces*, 2019, **11**, 34997−35004.
49. OttakamThotiyl.M.M, Freunberger.S.A, Peng.Z, Bruce.P.G, *J.Am.Chem.Soc*, 2013, **135**, 494–500.
50. Itkis.D.M, Semenenko.D.A, Kataev.E.Y, Belova.A.I, Neudachina.V.S, Sirotina.A.P, Hävecker.M, Teschner.D, Knop-Gericke.A, Dudin.P, Barinov.A, Goodilin.E.A, Shao-Horn.Y, Yashina.L.V, *Nano Lett*, 2013, **13**, 4697−4701.
51. Mahne.N, Schafzahl.B, Leypold.C *et al, Nat Energy,* 2017*,* **2,** 17036
52. Mourad.E, Petit.Y.K, Spezia.R et al, Energy Environ. Sci, 2019, **12**, 2559-2568
53. Ruiz de Larramendi.I, Ortiz-Vitoriano.N, *Front. Chem*, 2020, **8**, 605
54. Petit.Y.K, Leypold.C, Mahne.N et al, Angew. Chem. Int. Ed, 2019, **58**, 6535-6539
55. Lozano.I, Cordoba.D, Rodriguez.H.B et al, *Journal of Electroanalytical Chemistry*, 2020, **872**, 1142652
56. Lu.Y.C, Gasteiger.H.A, Shao-Horn.Y, *J. Am. Chem. Soc,* 2011, 133, **47**, 19048-19051.
57. Galiote.N.A, Ulissi.U, Passerini.S, Huguenin.F, *J. Phys. Chem. C*, 2018, **122**, 15826−15834.
58. Wang.J, Liu.L, Chou.S, Liu,H, Wang.J, *J. Mater. Chem. A*, 2017,**5**, 1462-1471.
59. Lu.M, Chen.D, Xu.C, Zhan.Y, Lee.J.Y, *Nanoscale*, 2015, **7**, 12906-12912.
60. Guo.K, Li.Y, Yuan.T, Dong.X, *J Solid State Electrochem*, 2015, **19**, 821–829.
61. Jung.C.Y, Zhao.T.S, Zeng.L, Tan.P, *Journal of Power Sources*, 2016, **331**, 82-90.

62. Tan.P, Shyy.W, Wu.M.C, Huang.Y.Y, Zhao.T.S, *Journal of Power Sources*, 2016, **326**, 303–312.
63. Dong.H, Tang.P, Zhang.S, Xiao.X, Jin.C, Gao.Y, Yin.Y, Li.B, Yang.S, *RSC Adv*, 2018, **8**, 3357–3363.
64. Ge.J, Du.G, Zhang.M, Kalam.A, Ding.S, Su.Q, Xu.B, Al-Sehemi.A.G, *Energy Technology*, 2020, **8**, 3, 1901257.
65. Wu.M.C, Zhao.T.S, Tan.P, Jiang.H.R, Zhu.X.B, *Electrochimica Acta,* 2016, **211**, 545–551.
66. Jung.J.W, Jang.J.S, Yun.T.G, Yoon.K.R, Kim.I.D, *ACS Appl Mater Interfaces*, 2018, **10**, 6531−6540.
67. Shen.S, Wu.A, Xia.G, Wei.G, Yan.X, Zhang.Y, Zhu.F, Yin.J, Zhang.J, *Nano Res*, 2019, **12**, 69–75.
68. Zhang.P, He.M, Xu.S, Yan.X, *J. Mater. Chem. A*, 2015, **3**, 10811-10818.
69. Zhang.D, Wang.B, Jiang.Y, Zhou.P, Chen.Z, Xu.B, Yan.M, *Journal of Alloys and Compounds*, 2015, **653**, 604-610.
70. Zeng.J, Francia.C, Amici.J, Bodoardo.S, Penazzi.N, *Journal of Power Sources*, 2014, **272**, 1003–1009.
71. Cho.S.A, Jang.Y.J, Lim.H.D, Lee.J.E, Jang.Y.H, Nguyen.T.T.H, Mota.F.M, Fenning.D.P, Kang.K, Shao-Horn.Y, Kim.D.H, *Adv. Energy Mater*, 2012, **7**, 1700391.
72. Wang.L, Chen.S, Hei.J, Gao.R, Liu.L, Su.L, Li.G, Chen.Z, *Nano Energy*, 2020, **71**, 104570.
73. Chen.X, Kuang.P, Chen.C, Zhang.X, Huang.T, Zhang.L, Yu.A, *Int. J. Electrochem. Sci*, 2018, **13**, 3309 – 3316.
74. Gong.H, Xue.H, Wang.T, Guo.H, Fan.X, Song.L, Xia.W, He.J, *ACS Appl. Mater. Interfaces,* 2016, 8, **28**, 18060–18068.
75. Wang.P.X, Shao.L, Zhang.N.Q, Sun.K.N, *Journal of Power Sources*, 2016, **325**, 506-512.
76. Li.P, Sun.W, Yu.Q, Yang.P, Qiao.J, Wang.Z, Rooney.D, Sun.K, *Solid State Ionics*, 2016, **289**, 17-22.
77. Zou.L, Cheng.J, Jiang.Y, Gong.Y, Chi.B, Pu.J, Jian.L, *RSC Adv*, 2016, **6**, 31248-31255.
78. Hung.T.F, Mohamed.S.G, Shen.C.C, Tsai.Y.Q, Chang.W.S, Liu.R.S, *Nanoscale*, 2013, **5**, 12115-12119.
79. LI.P, Sun.W, Yu.Q, Guan.M, Qiao.J, Wang.Z, Rooney.D, Sun.K, *Materials Letters*, 2015, **158**, 84-87.
80. Huang.Z, Chi.B, Jian.L, Youyi.S, Liu.Y, *Journal of Alloys and Compounds*, 2017, **695**, 3435-3444.
81. Kim.J.G, Noh.Y, Kim.Y, Lee.S, Kim.W.B, *Nanoscale*, 2017, **9**, 5119-5128.
82. Liu.J, Zhao.Y, Li.X, Wang.C, Zeng.Y, Yue.G, Chen.Q, *Nano-Micro Lett*, 2018, **10**, 22.
83. Liu.G, Chen.H, Xia.L, Wang.S, Ding.L.X, Li.D, Xiao.K, Dai.S, Wang.H, *ACS Appl. Mater. Interfaces*, 2015, 7, **40,** 22478–22486.
84. Oh.Y.J, Kim.J.H, Lee.J.Y, Park.S.K, Kang.Y.C, *Chemical Engineering Journal*, 2020, **384**, 123344.
85. Zhu.J, Metzger.M, Antonietti.M, Fellinger.T.G, *ACS Appl. Mater. Interfaces*, 2016, 8, **39**, 26041–26050.
86. Sevim.M, Sener.T, Metin.O, *International Journal of Hydrogen Energy*, 2015, **40**, 10879-10882.
87. Sevim.M, Francia.C, Amici.J, Vankova.S, Sener.T, Metin.O, *Journal of Alloys and Compounds*, 2016, **683**, 231-240.

88. Zahoor.A, Christy.M, Jeon.J.S, Lee.Y.S, Nahm.K.S, *J Solid State Electrochem*, 2015, **19**, 1501–1509.
89. Chen.L.Y, Guo.X.W, Han.J.H, Liu.P, Xu.X.D, Hirata.A, Chen.M.W, *J. Mater. Chem. A*, 2015, **3,** 3620-3626.
90. Zahoor.A, Christy.M, Kim.Y, Arul.A, Lee.Y.S, Nahm.K.S, *J Solid State Electrochem*, 2016, **20**, 1397–1404.
91. Agyeman.D.A, Park.M, Kang.Y.M, *J. Mater. Chem. A*, 2017, **5**, 22234-22241.
92. Oh.M.Y, Lee.J.J, Park.H.S, Kim.T.Y, Lee.Y.S, Vanchiappan.A, Nahm.K.S, *Journal of Industrial and Engineering Chemistry*, 2019, **80**, 686-695.
93. Li.X, Zhu.T, Wen.C, Yang.Y, Ma.S, Huang.X, Li.H, Sun.G, *Eletrochimica Acta*, 2019, **317**, 367-374
94. Read.J, *Journal of Electrochemical Society*, 2002, **149**, A1190–A1195.
95. Visco.S.J, Nimon.E, Katz.B, Jonghe.L, Chu.M.Y, *Books of Abstract, The 12th International Meeting on Lithium Batteries*, Nara,Japan, 27June -2July 2004, Abstract 53.
96. Visco.S.J, Nimon.E, Katz.B, Jonghe.L, Chu.M.Y, *Books of Abstract, The Electrochemical Society Meeting*, Cancun, Mexico, 29October–3November 2006, Abstract-0389.
97. Visco.S.J, Nimon.Y.S, Katz.B.D, *U.S.Patent*, 2007, US7,282,302,B2.
98. Wang.Y.G, He.P, Zhou.H.S, *Energy & Environmental Science*, 2011, **4**, 4994–4999.
99. Kumar.B, Kumar.J, Leese.R, Fellner.J.P, Rodrigues.S.J, Abraham.K.M, *Journal of Electrochemical Society*, 2010, **157**, A50–A54.
100. Kumar.B, Kumar.J, *Journal of Electrochemical Society*, 2010, **157**, A611–A616.
101. Christy.M, Arul.A, Zahoor.A, Moon.K.U, Oh.M.Y, Stephan.A.M, Nahm.K.S, *Journal of Power Sources*, 2017, **342**, 825–835.
102. Freunberger.S.A, Chen.Y, Peng.Z, Griffin.J.M, Hardwick.L.J, Bardé.F, Novák.P, Bruce.P.G, *J. Am. Chem. Soc*, 2011, **133**, 8040–8047.
103. McCloskey BD, Scheffler R, Speidel A, Bethune DS, Shelby RM, Luntz AC*, J Am Chem Soc* ,2011, **133**, 18038–41
104. Lim H, Park K, Gwon H, Hong J, Kim H, Kang K, *Chem Commun*, 2012, **48**, 8374–6
105. Balaish.M, Kraytsberg.A, Ein-Eli.Y, *Phys Chem Chem Phys*, 2014,**16**, 2801-2822
106. Xu.W, Hu.J, Engelhard.M.H, Towne.S.A, Hardy.J.S, Xiao.J, Feng.J, Hu.M.Y, Zhang.J, Ding.F, Gross.M.E, Zhang.J.G, *J. Power Sources*, 2012, **215**, 240–247.
107. Sharon.D, Afri.M, Noked.M, Garsuch.A, Frimer.A.A, Aurbach.D*, J.Phys.Chem. Lett*, 2013, **4**, 3115–3119.
108. Knipping.E, Aucher.C, Guirado.G, Aubouy.L, *New J. Chem*, 2018, 42, 4693-4699
109. Freunberger.S.A, Chen.Y, Drewett.N.E, Hardwick.L.J, Bardé.F, Bruce.P.G, *Angew. Chem. Int. Edit*, 2011, **50**, 8609–8613.
110. Takechi.K, Higashi.S, Mizuno.F, Nishikoori.H, Iba.H, Shiga.T, *ECSElectrochem. Lett*, 2012, **1**, A27–A29.
111. Wang H, Xie K, *Electrochim Acta*, 2012, **64**, 29–34.
112. Nasybulin.E, Xu.W, Engelhard.M.H, Nie.Z, Burton.S.D, Cosimbescu.L, Gross.M.E, Zhang.J.G, *J. Phys. Chem. C*, 2013, **117**, 2635–2645.
113. Read.J, *J. Electrochem. Soc*, 2006, **153**, A96.
114. Younesi.R, Veith.G.M, Johansson.P, Edström.K, Vegge.T, *Energy and Environmental Science* 2015, **8**, 1905–1922.

115. Younesi.R, Urbonaite.S, Edström.K, Hahlin.M, *J. Phys. Chem. C*, 2012, **116**, 20, 673–680.
116. Laoire.C.O, Mukerjee.S, Abraham.K.M, Plichta.E.J and Hendrickson.M.A, *J. Phys. Chem. C*, 2009, **113**, 20127–20134.
117. Younesi.R, Hahlin.M, Björefors.F, Johansson.P and Edström.K, *Chem. Mater*, 2013**, 25**, 77–84.
118. Younesi.R, Urbonaite.S, Edström.K and Hahlin.M, *J. Phys. Chem. C*, 2012, **116**, 20673–20680.
119. Veith.G.M, Nanda.J, Delmau.L.H and Dudney.N.J, *J. Phys. Chem. Lett*., 2012, **3**, 1242–1247
120. Nasybulin.E, Xu.W, Engelhard.M.H, Nie.Z, Burton.S.D, Cosimbescu.L, Gross.M.E and Zhang.J.G, *J. Phys. Chem. C*, 2013, **117**, 2635–2645.
121. Johnson.L, Li.C, Liu.Z, Chen.Y, Freunberger.S.A, Tarascon.J.M, Ashok.P.C, Praveen.B.B, Dholakia.K and Bruce.P.G*, Nat. Chem*., 2014, **6**, 1–9.
122. Abraham.K.M, *J. Electrochem. Soc*., 2015, **162**, A3021–A3031.
123. Wang.Y, Xia.Y, *Nat. Chem*, 2013, **5**, 445–447
124. Liang.Z, Lu.Y.C, *J. Am. Chem. Soc*, 2016, **138**, 24, 7574–7583
125. Ko.Y, Park.H, Lee.B, Bae.Y, Park.S.K, Kang.K, *J. Mater. Chem. A*, 2019,**7**, 6491-6498
126. Chen.Y, Freunberger.S.A, Peng.Z, Fontaine.O, Bruce.P.G, *Nat. Chem*, 2013, **5**, 489–494.
127. Lim.H.D, Song.H, Kim.J, Gwon.H, Bae.Y, Park.K.Y, Hong.J, Kim.H, Kim.T, Kim.Y.H, Leprõ.X, Ovalle-Robles.R, Baughman.R.H, Kang.K, *Angew. Chem. Int. Ed*, 2014, **53**, 3926–3931.
128. Kwak.W.J, Hirshberg.D, Sharon.D, Afri.M, Frimer.A.A, Jung.H.G, Aurbach.D, and Sun..K, *Energy Environ. Sci*, 2016, **9**, 2334.
129. Bergner.B.J, Schurmann.A, Peppler.K, Garsuch.A, and Janek.J*, J. Am. Chem. Soc*, 2014, **136**, 15054.
130. Bergner.B.J, Hofmann.C, Schurmann.A, Schroder.D, Peppler.K, Schreiner.P.R, and Janek.J, *Phys. Chem. Chem. Phys*, 2015, **17**, 31769
131. Chen.Y, Freunberger.S.A, Peng.Z, Fontaine.O, and Bruce.P.G, *Nat. Chem*, 2013, **5**, 489 (2013)
132. Yang.H, Wang.Q, Zhang.R, Trimm.B.D, and Whittingham.M.S, *Chem. Commun*, 2016, 52, 7580.
133. Lim H.D, Lee.B, Zheng.Y, Hong.J, Kim.J, Gwon.H, Ko.Y, Lee.M, Cho.K, and Kang.K, *Nat. Energy*, 2016, **1**, 16066.
134. Nelson.R.F, Leedy.D.W, Seo.E.T, and Adams.R.N*, Z. Anal. Chem*, 1966, **224**, 184.
135. Liang.Z and Lu.Y.C, *J. Am. Chem*. Soc, 2016, **138**, 7574.
136. Kwak.W.J, Hirshberg.D, Sharon.D, Shin.H.J, Afri.M, Park.J.B, Garsuch.A, Chesneau.F.F, Frimer.A.A, Aurbach.D, and Sun.Y.K, *J. Mater. Chem*. A, 2015**, 3**, 8855.
137. Zhu.Y.G, Jia.C, Yang.J, Pan.F, Huang.Q, and Wang.Q, *Chem. Commun*, 2015, **51**, 9451.

Figure table

Figure 1: Power density and energy density obtained for fuel cells, batteries, capacitors, and ultracapacitors 2
Figure 2: Illustration of charging (a) and discharging (b) process in batteries 3
Figure 3: Representation of discharging (a) and charging (b) phenomenon in Li-ion batteries 5
Figure 4: Representation of a traditional Li-S batteries 6
Figure 5: Graph representing the energy density (practical and theoretical) of different kinds of batteries compared to gasoline.[15] 6
Figure 6: Operating principle of a Li-O_2 battery during (a) discharge and (b) charge 8
Figure 7: (a) Illustration of the fabrication of different porous carbon cathodes derived from a triazine-based covalent organic polymer (TCOP); (b) N_2 adsorption-desorption isotherms and (c) pore size distributions of C-800, AC-950, and CMK- 3; SEM microphotographs of (d) C-800, (e) AC-950, and (f) CMK-3; (f) 1st discharge-charge curves of Li-O_2 cells with the C-800, AC-950, and CMK-3 electrodes at a current density of 200 mA.g^{-1}. [19] 10
Figure 8: (a) N_2 isotherm and pore size distribution measured on buckypaper, (b) discharge curves from Li-O_2 cells made with different electrode thicknesses, (c) SEM image of the buckypaper, SEM images of the oxygen electrode surfaces at (d) separator and (e) oxygen sides after discharge. [21] 12
Figure 9: SEM image of (a) the cross section of the gradient porous cathode (b) the oxygen-side, (c) middle, and (d) separator-side layer, (e) Galvanostatic discharge curves at 0.1 mA/cm^2, SEM image of the cathode after discharge (f) uniform porous cathode (g) and gradient porous cathode. [22] 14
Figure 10: First Galvanostatic discharge curves for all carbon. [33] 15
Figure 11: Discharge–charge performance of lithium-oxygen batteries with Graphene nanosheet, BP-2000, and Vulcan XC-72 cathodes at a current density of 75 mA.g^{-1}.[35] 17
Figure 12: Structure of the rechargeable Li-oxygen battery based on graphene nanosheet as an O_2 electrode (hybrid electrolyte). [36] 17
Figure 13: (a) SEM images of the VACNTs-Ta, (b) First discharge-charge profiles of VACNTs-Ta, VACNTs-SS and CNT-P, (c) Scheme of the Li_2O_2 formation toward the VACNTs-TA .[39] 18
Figure 14: Cycling performances of CNF electrodes pyrolyzed at several temperature (a) CNF 1000, (b) CNF 1200 and (c) CNF 1400.[42] 18
Figure 15: (a) Schematic illustration for fabrication process of triple hierarchical porous carbon spheres (THPC) (b) SEM and (c) corresponding TEM images of THPC, (d) , N2 adsorption–desorption isotherms with pore size distribution curve for the USS and THPC in the inset (e) Discharge and charge profile at 100 mA.g^{-1} with a voltage window of 2.0–5.0 V for Super P and THPC carbon material.[43] 19
Figure 16: (a) The atomic geometry of O_2 molecule physically adsorbed on graphene (left) and N-doped graphene (right). The grey, red, and blue spheres are C, O, and N atoms, respectively. The numbers are the corresponding marked distances in angstrom, (b) Schematic view of O atom adsorbed on graphene (left) and N-doped graphene (right) with the local atomic distortions and adsorption energies of O atoms at different sites. [44] 20

Figure 17: (a) Schematic illustration of the preparation processes of N-3DG and 3DG, (b) SEM and (c) TEM images of N-3DG, (d), N_2 adsorption-desorption isotherms and (e) the corresponding pore size distribution curve of N-3DG,and Cycling performances of Li-O_2 batteries with (f) N-dopes and (g) pure carbon electrodes at a current density of 100 mA g^{-1} and cut-off capacity of 500 mAh g^{-1}.[45] ... 22
Figure 18: SEM images of the nitrogen doped carbon (a) NEC1; (b) NEC4; (c) NEC6; (d)NEC12 with insets of selected area electron diffraction (SAED) patterns respectively, (e) N_2adsorption/desorption isotherms with corresponding pore size distribution (inset) of the carbon materials (f) Capacity obtained with the different percentage N-doping electrode at a 200mA.g^{-1} current density and a 2.0-4.5V window, (g) Initial discharge-charge curves at a 200mA.g^{-1} current density for a 600 mAh.g^{-1} specific capacity, (h) Cyclic performances of the different N-doped cathodes at a 200mA.g^{-1} current density for a 600 mAh.g^{-1} specific capacity.[47] 23
Figure 19: Chemical transformations of superoxide species. The scheme illustrates chemical processes that are being initiated right after ORR [50] 25
Figure 20: Reaction free energy profiles for superoxide disproportionation LiO_2 disproportionation with itself, O_2^- or HO_2 to Li_2O_2 and molecular oxygen. [52] 26
Figure 21: ORR mechanism for Li^+ containing nonaqueous solvents [56] 27
Figure 22: (a) Potentials at 2 µA.cm^{-2} real as a function of calculated oxygen adsorption energy, ΔE_O relative to that of Pt. (b) Initial discharge profiles of Pd/C, Pt/C, Ru/C, Au/C, and VC at 100 mAh.g^{-1}.[56] 28
Figure 23: (a) SEM micrograph of the Pd/PNCNF-2, (b) Comparison of the initial discharge/charge profiles of the Li-O_2 batteries from 2.35 to 4.35 V for (a) the pure Pd, the pure PNCNF, and the Pd/PNCNF cathodes at 100 mA g^{-1}, (c, d), and the corresponding typical discharge/charge profiles. (e) ORR LSV profiles for the samples at a rotation speed of 1600 rpm and (f) OER LSV profiles of the different samples. [58] 30
Figure 24: (a-c) High resolution TEM images of AuPt/ HMCMS composite, (d,e) High resolution SEM images of AuPt/ HMCMS composite an their textural properties (f) First cycle discharge/charge profile obtained with AuPt/HMCMS, AuPt NPs and HMCMS electrodes.[59] 31
Figure 25: (a) Comparison of discharge capacity for 5 cycles of Li–O_2 batteries with pure KB, IrO_2+KB, and IrO_2/KB at 0.1 mA.cm^{-2}, (b) OER LSV profiles of the different samples, and discharge–charge profiles at different cycles of the Li–O_2 batteries with (c) pure KB, and (d) IrO_2/KB, with a limited capacity of 500 mAh.g^{-1} at 0.1 mA.cm^{-2}. [60] 32
Figure 26: SEM images of (A) the VACNT cathode and (B) the VACNT@RuO_2 cathode. SEM images on the cross-sectional surfaces of (C) the VACNT cathode and (D) the VACNT@RuO_2 cathode. The insets show high-resolution SEM images. (E) Comparison of the discharge-charge characteristics at 0.5 mA.cm^{-2} after fully discharged and charged. Comparison of the cycling stability at 0.5 mA $cm^{-2}$with a fixed capacity of 1.0 mAh.cm^{-2}. (F) CNT, (G) VACNT, and (H) VACNT@RuO2cathode.[61] 34
Figure 27: (a) Li-O_2 charging-discharging profile with different cathodes: Ketjen Black (KB), NiO-RuO_2/KB, NiO/KB and RuO_2/KB, (b) LSV curves of Ketjen Black (KB), NiO-RuO_2/KB, NiO/KB and RuO_2/KB cathodes with side products and (c) Surface area and pore volume of: Ketjen Black (KB), NiO-RuO_2/KB, NiO/KB and RuO_2/KB.[62] 36
Figure 28: (a) SEM image of NiO. (b) FESEM, (c) TEM and (d) HRTEM images of the layered nanosphere NiO, (e) lattice fringes and (f) hysteretic loop. (g) Schematic illustration of the synthesis process of NiO, (h) nitrogen adsorption/desorption isotherms and pore-size distribution of NiO, (i) Oxygen evolution reaction curves of NiO and Pt/C at a rotation rate of 1600 rpm with a scanning rate

of 10 mV s^{-1} discharge–charge profiles of the Li–O_2 batteries with (j) NiO catalyst, and (k) KB only, with a limited capacity of 800 mAh.g^{-1} at 0.1 mA.cm^{-2} within a 2.0 - 4.2 V voltage range, (l) Galvanostatic discharge/charge curves of Li–O2 batteries with a NiO catalyst at a current density of 0.1 mA cm^{-2} in the voltage range of 2.0–4.2 V vs. Li^+/Li. (m) Illustration of the catalytic reaction mechanism for the layered nanosphere NiO in Li–O_2 batteries [63] 37
Figure 29: (a) SEM and (b) TEM images of TiO_2 microspheres, nitrogen adsorption–desorption isotherm of (c) TiO_2 microspheres and (d) CNTs (e) The initial discharge/charge profiles of TiO2 microspheres and pure CNT electrodes under the capacity limit of 500 mAh g^{-1} at 100 mA g^{-1}. [64] 38
Figure 30: (a) Linear sweep voltammograms of OER in non-aqueous lithium-oxygen batteries with XC and Fe_2O_3/XC cathodes of 1 mVs^{-1} with and without initial discharge product and Discharge/charge curves in lithium–oxygen battery with (b) XC and (c) Fe_2O_3/XC cathode at 200 mA.g^{-1} with a fixed capacity. [65] 39
Figure 31: (a) Representative SEM images of 50% α-MnO_2/MWCNTs nanocomposite, (b) TEM image of the 50% α-MnO_2/MWCNT nanocomposite, discharge-charge voltage curves of different cycles for the (c) 3D 50% α-MnO_2/MWCNTs cathode (e) and pristine MWCNTs cathode. Variation of the terminal discharge voltage with the cycle number for (d) the 3D 50% α-MnO_2/MWCNTs hybrid cathode (f) and pristine MWCNTs cathode, (g) CV curves of pure MWCNTs and 50% α-MnO_2/ MWCNT electrodes between 2.0 and 4.5 V at 0.5 mV·s^{-1}. [67] 40
Figure 32: (a) SEM micrograph of as-deposited electrodes Co_3O_4/KB (80%), Charge and discharge profiles of (c) Co3O4/KB (80%), (d) pure KB electrodes, CV curve results of initial 3 cycles of (e) Co_3O_4/KB (80%), (f) KB electrodes at a constant scan rate at 0.5 mV s^{-1} from 2.0 to 4.3 V. [69] 41
Figure 33: (a-c) SEM and (d-e) TEM images of CeO_x/MC-600 under different magnifications, and (f) TEM micrograph of pure MC, (g) first charge/discharge profile tested at 100 mA g^{-1} for all cathodes, long term cycling performance of (h) CeO_x/MC- 600 and (i) Pure MC, (j) Schematic diagram for the improvement mechanism of CeO_x/MC-600. [72] 42
Figure 34: (a) SEM images, (b) TEM micrograph, (c) N_2 adsorption-desorption isotherms (d) and pore size distribution of $NiCo_2O_4$ (e) First discharge-charge profiles, 0.05 mA.cm^{-2} current density, of the Li-O_2 cell with $NiCo_2O_4$ and Super P electrodes. (f) Cycling stability of the Li-O_2 cell with the $NiCo_2O_4$ and pure carbon cathodes. [73] 44
Figure 35: (a) SEM, (b) TEM, (c) Nitrogen adsorption and desorption isotherms and (d) the corresponding pore size distributions of the mesoporous $CuCo_2O_4$ (e) CV curves of $CuCo_2O_4$/KB and KB carbon-only electrode at a scan rate of 0.1 mV s−1 (f) First discharge/charge profiles of Li-O_2 cells with the $CuCo_2O_4$/KB and KB electrodes with a restricting capacity of 500 mAh.g^{-1} at a constant current density of 100 mA.g^{-1} (g) and their cycling stability. [76] 45
Figure 36: (a) SEM of $MnCo_2O_4$ nanospheres, (b) Nitrogen adsorption–desorption isotherms of MnCo2O4 nanospheres and the pore size distribution (inset), (c) CV curves of $MnCo_2O_4$/KB and pure KB (d) and linear scanning voltammograms. First three cycles of Li-O_2 batteries made with (e) $MnCo_2O_4$/KB and (f) pure KB as cathode at the current density of 100 mA.g^{-1} within a 2.2–4.5 V voltage windows, and (g) first cycle with a limited capacity of 1000 mAh.g^{-1} at the current density of 100 mA.g^{-1} for both electrodes. [77] 46
Figure 37: (a) SEM and (b) TEM micrographs, LSV profiles of (c) ORR and (d) OER profiles, (e) CV curve of the mesoporous $ZnCo_2O_4$ and (f) Discharging capacities and corresponding potentials as a function of cycle numbers of the aprotic Li-O_2 battery with mesoporous $ZnCo_2O_4$ based cathode. [78] 47

Figure 38: Illustration of the overall fabrication process for the 3DOM CFO catalysts; (a) PS, (b) cobalt–iron precursor impregnated PS, (c) 3DOM CFO. (d) Schematic description of the discharging process of the as-fabricated 3DOM CFO catalyst, SEM images of (e) 3DOM CFO@60, and (f) 3DOM CFO@140, (g) Cycling performance of Li–O_2 cells with KB, CFO NPs, CFO@60, and CFO@140 catalysts for first five cycles at a current rate of 200 mA g^{-1} with a limited voltage window of 2.3 and 4.5 V, (h) discharge–charge curves of Li–O_2 cells with KB, CFO@60, and CFO@140 catalysts at a current rate of 200 mA g^{-1} with a limited capacity depth of 500 mAh.g^{-1} for the first cycle, (i) cyclability of the Li–O_2 cells and (j) round-trip efficiency with KB, CFO@60, and CFO@140 catalysts under a limited capacity of 500 mAh.g^{-1} at a current rate of 200 mA g^{-1}. [80] 50
Figure 39: (a) SEM micrograph, (b) TEM micrograph of CCO@rGO nanocomposites, and (c) Cyclic stability of the LOBs with CCO@rGO and CCO cathodes [82] 51
Figure 40: (a) SEM micrograph, (b) TEM micrograph, (c) Nitrogen adsorption−desorption isotherms and pore size distribution of HPNLSC, (d) CV curves of HPNLSC/KB and KB electrodes between 2.20 and 4.35 V at 0.1 mV s^{-1}, First five discharge–charge curves of Li–O_2 cells obtained within a voltage window between 2.20 and 4.35 V, at a current density of 0.025 mA.cm^{-2} and with (e) pure KB (f) HPNLSC/KB electrodes. Cyclic performance of Li–O_2 batteries at a current density of 0.1 mA.cm^{-2} with a limit capacity of 500 mAh.g^{-1} with (g) KB and (h) HPN-LSC/KB electrodes.[83] 52
Figure 41: (a) SEM and (b) TEM micrographs of the as-synthetised MoC–Mo_2C/NCNT, (c) CV curves recorded between 2.0 and 4.35 V at the scan rate of 0.1 mV.s^{-1} and (d) Initial charge discharge profile obtained within a 2.0 – 4.35 V voltage windows, at a current density of 200 mA.g^{-1} for Li-O_2 battery based on Mo_2C/NCNTs, Mo_2C/NCNTs, and Mo_2C@GC electrodes (e) First charge discharge profile and (f) cycling stability obtained with Mo_2C/NCNTs, Mo_2C/NCNTs, and Mo_2C@GC electrodes within Li-O_2 cells and performed at 500 mAh.g^{-1} with a current density of 200 mA.g^{-1}.[84] 54
Figure 42: (a) SEM micrograph and (b) TEM micrograph of typical M$(OH)_2$@CNS (M = Co,Fe), First charge discharge profile of Li-O_2 cells with (c) CNS@$Co(OH)_2$, (d) CNS@$Fe(OH)_3$, and (e) pure CNS electrode and (f) gas analysis of first discharge and charge of $Co(OH)_2$@CNS at 175 mA.g−1 by combined approach using a Baratron pressure transducer to investigate gas consumption during discharge and OEMS to analyse gas evolution during charge. Upper panel shows potential profile, middle panel absolute gas consumption/evolution, and lower panels gas consumption/evolution rates. Dashed lines indicate respective values for 2e^-/ O_2 and 4 e^-/O_2.[85] 56
Figure 43: TEM micrographs of (A) CoPt, (B) NiPt and (C) CuPt alloy NPs; Galvanostatic discharge tests at the limited capacity of 0.5 mAh cm^{-2} , (D) Capacity vs. cell voltage profiles for (A) at the 2nd cycle for the three cathodes (E) Capacity vs. number of cycles for the three cathodes. [87] 59
Figure 44 : (a) SEM images of Pd-deposited α-MnO_2 nanorods, (b) N_2 adsorption/desorption isotherm of Pd-deposited α-MnO_2 nanorod-catalysed Li–O_2 battery in comparison with α-MnO_2 nanorod, (c) LSV curves recorded in the oxygen-saturated 0.1 M KOH solution at a scan rate of 5 mV s−1 with a disk rotation rate of 1600 rpm. The ORR and OER polarization curves were obtained in the potential ranges of 0.3∼−0.8 and 0.3∼1.0 V, respectively (d) First charge discharge profile of Li-O_2 with Pd/α-MnO_2 nanorod, α-MnO_2 nanorod, and pure KB electrodes and (e) cycling performances of Li-O_2 cells made with Pd/α-MnO_2 nanorod electrodes at limited capacity of 500 mAh.g^{-1}.[88] 61
Figure 45: SEM micrographs of (a) C– TiO_2 (b) Pt, (c) Ir, and (d) Pt/Ir nanocomposites supported on C–TiO_2, (e) Electrochemical data obtained from the LSV curves, (f) The first discharge capacity of Pt, Ir, and Pt–Ir/C–TiO_2 catalysts in comparison with the KB cathode, cycling performance of the (g) Pt/C–TiO_2, (h) Ir/C–TiO_2, (i) Pt–Ir/C–TiO_2-catalyzed Li–O_2 battery limited to 500 mAh g^{-1}. [90] 62

Figure 46: (a) SEM micrograph of Pd@$NiCo_2O_4$ on carbon foam, (b) Initial deep discharge-charge curve of Pd@$NiCo_2O_4$, (c) Schematic illustration for the surface atomic arrangement of Pd@$NiCo_2O_4$.[91] 63
Figure 47: Composition of batteries related to the electrolytes.[18] 65
Figure 48: Scheme of discharge reaction explaining the formation of side products: Li Propyl Dicarbonate, Li Formate, Li Acetate, Li_2CO_3, CO_2, and H_2O. [102] 67
Figure 49: Mechanism of side reactions occurring with ether-based electrolytes during Li–air cell discharge. [105] 67
Figure 50: Degradation Mechanism of DMSO during discharge [107] 68
Figure 51: Most frequently used lithium salts in Li-O_2 batteries 70

Table 1: Characteristics of the main commercially available batteries 3
Table 2: Results obtained for Doo et al. study, comparison and link between porosity and battery performances. [20] 11
Table3: Surface area analysis data of cathodes coated on Al foil.[33] 15
Table 4: The discharge capacity of various carbon type and their related physical parameters.[34] 16
Table 5: Capacity reached, morphology and textural properties of the principal carbon-based cathodes for Li-O_2 batteries applications 24
Tableau 6: Capacity reached, metal oxide and carbon morphology, and decrease in overpotential compared to pure carbon-based cathodes for Li-O_2 batteries applications. 43
Table 7: Capacity reached, spinel and carbon morphology, and decrease in overpotential compared to pure carbon-based cathodes for Li-O2 batteries applications. 49
Table 8: Capacity reached, material nature, carbon morphology, and decrease in overpotential compared to pure carbon-based cathodes for Li-O_2 batteries applications. 57
Table 9: Advantages and inconvenient of all the reported cathode materials for lithium-oxygen batteries 63
Table 10: Comparison of batteries regarding electrolytes types 66
Table 11: Main solvents used for non-aqueous electrolyte with their advantages and inconvenient 69
Table 12: RM formula with their redox reaction and potentials 72

Chapter 2 - Objectives

The development of lithium-oxygen batteries, which possess higher energy density than lithium-ion batteries, have strong scientific and economic interest. Their development could result in higher energy storage, making autonomous devices such as electric cars more effective. Despite intensive research since the late 1990s, the subject is far from being fully understood. Understanding fundamental issues such as the influence of the electrolyte or the cathode structure is a key issue in the development of marketable batteries.

Current lithium oxygen batteries are complex systems and suffer mostly from instability problems. These problems affect all the components of the battery. The electrolyte is unstable towards superoxide and its degradation leads to the formation of insulating and insoluble products leading to a decrease in capacity, cyclability and an increase in the battery's overpotential. The main problem with the lithium anode is the formation of dendrites during cycling. Cathodes are mainly made of carbon which reacts with lithium peroxide to form insulating lithium carbonate, passivating the cathode surface, impeding the electron flow, increasing the overvoltage and degrading other components including the electrolyte.

In order to have a stable, high performance lithium-oxygen battery over a long period it is necessary to carry out an in-depth study of each component of the battery. However, working on all the components of the battery simultaneously is a monumental task, which is why this work will focus on the cathodes.

The main objective of this PhD is to design cathodes for lithium-oxygen battery applications. The cathode is the site of the electrochemical reactions that drive the performance of the battery. Two main methods to optimise the cathode are considered. The first is to modulate the architecture of the electrode to optimise the formation and decomposition of lithium peroxide on its surface. The second -is to use a catalyst to accelerate the kinetics of the OER/ORR reactions, to reduce the overpotential to avoid degrading the electrolyte.

The evolution of the project is based on the observation and evaluation of experimental data and the manuscript is composed of three parts: introductions and objective, results and discussion and conclusion and outlook. The part of results and discussion summaries all the results obtained and is divided into three chapters.

The first chapter aims to highlight the relationship between the structure of the cathodes and the resulting electrochemical performances of lithium-oxygen batteries. This duality will be investigated experimentally by using carbon-based materials with a hierarchical porosity following Murray's law.

The second chapter aims to evaluate the influence of the materials used in the cathodes on the performance of the batteries. To do so, results obtained from different cathodes containing various 3d metal oxides will be compared in order to evaluate their catalytic properties on the OER/ORR and their impact on the electrochemical results. This section will also aim to clarify the role of 3d metal oxides as cathode materials and serve as a reference for future cathode development.

The third chapter will aim to combine the main finding of the first two parts. The result will be a judicious mix between an optimised and suitable morphology and an adapted catalytic material allowing to optimise the formation and decomposition of lithium peroxide and thus increase the performance of the batteries. For this purpose, AB_2O_4 spinel structures combining two previously studied 3d metals will be synthesized and their electrochemical performances investigated.

Part II – Results and discussions

Chapter 3: Electrode design following Murray's law: towards a revolution in Li-O_2 batteries?

Abstract:

In conventional porous cathodes used for non-aqueous lithium oxygen batteries the rate of lithium peroxide formation is higher in the oxygen richest region and results in a gradual distribution decreasing from the air side to the separator side. This non-uniform distribution of the solid means that the pores on the air side are clogged first, making it impossible to exploit the rest of the cathode pore volume. This clogging of the oxygen-side cathode is accompanied by a decrease in discharge capacity, terminating the discharge process and resulting in a low discharge capacity. In this work, we fabricate a cathode structure with hierarchical micro/meso/macro porosity based on Murray's law by using a bottom-up, layer-by-layer evaporation-driven self-assembly process employing microporous nanocrystals as the primary building blocks.

The hierarchical micro/meso/macro porous cathode enables the capacity of a non-aqueous lithium-oxygen battery discharging at 150 $mA.g^{-1}$ to be 514 % higher than that by a uniform slurry based cathode and 42 % higher than that by a hierarchical micro/meso/macro porous cathode based on carbon nanotube. We suggest that the increased discharge capacity can be mainly attributed to the fact that the hierarchical micro/meso/macro porous cathode has a large specific surface area and increase the oxygen transport pathways.

I) Introduction

Non-aqueous lithium-oxygen batteries are considered as one of the most promising electricity storage devices, due to their high theoretical capacity (3.86 × 103mAh.g^{-1}) and energy density (1.14 × 104Wh.kg^{-1}), which is several times higher than that of Li-ion batteries.[1-4] However, the actual discharge capacity is far from the theoretical value.[5-9]

The principal problem with non-aqueous batteries comes from the main discharge product, lithium peroxide. In fact, the fundamental chemistry of lithium-oxygen batteries involves lithium dissolution and deposition at the lithium anode and oxygen reduction reaction (ORR) and oxygen evolution reaction (OER) at the cathode. During the discharge, the reduction of oxygen leads to the formation of lithium superoxide LiO_2 through a one electron transfer. This superoxide can react with another lithium cation Li^+ and an electron or undergo a dismutation reaction, to form lithium peroxide Li_2O_2. To be rechargeable, the Li_2O_2 previously formed during discharge must be able to be electrochemically decomposed into Li^+ and O_2 during charging. The decomposition of lithium superoxide is based on two main reactions involving a one or two-electron process. As Li_2O_2 is an insulating solid it is essential to decompose it as it could passivate the surface of the electrode and will clog the pores of the cathode by its accumulation during discharge. [10]

The oxygen concentration in the porous cathode decreases from the oxygen side to the separator side during discharge. The formation of lithium peroxide is directly related to the oxygen concentration, higher oxygen concentration will result in a higher reaction rate. Therefore, the formation of Li_2O_2 will be higher at the oxygen side, decrease toward the separator side. [11-13] This Li_2O_2 formation gradient means that the porosity on the separator side is not fully exploited as the pores on the oxygen side will be blocked first preventing oxygen diffusion afterwards. Thus, the cathode porosity is not fully exploited and reduces the capacity of the battery. The control of cathode porosity is of key parameter for high performance Li-O_2 battery.

Currently, studies on cathode have focused on carbon structures with mesopores and macropores. [14- 16] However, these pores are blocked and passivated by the accumulation of Li_2O_2 during discharge and by insoluble side-products, which causes capacity fading. Micropores have often been considered unnecessary due to their small size (<2nm), as they cannot store a large amount of Li_2O_2. [17-18] However, micropores can still be useful in a hierarchical structure to optimise oxygen transport. The above-mentioned issue can be solved by designing a porous cathode with a gradient distribution in pore size. This gradient will allow a more even oxygen transport pathway along the electrode thickness.

In this work, we fabricate a cathode structure with hierarchical micro/meso/macro porosity based on the generalised Murray's law. The hierarchically porous cathode is formed using a bottom-up, layer-by-layer evaporation-driven self-assembly process employing microporous nanocrystals as the primary building blocks under controlled humidity conditions. This specific gradient porous cathode was tested in a non-aqueous lithium-oxygen battery and compared with a slurry-based carbon powder cathode. Because of the optimized design of the cathode and the efficient formation and decomposition of Li_2O_2, Li–O_2 cells exhibited a higher discharge capacity.

II) Materials and Methods

II.1) Synthesis of metal oxide nanoparticles

ZnO nanoparticles were prepared under an argon atmosphere by a mild temperature organic solution reaction.[19] In a typically synthesis, 0.002 mol of the zinc acetylacetonate was mixed with 0.088 mol of oleylamine and 153mM of triphenylphosphine. The mixture was heated for one hour to 80°C, the resulting solution was then quickly heated to 150°C. Once the temperature is reached, the temperature was maintained for one hour. After cooling to room temperature, excess ethanol was added to the solution to give a precipitate which was isolated by centrifugation. Then, the nanoparticles were washed fully with ethanol and isolated by centrifugation, before being air-dried at 80°C overnight. Figure 1 resumes the experimental procedure.

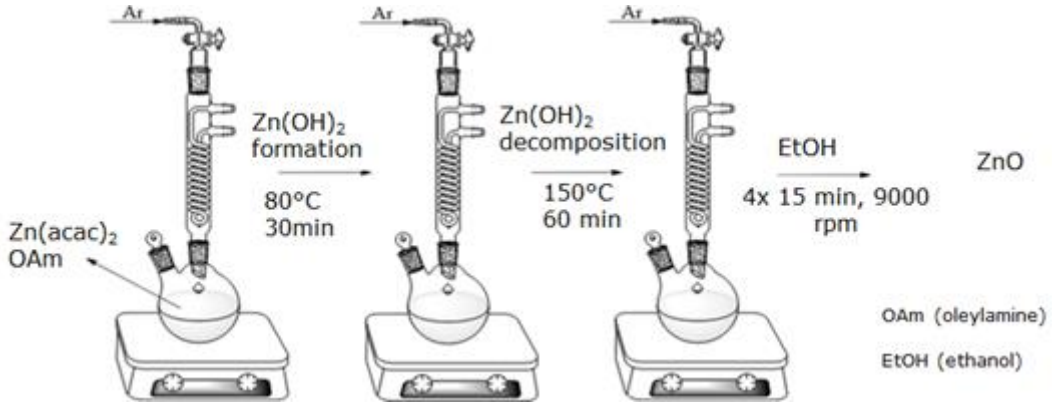

Figure 1 : Experimental conditions of the formation of zinc oxide from zinc acetylacetonate and oleylamine

II.2) Cathode electrode preparation

In order to design the Murray's material, a 2.5 $mg.mL^{-1}$ suspension of zinc oxide nanoparticles in hexane was used to cover a stainless steel mesh (mesh size: 100*100mm, 26% open area). The deposition is carried out under controlled humidity conditions. Once the solvent has completely evaporated, previous steps are repeated until 10 mL of suspension has been used. The cathode is then dried under vacuum at 100 ◦C for one night before being used in an accumulator. The same procedure was used with carbon nanoparticles only was used as reference.

A second method to elaborate O_2-electrodes is used. A slurry was prepared by mixing the as-prepared nanoparticles, carbon black, and poly(vinylidene difluoride) (PVDF) with N-methyl-2-pyrrolidone (NMP) in a 60 : 30 : 10 weight ratio. The obtained slurry was spread on a stainless-steel mesh (mesh size: 100*100mm, 26% open area) and dried at 120°C under vacuum overnight. After that, the steel mesh was cut into several circles of 1.32 cm^2 each. A slurry with pure carbon black, PVDF, in NMP 90: 10 was prepared to provide a reference.

II.3) Electrochemical measurements

To perform electrochemical measurements, homemade Li-O_2 battery cells were designed following Swagelok cells structure (Figure 2). The cell was made of an electrolyte consisting of 0.25M lithium bis(trifluoromethanesulfonyl)imide in 1,2-Dimethoxyethane, a lithium foil used as anode, the as prepared O_2 –electrode used as cathode, and a glass fiber separator. The cell was assembled in an argon-filled glove box where moisture and oxygen concentrations were less than 1 ppm.

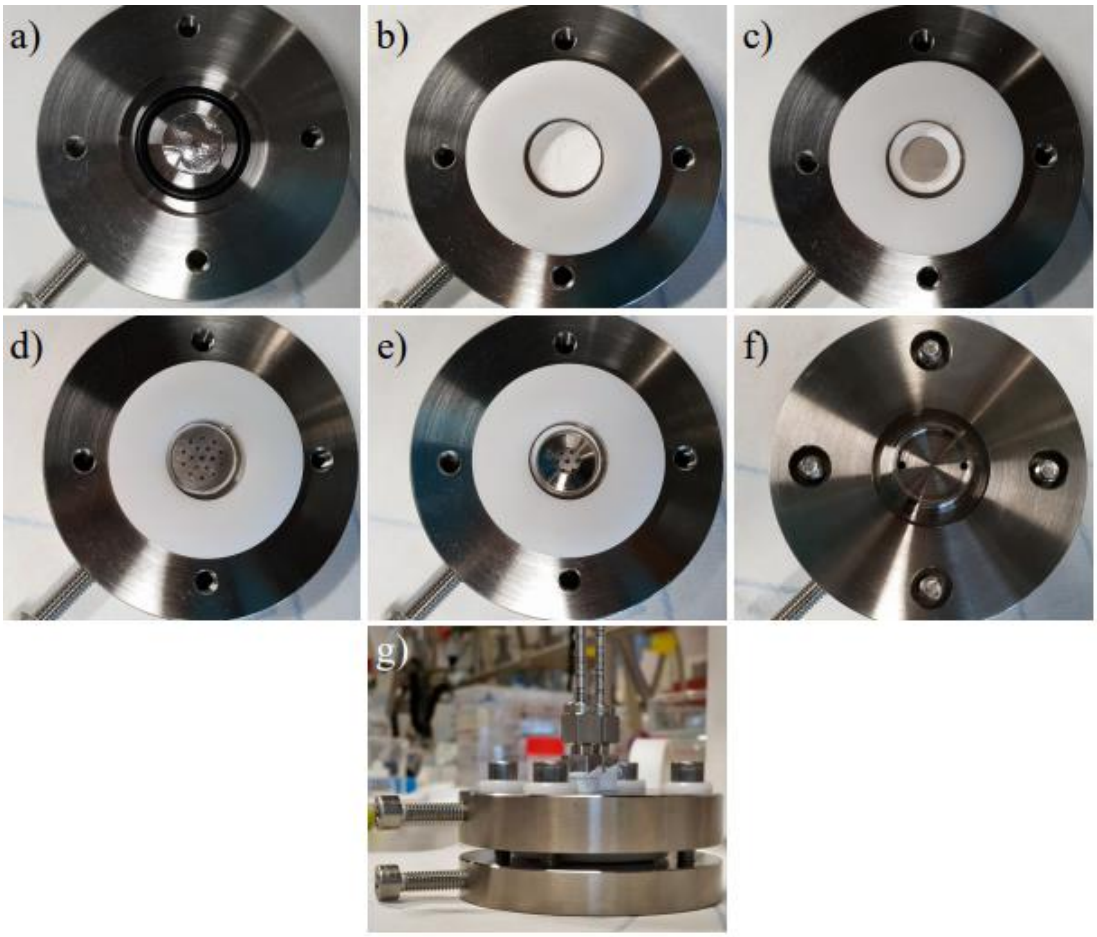

Figure 2 : **Assembly of the different battery elements: (a) lithium disc, (b) glass fibre separator soaked in electrolyte, (c) cathode, (d) perforated steel plate, (e) compression spring, (f) top part and (g) assembled battery.**

Once built up, batteries were put under high purity oxygen flux for several seconds, and maintained under an O_2 atmosphere at a pressure of 1 atm for 10 hours before performing the electrochemical measurements. The galvanostatic discharge-charge tests were performed thanks to a LANHE CT2001A multi-channel battery tester with a voltage between 2 and 4.7 V or 2.2 and 4.4V and at a current rate of 150 $mA.g^{-1}$. The specific capacities obtained were normalized by the carbon weight used in the cathode.

Electrochemical impedance spectroscopy (EIS) and cyclic voltammetry was performed thanks to a Princeton Applied Research, VersaSTAT 3, potentiostat/galvanostat. Galvanostatic charge

and discharge tests were carried out between 2 and 4.5V (vs LI/LI^+), with a scanning rate of 0.1 $mV.s^{-1}$. Impedance response was collected by applying a constant AC voltage of 5mV, with 15 points per decade, and a scanning frequency between 0.01 and 100000 Hz.

II.4) Materials characterisation

XRD diffractograms of samples were recorded on a PANalytical X'Pert Pro diffractometer equipped with a direct optical positioning goniometric system and stuffed with a PIXcel 1D detector. The anode is made of copper and the emitted radiation correspond to the Kα ray (λ = 1.54184 Å). A 45 kV voltage and 30 mA current supply x-ray tubes. Diffractograms recording were done under room temperature, in 2θ configuration, with a step of 0.016711° each 24 seconds. Data were recorded and analysed thanks to Data Collector and HighScore Plus software.

Infrared spectroscopy was used to confirm the elimination of the oleylamine. Acquisitions were done between 500 and 4000 cm^{-1} with a Perkin Elmer Spectrum 65 FT IR Spectrometer. The results were treated thanks to Spectrum 10 Spectroscopy Software.

TEM micrographs were obtained using a TEM Tecnai 10 microscope composed of a LaB6 electron gun, an OSIS Magaview III camera, and configured in imaging mode with an accelerating voltage of 80 kV. SEM micrographs were obtained using a SEM JEOL-7500F with an accelerating voltage of 15 kV.

The size of nanoparticles was determined using Dynamic Light Scattering analyses (DLS) performed with a Nanoplus HD from Particulate systems. The experiments were carried out in hexane at 25°C and the laser was set up with a wavelength of 660 nm and a power of 70 mW.

X-Ray photoelectron spectroscopy was used to characterize the discharge products. The spectroscope is an Escalab 250 Xi from Thermo Scientific, made of a magnesium anode (Kα ray, hv=1253.6Ev). The experiments have been performed at room temperature and under reduced pressure.

Nitrogen physisorption analyses were done using an ASAP 2420 from Micromeritics. The samples were degassed overnight at 150 °C before the measurement. The pore size distribution for the porous nanoparticles was calculated via Horvath-Kawazoe method and the surface area via the Brunauere–Emmett–Teller (BET) method.

III) Results and discussions

III.1) Murray Material

The porosity of the cathode plays a key role in battery performance. Lithium peroxide is formed on the surface of the electrodes during discharge. It was found that the greater the porosity, the more lithium peroxide will be formed on the surface of the cathode. Designing a porous cathode with a gradient distribution in pore size will allow a more even oxygen transport pathway along the electrode thickness and optimise the lithium peroxide formation and will improve the performance of the battery. [20]

The Murray's law, described for the first time in 1926 is a mathematical equation which states that the cube of the radius of a parent vessel equals the sum of the cubes of the radii of the daughter vessels. [21] This law makes it possible to create a hierarchical model to optimise flows within a structure.[22] This law has been adapted to porous materials and gives the following equations (1), (2) .[19] Optimising the flow of oxygen into the cathode will allow uniform formation of lithium peroxide on its surface and should increase the performance of the battery.

$$h = \frac{d^2}{\pi D_{\text{meso}}^2} D_{\text{macro}} \tag{1}$$

$$l = \frac{(1-X)dD_{\text{meso}}^2}{nD_{\text{micro}}^2} = \frac{S_{\text{micro}}}{S}\frac{dD_{\text{meso}}^2}{nD_{\text{micro}}^2} \tag{2}$$

With h: film thickness, l: wall width and diameter, D_{macro}: diameter of macropore, d: diameter of nanoparticles, n: average number of micropores, S: specific surface area of all the nanoparticles, S_{micro}: surface area of the micropores, D_{micro}: diameter of micropores, D_{meso}: diameter of mesopores

This structure is assembled by the Layer-by-Layer Evaporation Induced Self-Assembly (LBL-EISA) method.[19] LBL-EISA is based on the breath figure phenomenon. This phenomenon is composed of several steps (Figure 3). First, a suspension of nanoparticles in an organic solvent is applied to a support. The evaporation of the solvent will cool the substrate, condense the water in the atmosphere, and push the nanoparticles to the edge of the liquid water. The water will then evaporate and leave a surface without nanoparticles. This step is repeated several times to form the final structure containing hierarchical porosity. In order to comply with Murray's law derived from porous materials. The compound must contain three types of porosity: micro/meso and microporosity and this porosity have to be hierarchical. Macoporosity have to be connected to mesoporosity and mesoporosity to microporosity. The LBL-EISA allows to obtain a connected meso/macro porosity. Macropores are the result of water evaporation and mesopores are the gap between the nanoparticles. To connect microporosity to the mesoporosity, the microporosity must be located within the nanoparticles used to form the material. If all these conditions are met, the hierarchical structure interconnecting the three types of porosity is obtained (Figure 4).

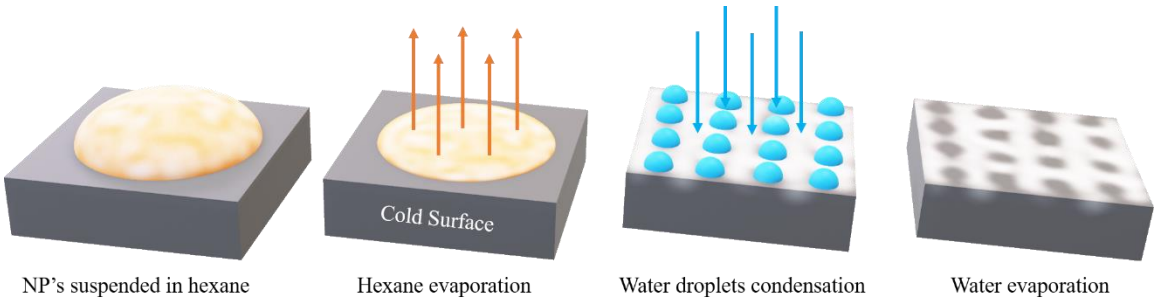

Figure 3: Scheme representing the Breath Figure phenomenon

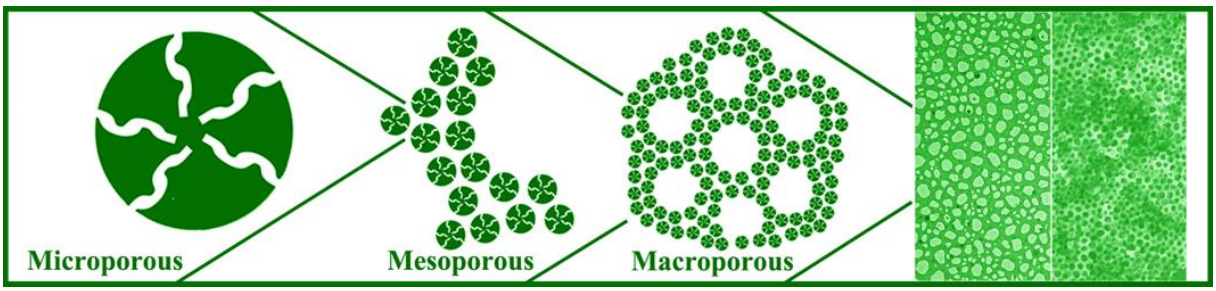

Figure 4: Schematic representing the interconnections between pores in the Murray structure

To synthetise the building unit microporous nanoparticles, of hierarchically micro-meso-macroporous materials which obey the generalised Murray's law, the thermal decomposition which is often used for the preparation of microporous nanoparticles is employed is this study. This method implies thermal degradation of a metal-organic precursor in oleylamine. The oleylamine molecule acts as a surfactant, as a solvent, but also as a reducing agent. Using this method, Zheng et al. obtained microporous cobalt (II) oxide (CoO) nanoparticles from 13 nm to 50 nm.[23] They were also able to synthesize microporous zinc oxide (ZnO) nanoparticles of 30 nm.[19]

Zheng et al.[19] used porous zinc oxide nanoparticles to form a structure with hierarchical macro/meso/micropores following Murray's law in lithium-ion batteries and showed unprecedent performance. Given these outstanding results, an attempt was made to synthetise such material to test it in lithium-oxygen batteries.

III.2) ZnO nanoparticles synthesis

III.2) Zno synthesis

Nanoparticles are the first building blocks of Murray's structure. They must fulfil three conditions in order to maximise this structure. The nanoparticles must contain micropores, be spherical in order to maximise the size of the micropores (space between the nanoparticles) and according to Equations 2 and 3 have a size of 35 nm.

The ZnO nanoparticles were synthesized according to the procedure described in the experimental part. Figure 5 presents a suggested mechanism for the formation of zinc oxide, adapted from the synthesis of cadmium oxide (CdO).[24] $Zn(acac)_2$ is first converted to zinc hydroxide ($Zn(OH)_2$) before being dehydrated to form zinc oxide. This dehydration allows the formation of channels by releasing water molecules into the solution, which leads to the formation of pores inside the particles.

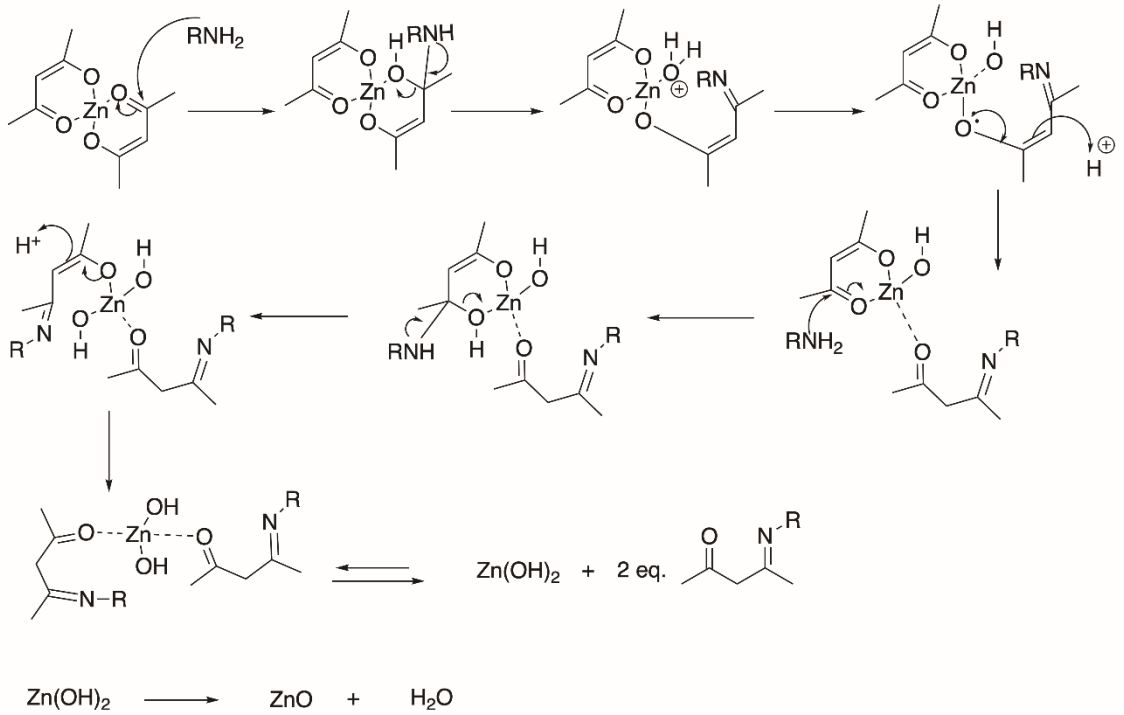

Figure 5: Reaction mechanism for the formation of zinc oxide from zinc acetylacetonate and oleylamine (R = C_8H_{16}-CH--CH-C_8H_{17})

III.2.1) Effect of experimental conditions on the formation of microporous ZnO nanoparticles

To obtain a structure with hierarchical porosity according to Murray's law, the nanoparticles following the research of Zheng et al.[19] must have a spherical morphology, a size of 35 nm, and possess

micropores. The synthesis parameters were modified to study their influence on the structural, textural and morphological properties of the nanoparticles in order to select the optimal parameters to design the best hierarchically macro/meso/micropores cathode following Murray's law. The syntheses are based on a protocol reported in the literature for the synthesis of metal oxide nanoparticles from metallo-organic precursors and oleylamine.[19,23] This synthesis is a two steps process. The first is the formation of zinc hydroxide from zinc acetylacetonate and the second is the formation of zinc oxide from the hydroxide.

III.2.1.a) Effect of reaction temperature during zinc hydroxide formation on zinc oxide nanoparticles

The first parameter to be studied is the influence of temperature during zinc hydroxide formation. Several temperatures were tested: 80°C, 100°C, 125°C and 150°C. After 30 minutes, the mixture was heated at 150°C for one hour to form zinc oxide.

The crystallinity of the samples was studied by X-ray diffraction. The XRD diffractograms of obtained samples depicted in Figure 6 show that the phase obtained for each temperature is the wurtzite phase (JCPDS 79-0208). The change in reaction temperature used during the formation of zinc hydroxide does not change the crystalline phase of the final zinc oxide.

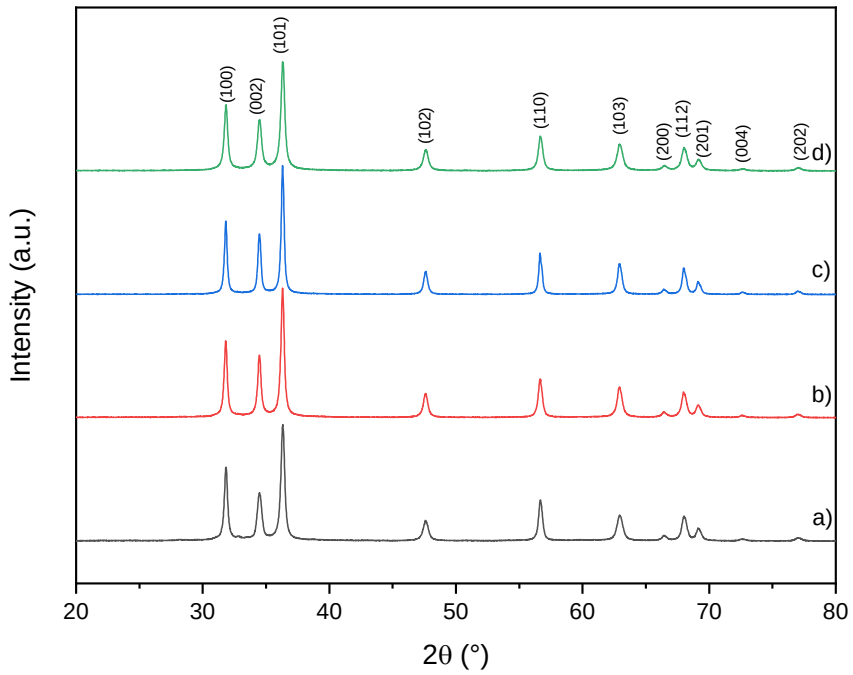

Figure 6: Diffractograms of nanoparticles obtained at different reaction temperatures in the formation of zinc hydroxide: (a) 80 °C, (b) 100 °C, (c) 125 °C and (d) 150 °C.

The morphologies of obtained materials were observed using TEM micrographs (Figure 7). Nanoparticles present a hexagonal shape for each temperature. This shape is characteristic of the wurtzite crystalline phase. The shape of the nanoparticles is the same for all samples, which means that the change in temperature does not modify their morphology. The presence of micropores can also be observed, they are identified by thin white lines.

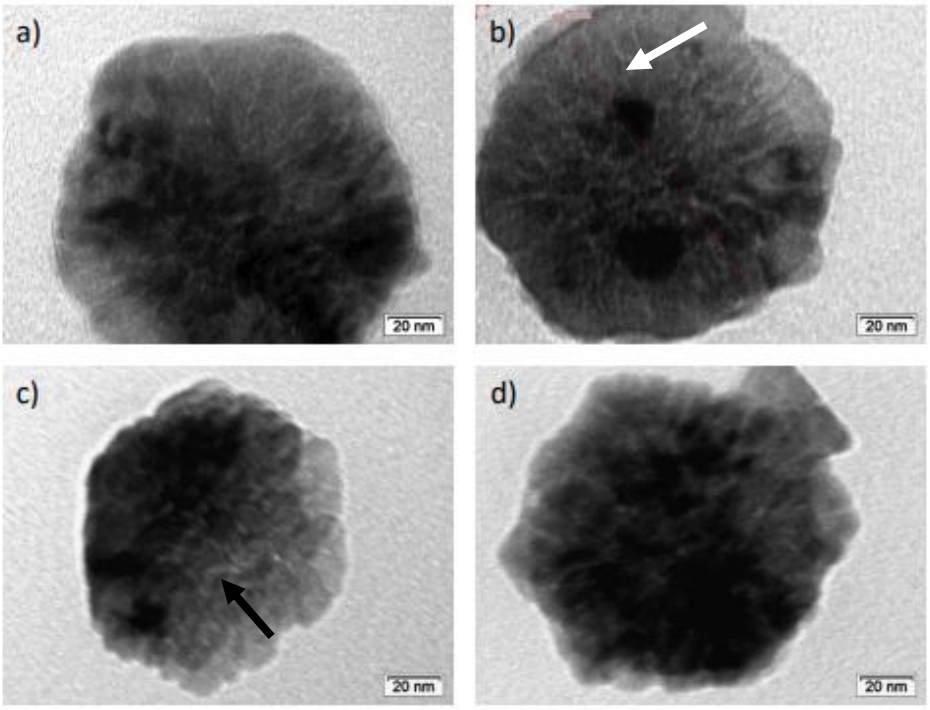

Figure 7: TEM micrographs **of nanoparticles obtained at different reaction temperatures in the formation of zinc hydroxide: (a) 80 °C, (b) 100 °C, (c) 125 °C and (d) 150 °C. The arrows show micropores.**

In order to confirm the presence of micropores, nitrogen physisorption analysis was performed on each sample. The isotherms obtained and the respective pore size distributions are shown in Figure 8.

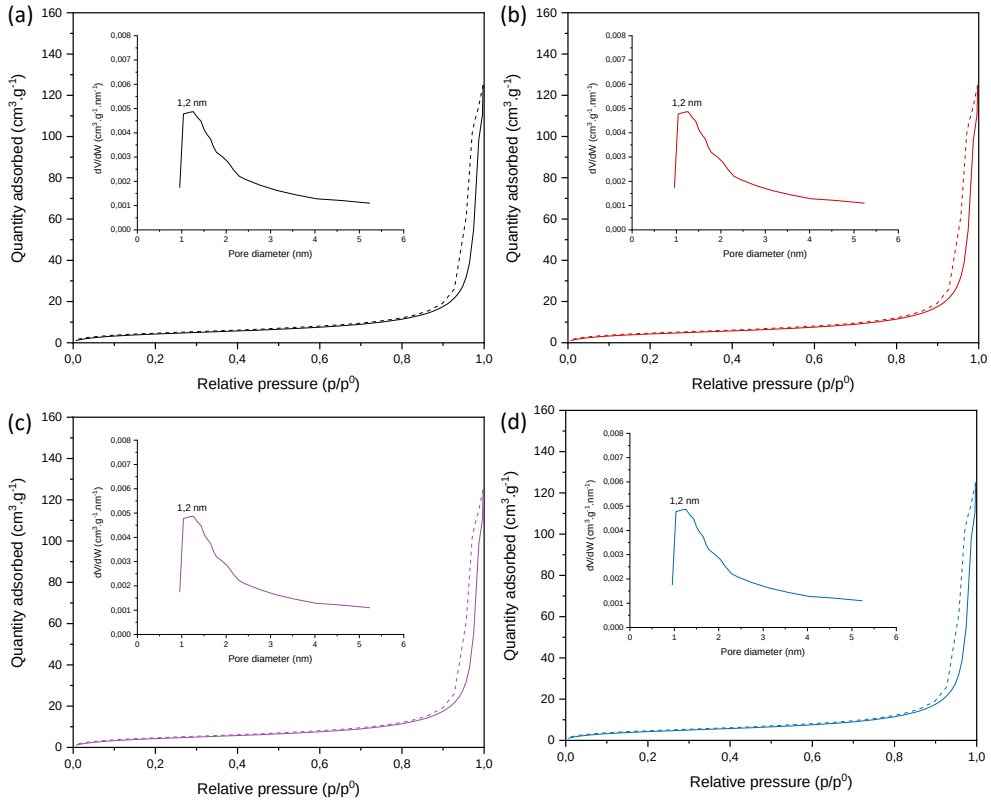

Figure 8: Nitrogen adsorption and desorption isotherms and micropore size distribution for ZnO nanoparticles obtained at different temperatures during zinc hydroxide formation: (a) 80 °C, (b) 100 °C, (c) 125 °C and (d) 150 °C.

The isotherms obtained are characteristic of mesoporous materials. These interparticle mesopores are induced by the random assembly of nanoparticles. The H3 type hysteresis indicates a slit-like pore shape. The specific surface area of the samples is between 14 and 15 $m^2.g^{-1}$, the difference between different samples is not significant. The pore size distributions obtained by the Horvath-Kawazoe (H-K) method confirm the presence of micropores with a diameter of 1.2 nm for each sample, in good agreement with the TEM observations. The specific surface area decreases slightly with the rise in temperature, therefore temperature of 80°C has been selected for the next step.

III.2.1.b) Effect of reaction time during zinc hydroxide formation on zinc oxide nanoparticles

The reaction time may also have an impact on the morphology of the particles. To perform this study different reaction times, 30, 60 and 90 minutes were selected.

The crystallinity of the sample was studied by X-ray diffraction. The obtained diffractograms (shown in Figure 9) demonstrate that the phase obtained for each sample is the wurtzite phase (JCPDS 79-0208), The reaction time variation of the zinc hydroxide formation does not change the crystalline phase of the final zinc oxide.

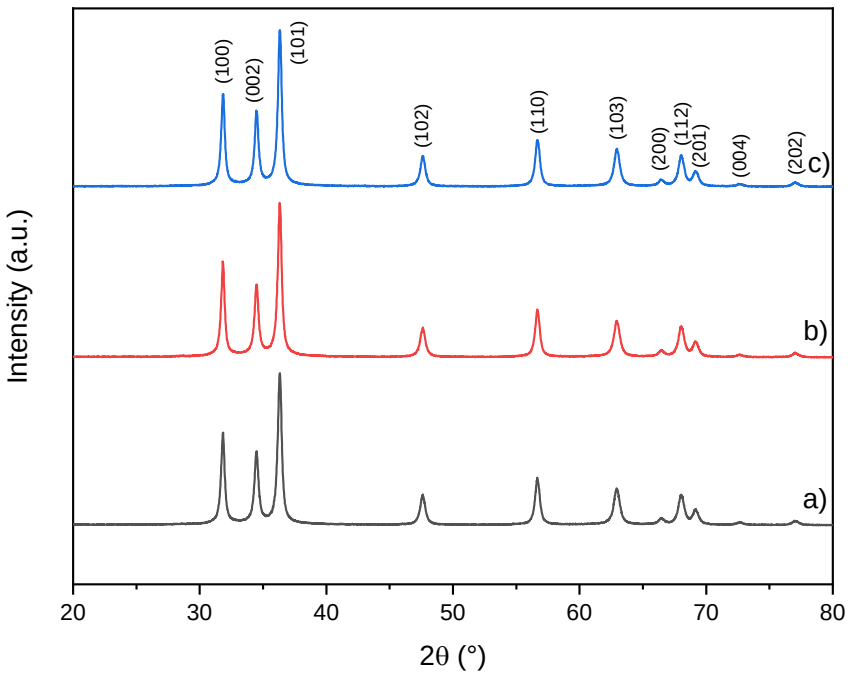

Figure 9: Diffractograms of nanoparticles obtained at different reaction time of zinc hydroxide formation: (a) 30 min, (b) 60 min, and (c) 90 min

The morphologies of nanoparticles were observed using TEM micrographs (Figure 10). All nanoparticles have a hexagonal shape, typical of the wurtzite crystalline phase. The shape of the nanoparticles is identical for all samples, indicating that reaction time does not modify the morphology. The presence of micropores is also observed.

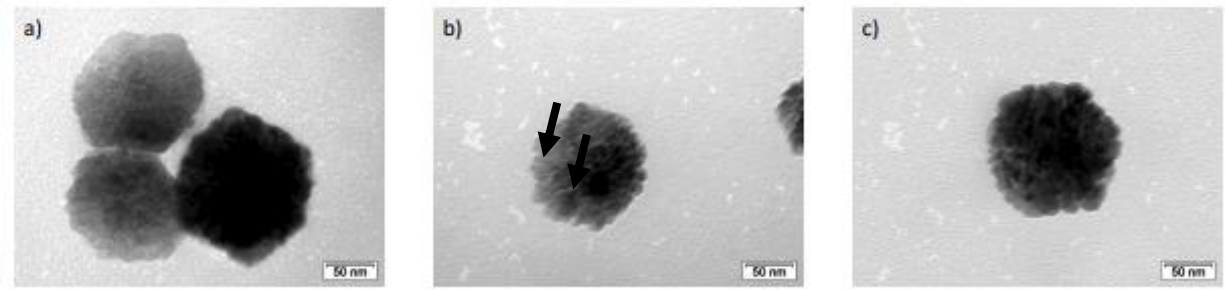

Figure 10: TEM micrographs of nanoparticles obtained at different reaction times of the zinc hydroxide formation: (a) 30 min, (b) 60 min, and (c) 90 min. The arrows show micropores.

In order to confirm the presence of micropores, nitrogen physisorption analysis was performed on each sample. The isotherms obtained and the respective pore size distributions are shown in Figure 11.

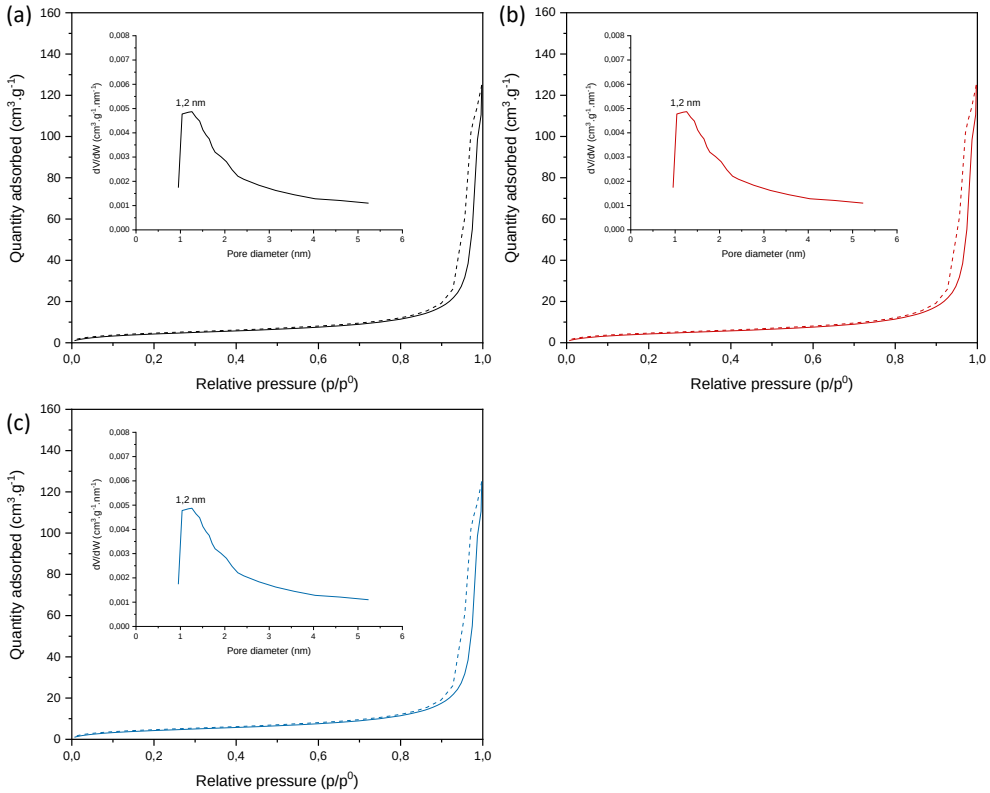

Figure 11: Nitrogen adsorption and desorption isotherms and micropore size distribution for ZnO nanoparticles obtained at different reaction times of the zinc hydroxide formation: (a) 30 min, (b) 60 min, (c) 90 min

Isotherms are characteristic of mesoporous materials with a H3 type hysteresis at high relative pressure P/P_0. All samples present a specific surface area of 14 to 15 $m^2.g^{-1}$, same as the results obtained previously. The diameter of the micropores, obtained by the H-K method, is 1.2 nm for all three samples. The reaction time for the formation of zinc hydroxide has no influence on the morphology of the ZnO nanoparticles. A time of 30 min was chosen for further study.

III.2.1.c) Effect of reaction temperature during zinc hydroxide decomposition on zinc oxide nanoparticles

The condition of the first step fixed (80°C, 30min). We need to optimise the conditions of the second step of the reaction which is the formation of zinc oxide from zinc hydroxide decomposition. The reaction time and temperature conditions will be modified in order to observe their consequences on the nanoparticle morphology. Temperatures of 80, 100, 125, and 150°C were tested.

The crystallinity of the sample was tested by X-ray diffraction. XRD diffractograms of the obtained samples are presented in Figure 12 and, show that all the crystalline phase obtained is that of wurtzite (JCPDS 79-0208). The temperature variation in the decomposition of zinc hydroxide to form zinc oxide does not change the crystalline phase of the final zinc oxide.

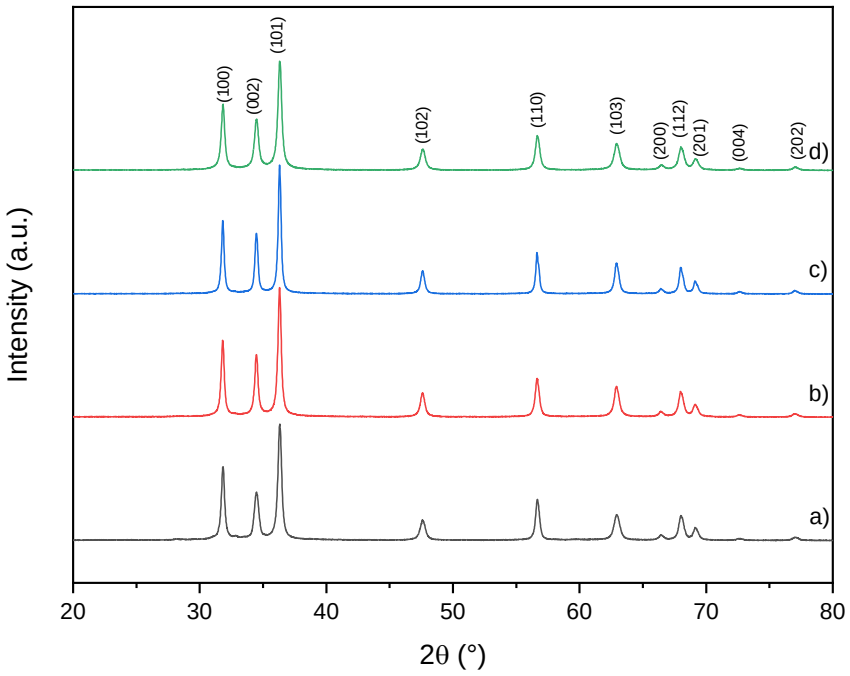

Figure 12: Diffractograms of nanoparticles obtained at different temperature in the formation of zinc oxide: (a) 80°C, (b) 100°C, (c) 125°C and (d) 150°C.

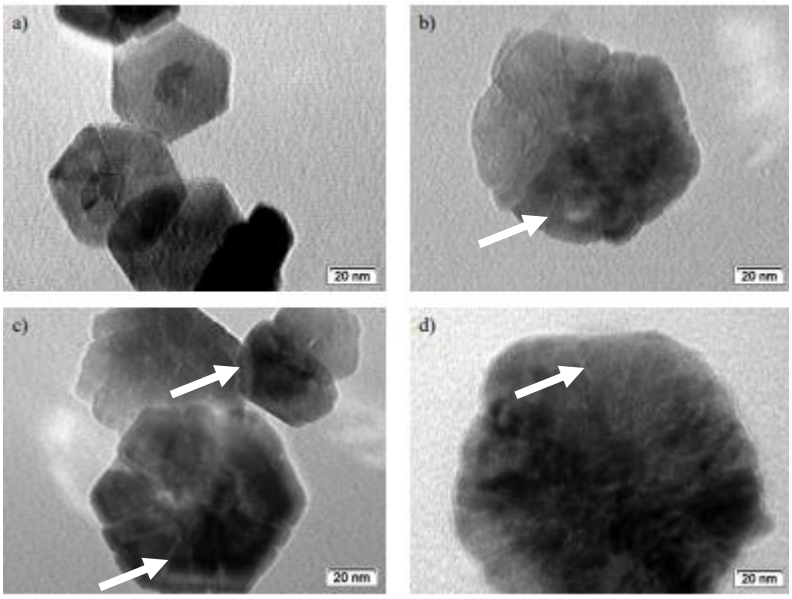

Figure 13: TEM micrographs of nanoparticles obtained at different temperature in the formation of zinc oxide: (a) 80°C, (b) 100°C, (c) 125°C and (d) 150°C. The arrows show micropores.

TEM micrographs are given in the Figure 13. Each particle has a hexagonal shape and in its center a brighter area, corresponding to the micropores formed during the dehydration of zinc hydroxide. Regarding the particle size, nanoparticles synthesised at 80 °C reach 60±4 nm while those produced at 150 °C 139±10 nm. The higher the temperature, the larger the size of nanoparticles. This temperature-dependent growth of particles is a well-known phenomenon.[25]

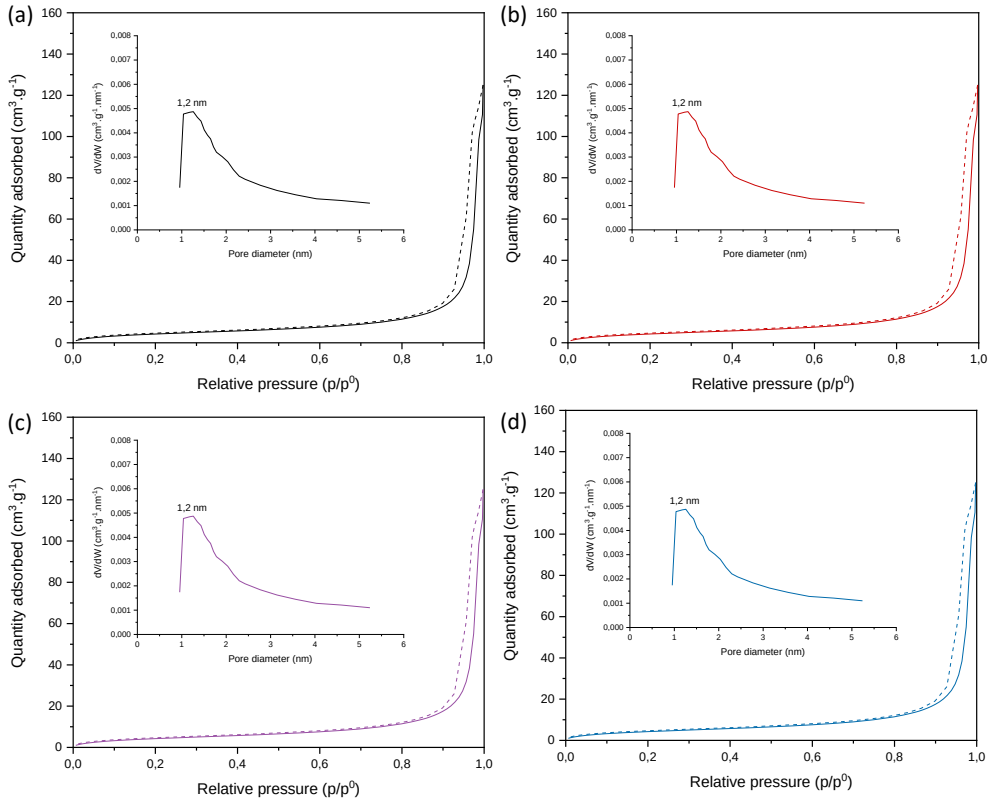

Figure 14: Nitrogen adsorption and desorption isotherms and micropore size distribution for ZnO nanoparticles obtained at different temperature during zinc oxide formation: (a) 80°C, (b) 100°C, (c) 125°C (d) 150°C

Isotherms of the obtained samples shown in Figure 14 are characteristic of mesoporous materials. Specific surface area increased from 14 to 20 $m^2.g^{-1}$, which is consistent with the change in size of the nanoparticles, the largest the nanoparticles the lowest the specific surface. The diameter of the micropores obtained by the H-K method is 1.2 nm for all samples. Thus, above results suggest that the temperature of the zinc oxide formation has no influence on the micropores dimension. The temperature of 150°C was selected for the further study.

III.2.1.d) Effect of reaction time during zinc hydroxide decomposition on zinc oxide nanoparticles

The effect of reaction time during zinc hydroxide decomposition on zinc oxide formation where also investigated. The times selected was 30, 40, 50, and 60 min while the temperature was set at 150°C.

XRD diffractograms are presented in Figure 15, and show that the crystalline phase obtained for each sample is the wurtzite phase (JCPDS 79-0208). The variation of time during zinc hydroxide decomposition does not change the crystalline phase of the final zinc oxide.

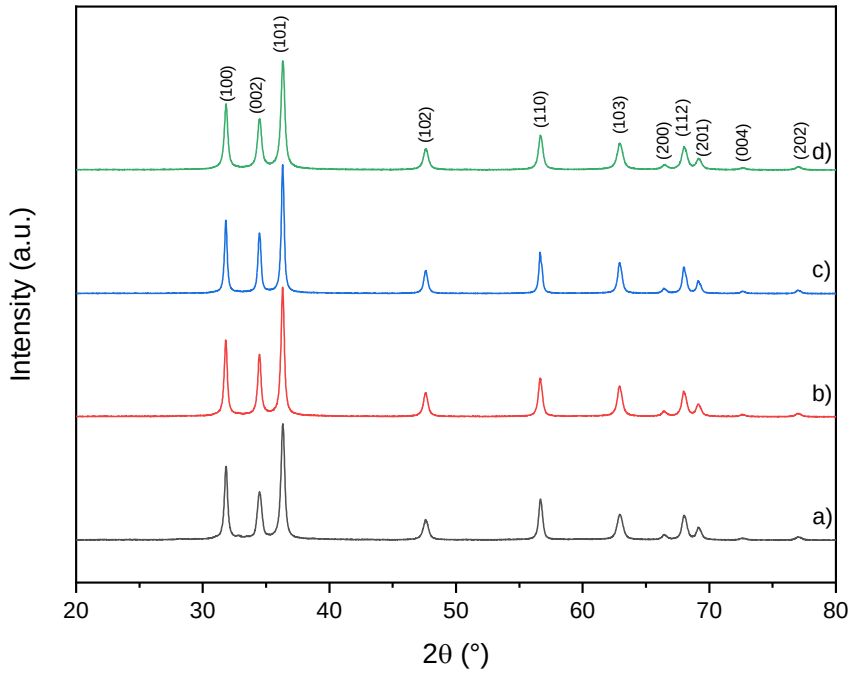

Figure 15: Diffractograms of nanoparticles obtained at different reaction times of the formation of zinc oxide: (a) 30 min, (b) 40 min, (c) 50 min and (d) 60 min.

The morphology of nanoparticles was observed via TEM. As for the previous samples, these nanoparticles present thinner, lighter areas, characteristic of intraparticle micropores (Figure 16). The particles in Figures 16.a to 16.c show irregular shapes while sample 16.d, synthesized for 60 minutes at 150 ◦C, shows hexagonal shaped particles. This reaction time of 60 min allows the nanoparticles to grow uniformly, resulting in a homogenisation of their forms.

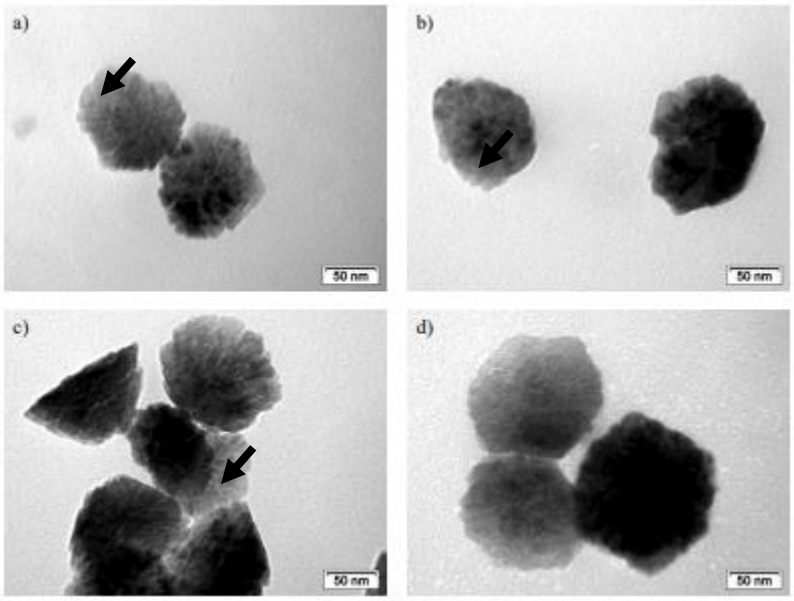

Figure 16: TEM micrographs of nanoparticles obtained at different reaction times of the formation of zinc oxide: (a) 30 min, (b) 40 min, (c) 50 min and (d) 60 min

The microporosity observed on the micrographs was confirmed via nitrogen physisorption. The isotherms are presented in Figure 17 and are characteristic of mesoporous material represented by a slit-type H3 pores hysteresis. The surface area of all samples is 16 $m^2.g^{-1}$ and the micropores size is 1.2 nm. These results indicate that the reaction time of the formation of zinc oxide nanoparticles influences the shape of the nanoparticles but not their micropore size. Increasing the reaction time, a better homogenization of the shape of the nanoparticles can be achieved. A time of 60 minutes was selected for the rest of the study.

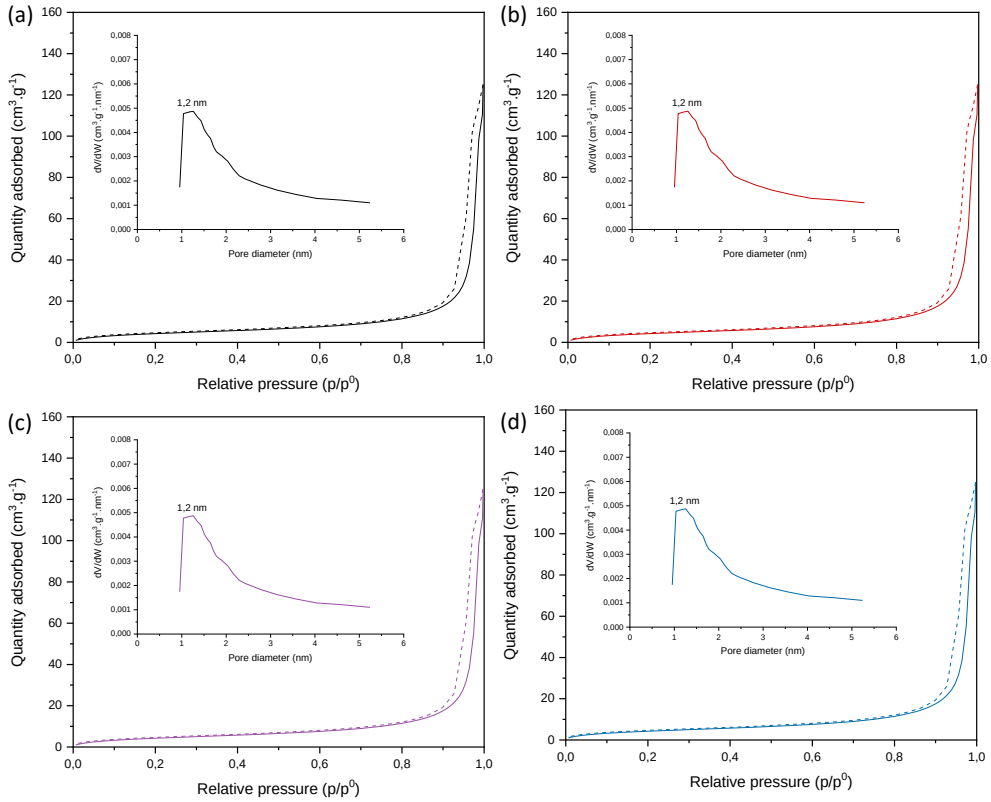

Figure 17: Nitrogen adsorption and desorption isotherms and micropore size distribution for ZnO nanoparticles obtained at different reaction times during zinc oxide formation: (a) 30 min, (b) 40 min, (c) 50 min and (d) 60 min

III.2.1.e) Effect of an addition of a capping agent

One of the requirements of nanoparticles is to have a spherical morphology, however most of the nanoparticles obtained have a hexagonal morphology. One possibility to achieve a spherical shape would be to add a capping agent to control the growth of the nanoparticle.[26] A capping agent is an amphiphilic molecule with a polar head group and a non-polar hydrocarbon tail. Due to the amphiphilic nature, they can change the superficial tension between two surfaces and could enhance the compatibility with another phase. The non-polar tail interacts with the medium while the polar head interacts with the metal. The capping agent chosen is the triphenylphosphine (TPP). TPP is a Lewis base and can bind to a Lewis acid; this interaction is shown in Figure 18. TPP increase the steric hindrance

and creates a spherical layer around the nucleation point leading to the formation of spherical nanoparticles.

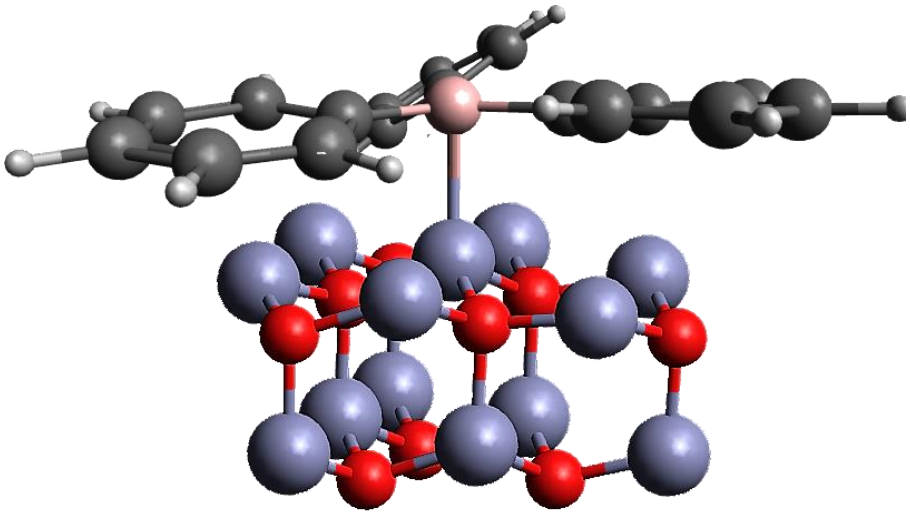

Figure 18: Representation of the interaction between TPP and zinc atoms on the surface of nanoparticles (pink is for P, blue for Zn, red for O, black for C, and white for H).

The TPP concentrations tested are 0, 77, 153 and 229 mM. The crystallinity of the sample was studied by X-ray diffraction. The XRD diffractograms are illustrated in Figure 20 and show that the phase obtained for each sample is the wurtzite phase (JCPDS 79-0208). The addition of TTP does not change the crystalline phase of the final zinc oxide.

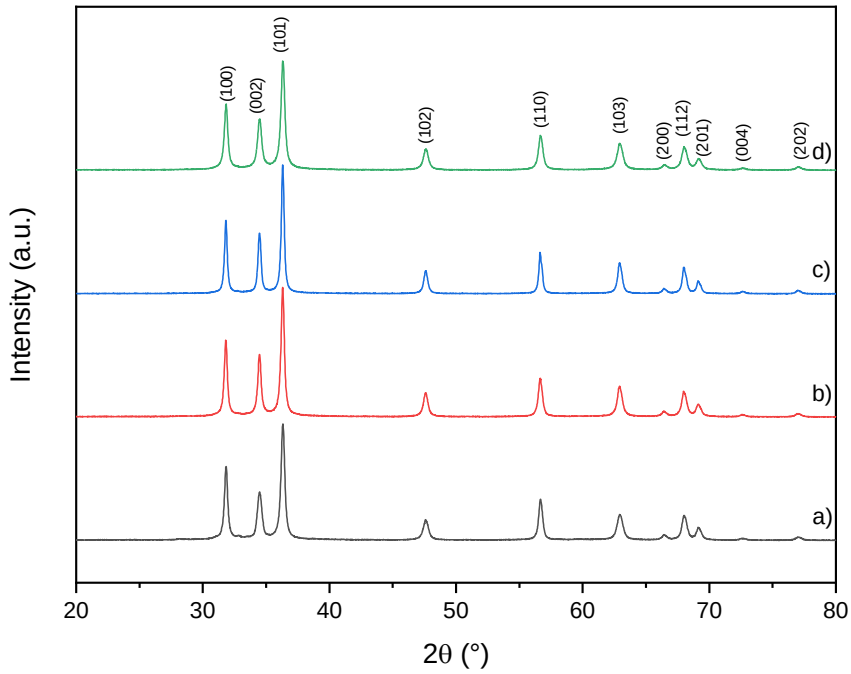

Figure 19: Diffractograms of ZnO nanoparticles obtained with different TPP concentration: (a) 0 mM, (b) 77 mM, (c) 153 mM and (d) 229 mM.

The morphology of the nanoparticles can be observed in Figure 20. The micrographs still show hexagonal nanoparticles for a TPP concentration of 0 and 77 mM. For a concentration of 153 mM the morphology becomes spherical and for 229 mM this morphology remains spherical. The results obtained prove that the addition of TPP at a concentration of 153 mM results in spherical rather than hexagonal particles, while further increase in the concentration of TPP (229 mM) doesn't lead to any further change in the shape of the nanoparticles.

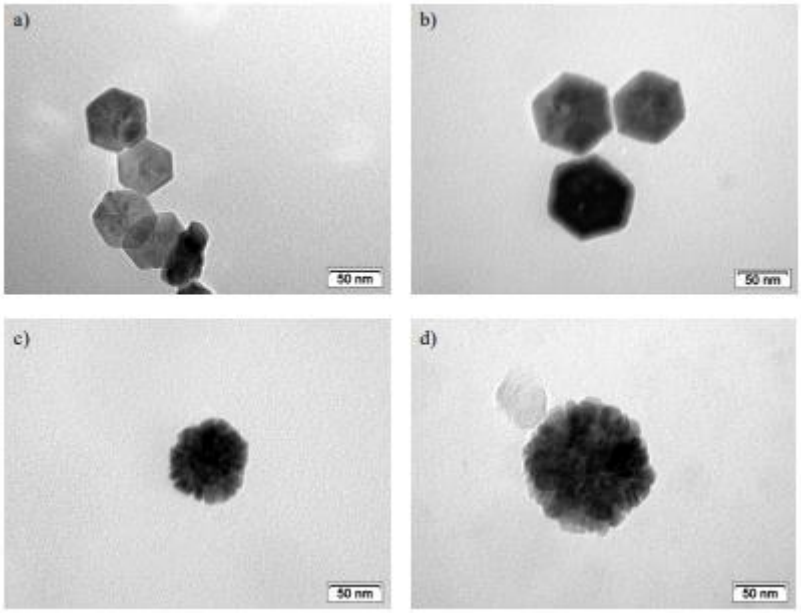

Figure 20: TEM micrographs of ZnO nanoparticles obtained using different TPP concentration: (a) 0 mM, (b) 77 mM, (c) 153 mM and (d) 229 mM.

Nitrogen physisorption was performed in order to determine the porosity of the samples. The isotherms obtained and the pore size distributions calculated by the Horvath-Kawazoe method are shown in Figure 21. The isotherms are characteristics of mesoporous materials with a characteristic hysteresis H3 of slit pores. The diameter of the micropores is 1.2 nm and is identical for all samples. The specific surface area is 25 $m^2.g^{-1}$ which is higher than all the previously obtained nanoparticles. This higher specific surface area could come from the spherical morphology of the nanoparticles. To conclude, the addition of triphenylphosphine during synthesis can tune the shape of the nanoparticles but has no influence on the textural properties.

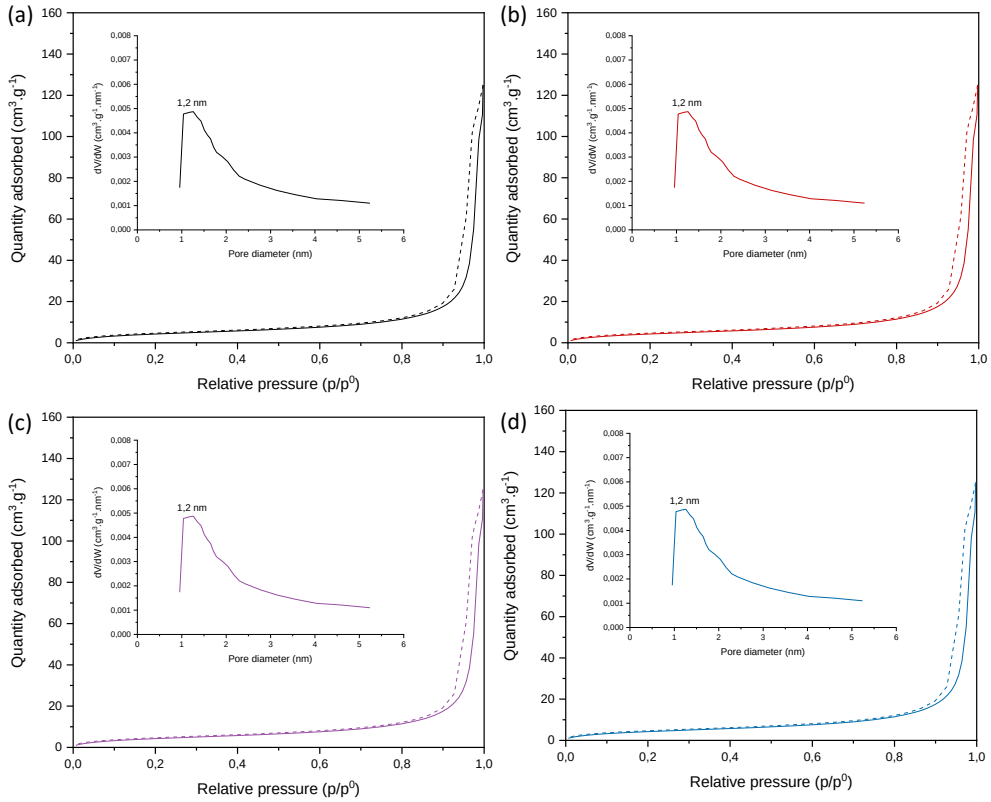

Figure 21: Nitrogen adsorption and desorption isotherms and micropore size distribution for ZnO nanoparticles obtained using different TPP concentration: (a) 0 mM, (b) 77 mM, (c) 153 mM and (d) 229 mM.

III.2.1.f) Effect of zinc precursor concentration

One of the key characteristics of nanoparticles for the design of a hierarchical micro/meso/macro porous material is the size of the nanoparticles. One way to control the size of the nanoparticles would be to vary the precursor/medium ratio. A decrease in the precursor/medium concentration ratio will result in greater species isolation due to increased oleylamine and TPP concentration and should lead to a decrease in particle size. This phenomenon has already been observed for iron oxide particles by Asadi et al.[27] They explained this phenomenon by the decrease in the concentration of growth species in the reaction medium. At high precursor/medium ratio the concentration of monomer in solution is high. The concentration of the available monomers at the interface of the nuclei (the crystal growth front) is close to that of the bulk solution. The diffusion distance for monomers is shorter, which leads to a higher mass transfer and therefore higher growth rate and thus bigger nanoparticles

The parameters chosen for this experiment are those previously determined, temperatures of 80°C and 150°C for 30 and 60 min respectively. The precursor concentrations chosen for this study are 15mM, 20mM, 22mM, 27mM, 33mM, and 42mM.

The crystallinity of the sample was studied by X-ray diffraction. The XRD diffractograms of the obtained samples are illustrated in Figure 22 and show that the phase obtained for each sample is the

wurtzite phase (JCPDS 79-0208). The variation of zinc precursor concentration does not change the crystalline phase of the final zinc oxide.

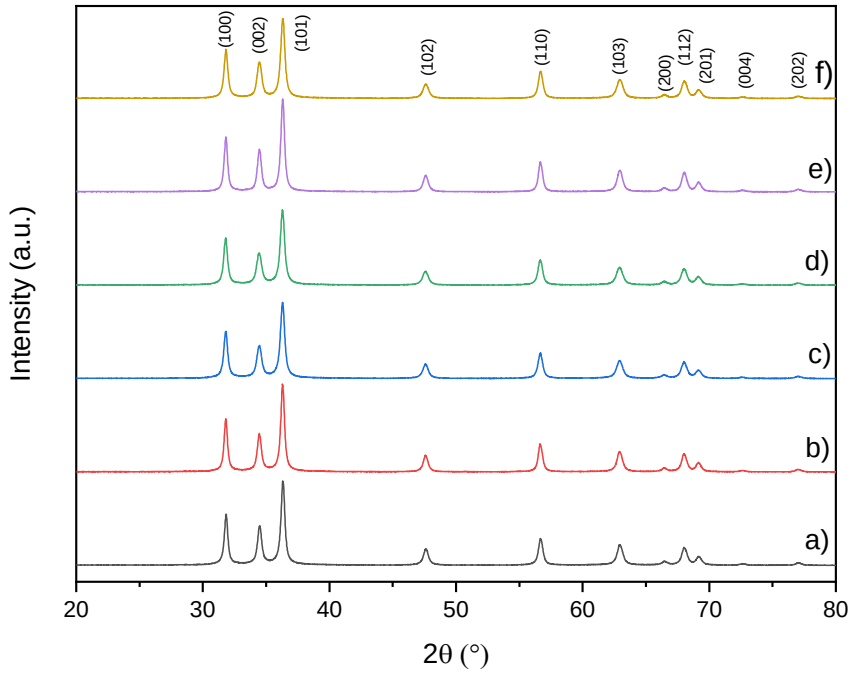

Figure 22: Diffractograms of ZnO nanoparticles obtained using different zinc precursor concentrations: (a) 42 mM, (b) 33 mM, (c) 27 mM, (d) 22 mM. (d) 20 mM. and (f) 15 mM.

The morphology of nanoparticles was observed via TEM. As for the previous samples, these nanoparticles present thinner, lighter areas, characteristic of intraparticle micropores (Figure 23). All the nanoparticles are spherical. Moreover, the size of these nanoparticles seems decreases with the zinc acetylacetonate concentration and could confirms our starting hypothesis.

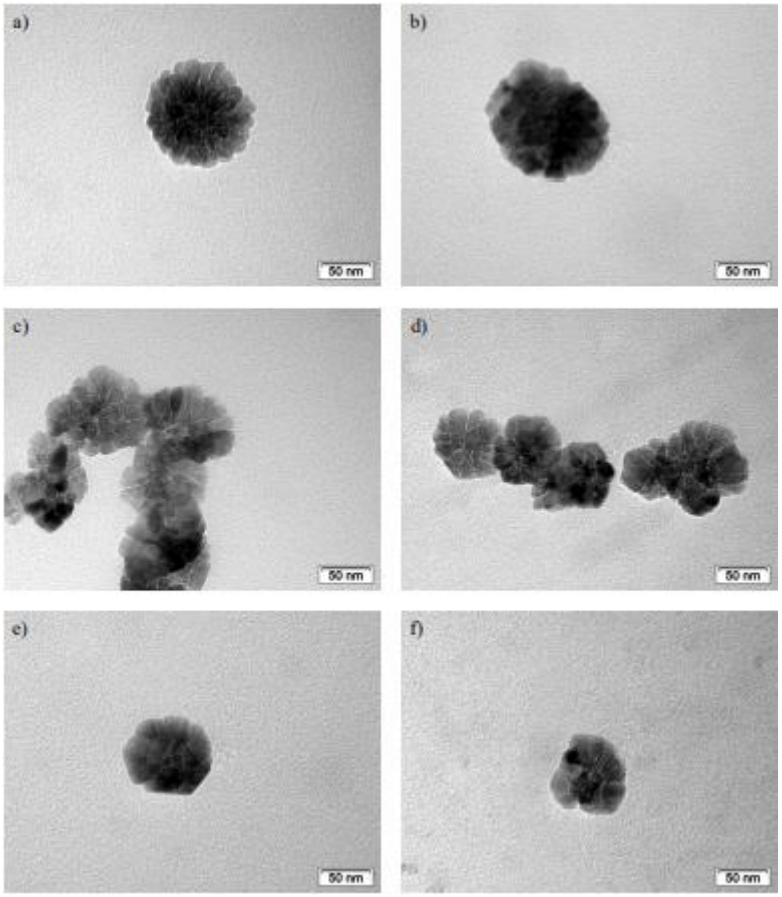

Figure 23: TEM micrographs of ZnO nanoparticles obtained using different zinc precursor concentration: (a) 42 mM, (b) 33 mM, (c) 27 mM, (d) 22 mM. (d) 20 mM. and (f) 15 mM.

Dynamic light scattering technique was used to correlate the particle size with the concentration of zinc precursors. This correlation is presented in Figure 24, and shows a linear relationship. The particle size increases with the zinc precursor concentration, confirming our initial hypothesis.

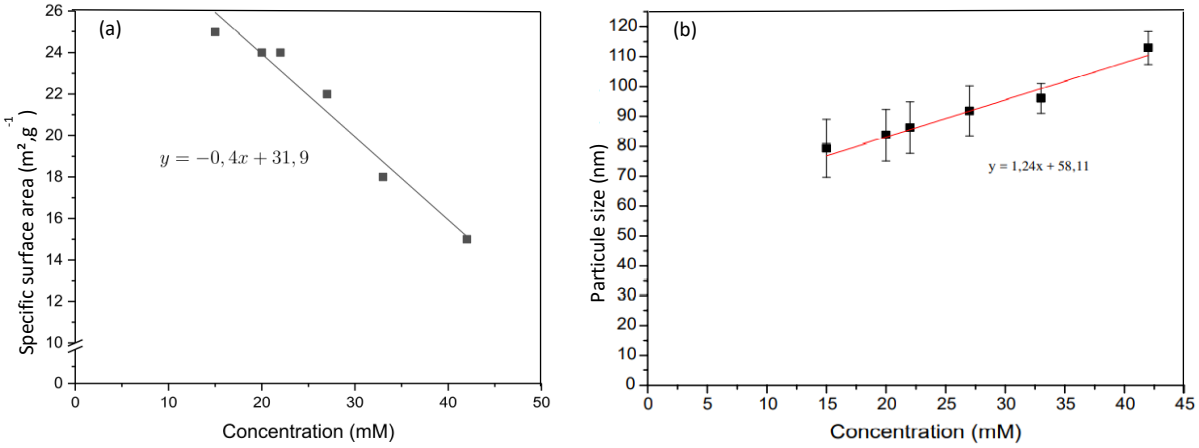

Figure 24: (a) Evolution of particle size and (b) specific surface area as a function of zinc precursor concentration with standard deviations

Nitrogen physisorption was performed to determine the porosity of the samples. The isotherms obtained and the pore size distributions calculated by the Horvath Kawazoe method are shown in

Figure 26. These isotherms are of type IV and have a H3 hysteresis which is characteristic of maesoporous materials with "slit-shaped" interparticle pores created by the assembly of the particles. The diameter of the micropores is identical for all samples meaning that it does not change with the size of the nanoparticles. The specific surface area is related to the concentration of zinc acetylacetonate. Figure 25 shows the evolution of the specific surface area as a function of the concentration of the zinc precursor. It indicates an increase in specific surface area with the decrease in the concentration of $Zn(acac)_2$ which is consistent with previous observations. Indeed, when the concentration of zinc precursor decreases, the size of the nanoparticles decreases, and leads to an increase in the specific surface area.

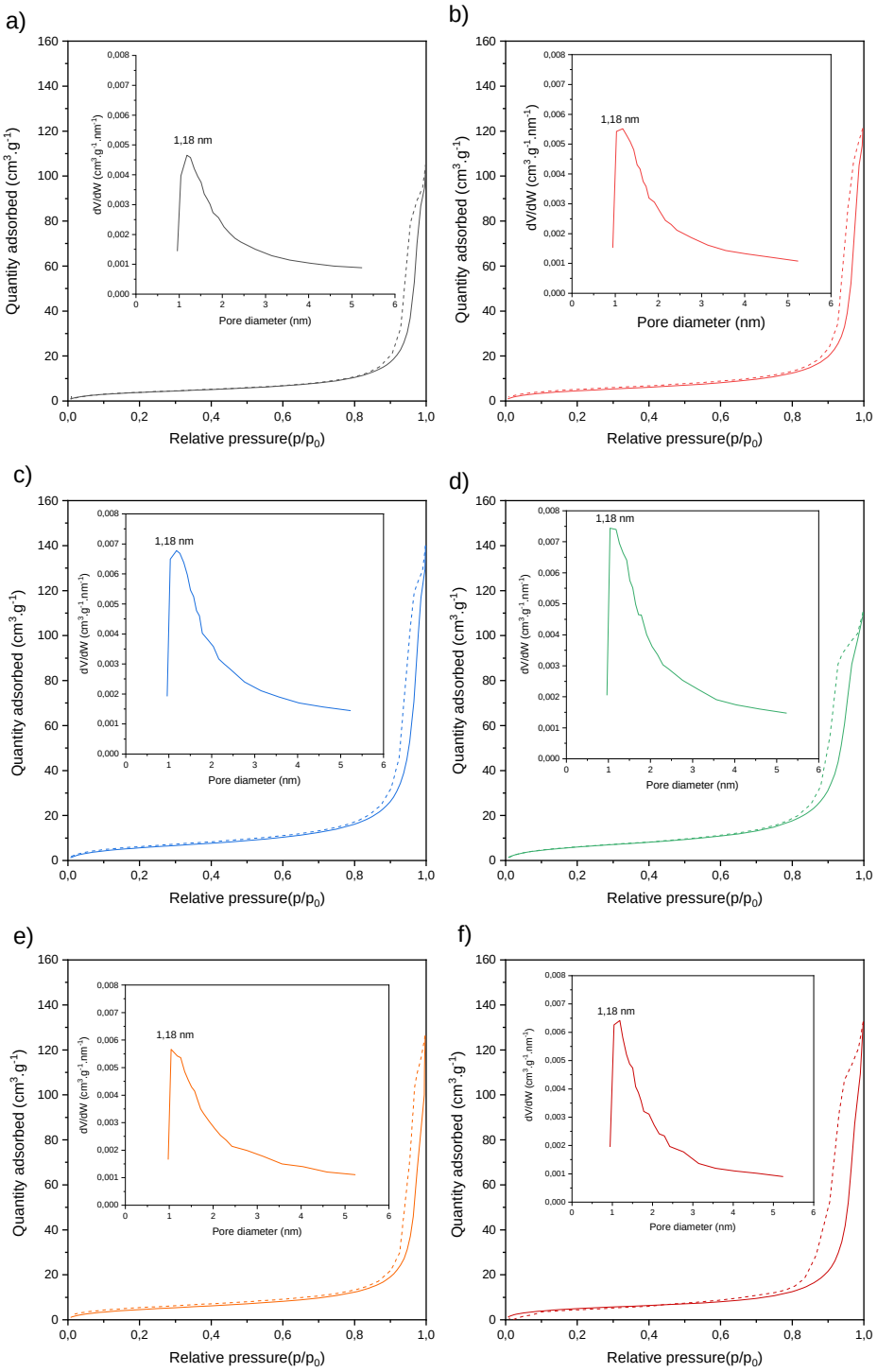

Figure 25: Nitrogen adsorption and desorption isotherms and micropore size distribution for ZnO nanoparticles obtained using different zinc precursor concentration: a) 42 mM, (b) 33 mM, (c) 27 mM, (d) 22 mM. (d) 20 mM. and (f) 15 mM.

In this section, all the parameters influencing the properties of zinc oxide nanoparticles during their synthesis are summarized in the Table 1. It shows that the time reaction of $Zn(OH)_2$ decomposition and the concentration of TPP influence the nanoparticles shape while the temperature reaction of $Zn(OH)_2$ decomposition and the concentration of $Zn(acac)_2$ influence the nanoparticles size and the specific

surface area. The parameters that have been selected for the rest of the study are reported in the experimental part.

Table 1 : **Table summarising the influences of the synthesis parameters on the different characteristics of ZnO nanoparticles**

	Pore size	Nanoparticles Shape	Crystallinity	Specific surface area	Nanoparticles size
T° $Zn(OH)_2$ formation	X	X	X	X	X
t $Zn(OH)_2$ formation	X	X	X	X	X
T° $Zn(OH)_2$ decomposition	X	X	X	V	V
t $Zn(OH)_2$ decomposition	X	V	X	X	X
[TPP]	X	V	X	X	X
[$Zn(acac)_2$]	X	X	X	V	V

III.3) Assembly of the hierarchically micro/meso/macroporous structure following Murray's law

The previous section showed the influence of the parameters on the morphology and the texture of ZnO nanoparticles. The next step is to create a nanoparticle suspension and to drop cast it on a support to form the final material. The aim of this section will be to perform an assembly of nanoparticles according to Murray's law and to determine the main parameters influencing its design.

III.3.1) Effect of the concentration of the suspension on the formation of the hierarchically micro/meso/macroporous structure

The hierarchical porous structure is assembled via a Layer-by-Layer Evaporation Induced Self-Assembly (LBL-EISA) method. The first challenge to synthetise this kind of material is to obtain homogenous layers. Different suspensions of nanoparticles at different concentrations were drop casted and analysed by TEM. The concentrations tested were 0.5, 1 and 2.5 mg.L^{-1}, and the resulting micrographs are presented in Figure 26.

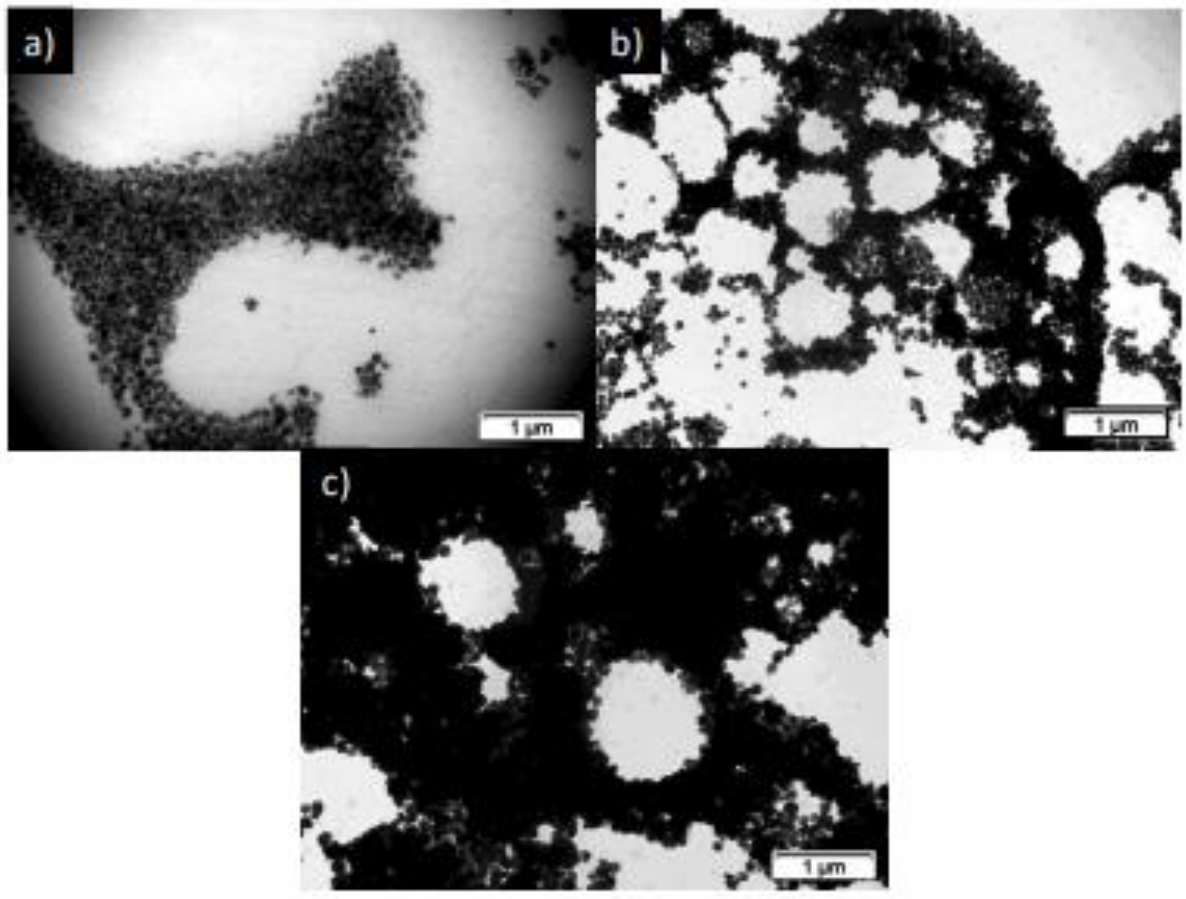

Figure 26: TEM micrographs of nanoparticle deposits made from suspensions of different concentrations: (a) 0.5 mg.mL^{-1}, (b) 1 mg.mL^{-1}, and (c) 2.5 mg.mL^{-1}

At a concentration of 0.5 mg.mL^{-1} the structure does not show well-defined macropores. When the concentration is increased to 1 mg.mL^{-1}, pores begin to appear. However, this concentration is still not sufficient to achieve to a uniform macropore distribution on the support. By increasing the concentration to 2.5 mg.mL^{-1}, the structure presents well-defined macropores with almost complete surface coverage. As a result, these micrographs indicate that a minimum concentration of 2.5 mg.mL^{-1} must be used to obtain the final structure. Once the nanoparticle concentration has been determined and the monolayer established, the deposits are repeated in order to obtain a thick material.

Material morphology is characterized by scanning electron microscopy and is shown in Figure 27. All samples present a structure with macropore and they seem to be homogeneously distributed in the material. However, a first observation leads to the hypothesis that the structure becomes more and more homogeneous by increasing the concentration of nanoparticles. This hypothesis is confirmed thanks to the pore size distribution (Figure 27). These distributions were obtained from different micrographs on an average population of 300 pores.

As the concentration increases, the standard deviation of the distribution decreases. Therefore, the structure formed with a concentration of 2.5 mg.mL^{-1} shows a pore size distribution with a maximum at 2.7 µm while the one made with 5 mg.mL^{-1} exhibits a maximum at 1.8 µm. The maximum of the distribution decreases to 1.1 µm and 0.8 µm when the concentration reaches 7.5 mg.mL^{-1} and 10 mg.mL^{-1} respectively. High concentration of the suspension increases the density of the particles that organise themselves around the water droplets formed on the surface during the evaporation of the solvent and limits their expansion, resulting in smaller macropores.

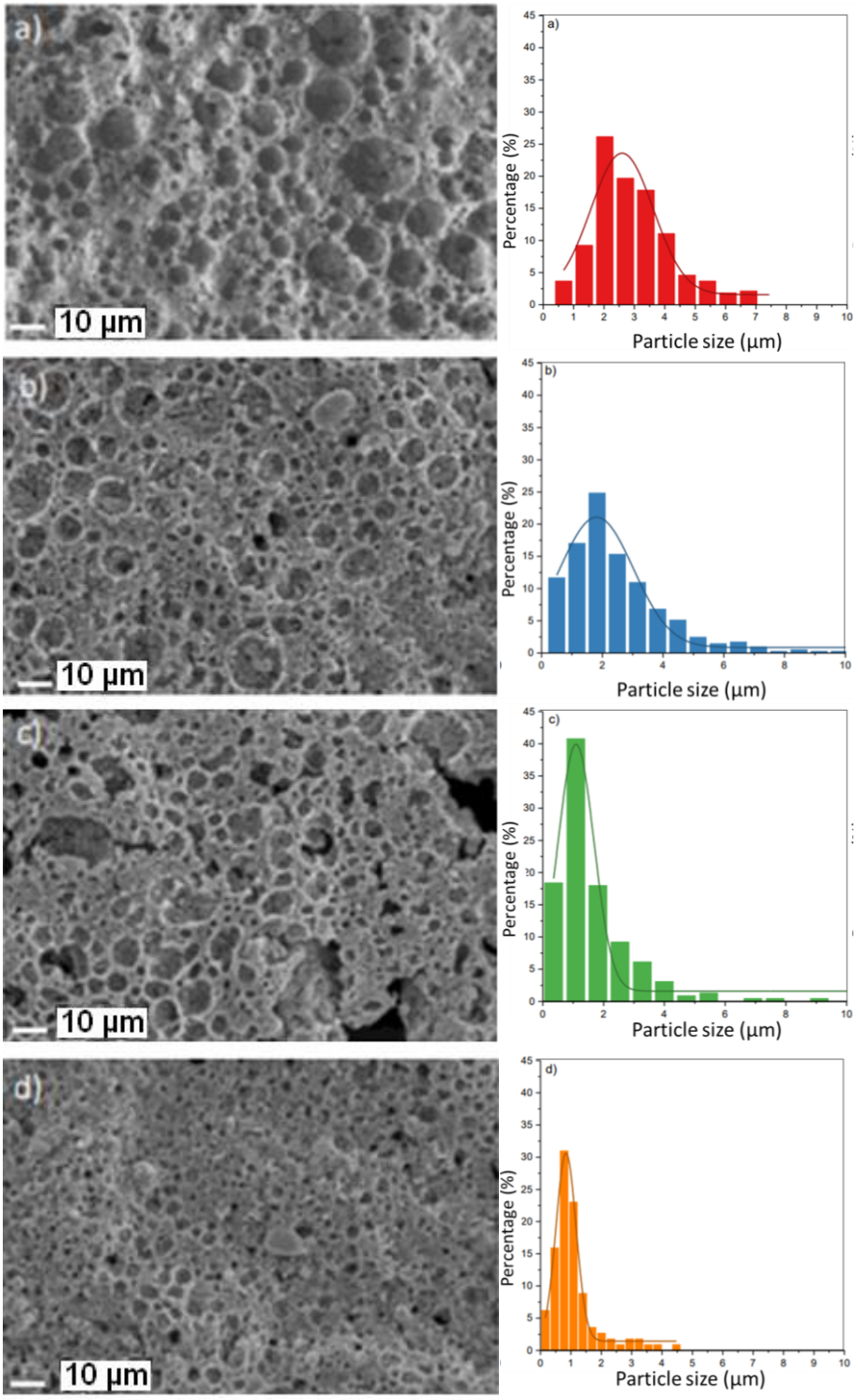

Figure 27: SEM micrographs and macropore size distribution of porous structure made from suspensions of different concentrations: (a) 2.5 mg.mL^{-1}, (b) 5 mg.mL^{-1}, (c) 7.5 mg.mL^{-1} and (d) 10 mg.mL^{-1}

III.3.2) Effect of the relative humidity rate on the hierarchically micro/meso/macroporous structure.

The macropores within the structure are caused by the condensation of water from the atmosphere. It is important to control the atmospheric relative humidity in order to regulate the size of the macropores. Experimentally, several 2.5 $mg.ml^{-1}$ nanoparticle suspensions were drop casted under different humidity levels (60, 70, and 80%). We expect to see a concerted increase in the size of macropores with the moisture content.

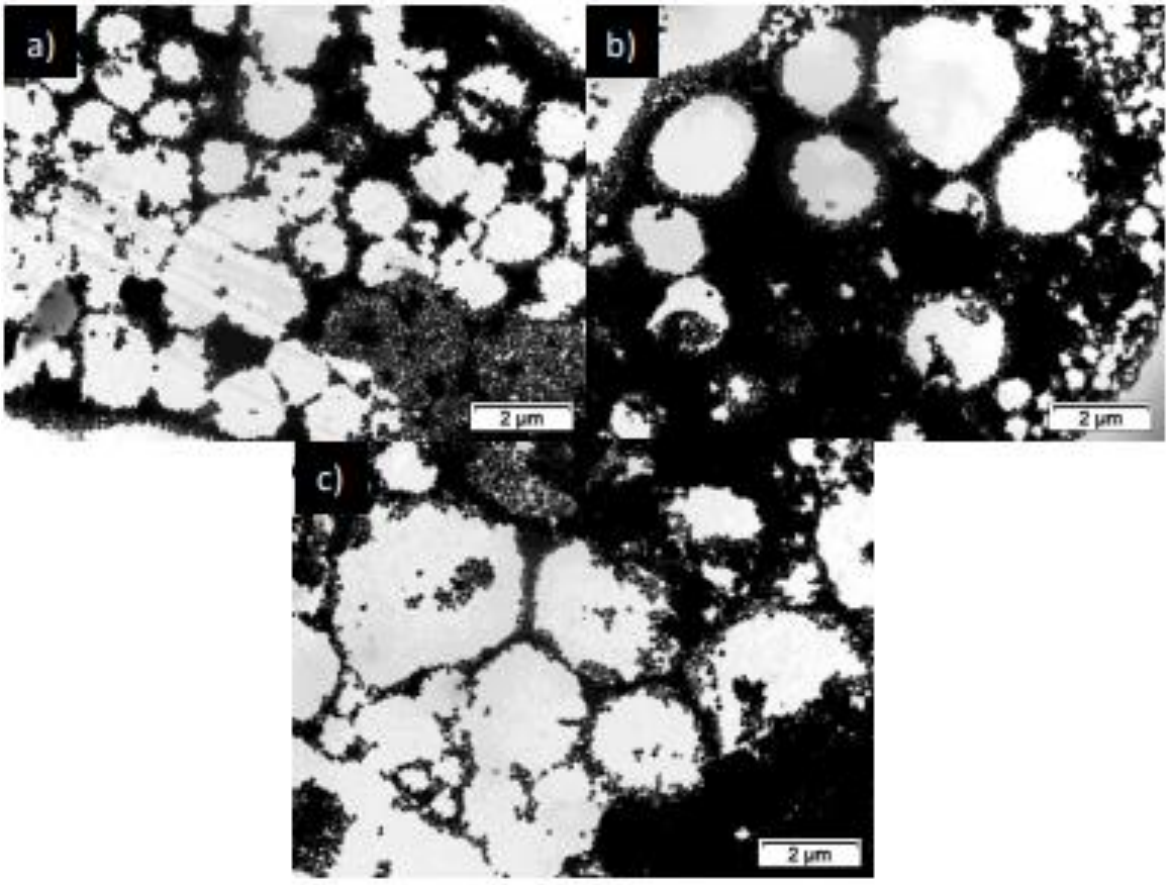

Figure 28: TEM micrographs of nanoparticle deposits made from a 2.5 $mg.mL^{-1}$ suspensions at different relative humidity levels: (a) 60%, (b) 70%, and (c) 80%

TEM micrographs of the first deposited layer at (a) 60%, (b) 70%, and (c) 80% are presented in Figure 28 and show that all sample presents macropores. Moreover, the size of the macropores increase as a function of moisture content and confirm the initial expectation.

Several monolayers were deposited to form the final material. The SEM micrographs and the distribution of macropores can be seen in Figure 29. All the samples have macropores. The pore size in the bulk material increases with the relative humidity during deposition. The higher the humidity, the more water droplets condense, leading to a larger volume and pore size. This phenomenon has already been observed for polymer film deposition.[28] The distribution of pore sizes is wider with the moisture content. The pore size increases gradually from 1.89, 2.70, 3.0, 3.5 to finally 3.8 µm for the assembled structure at a humidity of 40, 50, 60, 70 and 80% respectively,

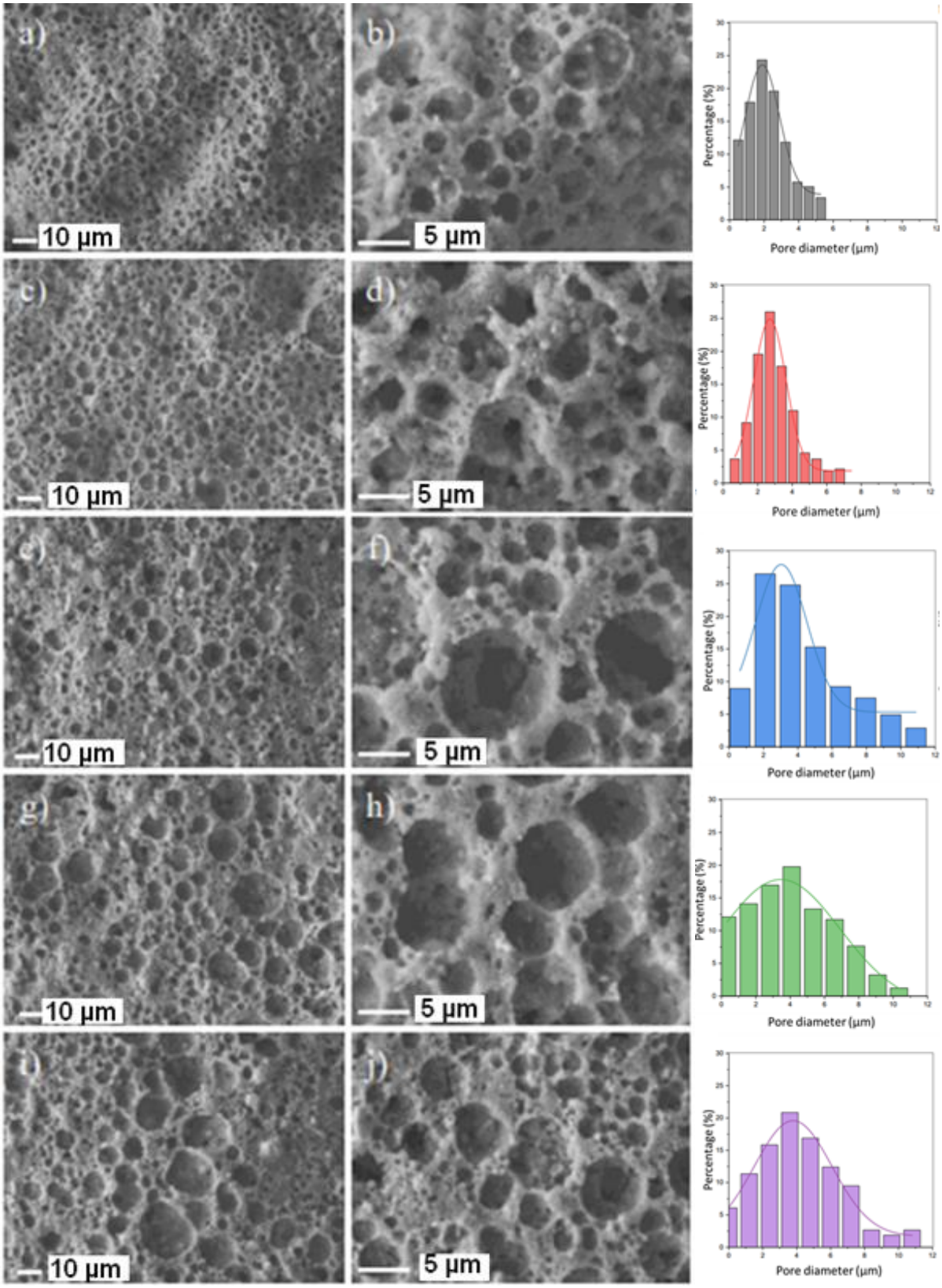

Figure 29:SEM micrographs and macropore size distribution of porous structure made from a 2.5 mg.mL^{-1} suspensions at different relative humidity levels: (a,b) 40%, (c,d) 50%, (e,f) 60%, (g,h) 70%, and (I,j) 80%

To sum up, this part studied the formation of the hierarchical porous structure following Murray's law based on zinc oxide nanoparticles. It has been shown that the porosity induced by water droplets condensation during the evaporation of the solvent could be controlled and depends on several factors.

Firstly, controlling atmospheric humidity during the deposition of nanoparticles regulate porosity by changing the amount of water available for condensation. The higher the relative humidity, the larger the size of the pores.

Secondly, the concentration of the suspension during deposition can be modified to tune the pore size. The higher the concentration, the more the expansion of water droplets is restricted. As a consequence, the higher the concentration, the smaller the pore size.

The hierarchical porous structure is obtained, However, due to lack of data it is not possible to conclude whether Murray's structure has been obtained. The next step will be to test the hierarchically micro/meso/macroporous structure as cathode for lithium oxygen battery applications.

IV) Electrochemical test

IV.1) Cathode with hierarchical micro/meso/macroporous structure

IV.1.1) Cathode based on zinc oxide nanoparticles

A hierarchically micro/meso/macroporous structure has been synthetised following the instructions in the experimental part and has been tested as cathode in lithium-oxygen batteries. The charge/discharge profiles of the first 4 cycles are shown in Figure 30. The maximum capacity reached is 6 mAh.g^{-1} which is an insufficient performance.

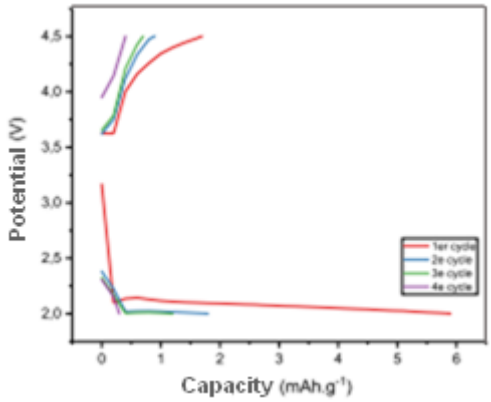

Figure 30: Galvanostatic charge/discharge profiles obtained with a cathode made by porous zinc oxide at 150 mA.g^{-1} within a 2-4.5 V voltage window

To understand that result, the cathode was recovered after the test and analysed by scanning electron microscopy. The SEM micrographs before and after testing are reported in figure 31 and show that the post-cycle structure is destroyed, explaining the low performance of the battery. Most of the initial porosity disappeared to make way for unorganized clusters. This destruction of the structure is due to its fragility, which cannot withstand the mechanical stresses generated by the deposit during the discharge of lithium peroxide.

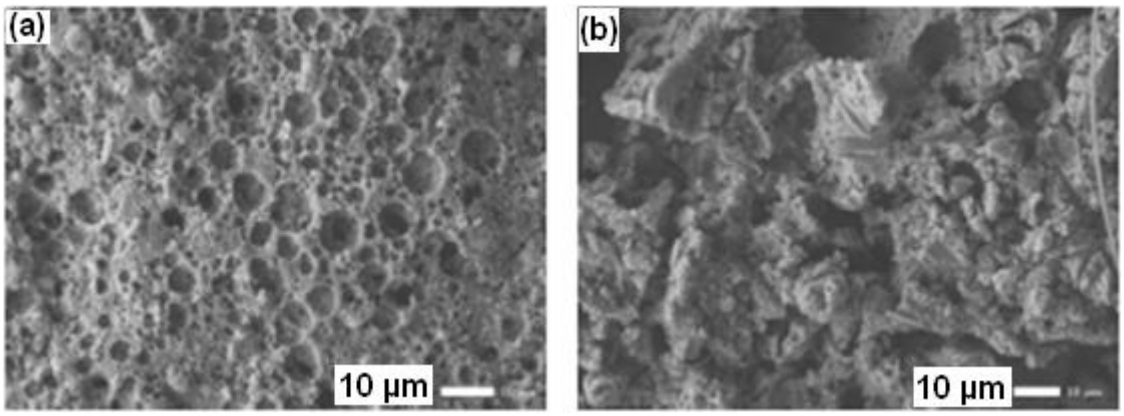

Figure 31: SEM micrographs of porous zinc oxide nanoparticle assembly (a) before and (b) after cycling

In order to reduce the mechanical fragility of the resulting structure, 10 mg.mL^{-1} of poly(vinylidene difluoride) (PVDF) was added into the suspension during the deposition process. PVDF is a conductive polymer that acts as a binder within the structure. The structure and the galvanostatic performances obtained are shown in Figure 32.

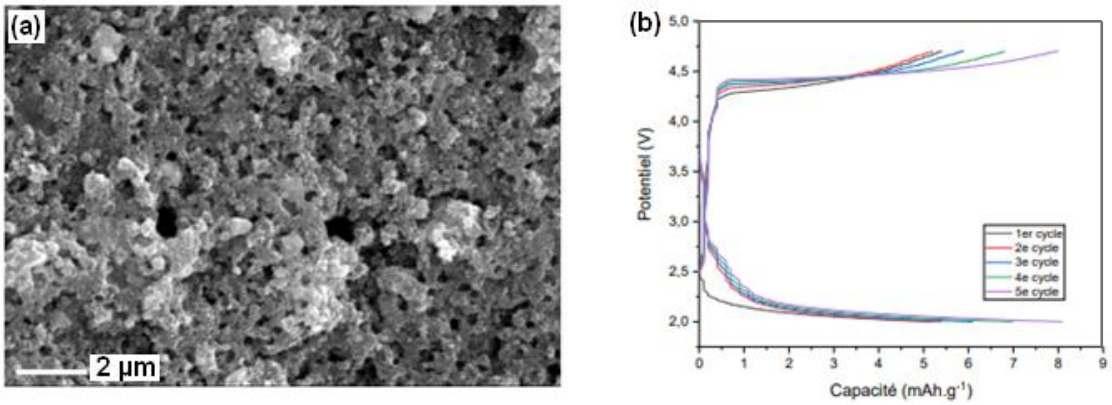

Figure 32: (a) SEM micrograph of the cathode made by porous zinc oxide nanoparticles assembly combined with PVDF, and it's (b) respective galvanic performance at 150 mA.g^{-1} within a 2-4.5 V voltage window

From a morphological point of view, the structure obtained has a poorer organisation and a lower macroporosity than the material without binder. The pores size is smaller. This difference in morphology is explained by the use of the polymer but also by the use of acetone to dissolve the polymer before inserting it into the medium. Acetone is miscible with water, but do not have the same volatility as hexane, and thus, could cause these morphological differences.

The performances obtained with this material are very poor, with a maximum capacity of 8 mAh.g^{-1}. In view of the poor performance obtained and the high fragility of the material, deep optimisation should be realised.

As zinc oxide does not have a high conductivity, and as the material do not allow to reach with battery performances, the same structure has been tested with carbon nanoparticles.

IV.1.2) Cathode based on carbon nanoparticles

Carbon nanoparticles (Commercial Super P, specific surface area 65 m².g^{-1}, micropore: 0.9 nm) were dispersed and assembled according to the same protocol as with zinc oxide nanoparticles. The SEM micrographs are presented in Figure 33. The structure has macropores induced by the water condensation during the solvent evaporation based on the breath figure process. The visible macropores have an average size of 2 µm.

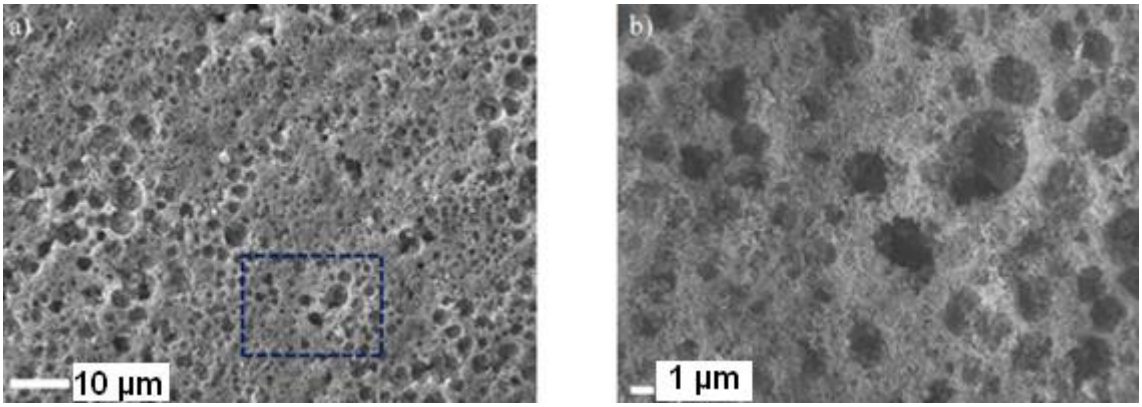

Figure 33: SEM micrographs of the cathode made by porous carbon assembly.

The obtained structure was tested as a cathode in a lithium oxygen battery. To evaluate the impact of the hierarchical porosity of the cathode, a non-porous carbon slurry made of carbon nanoparticles were made and its results were compared to the porous cathode.

The galvanostatic charging and discharging profiles on the first tenth cycles of both cathodes are shown in Figure 34 a,b. The graphs present the evolution of the capacity on charge (top) and on discharge (bottom) as function of the cycle. In the case of the hierarchically micro/meso/macroporous structure, the capacity obtained in the second cycle is much higher than that of the first one. The main hypothesis that would come from the time needed to reach the optimal diffusion of the electrolyte within the cathode. The capacity of the first cycle is 874 mAh.g^{-1} and that of the second is 2236 mAh.g^{-1}, which corresponds to an increase of 110% and 514% compared to the values obtained with batteries made of slurry carbon cathode (416 mAh.g^{-1}). These results show that the porosity of the cathode plays a key role in the performance. But more than the porosity itself, it is the interconnection between the three types of pores, which increases the diffusion of reactants within the cathode, that improves the performance of the battery.

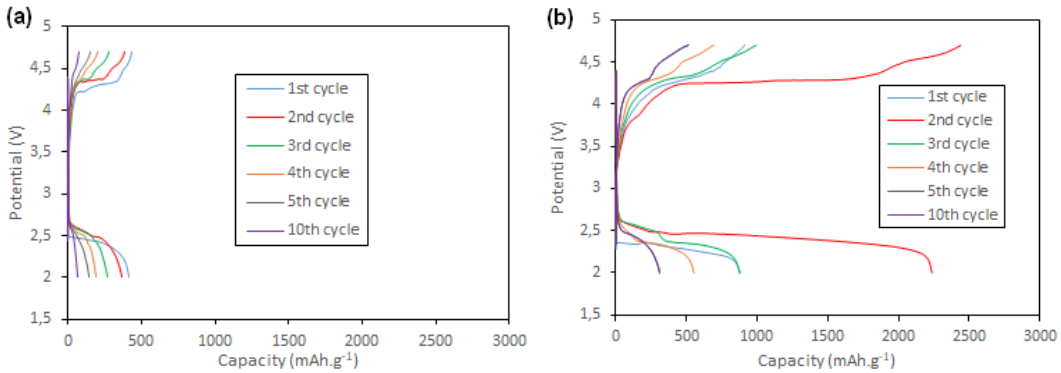

Figure 34: Galvanostatic charge/discharge profiles obtained with (a) a carbon slurry cathode and (b) cathode made by carbon nanoparticles assembly at 150 mA.g^{-1} within a 2-4.7 V voltage window

IV.1.3) Cathode based on carbon nanotubes assembly

A hierarchically micro/meso/macroporous structure was assembled with carbon nanotubes (specific surface area: 114$m^2.g^{-1}$, micropore size: 1.35 nm) using the same method as above. The advantage of carbon nanotubes is that they possess a higher conductivity than carbon nanoparticles, however, in this configuration, they will not be able to arrange themselves optimally to form an optimal hierarchically micro/meso/macroporous structure. The resulting structure is presented in Figure 35, and show a fibrous network with large macropores coming from solvent evaporation.

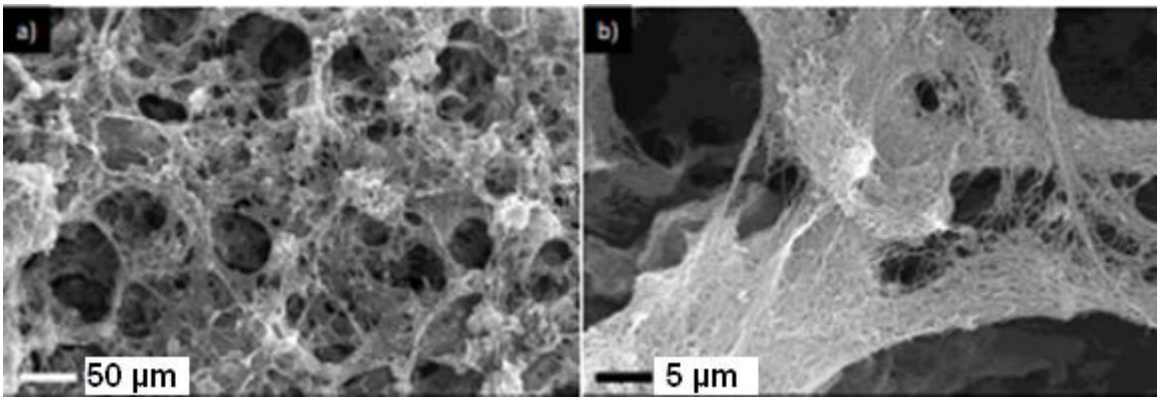

Figure 35: SEM micrographs of the cathode made by carbon nanotube assembly.

This structure has been tested as a cathode within a lithium-oxygen battery, and the results are presented in Figure 36. The galvanostatic charges and discharges show a maximum capacity of 957 $mAh.g^{-1}$, which is 42% more than that obtained with the slurry carbon cathode. This increase in performance is significant but less than the one achieved with carbon nanoparticles (514 %). This difference is probably due to the change in organisation and pore volume from one structure to another and confirms the advantage of using spherical nanoparticles to obtain a hierarchical micro/meso/macroporous structure.

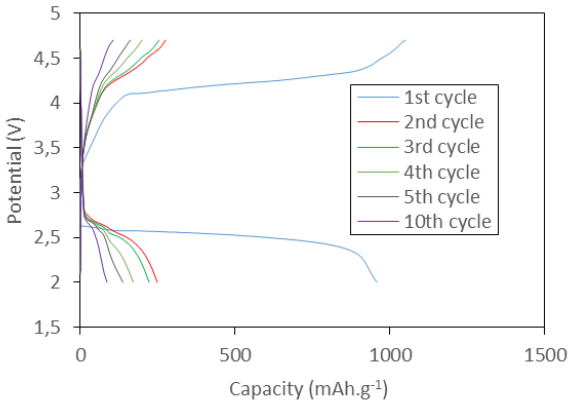

Figure 36: Galvanostatic charge/discharge profiles obtained with a carbon nanotubes assembly cathode at 150 $mA.g^{-1}$ within a 2-4.7 V voltage window

IV.1.4) Cathode based on zinc oxide/carbon assembly and slurry

As previously stated, the use of zinc oxide alone as cathode material for lithium-oxygen batteries does not provide expected results due to the fragility of zinc oxide assembly. In order to study the catalytic capacity of zinc oxide on OER/ORR processes two electrodes were made. The first one were prepared via LBL-EISA from a ZnO nanoparticles, carbon black, and poly(vinylidene difluoride) (PVDF) in a 60 : 30 : 10 weight ratio suspension. The second electrode is a slurry composed of 60% zinc oxide nanoparticles, 30% carbon and 10% PVDF.

The morphology of the cathode synthetised via LBL-EISA were studied by SEM, and the micrograph is shown in Figure 37. This structure doesn't have microporosity. This change in morphology compared to electrodes made of pure carbon or zinc oxide is certainly due to the difference in density between the two particles. When atmospheric water condenses and evaporates during the blast pattern phenomenon, the lighter carbon particles will move faster than the zinc nanoparticles. This difference in diffusion between the two nanoparticles could lead to the reduction or even suppression of macropores.

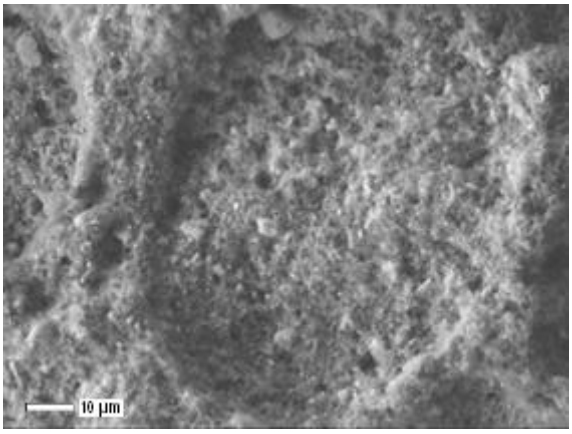

***Figure 37 : S*EM micrographs of the cathode made by a ZnO, C, PVDF, 60 : 30 : 10 weight ratio suspension assembly.**

The resulting charge and discharge profiles obtained with the slurry cathode are presented in Figure 38. It shows that the addition of zinc oxide provides a 500% increase in capacity for the first cycle, reflecting its potential catalytic efficiency for the oxygen evolution and reduction process. One hypothesis is that zinc oxide needs a conductive agent (in this case carbon) in order to influence the kinetic of the OER/ORR processes. However, these mechanisms remain unclear and require further study.

The increase in overpotential and the decrease in capacity could be attributed to degradations occurring during cycling. These degradations lead to the formation of insoluble and insulating product that can accumulate on the cathode surface, reducing electron transfer, increasing the overpotential, and blocking the pores. As the pores are no longer accessible, the formation of lithium peroxide is reduced and leads to a decrease in the capacity.

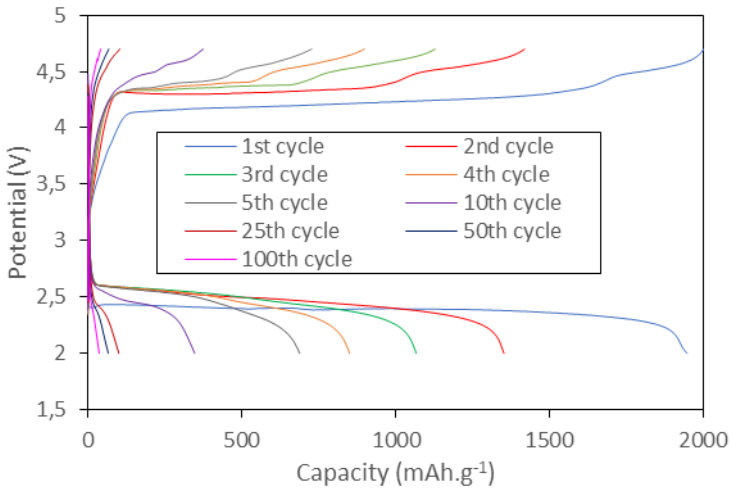

Figure 38: Galvanostatic charge/discharge profiles obtained with a zinc oxide/carbon slurry cathode at 150 mA.g^{-1} within a 2-4.7 V voltage window

In order to check the presence of degradation products, XPS analyses were performed on the zinc oxide/carbon slurry cathode at 10 and 100 cycles. The results are shown in Figure 39. The attribution of the different peaks on the C1s and O1s spectra is done directly on the figure and confirms the presence of lithium carbonate (Li_2CO_3, C1s ~ 290,5 eV, O1s ~ 533 eV). Moreover, the amount of lithium carbonate increased between the tenth and the hundredth cycle. This carbonate mainly comes from the degradation of the electrolyte. The degradation of the electrolyte is confirmed by the presence of the O-C-O (C1s ~ 286 eV, O1s ~ 534 eV) and O-C=O bonds (C1s ~ 288 eV, O1s ~ 534 eV). The full mechanism of electrolyte degradation is presented in Figure 40. Moreover, the presence of lithium peroxide (Li_2O_2 O1s ~ 531 eV) reveals a non-optimal oxidation process during charging which can reflect the limited catalytic activity of zinc oxide.

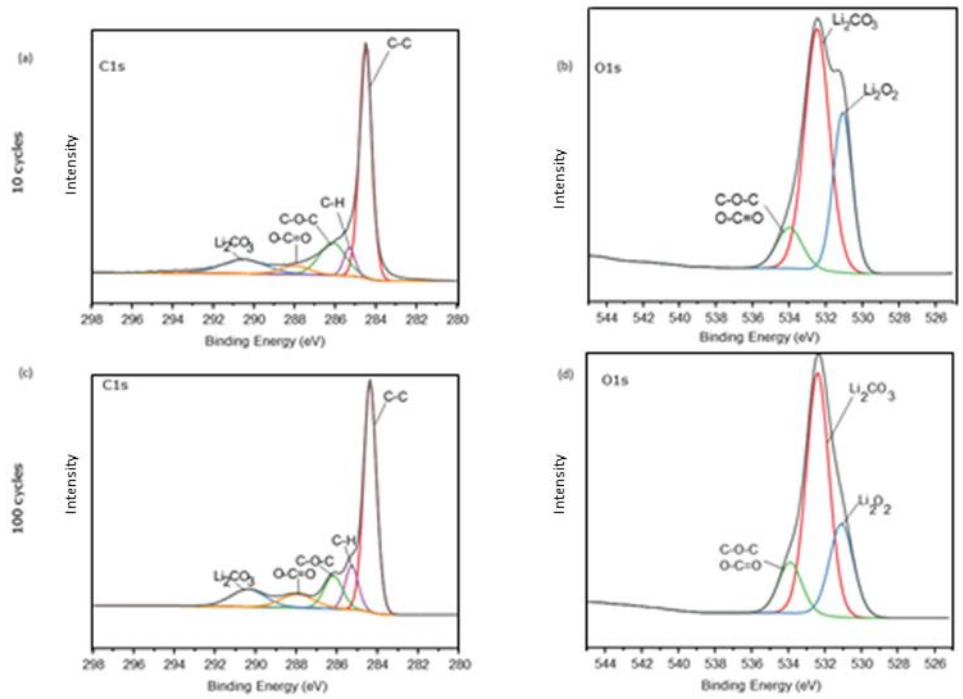

Figure 39: C1s and O1s XPS spectra of (a,b) a zinc oxide/carbon slurry based cathode after 10 cycles, and (c,d) after 100 cycles at 150 mA.g^{-1}

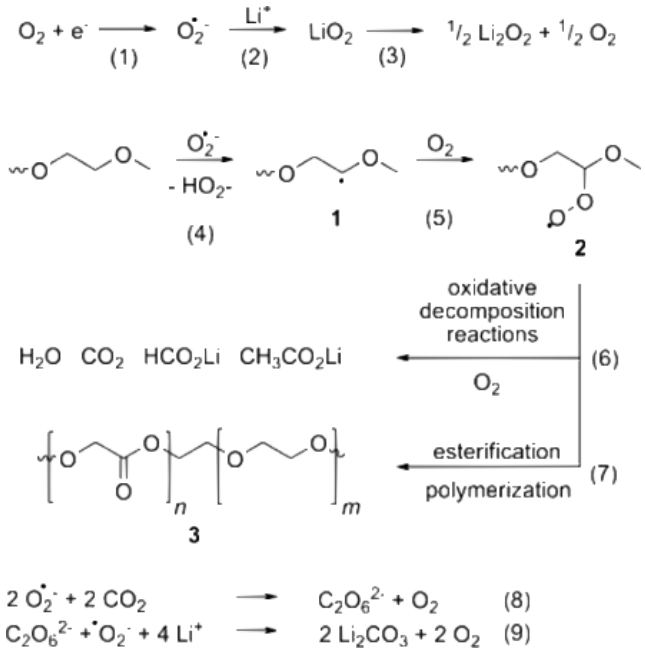

Figure 40: Mechanism of electrolyte degradation.[24]

Conclusion

In summary, we have designed and fabricated a hierarchically micro/meso/macroporous zinc oxide structure. Microporous nanoparticles were synthesized and optimized in order to have a maximum control over their morphology, organisation and porosity. Then, they were suspended in an organic solvent and deposited layer by layer in order to achieve the desired final structure. This zinc oxide structure has been tested as a cathode material in lithium-oxygen batteries but did not give expected results due to its high brittleness.

The same structure was assembled from carbon nanoparticles and carbon nanotubes and led to an increase in capacity at the first cycle of 110% compared to a carbon slurry-based cathode without hierarchical structure. These results confirm the importance of the cathode structure evoked during the introduction; indeed, the presence of hierarchical porosity leads to an increase in the specific surface area and greater diffusion of reagents improving the formation of lithium peroxide and leading to a higher capacity.

Finally, a carbon and zinc oxide slurry-based cathode were prepared in order to increase the conductivity and to evaluate the catalytic activity of zinc oxide. Capacity results showed an improvement of nearly 500% on the first cycle, revealing the activity of zinc oxide on both oxidation and reduction processes. However, the presence of lithium peroxide found by XPS analysis suggests that this catalytic activity is limited.

This work highlighted the impact of Murray's structure on the battery's capacity. This structure led to a greater diffusion of electrolyte and oxygen, which increased the amount of lithium peroxide formed during discharge. It is now established that the Murray structure has significant advantages when used as a cathode in lithium-oxygen batteries. However, the fragility of the Murray's structure limits its use. A possible way to consolidate this structure would be to sinter it. Sintering consists of increasing the mechanical properties of the material by densification.[28] It can be defined as the consolidation, under the action of heat, of a granular structure without its total fusion. However, the densification of the structure can lead to a decrease in porosity and should be taken into account with regard to Murray's structure.

The next step of the study will be to evaluate the catalytic activity of metal oxides from 3d metals in order to determine their performance within cathodes for lithium oxygen batteries.

Bibliography

1 Bruce.P.G, Freunberger.S.A, Hardwick.L.J and Tarascon.J.M, *Nat. Mater*, 2012, **11**, 19–29.

2 Bhatt.M.D, Geaney.H, Nolan.M and O'Dwyer.C, Phys. Chem. Chem. Phys., 2014,**16**, 12093-12130.

3 Girishkumar.G *et al*, *J. Phys. Chem. Lett*, 2010, **1**.

4 Abraham.K.M and Jiang.Z, *J. Electrochem. Soc*, 1996, **143**,1.

5 OttakamThotiyl.M.M, Freunberger.S.A, Peng.Z, Bruce.P.G, *J.Am.Chem.Soc*, 2013, **135**, 494–500.

6 Itkis.D.M, Semenenko.D.A, Kataev.E.Y, Belova.A.I, Neudachina.V.S, Sirotina.A.P, Hävecker.M, Teschner.D, Knop-Gericke.A, Dudin.P, Barinov.A, Goodilin.E.A, Shao-Horn.Y, Yashina.L.V, *Nano Lett*, 2013, **13**, 4697−4701.

7 Freunberger.S.A, Chen.Y, Peng.Z, Griffin.J.M, Hardwick.L.J, Bardé.F, Novák.P, Bruce.P.G, *J. Am. Chem. Soc*, 2011, **133**, 8040–8047.

8 Balaish.M, Kraytsberg.A, Ein-Eli.Y, *Phys Chem Chem Phys*, 2014,**16**, 2801-2822

9 Younesi.R, Urbonaite.S, Edström.K and Hahlin.M, *J. Phys. Chem. C*, 2012, **116**, 20673–20680.

10 Johnson.L, Li.C, Liu.Z et al, *Nature Chem,* 2014*,* **6**, 1091–1099.

11 Adams.B.D, Radtke.C, Black.R, Trudeau.M.L, Zaghib.K, Nazar.L.F, *Energy Environ. Sci*, 2013, **6**, 1772-1778.

12 Li.X, Faghri.A, *J. Electrochem. Soc*, 2012, **159**, A1747-1754.

13 Shapatsombut.U, Cheng.H, Scott.K, *J. Power. Sources*, 2013, **227**, 243-253.

14 Xiao.J, Mei.D, Li.X, Xu.W, Wang.D, Graff.G.L, Bennett.W.D, Nie.Z, Saraf.L.V, Aksay.I.A, Liu.J, and Zhang.J.G, *Nano Lett*, 2011, **11**, 5071.

15 Z. Guo.Z, Zhou.D, Dong.X, Qiu.Z, Wang.Y, and Xia.Y, *Adv. Mater*,2013, **25**, 5668.

16 Park.J.B, Lee.L, Yoon.C.S, and Sun.Y.K, *ACS Appl. Mater. Interfaces*,2013, **5**, 13426.

17 Younesi.R, Singh.N, Urbonaite.S, and Edström.K, *ECS Trans*,2010, **25**, 121.

18 Xie.J, Yao.X, Cheng.Q, Madden.I.P, Dornath.P, Chang.C, Fan.W, and Wang.D, Angew. *Chem. Int. Ed*, 2015, **54**, 4299

19 Zheng.X, Shen.G, Wang.C, Li.Y, Dunphy.D, Hasan.T, Brinker.C.J, Su.B.L, *Nat.Commun*, 2017, **8**, 1–9.

20 Jeong.M.G, Kwak.W.J, Islam.M, Park.J, Byon.H.R, Jang.M, Sun.Y.K, Jung.H.G, *Journal of The Electrochemical Society*, 2019, 166, **4**, A455-A463.21

21 Murray.C.D, *PNAS*, 1926, **12**, (3), 207-214

22 Rosenberg.E*, Journal of Theoritical Biology*, 2021, **512**, 11.563

23 Zheng.X, Shen.G, Li.Y, Duan.H, Yang.X, Huang.S, Wang.H, Wang.C, Deng.Z, Su.B.L, J*. Mater. Chem. A*, 2013,**1**, 1394–1400.

24 Kim.T, Jung.Y.K, Lee.J.K, *J. Mater. Chem. C*, 2014, **2**, 5593–5600.

25 Nguyen.T, Thanh.K, Maclean.N, Mahiddine.S, *Chem. Rev,* 2014, **114**, 15, 7610–7630.

26 Javed.R, Zia.M, Naz.S et al, *J Nanobiotechnol, 2020,* **18,** 172.

27 Sharifi Dehsari.H, Halda Ribeiro.A, Ersöz.B, Tremel.W, Jakob.G, Asadi.K, *CrystEngComm*, 2017, **19**, 6694–6702.

28 Durand.G.R, Bizot.Q, Herbert.N, Quemere.S, Pasturel.M, Zhang.X.H, and Merdrignac-Conanec.O, *Journal of the American Ceramic Society*, 2019, **103**, 4, 2328-2339.

Figure Table

Figure 1 : Experimental conditions of the formation of zinc oxide from zinc acetylacetonate and oleylamine..... 88
Figure 2 : Assembly of the different battery elements: (a) lithium disc, (b) glass fibre separator soaked in electrolyte, (c) cathode, (d) perforated steel plate, (e) compression spring, (f) top part and (g) assembled battery...... 89
Figure 3: Scheme representing the Breath Figure phenomenon 92
Figure 4: Schematic representing the interconnections between pores in the Murray structure 92
Figure 5: Reaction mechanism for the formation of zinc oxide from zinc acetylacetonate and oleylamine (R = C_8H_{16}-CH--CH-C_8H_{17}) 93
Figure 6: Diffractograms of nanoparticles obtained at different reaction temperatures in the formation of zinc hydroxide: (a) 80 °C, (b) 100 °C, (c) 125 °C and (d) 150 °C. 94
Figure 7: TEM micrographs of nanoparticles obtained at different reaction temperatures in the formation of zinc hydroxide: (a) 80 °C, (b) 100 °C, (c) 125 °C and (d) 150 °C. The arrows show micropores. 95
Figure 8: Nitrogen adsorption and desorption isotherms and micropore size distribution for ZnO nanoparticles obtained at different temperatures during zinc hydroxide formation: (a) 80 °C, (b) 100 °C, (c) 125 °C and (d) 150 °C. 96
Figure 9: Diffractograms of nanoparticles obtained at different reaction time of zinc hydroxide formation: (a) 30 min, (b) 60 min, and (c) 90 min 97
Figure 10: TEM micrographs of nanoparticles obtained at different reaction times of the zinc hydroxide formation: (a) 30 min, (b) 60 min, and (c) 90 min. The arrows show micropores. 97
Figure 11: Nitrogen adsorption and desorption isotherms and micropore size distribution for ZnO nanoparticles obtained at different reaction times of the zinc hydroxide formation: (a) 30 min, (b) 60 min, (c) 90 min 98
Figure 12: Diffractograms of nanoparticles obtained at different temperature in the formation of zinc oxide: (a) 80°C, (b) 100°C, (c) 125°C and (d) 150°C. 99
Figure 13: TEM micrographs of nanoparticles obtained at different temperature in the formation of zinc oxide: (a) 80°C, (b) 100°C, (c) 125°C and (d) 150°C. The arrows show micropores. 99
Figure 14: Nitrogen adsorption and desorption isotherms and micropore size distribution for ZnO nanoparticles obtained at different temperature during zinc oxide formation: (a) 80°C, (b) 100°C, (c) 125°C (d) 150°C 100
Figure 15: Diffractograms of nanoparticles obtained at different reaction times of the formation of zinc oxide: (a) 30 min, (b) 40 min, (c) 50 min and (d) 60 min. 101

Figure 16: TEM micrographs of nanoparticles obtained at different reaction times of the formation of zinc oxide: (a) 30 min, (b) 40 min, (c) 50 min and (d) 60 min 101
Figure 17: Nitrogen adsorption and desorption isotherms and micropore size distribution for ZnO nanoparticles obtained at different reaction times during zinc oxide formation: (a) 30 min, (b) 40 min, (c) 50 min and (d) 60 min 102
Figure 18: Representation of the interaction between TPP and zinc atoms on the surface of nanoparticles (yellow is for P, blue for Zn, red for O, black for C, and white for H). 103
Figure 19: Diffractograms of ZnO nanoparticles obtained with different TPP concentration: (a) 0 mM, (b) 77 mM, (c) 153 mM and (d) 229 mM. 103
Figure 20: TEM micrographs of ZnO nanoparticles obtained using different TPP concentration: (a) 0 mM, (b) 77 mM, (c) 153 mM and (d) 229 mM. 104
Figure 21: Nitrogen adsorption and desorption isotherms and micropore size distribution for ZnO nanoparticles obtained using different TPP concentration: (a) 0 mM, (b) 77 mM, (c) 153 mM and (d) 229 mM. 105
Figure 22: Diffractograms of ZnO nanoparticles obtained using different zinc precursor concentrations: (a) 42 mM, (b) 33 mM, (c) 27 mM, (d) 22 mM. (d) 20 mM. and (f) 15 mM. 106
Figure 23: TEM micrographs of ZnO nanoparticles obtained using different zinc precursor concentration: (a) 42 mM, (b) 33 mM, (c) 27 mM, (d) 22 mM. (d) 20 mM. and (f) 15 mM. 107
Figure 24: (a) Evolution of particle size and (b) specific surface area as a function of zinc precursor concentration with standard deviations 107
Figure 25: Nitrogen adsorption and desorption isotherms and micropore size distribution for ZnO nanoparticles obtained using different zinc precursor concentration: a) 42 mM, (b) 33 mM, (c) 27 mM, (d) 22 mM. (d) 20 mM. and (f) 15 mM. 109
Figure 26: TEM micrographs of nanoparticle deposits made from suspensions of different concentrations: (a) 0.5 mg.mL^{-1}, (b) 1 mg.mL^{-1}, and (c) 2.5 mg.mL^{-1} 111
Figure 27: SEM micrographs and macropore size distribution of porous structure made from suspensions of different concentrations: (a) 2.5 mg.mL^{-1}, (b) 5 mg.mL^{-1}, (c) 7.5 mg.mL^{-1} and (d) 10 mg.mL^{-1} 113
Figure 28: TEM micrographs of nanoparticle deposits made from a 2.5 mg.mL^{-1} suspensions at different relative humidity levels: (a) 60%, (b) 70%, and (c) 80% 114
Figure 29:SEM micrographs and macropore size distribution of porous structure made from a 2.5 mg.mL^{-1} suspensions at different relative humidity levels: (a,b) 40%, (c,d) 50%, (e,f) 60%, (g,h) 70%, and (I,j) 80% 115
Figure 30: Galvanostatic charge/discharge profiles obtained with a cathode made by porous zinc oxide at 150 mA.g^{-1} within a 2-4.5 V voltage window 117
Figure 31: SEM micrographs of porous zinc oxide nanoparticle assembly (a) before and (b) after cycling 117
Figure 32: (a) SEM micrograph of the cathode made by porous zinc oxide nanoparticles assembly combined with PVDF, and it's (b) respective galvanic performance at 150 mA.g^{-1} within a 2-4.5 V voltage window 118
Figure 33: SEM micrographs of the cathode made by porous carbon assembly. 119
Figure 34: Galvanostatic charge/discharge profiles obtained with (a) a carbon slurry cathode and (b) cathode made by carbon nanoparticles assembly at 150 mA.g^{-1} within a 2-4.7 V voltage window 119
Figure 35: SEM micrographs of the cathode made by carbon nanotube assembly. 120
Figure 36: Galvanostatic charge/discharge profiles obtained with a carbon nanotubes assembly cathode at 150 mA.g^{-1} within a 2-4.7 V voltage window 120

Figure 37 : SEM micrographs of the cathode made by a ZnO, C, PVDF, 60 : 30 : 10 weight ratio suspension assembly. 121
Figure 38: Galvanostatic charge/discharge profiles obtained with a zinc oxide/carbon slurry cathode at 150 mA.g^{-1} within a 2-4.7 V voltage window 122
Figure 39: C1s and O1s XPS spectra of (a,b) a zinc oxide/carbon slurry based cathode after 10 cycles, and (c,d) after 100 cycles at 150 mA.g^{-1} 123
Figure 40: Mechanism of electrolyte degradation.[24] 123

Chapter 4: 3d metal oxides as cathode materials for Li-O_2 batteries

Abstract:

The expansion and growth of new energy-intensive industries is leading to the development of new devices to ensure optimal storage and distribution of energy sources such as electricity. Li-ion batteries have an energy density of (≈400 W.h.kg^{-1}). Under the best of conditions this type of battery is only likely to increase this performance by a factor of 2. The use of Li-O_2 batteries could allow the capacity to be multiplied by 5 to 10 compared to Li-ion. Here, we explore the influence of 3d metal oxides as cathode material on the performance of a non-aqueous Li-O_2 battery. Of all the metal oxides studied, the highest initial capacity was observed with TiO_2 (6448 mAh.g^{-1}), the lowest overpotential with Co_3O_4(1.464 V) and the highest cycle number at 500 mAh.g^{-1} with Mn_3O_4 (417 cycles).

Introduction

Nowadays, the increase in energy consumption, especially electricity consumption, has exploded and is mainly due to the intensification and expansion of new resource-demanding industries. The explosion of these demands has led to the requirement for new devices to ensure optimal storage and distribution of sources.[1,2]

Among those, lithium-ion batteries stand out owing to their energy density (≈400 W.h.kg^{-1}), which is significantly higher than those of nickel-cadmium batteries (≈60 W.h.kg^{-1}) and lead-acid batteries (≈40 W.h.kg^{-1}). [3,4] However, the energy density of lithium-ion batteries remains insufficient compared to thermal appliances with energy densities equal to 13,000 W.h.kg^{-1}.[5] Recently, aprotic lithium-oxygen batteries have attracted intensive attention, owing to their high theoretical energy density of 11,680 W.h.kg^{-1} surpassing lithium-ion batteries.[6-7] This technology is governed by the reversible chemical reaction Li + O_2 ↔ Li_2O_2 and, the redox couple is characterized by a high specific energy due to a low atomic mass of the both reactants and a potential of 3.0 V.[7]

Nevertheless, the practical energy density is still far from the theoretical value.[8] The most important challenge to overcome on the air electrode is the high polarisation induced by the high activation energy needed to produce and oxidise Li_2O_2 during cycling. Therefore, it is necessary to create a chemically stable porous cathode with an efficient conductivity and catalytic activity able to reduce the polarisation and the activation energy of oxygen reduction (ORR) and/or evolution (OER). [6]

Carbon materials have been widely used in these cathodes mainly for their light weight, low cost and good electrical conductivity.[9-13] Unfortunately, the catalytic activity of carbon materials regarding the OER/ORR processes is low and can be the origin of many degradations within the battery leading to the formation of insoluble species such as lithium carbonate. The latter will passivate the cathode and obstruct the electron flow leading to an increase in voltage, and consequently, to an elevation of the overvoltage which will degrade the electrolyte during charging.[14-16]

The stabilization of the cathode is thus of prime importance. It is necessary to investigate the relationship between catalytic activity and electric conduction in the electrocatalytic processes. Transition metal oxides have attracted interest as a catalyst for their low cost and outstanding catalytic activity. [17-18]

Bruce *et al*. studied the catalytic effect of several metal oxides on the electrochemical properties of the battery (Fe_2O_3, NiO, Fe_3O_4, NiO, Co_3O_4 and CuO). They found that these oxides assist the reduction of O_2 to O_2^{2-} and its subsequent oxidation. This catalytic effect leads to the reduction of overpotential and maximise the capacity of the battery. Consequently, they have shown that the use of 2.5% manganese dioxide in a carbon matrix decreases the charging voltage of 0.5 V and increased the retention of capacity on cycling. This study also illustrated that iron oxide Fe_3O_4 allows a good capacity retention and that cobalt oxide Co_3O_4 allows the best compromise between discharge capacity and retention on cycling. [19]

Recent study by *Kim et al* investigated via cyclic voltammetry the effect of carbon nanotubes-bridged hollow Fe_2O_3 nanoparticles (H-Fe_2O_3/ CNT) on the specific electrochemical reactions of Li–O_2 cells. Redox and currents peaks of H-Fe_2O_3/ CNT are much higher than those of carbon black (KB) electrode indicating that OER and ORR processes are more reversible, confirming the good catalytic activity of

the hollow Fe_2O_3 nanoparticles. As regards battery performance, the activity of the catalyst leads to a decrease of the overpotential at charge of 0.47 V. [20]

10 wt% vanadium oxide were introduced within a black carbon matrix by Yoon et al, and a maximum capacity of 2,260 mA h g^{-1} can be achieved. Moreover, the overpotential has decreased compared to the pure carbon reference electrode, revealing the catalytic efficiency of V_2O_5 for the reaction between Li^+ and O_2. [21] The incorporation of 30 wt% titanium dioxide in form of microspheres into carbon nanotubes can increase capacity from 1794 to 6590 mAh g^{-1} with a reduction of the overpotential by 0.25 V. [22] Although metal oxides show clearly very promising results, it is very difficult to draw an evident comparison as the experimental conditions are different. No comprehensive study on the relationship between physicochemical behaviour of metal oxides and their performances as electrode materials in Li-O_2 batteries were done.

In this work, we propose to investigate the behaviour of 3d transition metal oxides (MOx = Cr_2O_3, Cu_2O, CuO, CoO, Co_3O_4, Fe_3O_4, Fe_2O_3, MnO, MnO_2, Mn_2O_3, Mn_3O_4, NiO, Sc_2O_3, TiO_2, VO_2, V_2O_5 and ZnO) as cathode materials. The combination of the catalytic function for the oxygen evolution and the oxygen reduction reaction and the electric conduction resulting in the electrocatalytic effect in the Li-O_2 cell is evaluated. Of all the metal oxides studied, the highest initial capacity was observed with TiO_2 (6448 mAh.g^{-1}), the lowest overpotential with Co_3O_4(1.559 V) and the highest cycle number at 500 mAh.g^{-1} with Mn_3O_4 (417 cycles). This study aims to screen a number of 3d metal oxides as cathode material to establish which ones give promising performance, and can be used as a basis for further investigation. Amongst these investigations several suggestions can emerge: the first one would be to select a 3d metal oxide regarding their electrochemical characteristics according to the desired experimental conditions. Secondly, it would be worthwhile to modify the shape of the catalysts to maximise the formation and decomposition of lithium peroxide. Finally, it would be interesting to create a metal oxide coating on a hierarchical carbon base to enhance the electrochemical reaction during the charge-discharge cycles to improve the performance of the battery.

Results and discussion

3d metal oxides have been prepared by different processes taken and adapted from the literature such as mild temperature organic solution reaction and sol-gel process. The details of these syntheses are described in the experimental part and the reaction mechanisms of the synthesis are available in the supporting information (Figure S1). Moreover, the absence of organic impurities coming from the mild reaction mixture in the final nanoparticles has been confirmed by infrared analysis (Figure S2).

The crystallinity and crystalline phase of obtained materials were studied by X-ray diffraction. The diffractograms are shown in Figure 1 and confirm that all the obtained 3d metal oxides are well crystalline. These metal oxides can be divided into six main categories according to their geometrical systems which are summarised in Table 1.

The morphology of the obtained particles was studied by transmission electronic microscopy (TEM) (Figure 2). All particles are nano-sized. Most of them have spherical shapes except for Mn_3O_4 (Figure 2k) and V_2O_5 (Figure 2p), which have a cubical shape. The average size of nanoparticles was determined by statistical counting on a population of 300 and is reported in Table 1. Micropores are observable within CoO (Figure 2a) and ZnO nanoparticles (Figure 2b). Nitrogen physisorption analysis was performed (Figure S3) and confirmed the presence of micropores. The isotherms obtained are characteristic of mesoporous materials. These mesopores are induced by the random assembly of nanoparticles. The H3 type hysteresis indicates a slit-like pore shape. The specific surface area for each metal oxide, was determined via Brunauer, Emmett and Teller (BET) method and summarised in Table 1.

Physical properties of 3d metal oxides such as morphology, particle size, surface area could impact the performances of the battery. As the formation of lithium peroxide during discharge takes place on the surface of the cathode. It will be interesting to try to link the capacities obtained with each battery to the specific surface of the nanoparticles.

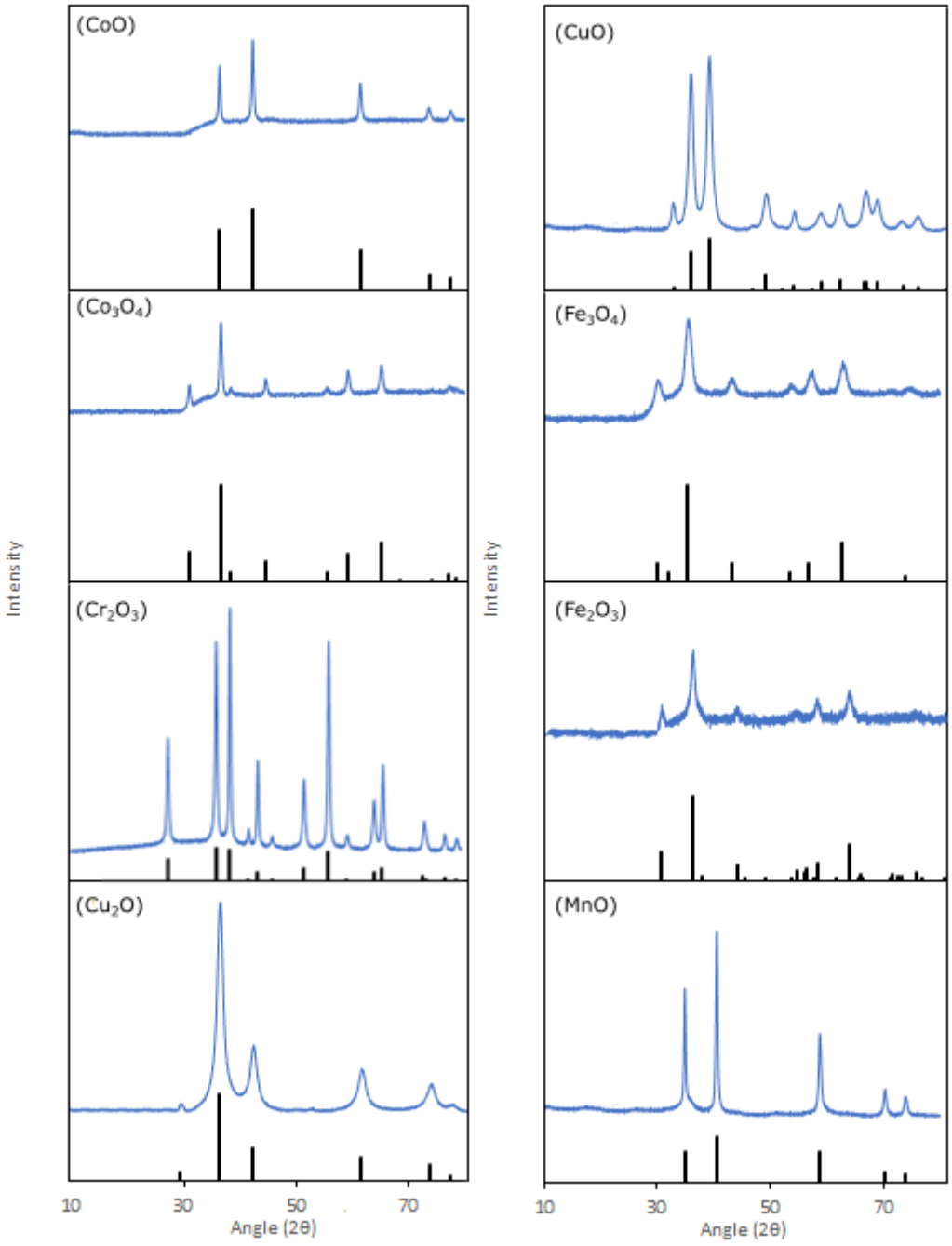
(CoO)
(Co3O4)
(Cr2O3)
(Cu2O)
(CuO)
(Fe3O4)
(Fe2O3)
(MnO)
Intensity
Intensity
10
30
50
70
Angle (2θ)
10
30
50
70
Angle (2θ)

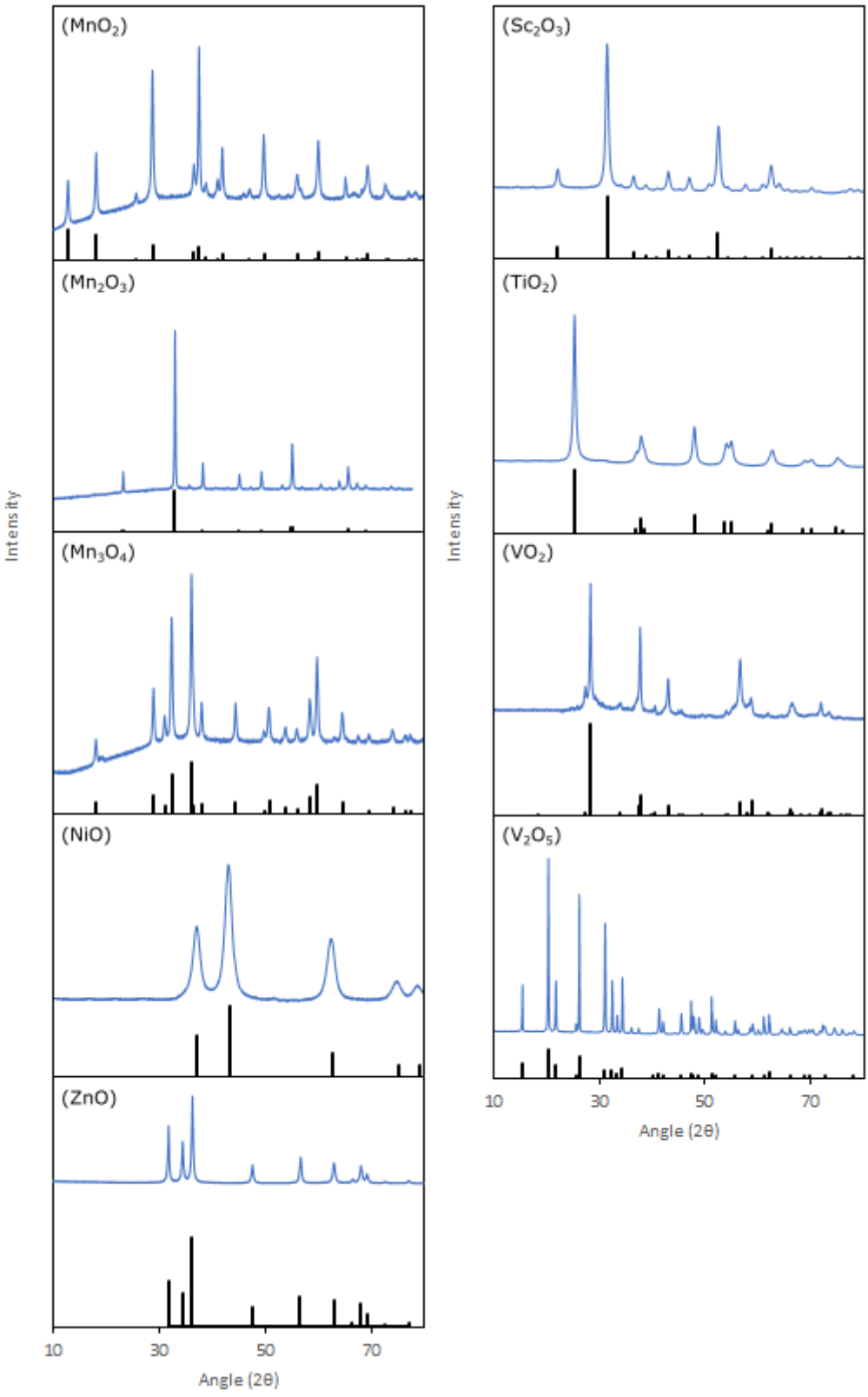

Figure 1: ***Powder X-ray diffraction pattern of the as synthesized CoO, Co_3O_4, Cr_2O_3, Cu_2O, CuO, Fe_3O_4, Fe_2O_3, MnO, MnO_2, Mn_2O_3, Mn_3O_4, NiO, Sc_2O_3, TiO_2, VO_2, V_2O_5 and ZnO (blue) with their references (black).***

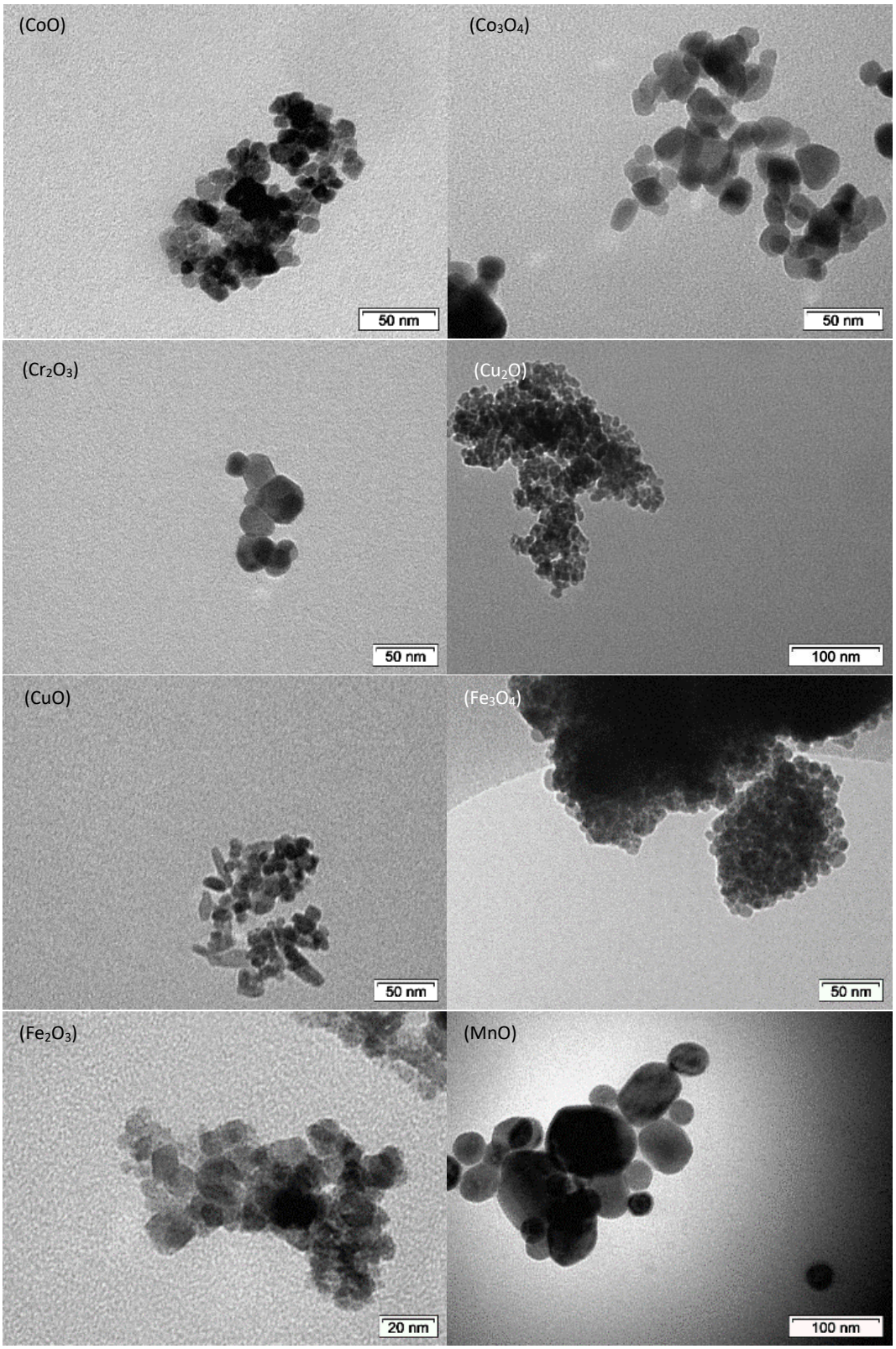
(CoO)
50 nm
(Co_3O_4)
50 nm
(Cr_2O_3)
50 nm
(Cu_2O)
100 nm
(CuO)
50 nm
(Fe_3O_4)
50 nm
(Fe_2O_3)
20 nm
(MnO)
100 nm

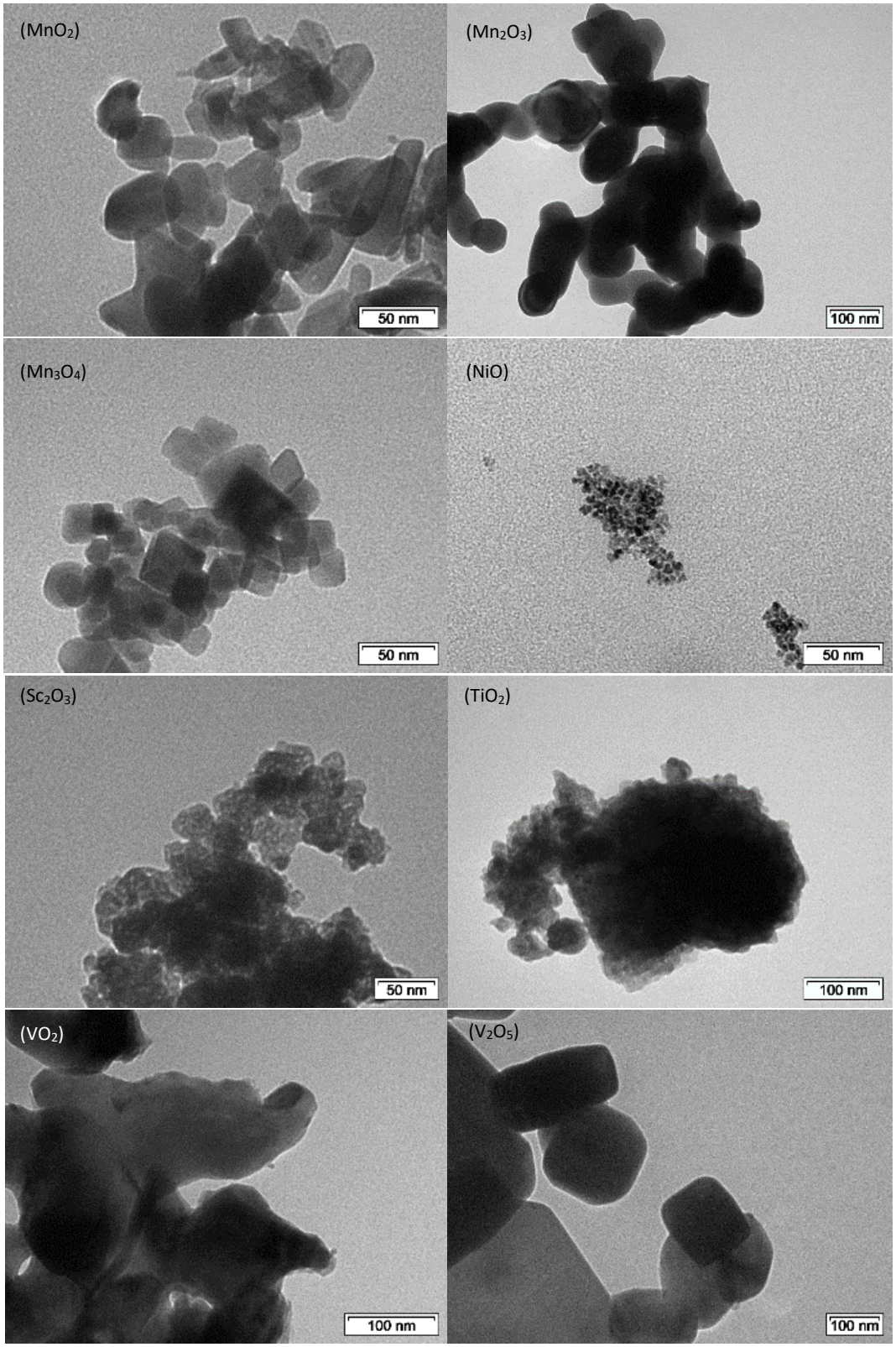
(MnO_2)
50 nm
(Mn_2O_3)
100 nm
(Mn_3O_4)
50 nm
(NiO)
50 nm
(Sc_2O_3)
50 nm
(TiO_2)
100 nm
(VO_2)
100 nm
(V_2O_5)
100 nm

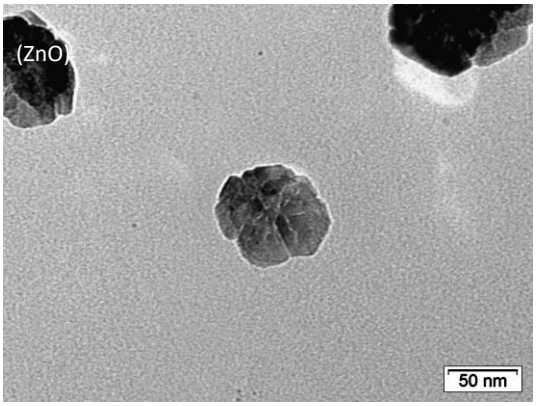

Figure 2: Bright-field TEM micrographs demonstrating morphology and particle size distribution of the as-synthetized metal oxide nanoparticles CoO, Co_3O_4, Cr_2O_3, Cu_2O, CuO, Fe_3O_4, Fe_2O_3, MnO, MnO_2, Mn_2O_3, Mn_3O_4, NiO, Sc_2O_3, TiO_2, VO_2, V_2O_5, ZnO.

Table 1: Summary of all crystalline system, space group, nanoparticle and micropore size, and specific surface area of the as synthetised metal oxides.

Metal Oxide	System	Space Group	Nanoparticle size (nm)	Micropores size (nm)	Specific Surface Area ($m^2.g^{-1}$)
Sc_2O_3	Cubic	Ia-3	81		18
TiO_2	Tetragonal	$I4_1/amd$	232		49
VO_2	Monoclinic	C2/m	400		14
V_2O_5	Orthorhombic	Pmn2	400		13
Cr_2O_3	Trigonal	R-3c	28		38
MnO	Cubic	Fm-3m	76		20
MnO_2	Tetragonal	I4/m	75		51
Mn_2O_3	Orthorhombic	Pbca	144		10
Mn_3O_4	Tetragonal	$I4_1/amd$	55		22
Fe_2O_3	Tetragonal	$P4_12_12$	12		133
Fe_3O_4	Cubic	Fd-3m	75		8
CoO	Cubic	Fm-3m	55	1.89	18
Co_3O_4	Cubic	F-43m	19		42
NiO	Cubic	Fm-3m	5		71
Cu_2O	Cubic	Pn.3n	75		16
CuO	Monoclinic	C2/c	17		62
ZnO	Hexagonal	$P6_3mc$	95	1.49	16

Electrochemical studies

The catalytic activity of metal oxides on OER/ORR process is a key to improve the performance of lithium oxygen batteries. In aprotic Li-O_2 batteries, MOx/Carbon materials do not act as a conventional electrocatalyst to lower the activation energy through electron transfer. They act as a promoter to improve the surface transport of Li_xO_2 species, by reducing their binding energy during electrochemical processes. Luntz et al. [23] were the first to observe this phenomenon and it was confirmed a few years later by Nazar et al. [24] Metal oxides have fewer dangling bonds and thus have less affinity for superoxide than carbon. This property will increase the mass surface transport of Li_xO_2 species and hence the reaction kinetics at the electrode surface. During the reduction process, Li_xO_2 is formed on the surface of the carbon, and the mobility of this peroxide is enhanced by the presence of MOx, which improves the kinetics of formation of Li_2O_2.

Specific electrochemical reactions of Li–O_2 cells, involving 3d metal oxides and carbon super P (SP) (reference sample) electrodes, were examined by cyclic voltammetry (CV). The results obtained are reported in Figure 3. Cyclic voltammograms are generally described into two parts: the reduction peak, also known as the result of the ORR process, and the oxidation peak being that of the OER process. The current of the two first oxidation and reduction is reported in Table 2.

Table 2: First two oxidation and reduction current observed for all 3d metal oxides used as cathode in Li-O_2 batteries.

	ORR 1st peak ($A.g^{-1}$)	ORR 2nd peak ($A.g^{-1}$)	OER 1st peak ($A.g^{-1}$)	OER 2nd peak ($A.g^{-1}$)
CoO	-3.12	-2.80	10.1	9.72
Co_3O_4	-2.39	-2.12	2.19	2.01
Cr_2O_3	-1.06	-0.68	1.22	0.66
Cu_2O	-1.63	-1.23	1.44	0.76
CuO	-4.75	-3.24	3.55	3.01
Fe_3O_4	-2.56	-2.51	0.77	0.76
Fe_2O_3	-3.04	-2.32	1.08	0.90
MnO	-3.16	-2.79	0.94	0.72
MnO_2	-2.25	-2.01	2.29	2.28
Mn_2O_3	-2.44	-1.83	1.22	0.96
Mn_3O_4	-1.59	-1.56	1.96	1.95
NiO	-1.96	-1.67	1.95	1.52
Sc_2O_3	-3.22	-2.35	0.96	0.95
TiO_2	-3.69	-2.60	1.19	0.87
VO_2	-3.11	-2.50	0.86	0.58
V_2O_5	-1.87	-1.75	0.91	0.53
ZnO	-	-	0.04	0.04
C	-2.50	-1.09	1.80	0.89

The initial reduction peak of MOx and SP cathodes is located at the same position indicating an identical electrochemical reaction ($2\ Li^+ + O_2 + 2e^- \Rightarrow Li_2O_2$). The lower the current, the higher the kinetics of the oxygen reduction reaction. A lower reduction current is observed for Sc_2O_3, Fe_3O_4, Fe_2O_3, TiO_2, VO_2, CoO, CuO, and MnO, electrodes which reflects a faster ORR kinetics over SP cathode. The lowest current is observed with the CuO electrode indicating its fastest ORR kinetic. Cr_2O_3

electrode has a higher current than the reference throughout the test, indicative of a slower kinetic for the oxygen evolution reaction.

The maximum oxidation peak observed for MOx and SP cathodes is located around 4V and refer to the $Li_2O_2 \Rightarrow 2Li^+ + 2\ e^- + O_2$ electrochemical reaction. Initially, NiO, CoO, CuO, MnO_2, Mn_2O_3, and Co_3O_4 electrodes exhibit a sharper and larger peak area which shows a faster OER kinetics over SP cathode. It is interesting to note that the peak obtained with the CoO electrode is significantly higher than that of the other MOx cathodes, illustrating a high influence on the OER kinetic of CoO. From the second cycle, almost all MOx cathode exhibit a higher current than the SP cathode and confirm their faster OER kinetics over SP cathode induced by the MOx catalyst. Cyclic voltammograms of the electrode made by ZnO (Figure 3q) has no oxidation and reduction peaks. It does not have positive effect on the OER/ORR kinetics. On the contrary, the addition of CoO and CuO in the Super P carbon matrix allowed to increase the kinetics of the oxygen evolution and reduction reaction. This increase in kinetics leads to a better formation and decomposition of lithium peroxide and consequently increase the reversibility of the process.

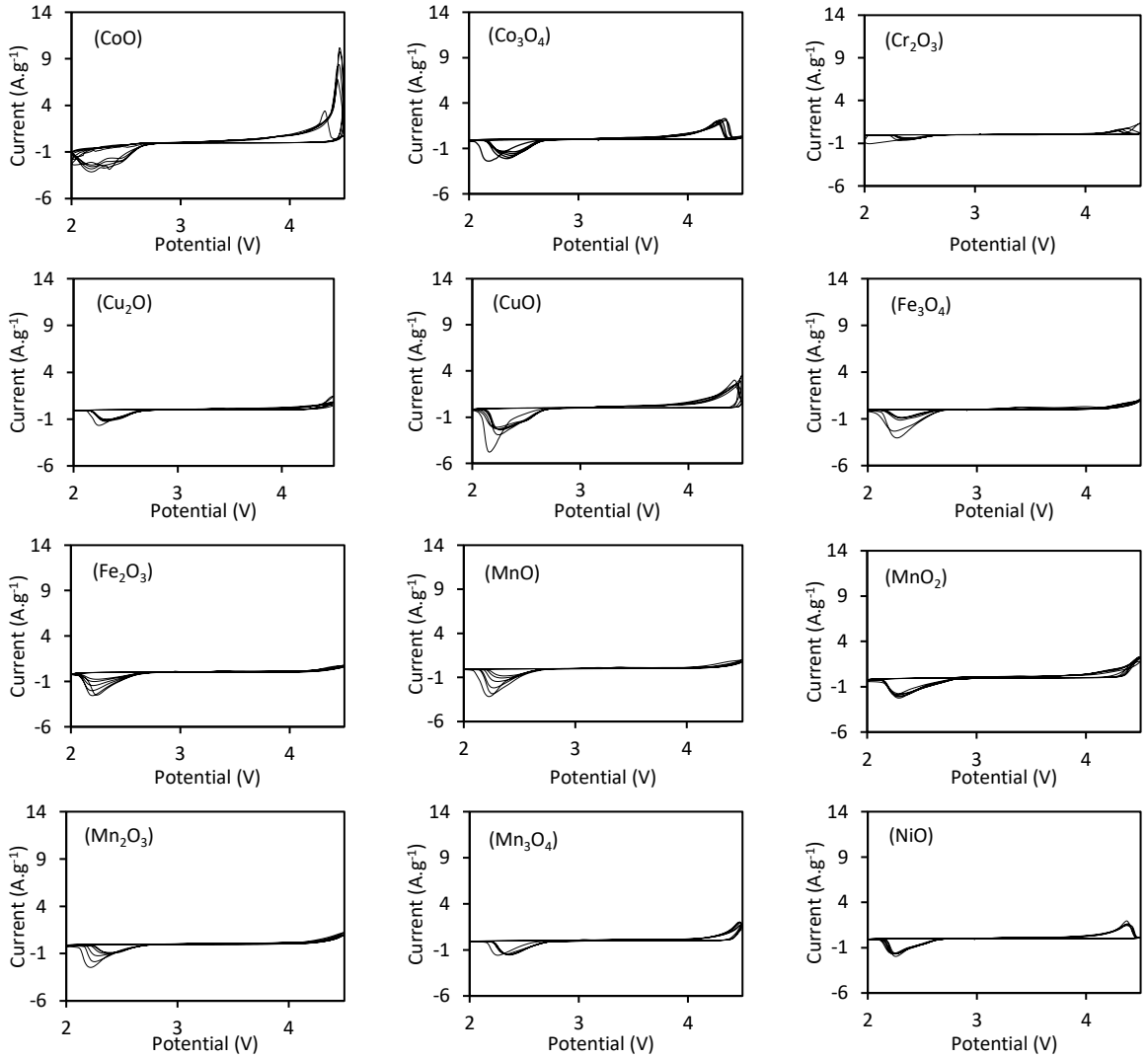

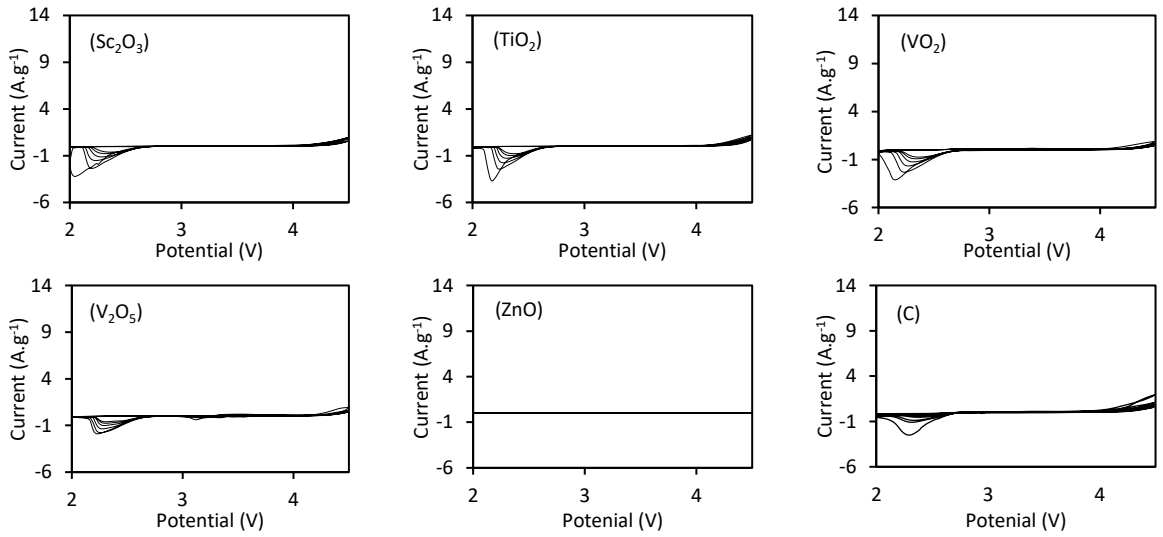

Figure 3: Cyclic voltammograms obtained from CoO, Co_3O_4, Cr_2O_3, Cu_2O, CuO, Fe_3O_4, Fe_2O_3, MnO, MnO_2, Mn_2O_3, Mn_3O_4, NiO, Sc_2O_3, TiO_2, VO_2, V_2O_5, ZnO, and pure C based electrodes in lithium-oxygen batteries application.

The electrocatalytic effect of the MOx on the electrochemical properties of a Li-O_2 cell was evaluated under a fixed cut-off capacity of 500 mAh.g^{-1} at a current density of 150 mA.g^{-1} and shown in Figure 4. For comparison, a battery was built with a pure carbon electrode. However, the battery made by pure carbon cannot achieve the targeted capacity of 500 mAh.g^{-1}.

The typical profile shows a discharge plateau reached after a smooth decrease in potential, and two plateaus above 4V on charge. The first charge plateau corresponds to the decomposition of bulk Li_2O_2, and matches potential observed with cyclic voltammetry. The second plateau corresponds to the decomposition of lithium carbonate resulting from the reaction between Li_2O_2 and carbon, and from the degradation of the electrolyte.[25] These phenomena were first observed by McCloskey et al.[26] and subsequently confirmed by Tarascon et al.[27]

The charge and discharge profile of vanadium (Figure 4 c,d) and manganese (Figure 4 f-i) oxide-based electrodes are atypical compared to traditional profiles. Several plateaus are observed during discharge and charge and correspond to the formation and decomposition of intermediates between metal oxide and lithium.[28-30] For examples, regarding V_2O_5-based electrode (Figure 4d) the first species to appear on discharge is α-$Li_xV_2O_5$ ($x < 0.01$) which turn into ε-$Li_xV_2O_5$ ($0.35 < x < 0.7$) phase after further lithiation and then into δ-$Li_xV_2O_5$ ($x = 1$) phase and finally into γ-$Li_xV_2O_5$ ($1 < x < 2$).[28-29] For Mn_3O_4 (Figure 4i) the discharge slop can be divided in 2 regions with an inflexion point at ~2.70 V. The first segment corresponds to the lithiation of the oxide leading to the formation of $LiMn_3O_4$ and the second part corresponds to the gradual transformation of $LiMn_3O_4$ into MnO_2.[30] This lithiation of manganese and vanadium oxides largely explains the number of cycles achieved, as these side reactions actively participate in the electrochemical reactions within the battery.

The number of cycles reached reflects the cycling stability of the battery (Figure 5a). The Li-O_2 cell made with Mn_3O_4 and TiO_2 can reach 416 and 350 cycles, respectively at a capacity of 500 mAh.g^{-1}. This exceptional stability could come from the high catalytic activity toward ORR process for TiO_2 and from the catalytic activity coupled to the lithiation process for Mn_3O_4. The catalytic activity of metal oxides on the reaction kinetics of lithium peroxide formation and decomposition was previously

determined by CV. The higher the resulting current, the greater the electron transfer to the oxygen and the higher the reaction kinetics. This increase in kinetics leads to a better formation and decomposition of lithium peroxide and consequently increase the reversibility of the process leading to a higher number of cycles. Batteries made with Cr_2O_3 and ZnO reached only 11 and 10 cycles respectively and confirm their poor catalytic activity for the OER/ORR previously observed by CV.

The charge and discharge plateau and the overpotential were evaluated for the 4th cycle at a capacity of 200 mAh.g^{-1}. The fourth cycle was chosen to give sufficient time for the system to stabilize. The results are presented in Figure 5 b,c, and d. Charge voltage plateau is linked to the OER and the discharge voltage plateau to the ORR. The higher the voltage of the discharge plateau is, the more effective the catalyst is. Likewise, the lower the voltage of the charge plateau, the more effective the catalyst is. A maximum discharge voltage of 2.827 V for CoO, and a minimum charge voltage plateau of 3.962 V for Co_3O_4 are observed. These results confirm the data collected with CV. Moreover, all MOx overpotentials match the CV values (Figure 5d).

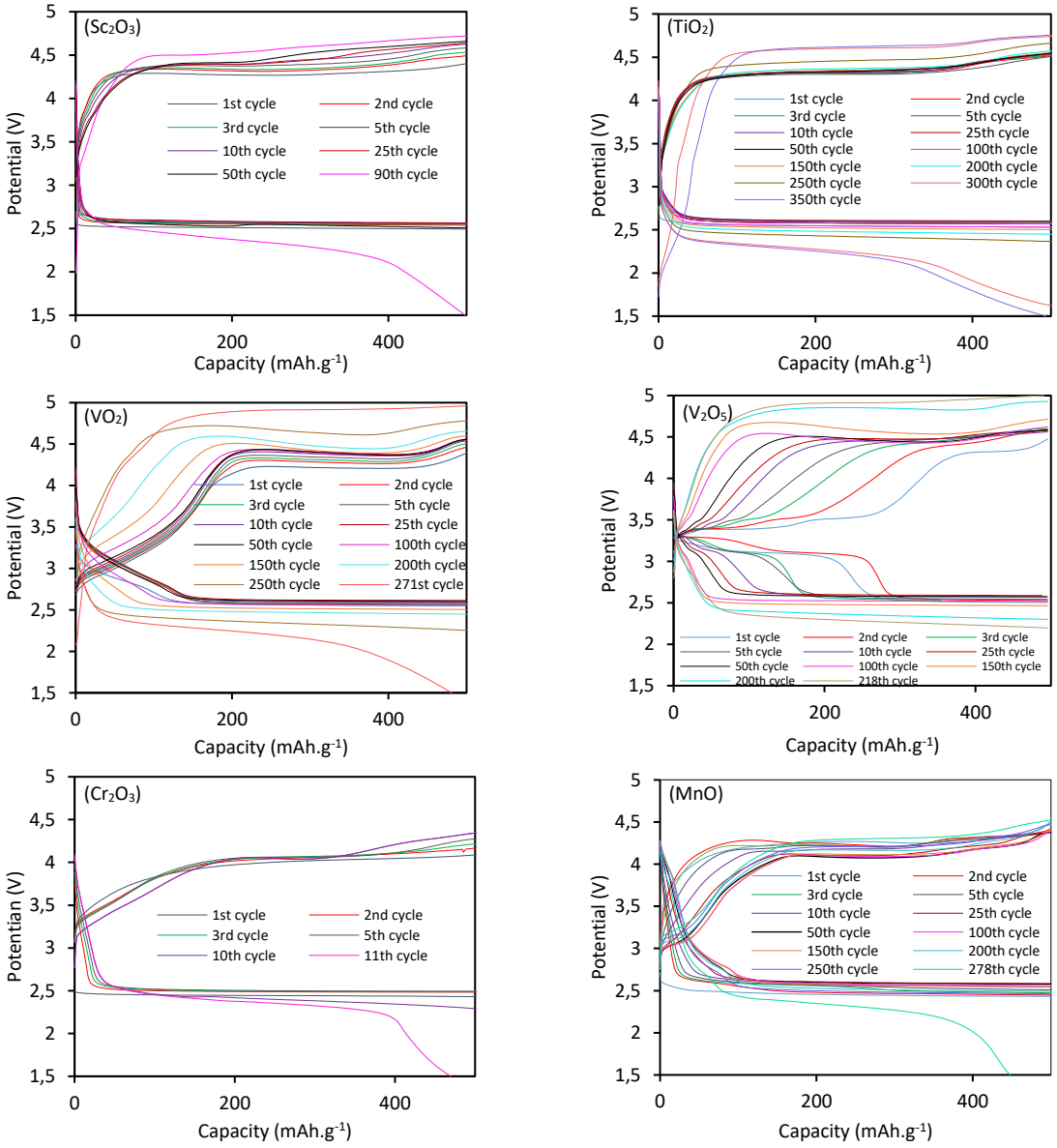

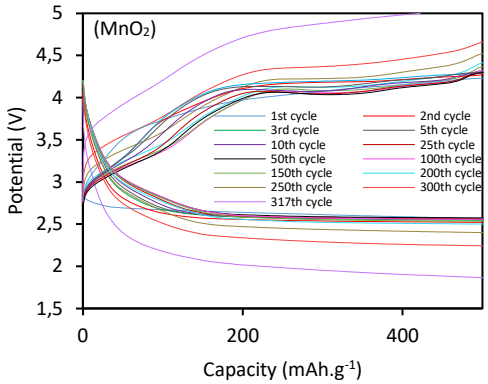
(MnO2)
Potential (V)
Capacity (mAh.g-1)
1st cycle
2nd cycle
3rd cycle
5th cycle
10th cycle
25th cycle
50th cycle
100th cycle
150th cycle
200th cycle
250th cycle
300th cycle
317th cycle

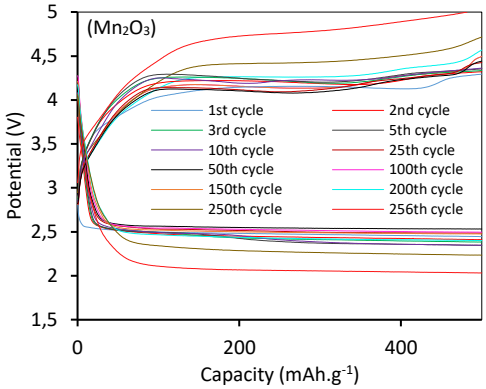
(Mn2O3)
Potential (V)
Capacity (mAh.g-1)
1st cycle
2nd cycle
3rd cycle
5th cycle
10th cycle
25th cycle
50th cycle
100th cycle
150th cycle
200th cycle
250th cycle
256th cycle

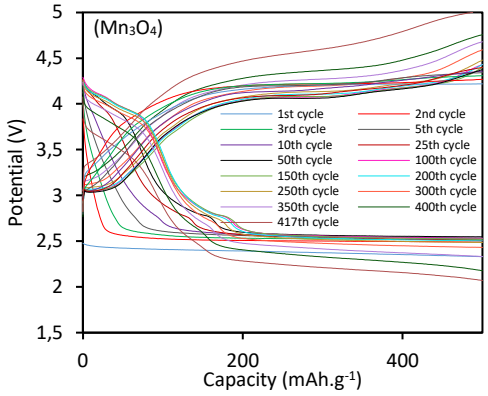
(Mn3O4)
Potential (V)
Capacity (mAh.g-1)
1st cycle
2nd cycle
3rd cycle
5th cycle
10th cycle
25th cycle
50th cycle
100th cycle
150th cycle
200th cycle
250th cycle
300th cycle
350th cycle
400th cycle
417th cycle

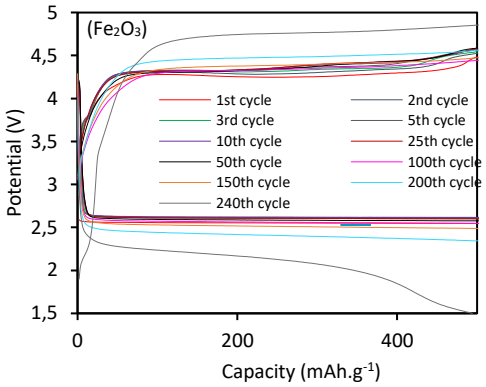
(Fe2O3)
Potential (V)
Capacity (mAh.g-1)
1st cycle
2nd cycle
3rd cycle
5th cycle
10th cycle
25th cycle
50th cycle
100th cycle
150th cycle
200th cycle
240th cycle

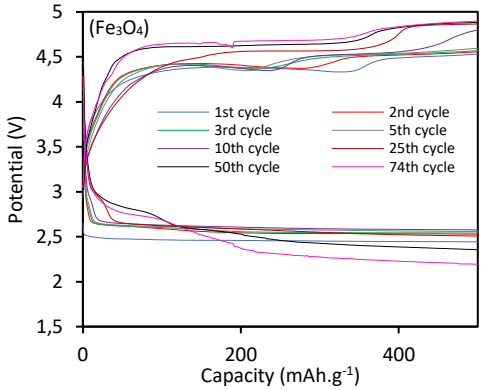
(Fe3O4)
Potential (V)
Capacity (mAh.g-1)
1st cycle
2nd cycle
3rd cycle
5th cycle
10th cycle
25th cycle
50th cycle
74th cycle

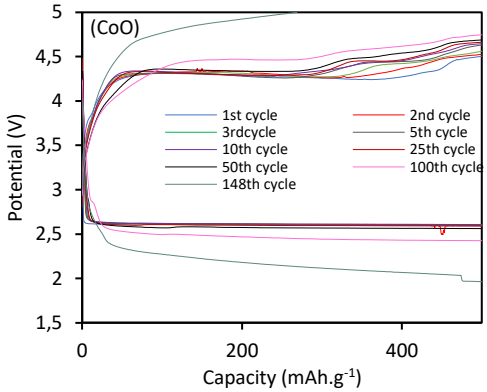
(CoO)
Potential (V)
Capacity (mAh.g-1)
1st cycle
2nd cycle
3rdcycle
5th cycle
10th cycle
25th cycle
50th cycle
100th cycle
148th cycle

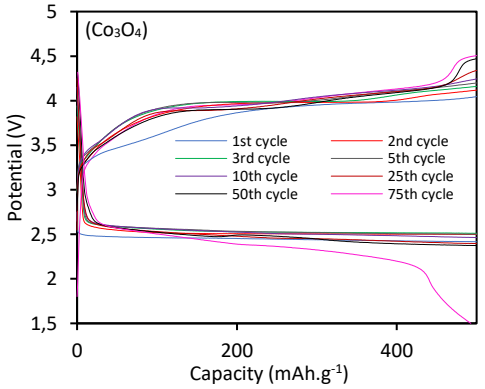
(Co3O4)
Potential (V)
Capacity (mAh.g-1)
1st cycle
2nd cycle
3rd cycle
5th cycle
10th cycle
25th cycle
50th cycle
75th cycle

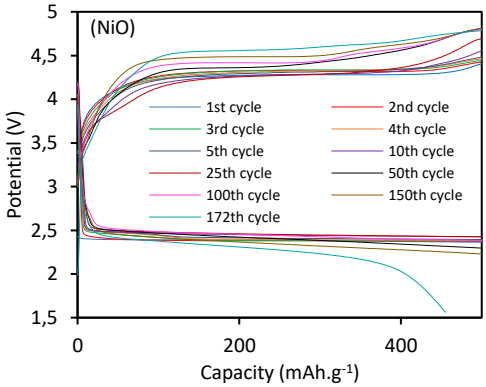
(NiO)
Potential (V)
Capacity (mAh.g-1)
1st cycle
2nd cycle
3rd cycle
4th cycle
5th cycle
10th cycle
25th cycle
50th cycle
100th cycle
150th cycle
172th cycle

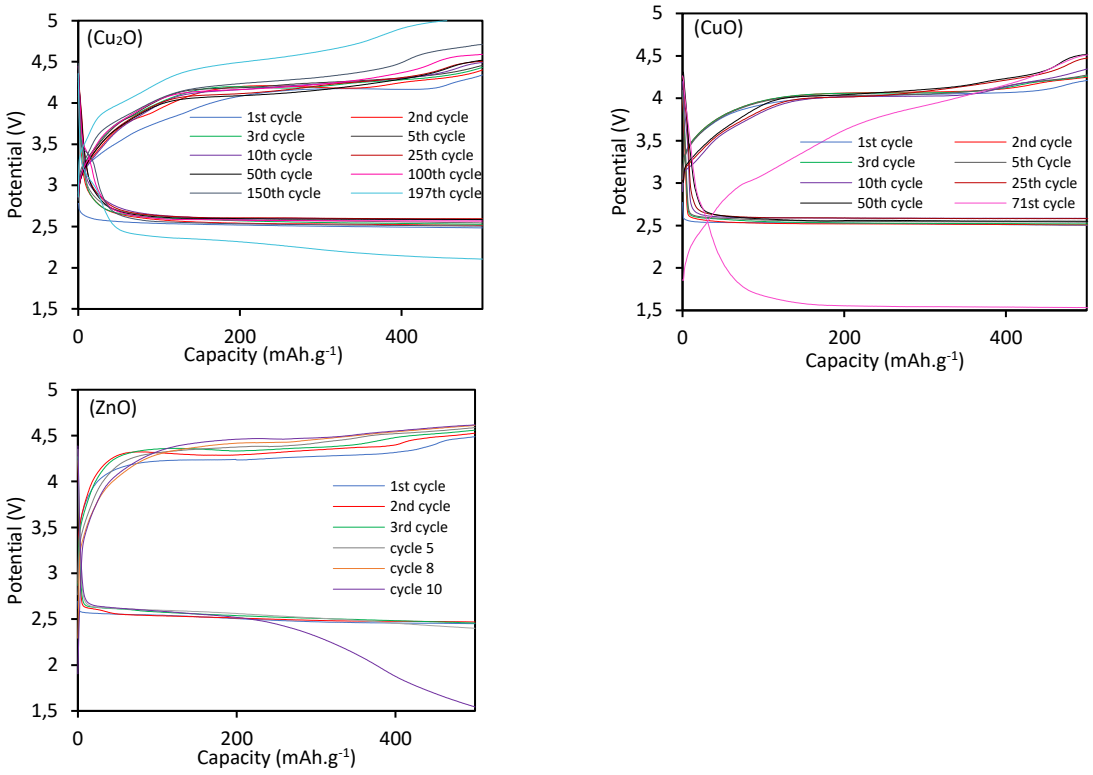

Figure 4: Cycling performances of Li-O_2 batteries with Sc_2O_3, TiO_2, VO_2, V_2O_5, Cr_2O_3, MnO, MnO_2, Mn_2O_3, Mn_3O_4, Fe_2O_3, Fe_3O_4, CoO, Co_3O_4, NiO, Cu_2O, CuO, and ZnO at the current density of 150 mA.g^{-1} and capacity fixed at 500 mAh.g^{-1}

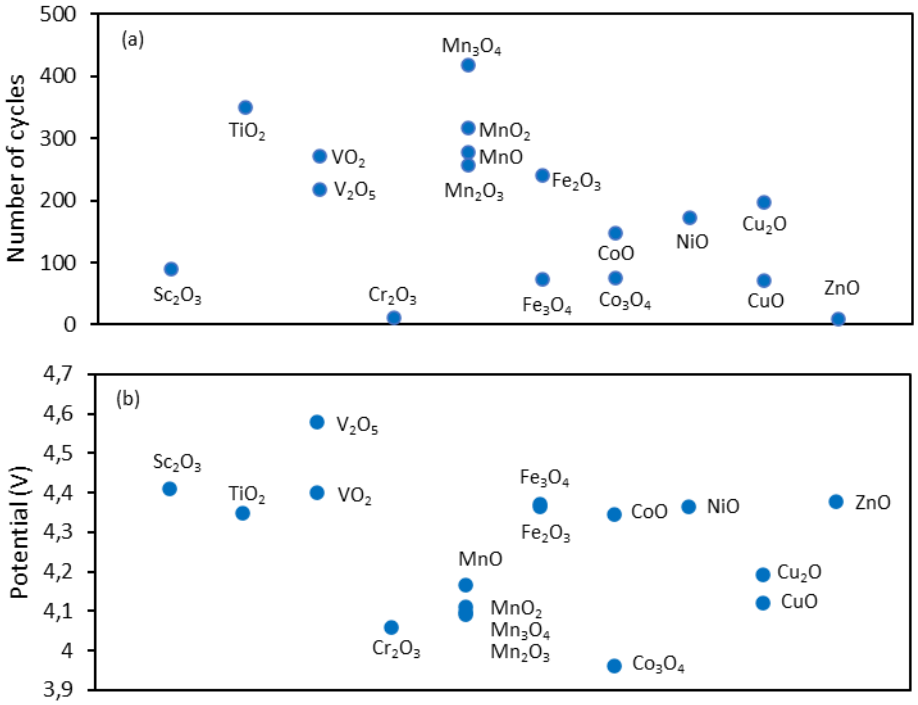

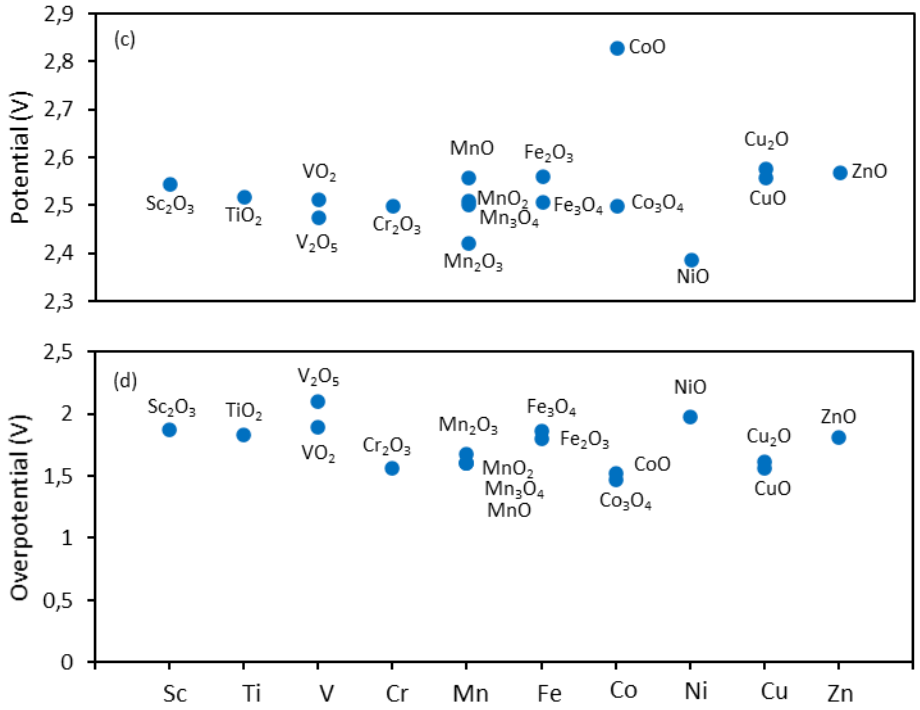

Figure 5: (a) number of cycles reached by each metal oxides while cycling at a specific capacity of 500 mAh.g^{-1} at a current density of 150 mA.g^{-1} and their respective (b) charge potential, (c) discharge potential, (d) overpotential for the 4th cycle at a capacity of 200 mAh.g^{-1}

The charge-discharge cycles at open capacity were measured over 100 cycles, under an oxygen pressure of 1 atm and at a current density of 150 mA.g^{-1}. The potential window has been set according to the previously tested cyclic stability. Two windows emerged, first ranging from 2.0 to 4.7 V and second from 2.2 to 4.4V. The charge-discharge cycles profiles and associated efficiencies of all Li-O_2 batteries made with MOx/SP cathodes are reported in Figure S4.

Figure 6a shows the first discharge capacity of Li-O_2 cells built with 3d MOx and SP electrodes. The specific capacity of all 3d MOx is 3.5 ~ 14.9 times higher than those of SP demonstrating the positive impact of MOx on battery performance. Importantly, TiO_2 and NiO electrodes have exceptional capacities reaching 6447 and 6090 mAh.g^{-1} respectively. This impressive initial capacity is explained by the high catalytic activity of TiO_2 and NiO on the oxygen reduction reaction.

The electrocatalytic activity of 3d MOx cathodes can also be estimated from the overpotential (Figure 6b). The overpotential represents the voltage between the charge-discharge plateau characteristic of the OER and ORR process respectively. The charge and discharge plateau values are available in Figure S5. All MOx electrodes overpotentials are generally lower than that of the SP cathode, confirming the enhancement of the electrocatalytic activity of the Li-O_2 battery. Three MOx electrodes have excellent overpotentials, 1.581, 1.596, and 1.559V for CuO, CoO, and Co_3O_4 respectively, which represents a decrease of 0.65V compared to that of SP cathode. These data are in agreement with the results obtained in the CV. Indeed, CoO, CuO and Co_3O_4 have the highest kinetics for oxygen reduction and evolution reactions, leading thus to the lowest overpotentials.

In order to evaluate long-term performance, capacity of the 100th cycle has been determined and reported in Figure 6c. Batteries made with CoO and Co_3O_4 cathodes can reach a capacity of 397 and 472 mAh.g^{-1}, respectively with an efficiency close to 100%, confirming their high stability and all previous data on their catalytic activities. These results demonstrated that the use of MOx cathodes reduces overvoltage in the lithium-oxygen batteries due to their high catalytic activities for the OER and ORR, resulting in improved performances, especially in capacity.

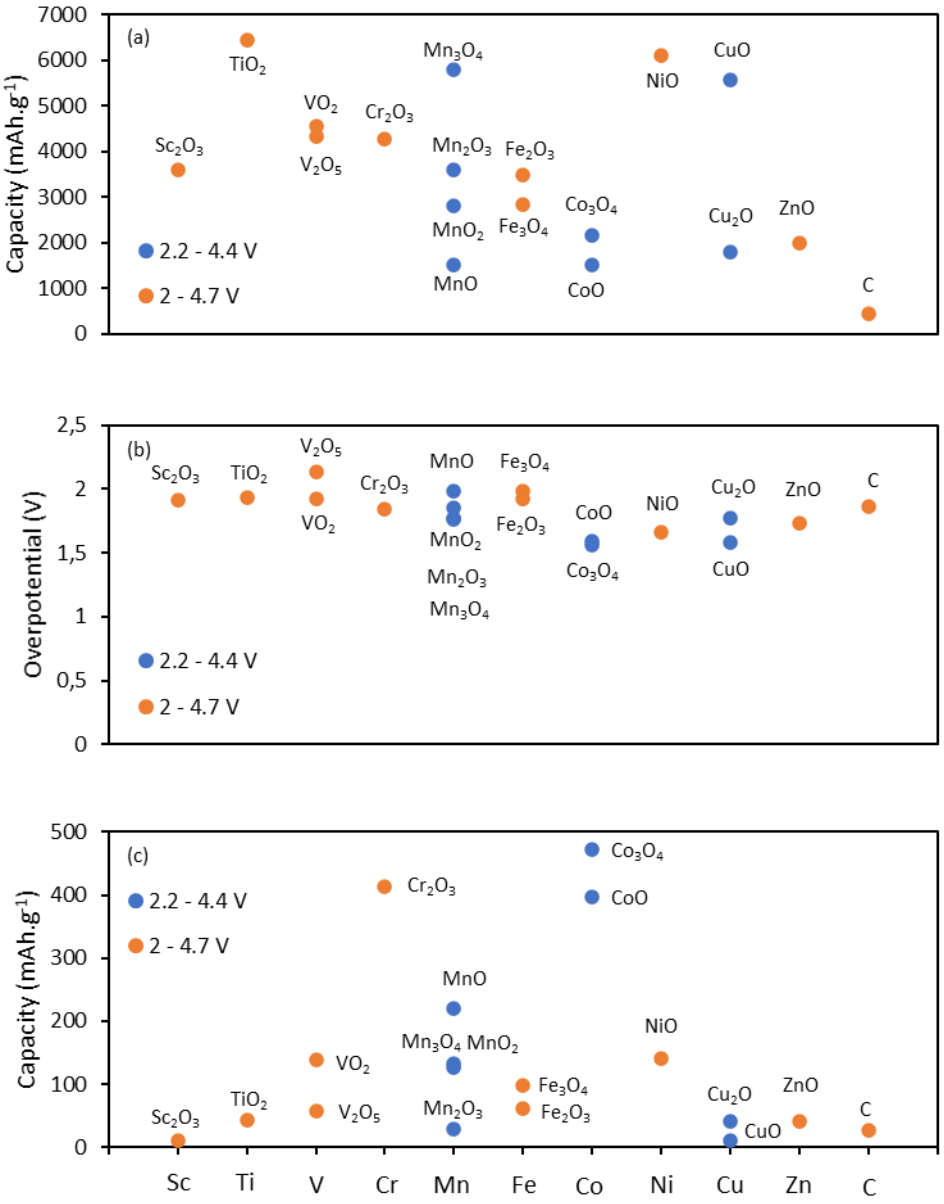

Figure 6: (a) First discharge capacity (b) overpotential and (c) capacity of the hundredth cycle obtained for all metal oxides at 150 mA.g^{-1} within a 2-4.7 V or 2.2-4.4 V voltage window.

Other than these chemical properties of 3d MOx, physical properties such as morphology, particle size, surface area, should be taken into account. Figure 7 links the first discharge capacity to the specific surface of the nanoparticles. The capacity was normalised by the weight of metal oxide and then divided by the specific surface area to give a capacity per metal oxide surface. Vanadium and manganese-based oxides have the highest capacity. Comparing with figure 6a it can be seen that these

oxides already have a high capacity when normalised by their mass only. This high capacity is partly explained by the lithiation phenomena already discussed above.

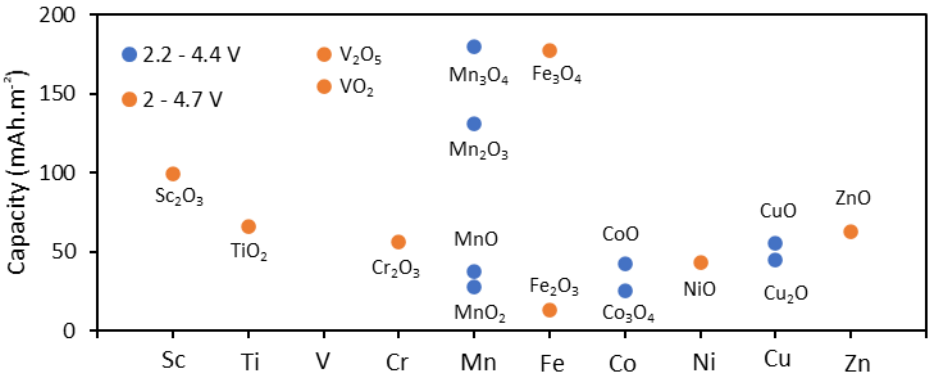

Figure 7: First discharge capacity obtained for all metal oxides at 150 mA.g^{-1} within a 2-4.7 V or 2.2-4.4 V voltage window.

Another important parameter, often underestimated, to be considered, is the internal resistance of the battery. For this purpose, an impedance analysis was carried out and the results were processed in the form of a Nyquist diagram depicted in Figure 8 a,b. Most of the resistance in Li-O_2 batteries comes from the insulating lithium peroxide produced during discharge and the conductivity of the cathode. In order to consider only the resistance of lithium peroxide without possible insulation of sub-products resulting from the degradation during cycles, measurements were taken after the first discharge. The semicircle of the Nyquist curve expresses the charge-transfer resistance. Higher charge-transfer resistance leads to a slower charge-transfer kinetics. The charge-transfer resistance has been calculated and summarized in Figure 8c.

Carbon electrode is used as a reference and exhibits an internal resistance of 1138 kohms.g^{-1}. Surprisingly, the use of Cr_2O_3, Mn_2O_3, and MnO_2 electrodes leads to a higher internal resistance value of 1556, 1322, and 1814 kohms.g^{-1}, respectively. The higher internal resistance induced by these oxides could lead to a rapid decrease of capacity during cycling as it will drive up the voltage and cause degradations, such as that of the electrolyte.

Fe_2O_3 (360 kohms.g^{-1}), NiO (312 kohms.g^{-1}), MnO (255 kohms.g^{-1}), and CoO (286 kohms.g^{-1}) electrodes reduce their internal resistance within the battery by almost four times compared to the carbon cathode. This significant decrease in internal resistance could reflect a stabilization of the system potentially leading to an increase in the number of cycles during cycling, and help to prevent the degradations within the battery, thus limiting the formation of side products.

It is worth noting that the origins of the internal resistance of Li-O_2 batteries are multiple. The measured resistance considers the whole cell, including the lithium anode, the electrolyte, and the cathode. The main cathode related parameters influencing the resistance are: the conductivity of the 3d metal oxides, and the shape and thickness of the deposited lithium peroxide. As a consequence, it is not obvious to identify the individual impact of each parameter on the final resistance.

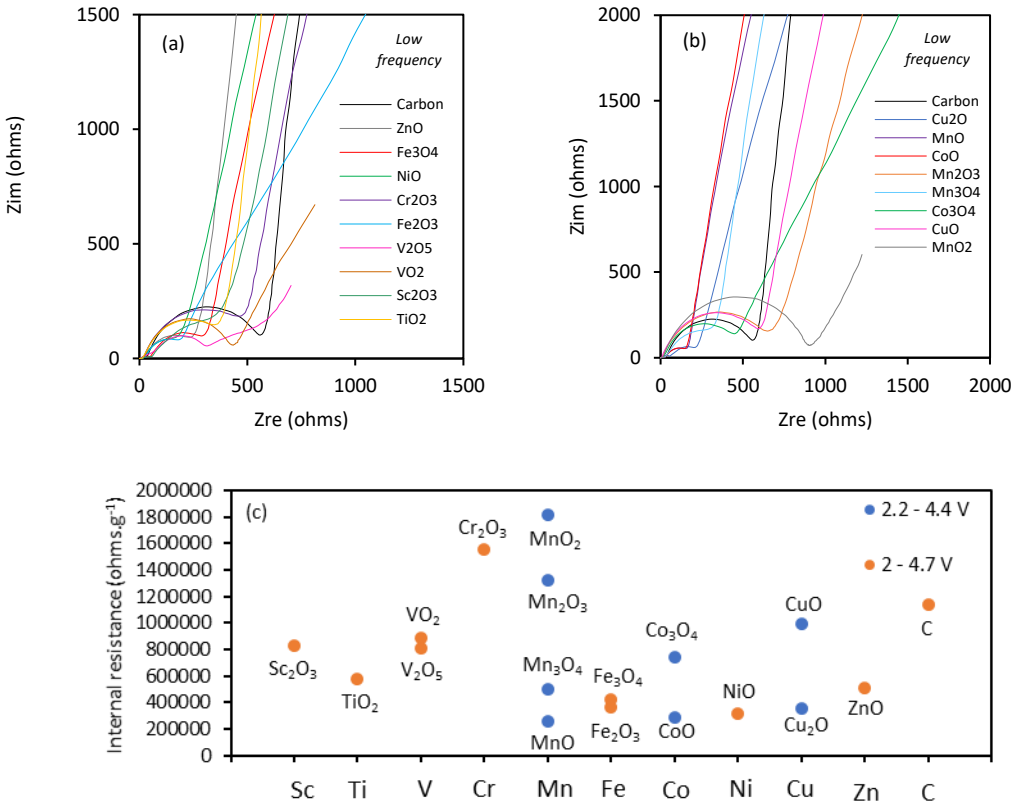

Figure 8: Experimental Nyquist plot for (a) pure carbon, Cr_2O_3, Fe_3O_4, Fe_2O_3, NiO, Sc_2O_3, TiO_2, VO_2, V_2O_5, ZnO, and (b) pure carbon, CoO, Co_3O_4, Cu_2O, CuO, MnO, MnO_2, Mn_2O_3, Mn_3O_4 based electrodes in lithium-oxygen batteries after the first discharge and (c) their resulting internal resistances.

To investigate the possible degradations and the chemical species present at the end of 100th cycle, XPS analyses were carried out. C1s and O1s spectra of each metal oxide and their respective deconvolutions are shown in Figure 9 and Figure S6.

The analysis of C1s spectra evidences the presence of lithium carbonate in all samples reflecting the reaction between carbon and lithium. In addition, the presence of CF_3, C-O-C, and O-C=O bonds confirms the hypothesis of electrolyte degradations. These degradations leading to the formation of side products passivating the cathode have already been highlighted by Carboni et al [31] and partly explains the decrease in battery performance over the cycles. A qualitative analysis of the amount of lithium carbonate is made by calculating the ratio between the peak area of the C-C and CO_3 bonds. Results are shown in Table 3. The smaller the ratio, the more $LiCO_3$ is present. The evolution of the different ratios follows that of the maximum number of cycles obtained in Figure 5a. This result is consistent with the fact that the more cycles the batteries do, the more lithium carbonate is created. This is confirmed with ZnO which has the lowest amount of carbonate but also cycles the least.

Furthermore, the analysis of the O1s spectra reveals the presence of lithium peroxide in some cathodes, indicating a non-optimal dissolution of lithium peroxide during charging and will also contribute to the passivation of the cathode and therefore to the drop in performance. Reducing the formation of these reaction products would be a major subject of research in order to obtain an ultra-efficient lithium-oxygen battery.

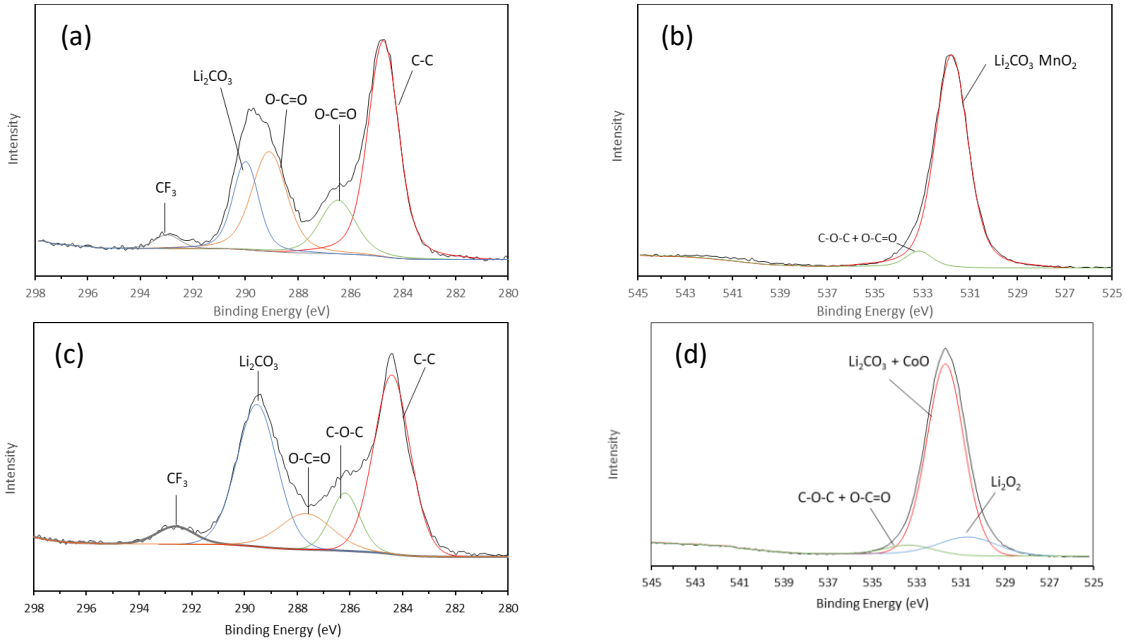

Figure 9: C1s and O1s XPS spectra of (a,b) MnO_2, and (c,d) CoO obtained after 100 cycles at 150 mA.g^{-1}

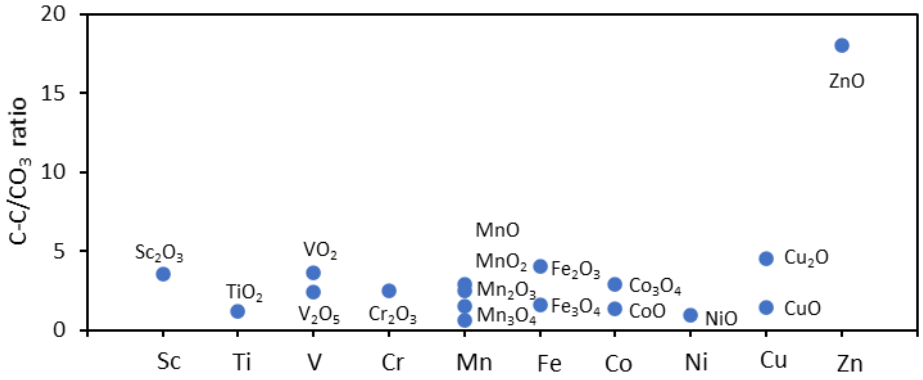

Figure 10: XPS post cycling C-C/CO_3 bonds ratio of all 3d metal oxide used as cathode in Li-O_2 battery

The relationship between the oxidation stage of the 3d metal centres and the electrochemical performance can be established using the previous results for V, Fe, Cu and Co atoms.

The maximum capacity achieved increases with the number of oxidations of the metal centre (Figure 6 a). It increases from 4320 to 4543, 2845 to 3488, 1783 to 5551 and 1515 to 2147 mAh.g^{-1} for the V_2O_5/VO_2, Fe_3O_4/Fe_2O_3, CuO/Cu_2O and Co_3O_4/CoO, respectively. The increase in discharge capacity reflects the ability of the cathode to form Li_2O_2. The higher it is, the more Li_2O_2 is formed. Therefore, increasing the number of 3d metal oxide oxidations improves the ORR process and increases the capacity of the battery in a fixed window of potential.

Number of cycles and the capacity reached after 100 cycles increase inversely to the degree of oxidation of 3d metal oxide (Figure 5a and 6c). Regarding the number of cycles, V_2O_5/VO_2, CuO/Cu_2O and Co_3O_4/CoO reach 218-271, 71-197, and 75-148 cycles, respectively. However, iron atoms do not follow this tendency, its number of cycles increases from 74 to 240 cycles from Fe_3O_4 to Fe_2O_3. For capacity, V_2O_5/VO_2, CuO/Cu_2O and Fe_2O_3/Fe_3O_4 reach 58-139, 11-42 and 61-99 mAh.g^{-1} respectively.

The two cobalt oxides have the two highest capacities but do not follow the previous trend. Co_3O_4 reaches 472 and CoO 397 mAh.g^{-1}.

Manganese-based oxides were excluded from this study due to the lithiation occurring during the charge-discharge cycles, making it impossible to find consistent correlations between the species. Nevertheless, it is noted that Mn_3O_4 gives some excellent results.

The variation of electrochemical properties according to the degree of oxidation of the 3d transition metal oxides can be a very interesting property to modulate the characteristics of the battery depending on its desired specifications.

The crystal system of the 3d metal oxides also seems to have an effect on the electrochemical performance of the battery. Cubic systems have the lowest first discharge capacity at fixed potential but the highest hundredth capacity.

The effect of crystallographic structure on the electrochemical performance of the battery have already been investigated by Cheng et al.[32] They synthetised diverse crystallographic forms of manganese dioxide MnO_2 (α, β, γ) and showed that the organisation of the [MnO_6] octahedron according to the crystal system led to the formation of various tunnels. α-MnO_2, possess (2x2) and (1x1) tunnels surrounded by double binding octahedral chains. β-MnO_2 is made of (1x1) tunnels separated by single chains and γ-MnO_2 consists of (1x1) and (1x2) tunnels enveloped in double chains. The catalytic activity of the different crystalline forms of MnO_2 on ORR were tested by LSV and followed the order: α- > β- > γ-MnO_2. The increase in catalytic activity as a function of the crystal system is explained by the modulation of oxygen diffusion within the tunnels formed by the [MnO_6] octahedra creating more nucleation sites and allowing more lithium peroxide to be formed and consequently increasing the capacity of the battery.

Conclusion

3d metal oxides (MOx) were used as cathode material in lithium-oxygen batteries. The MOx electrodes demonstrated significant improvement in the round-trip efficiency and specific capacity over the carbon cathode. The electrocatalytic properties of these MOx cathodes were determined. They promote the catalytic activities of OER and ORR processes and lead to a decrease of the overpotential, and an increase of the specific capacity. All 3d MOx electrodes have improved the performance of the battery.

Among the most significant improvements, it has been shown that the use of Co_3O_4 electrode reduces overpotential to 1.464 V, TiO_2 increases capacity to 6448 mAh.g^{-1} and Mn_3O_4 increases cycling stability to 417 cycles at 500 mAh.g^{-1}

These results have demonstrated that the Li-O_2 batteries with 3d metal oxides cathodes offer characteristics that lead to concrete performance improvements. This area of research could create excellent opportunities for the development of practical Li-O_2 batteries. However, the deterioration of the electrolyte remains important. It would be interesting to modify the electrolyte in order to increase the stability and thus exploit the battery's capacities to the maximum. Another improvement that could be envisaged following this study would be to mix several oxides in order to combine their electrochemical characteristics. These composites could reduce the overvoltage and increase the capacity of the batteries.

Experimental

Synthesis of 3d metal oxide nanoparticles

The Cu_2O, CoO, Fe_3O_4, MnO, NiO, and ZnO nanoparticles were prepared under an argon atmosphere by a mild temperature organic solution reaction. [33] In a typically synthesis, 0.002 mol of the considered metal acetylcetonate was mixed with 0.088 mol of oleylamine. The mixture was heated for one hour to different temperatures depending on the metal nature (200, 80, 200, 260, 80 and 80°C for Co, Cu, Fe, Mn, Ni, and Zn, respectively). The resulting solution was then quickly heated to higher temperature, depending on the nature of the metal (240, 150, 300, 280, 180 and 150°C for Co, Cu, Fe, Mn, Ni and Zn respectively). This temperature was maintained for one hour. After cooling to room temperature, excess ethanol was added to the solution, leading to the formation of a precipitate which was isolated by centrifugation. Then, the nanoparticles were washed fully with ethanol and recovered by centrifugation, before being air-dried at 80°C overnight.

Co_3O_4 nanoparticles were obtained by a co-precipitation method. 0.005 mol of $CoCl_2$ were mixed with 0.5g of Poly ethylene glycol.[34] Then, 0.0075 mol of ammonium carbonate were added dropwise under vigorous agitation. The resulting mixture is heated to 80°C for 6h. The violet powder thus obtained is completely washed with water and ethanol and dried at 80°C overnight, followed by a calcination at 400°C for 3 hours.

Cr_2O_3 nanoparticles were prepared using an equimolar mixture of 0.0015 mol of $Cr_2(SO_4)_3$ and urea in 52.5 mL of water. Then the pH of the solution was adjusted to 10 using a 4M NaOH solution. The mixture is then sealed in a 60mL Teflon lined stainless steel autoclave for hydrothermal treatment at 180°C for 24h. Once over, the powder was recovered, fully washed with water and ethanol, dried overnight at 80°C before being calcined at 600°C for 1 hour.[35]

CuO nanoparticles were synthetized at room temperature by mixing 0.024 mol of $CuCl_2$ with 0.0528 mol of NaOH in ethanol under sonication for 1h. The obtained black precipitate was recovered and fully washed with water and ethanol, dried overnight at 80°C before being calcined at 180°C for 150 minutes. [36]

The synthesis of Fe_2O_3 nanoparticles was achieved by mixing 0.006 mol of $FeCl_2$ and 0.012 mol of $FeCl_3$ salts in acidified water. Then, 100ml of a NaOH 1M solution was added dropwise until a precipitate occurred. The solid was recovered, wash with water and ethanol, and dried overnight at 80°C before being used for battery tests. [37]

MnO_2 nanoparticles were prepared by adding 0.0019 mol of $Mn(CH_3CO_2)_2$ in 100 mL $KMnO_4$ 1N followed by heating at 60°C for 3h. The obtained nanoparticles were then fully washed with water and ethanol, dried overnight at 80°C, and calcined at 450°C for 5 h. [38]

Mn_2O_3 nanoparticles were synthetized by adding 0.02 mol of $MnCl_2$ with 0.037 mol of NH_4HCO_3 in 18 mL of water. The suspension was stirred for 30 min and then heated at 80°C for another 30 min. The resulting white powder is then wash several times with water and ethanol and dried overnight at 80°C before being calcined at 700°C for 1h.[39]

The synthesis of Mn_3O_4 nanoparticles was performed by adding 0.0015 mol of $Mn(CH_3CO_2)_2$,$7.5*10^{-4}$ mol of n-butylamine, 0.0012 mol of KOH in a mixture made of 7.5 ml of water and 37.5 mL of ethanol. The mixture is then transferred in a 60mL Teflon lined stainless steel autoclave which was maintained at 180°C for 4h. The product obtained was washed several times with water and ethanol and then dried overnight at 80°C before being characterized. [40]

Sc_2O_3 nanoparticles were obtained via a simple sol-gel method. In a typical synthesis, 0.0015 mol of $Sc(NO_3)_3$, and 0.0215 mol of citric acid was added to a solution containing 5mL of H_2O and 10mL of ethanol. The mixture was then stirred at 80°C for 1h until a gel formed. The gel was dried in an oven at 120°C to form a powder which was calcined at 600°C for 2h. [41]

TiO_2 nanoparticles were synthetized via the decomposition of titanium butoxide in DMSO. $1.466*10^{-5}$ mol of titanium butoxide was added to $7.040*10^{-4}$ of DMSO before being heated at 190°C for 2h. After cooling naturally to room temperature, the nanoparticles were fully washed with ethanol and dried at 80°C overnight before being calcined at 450°C for 2h. [42]

VO_2 nanoparticles were generated by mixing $9.50*10^{-4}$ mol of Citric acid and 0.011 mol of NH_4VO_3 in a 50 mL mixture made of ethanol:H_2O (1:1) for 24h. The mixture was then placed in an oven at 110°C for 12 h until the solvent has evaporated completely. After cooling, the solid was then calcined under argon at 500°C for 8h. [43]

V_2O_5 nanoparticles were obtained by mixing 0.004 mol of NH_4VO_3 with $1.73*10^{-4}$ mol of Sodium Lauryl Sulphate in 100ml of ethanol/H_2O (1:1). The pH of the mixture was adjusted to 2 using nitric acid and this mixture was refluxed for 2 hours. After cooling naturally to room temperature, the solid was fully washed with water and ethanol before drying at 80°C overnight and then calcined at 400°C for 2h, and then at 600°C for another 2h. [44]

Materials characterisation

X-ray diffractograms of the samples were recorded on a PANalytical X'Pert Pro diffractometer equipped with a direct optical positioning goniometric system and stuffed with a PIXcel 1D detector. The anode is made of copper and the emitted radiation correspond to the Kα ray (λ = 1.54184 Å). A 45 kV voltage and 30 mA current supply x-ray tubes. Diffractograms were recorded under room temperature, in 2θ configuration, with a step of 0.016711° each 24 seconds. Data were analysed using Data Collector and HighScore Plus software.

Infrared spectroscopy was used to confirm the complete elimination of the oleylamine from the synthesised samples. The spectra were recorded between 500 and 4000 cm^{-1} with a Perkin Elmer Spectrum 65 FT IR Spectrometer. Data were analysed using Spectrum 10 Spectroscopy Software.

TEM micrographs were obtained using a TEM Tecnai 10 microscope composed of a LaB6 electron gun, an OSIS Magaview III camera, and configured in imaging mode with an accelerating voltage of 80 kV.

X-Ray photoelectron spectroscopy was used to analyse the chemical composition of the discharged products after cycling test. The spectroscope is an Escalab 250 Xi from Thermo Scientific, made of a magnesium anode (Kα ray, hv=1253.6Ev). The experiments were performed at room temperature and under reduced pressure.

Nitrogen physisorption analyses were done using an ASAP 2420 from Micromeritics. The samples were degassed overnight at 150 °C before the measurement. The pore size distribution for the porous nanoparticles was calculated via Horvath-Kawazoe method, and the specific surface area via Brunauer, Emmet and Teller (BET) method.

Electrochemical measurements

In order to elaborate the O_2-electrode, a slurry was prepared by mixing the as-prepared nanoparticles, carbon black (KB, 99.9+%, Alfa Aesar), and poly(vinylidene difluoride) (PVDF, M_W≈275, Sigma Aldrich,) with N-methyl-2-pyrrolidone (NMP, >99%, Sigma Aldrich,) in a 60 : 30 : 10 weight ratio. The slurry was spread on a stainless steel mesh (mesh size: 100*100mm, 26% open area) and dried at 120°C under vacuum overnight. After that, the steel mesh was cut into several circles of 1.32 cm^2 each. A slurry of carbon black, PVDF, in NMP 90 : 10 was also prepared using same protocol and used as a reference electrode.

To perform electrochemical measurements, homemade Li-O_2 were designed following Swagelok cells structure. The cell was made of an electrolyte consisting of 0.25M lithium bis(trifluoromethanesulfonyl)imide (LITFSI, ≥99% Sigma-Aldrich) in 1,2-Dimethoxyethane (DME, 99+%, Alfa Aesar), a lithium foil, used as reference and counter electrode, the as prepared O_2 –electrode used as cathode, and a glass fiber separator. The cell was assembled in an argon-filled glove box where moisture and oxygen concentrations were less than 1 ppm. The obtain batteries were put under high purity oxygen flux (99.999%) for several seconds, they were then maintained under an O_2 atmosphere at a pressure of 1 atm for 10 hours before the electrochemical measurements were performed.

The galvanostatic discharge-charge tests were performed using a LANHE CT2001A multi-channel battery tester with a voltage between 2 and 4.7 V or 2.2 and 4.4V and at a current rate of 150mA.g^{-1}. The specific capacities obtained were normalized by the carbon weight used in the cathode.

Electrochemical impedance spectroscopy (EIS) and cyclic voltammetry were performed via a Princeton Applied Research, VersaSTAT 3, potentiostat/galvanostat. Galvanostatic charge and discharge tests were carried out between 2 and 4.5V (vs LI/LI^+), with a scanning rate of 0.1

$mV.s^{-1}$. Impedance response was collected, after first discharge, by applying a constant AC voltage of 5mV, with 15 points per decade, and a scanning frequency between 0.01 and 100000 Hz.

Bibliography

1 C. Zhang, B. Su, K.Zhou, and S.Yang, *Journal of Cleaner Production*, 2019, **209**, 224–235.
2 A. Gellert, A.Florea, U. Fiore, F. Palmieri, and P. Zanetti, *International Journal of Information Management*, 2019, 1–11.
3 J. Wang, Y. Li, and X. Sun, *Nano Energy*, 2013, ***2***(4), 443–467.
4 R. Padbury, X. Zhang, *Journal of Power Sources*, 2011, **196** (10), 4436-4444
5 A. Kraytsberg, and Y. Ein-eli, *Journal of Power Sources*, 2011, **196**, 886–893.
6 K. M. Abraham and Z. Jiang, *J. Electrochem. Soc*, 1996, **143**,1
7 P. G. Bruce, S. A. Freunberger, L. J. Hardwick and J.-M. Tarascon*, Nat. Mater*, 2012, **11**, 19–29
8 P. Tan, H. R. Jiang, X. B. Zhu, L. An, C. Y. Jung, L. Wu, L. Shi, W. Shyy, and T. S. Zhao, *Applied Energy*, 2017, **204**, 780–806.
9 E. Frackowiak, and F. Béguin, *Carbon 39*, 2001, **39**, 937–950.
10 J. Xiao, D. Wang, W. Xu, D. Wang, R. E. Williford, J. Liu, and J. Zhang, *Journal of The Electrochemical Society*, 2010, **157**(4), 487–492.
11 Y. Li, X. Li, D. Geng, Y. Tang, R.Li, J. P. Dodelet, M. Lefevre, X. Sun, *Carbon*, 2013, **64**, 170–177.
12 M. Endo, C. Kim, K. Nishimura, T. Fujino, and K. Miyashita, *Carbon*, 2000, **38**, 183–197.
13 A. Eftekhari, *Materials Today Chemistry*, 2018, **7**, 1–4.
14 Q. Li, R. Cao, J. Cho, and G Wu, *Phys.Chem.Chem.Phys., 2014,* **16***,* 13568
15 D. M. Itkis, D. A. Semenenko, E. Y. Kataev, A. I. Belova, V. S. Neudachina, A. P. Sirotina, M. Haevecker, D. Teschner, A. Knop-Gericke, P. Dudin, A. Barinov, E. A. Goodilin, Y. Shao-Horn, L. V. Yashina, *Nano Letters*, 2013, **13**(10), 4697–4701.
16 B. D. McCloskey, A. Speidel, R. Scheffler, D. C. Miller, V. Viswanathan, J. S. Hummelshøj, and A. C. Luntz, *Journal of Physical Chemistry Letters*, 2012, **3**(8), 997–1001
17 C. Xia, C. Y. Kwok, C, and L. F. Nazar, *Science*, 2018, **361**, 777–781.
18 J. Suntivich, H. A. Gasteiger, N. Yabuuchi, H. Nakanishi, J. B. Goodenough, and Y. Shao-horn, *Nature Chemistry*, 2011**,** ***3***(7), 546–550
19 A. Debart, J. Bao, G. Armstrong, P.G. Bruce*, J. Power Sources*, 2007, **174**, 1177-1182
20 J.W. Jung, J.S. Jang, T.G. Yun, K.R. Yoon, I..D. Kim, *ACS Appl. Mater. Interfaces*, 2018, **10**, 6531−6540
21 S.H. Lim, B.K. Kim, W.Y. Yoon, *J Appl Electrochem,* 2012, **42**, 1045-1048
22 J. Ge, G. Du, M. Zhang, A. Kalam, S. Ding, Q. Su, B. Xu, A.G. Al-Sehemi, *Energy Technol*, 2020, **8**, 1901257
23 D. McCloskey, R. Scheffler, A. Speidel, D. S. Bethune, R. M. Shelby, A. C. Luntz*, J. Am. Chem. Soc*. 2011, **133**, 18038 – 18041.
24 R. Black, J. H. Lee, B. Adams, C.A. Mims and L. F. Nazar, *Angew. Chem. Int. Ed*, 2013, **52**, 392 – 396.
25 M. M. Ottakam Thotiyl, S. A. Freunberger, Z. Peng, and P. G. Bruce, *J. Am. Chem. Soc*, 2013, **135**, 494-500

26 B. D. McCloskey, D. S. Bethune, R. M. Shelby, G. Girishkumar, A. C. Luntz, *J. Phys. Chem. Lett,* 2011, **2**, 10, 1161-1166
27 F. Lepoivre, A. Grimaud, D. Larcher, J. M. Tarascon, *Journal of The Electrochemical Society*, 2016, **163** (6) A923-A929
28 C. Delmas, H. Cognac-Auradou, J. M. Cocciantelli, M. Menetrier, J. P. Doumerc, *Solid State Ionics*, 1994, **69**, 257-264
29 X. Xu, F. Xiong, J. Meng, Q. An, L. Mai, *Materials Today Nano*, 2020, **10**, 100073
30 X. Fang, X. Lu, X. Guo, Y. Mao, Y. S. Hu, J. Wang, Z. Wang, F. Wu, H. Liu, L. Chen, *Electrochemistry Communications*, 2010, **12**, 1520-1523
31 M. Carboni, A. Marrani, R. Spezia, S. Brutti, *J. Electrochem Soc*, 2018, **165**, 118–125
32 F. Cheng, Y. Su, J. Liang, Z. Tao, J. Chen, *Chem. Mater,* 2010, **22**, 3, 898–905
33 X. Zheng, G. Shen, C. Wang, Y. Li, D. Dunphy, T. Hasan, C.J. Brinker, B.L. Su, *Nat.Commun*, 2017, **8**, 1–9.
34 J. Chen, X. Mu, M. Du, Y. Lou*, Inorganic Chemistry Communication*, 2017, **84**, 241-245
35 V.S. Jaswal, A.K. Arora, J. Singh, M. Kinger, V.D. Gupta, *Oriental Journal of Chemistry*, 2014, **30**, 2.
36 H. Li et al. *RCS Adv*, 2016,**6**, 79343-79349
37 Kawasaki et al., *J Nanopart Res*, 2013, **15**, 1379
38 C.M. Julien et al., *Journal of Power Sources*, 2012, **202**, 291-298
39 M. Sharrouf et al., *Materials Sciences and Applications,* 2015**, 6**, 850-859
40 B. Gnana Sundara Raj et al., *Journal of Alloys and Compounds*, 2015, **636**, 234-240
41 S. Hosseini et al., *International journal of hydrogen energy*, 2018, **43**, 4961-4966
42 A. Mezni et al., *New J. Chem*, 2017,**41**, 5021-5027
43 W. Li et al., *RSC Adv*, 2014, **4**, 13026–13033
44 R.A. Tes et al., *Journal of Nanoscience and Nanotechnology*, 2015, **15**, 5, 3802-3808

Figure table

Figure 1: Powder X-ray diffraction pattern of the as synthesized CoO, Co_3O_4, Cr_2O_3, Cu_2O, CuO, Fe_3O_4, Fe_2O_3, MnO, MnO_2, Mn_2O_3, Mn_3O_4, NiO, Sc_2O_3, TiO_2, VO_2, V_2O_5 and ZnO (blue) with their references (black). 133
Figure 2: Bright-field TEM micrographs demonstrating morphology and particle size distribution of the as-synthetized metal oxide nanoparticles CoO, Co_3O_4, Cr_2O_3, Cu_2O, CuO, Fe_3O_4, Fe_2O_3, MnO, MnO_2, Mn_2O_3, Mn_3O_4, NiO, Sc_2O_3, TiO_2, VO_2, V_2O_5, ZnO. 136
Figure 3: Cyclic voltammograms obtained from CoO, Co_3O_4, Cr_2O_3, Cu_2O, CuO, Fe_3O_4, Fe_2O_3, MnO, MnO_2, Mn_2O_3, Mn_3O_4, NiO, Sc_2O_3, TiO_2, VO_2, V_2O_5, ZnO, and pure C based electrodes in lithium-oxygen batteries application. 139
Figure 4: Cycling performances of Li-O_2 batteries with Sc_2O_3, TiO_2, VO_2, V_2O_5, Cr_2O_3, MnO, MnO_2, Mn_2O_3, Mn_3O_4, Fe_2O_3, Fe_3O_4, CoO, Co_3O_4, NiO, Cu_2O, CuO, and ZnO at the current density of 150 mA.g^{-1} and capacity fixed at 500 mAh.g^{-1} 142
Figure 5: (a) number of cycles reached by each metal oxides while cycling at a specific capacity of 500 mAh.g^{-1} at a current density of 150 mA.g^{-1} and their respective (b) charge potential, (c) discharge potential, (d) overpotential for the 4th cycle at a capacity of 200 mAh.g^{-1} 143

Figure 6: (a) First discharge capacity (b) overpotential and (c) capacity of the hundredth cycle obtained for all metal oxides at 150 mA.g^{-1} within a 2-4.7 V or 2.2-4.4 V voltage window. 144
Figure 7: First discharge capacity obtained for all metal oxides at 150 mA.g^{-1} within a 2-4.7 V or 2.2-4.4 V voltage window. 145
Figure 8: Experimental Nyquist plot for (a) pure carbon, Cr_2O_3, Fe_3O_4, Fe_2O_3, NiO, Sc_2O_3, TiO_2, VO_2, V_2O_5, ZnO, and (b) pure carbon, CoO, Co_3O_4, Cu_2O, CuO, MnO, MnO_2, Mn_2O_3, Mn_3O_4 based electrodes in lithium-oxygen batteries after the first discharge and (c) their resulting internal resistances. 146
Figure 9: C1s and O1s XPS spectra of (a,b) MnO_2, and (c,d) CoO obtained after 100 cycles at 150 mA.g^{-1} 147
Figure 10: XPS post cycling C-C/CO_3 bonds ratio of all 3d metal oxide used as cathode in Li-O_2 battery..... 147

Table 1: Summary of all crystalline system, space group, nanoparticle and micropore size, and specific surface area of the as synthetised metal oxides. 136
Table 2: First two oxidation and reduction current observed for all 3d metal oxides used as cathode in Li-O_2 batteries. 137

Supplementary Information

ZnO analogous for CoO, NiO, Cu_2O, MnO, and Fe_3O_4

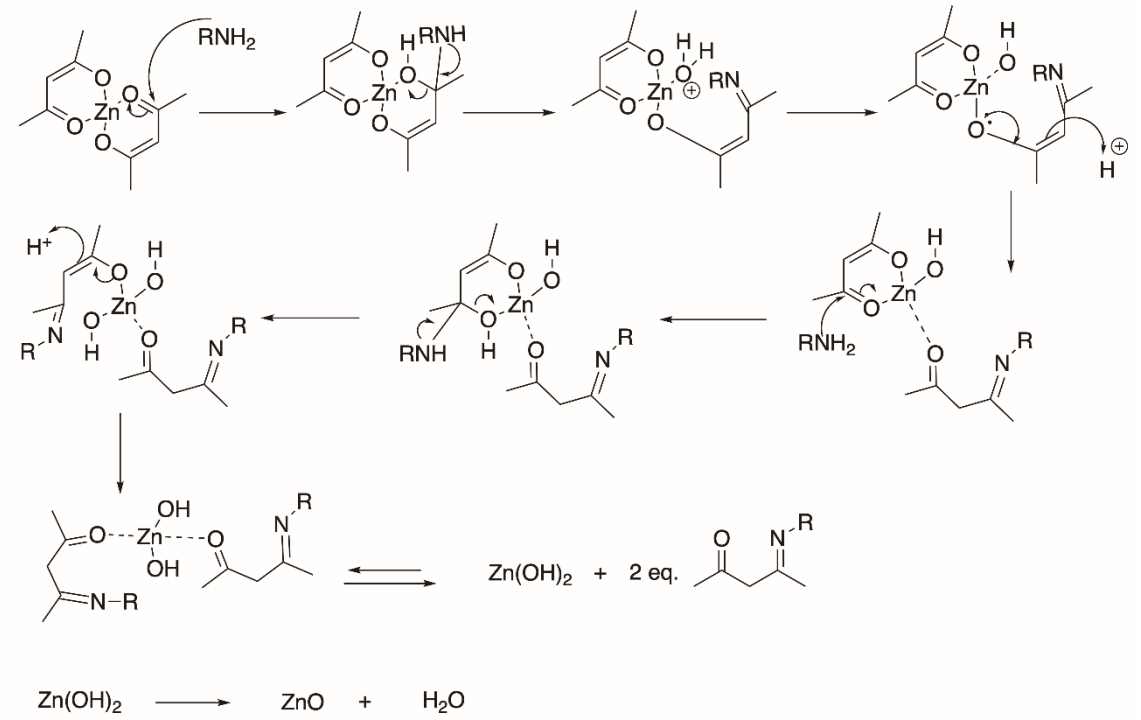

MnO_2

$KMnO_4 + Mn(CH_3CO_2)_2$ ➔ $CH_3COOK + 2\ MnO_2 + CH_3COOH$

Mn_2O_3

$MnCl_2 + (NH_4)HCO_3$ ➔ $MnCO_3 + NH_4Cl + HCl$

$2\ MnCO_3 + 0.5O_2$ ➔ $Mn_2O_3 + 2\ CO_2$

Mn_3O_4

$Mn(CH_3CO_2)_2 + 2KOH$ ➔ $Mn(OH)_2 + 2\ CH_3COOK$

$3Mn(OH)_2 + 0.5\ O_2$ ➔ $Mn_3O_4 + 3\ H_2O$

VO_2

$2\ NH_4VO_3 + C_6H_8O_7 + 5.5\ O_2$ ➔ $2\ VO_2 + 6\ CO_2 + 8\ H_2O + N_2$

V_2O_5

$2\ NH_4VO_3 + 2\ HNO_3 \rightarrow 2\ NH_4NO_3 + V_2O_5 + H_2O$

Fe_2O_3

$2\ FeCl_3 + FeCl_2 + 8\ NaOH + 0.5\ O_2 \rightarrow 3/2\ Fe_2O_3 + 8\ NaCl + 4\ H_2O$

Co_3O_4

$CoCl_2 + (NH_4)_2CO_3 \rightarrow CoCO_3 + 2\ NH_4Cl$

$3\ CoCO_3 + 0.5\ O_2 \rightarrow Co_3O_4 + 3\ CO_2$

Cr_2O_3

$Cr_2(SO_4)_3 + 6\ NaOH \rightarrow 2\ Cr(OH)_3 + 3\ Na_2SO_4$

$2\ Cr(OH)_3 \rightarrow Cr_2O_3 + 3\ H_2O$

CuO

$CuCl_2 + 2NaOH \rightarrow Cu(OH)_2 + 2\ NaCl$

$Cu(OH)_2 \rightarrow CuO + H_2O$

Sc_2O_3

$Sc(NO_3)_3 + C_6H_8O_7 \rightarrow Sc(C_6H_5O_7) + 3\ HNO_3$

$2\ Sc(C_6H_5O_7) + 9\ O_2 \rightarrow Sc_2O_3 + 5\ H_2O + 12\ CO_2$

TiO_2

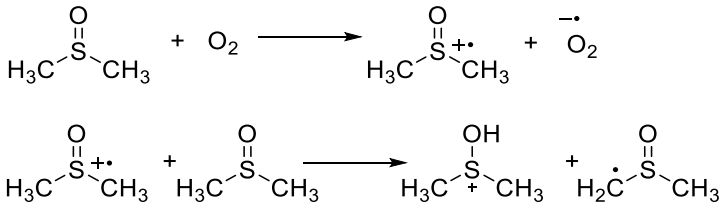

$Ti(OH)_4 \rightarrow TiO_2 + 2H_2O$

Fig S1: Reaction mechanism leading to the formation of each metal oxides

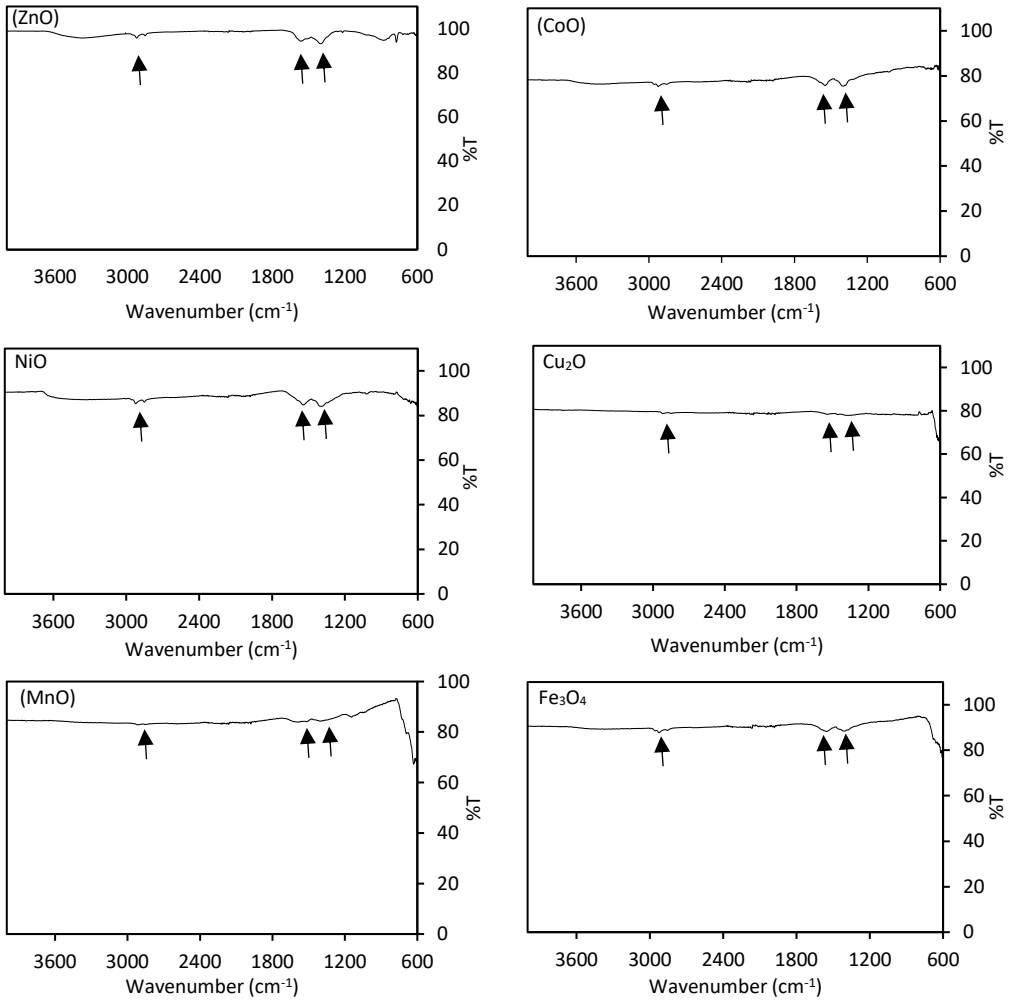
(ZnO)
(CoO)
NiO
Cu_2O
(MnO)
Fe_3O_4
%T
Wavenumber (cm^{-1})
100
80
60
40
20
0
3600
3000
2400
1800
1200
600

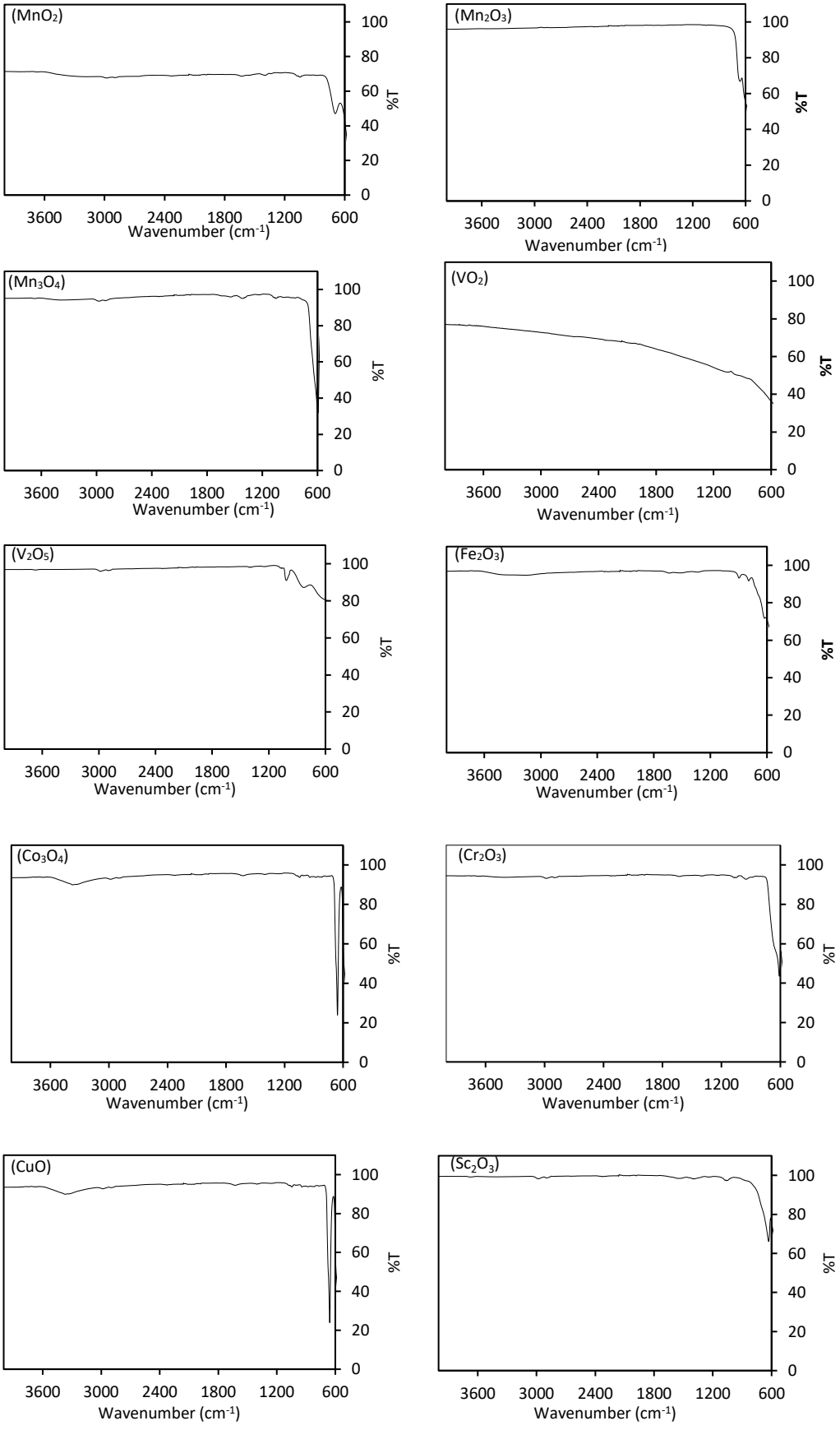
(MnO2)
(Mn2O3)
(Mn3O4)
(VO2)
(V2O5)
(Fe2O3)
(Co3O4)
(Cr2O3)
(CuO)
(Sc2O3)
%T
Wavenumber (cm-1)
3600 3000 2400 1800 1200 600
0 20 40 60 80 100

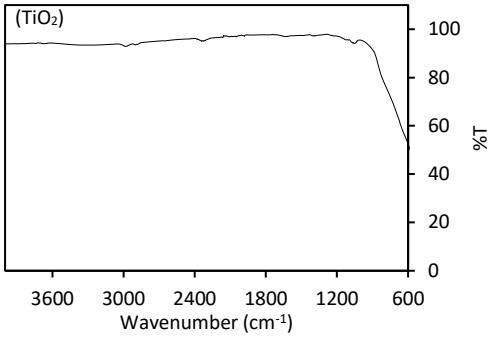

Fig S2: FTIR of the as synthetized ZnO, CoO, NiO, Cu_2O, MnO, Fe_3O_4, MnO_2, Mn_2O_3, Mn_3O_4, VO_2, V_2O_5, Fe_2O_3, Co_3O_4, Cr_2O_3, CuO, Sc_2O_3 and TiO_2 nanoparticles. (Arrows show the theoretical position of the peaks for the oleylamine)

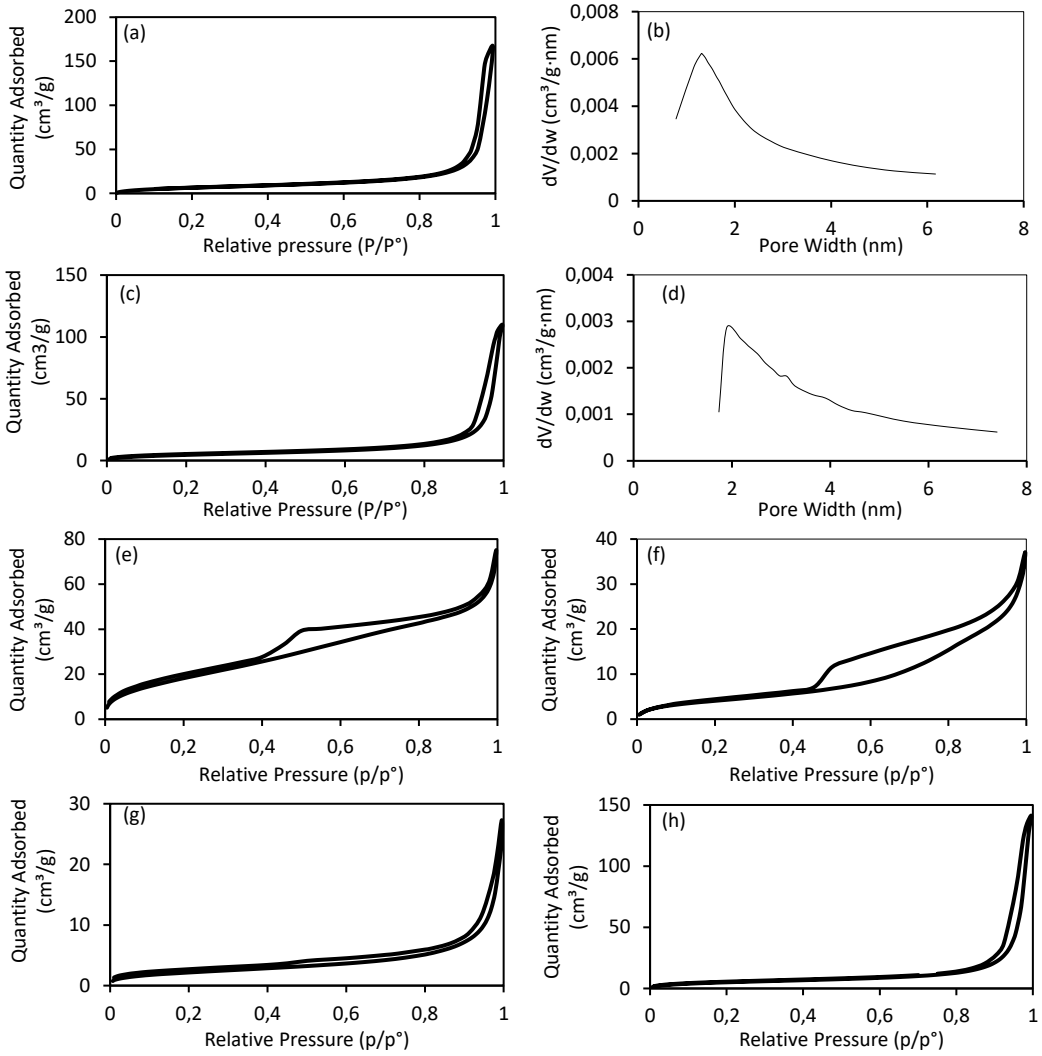

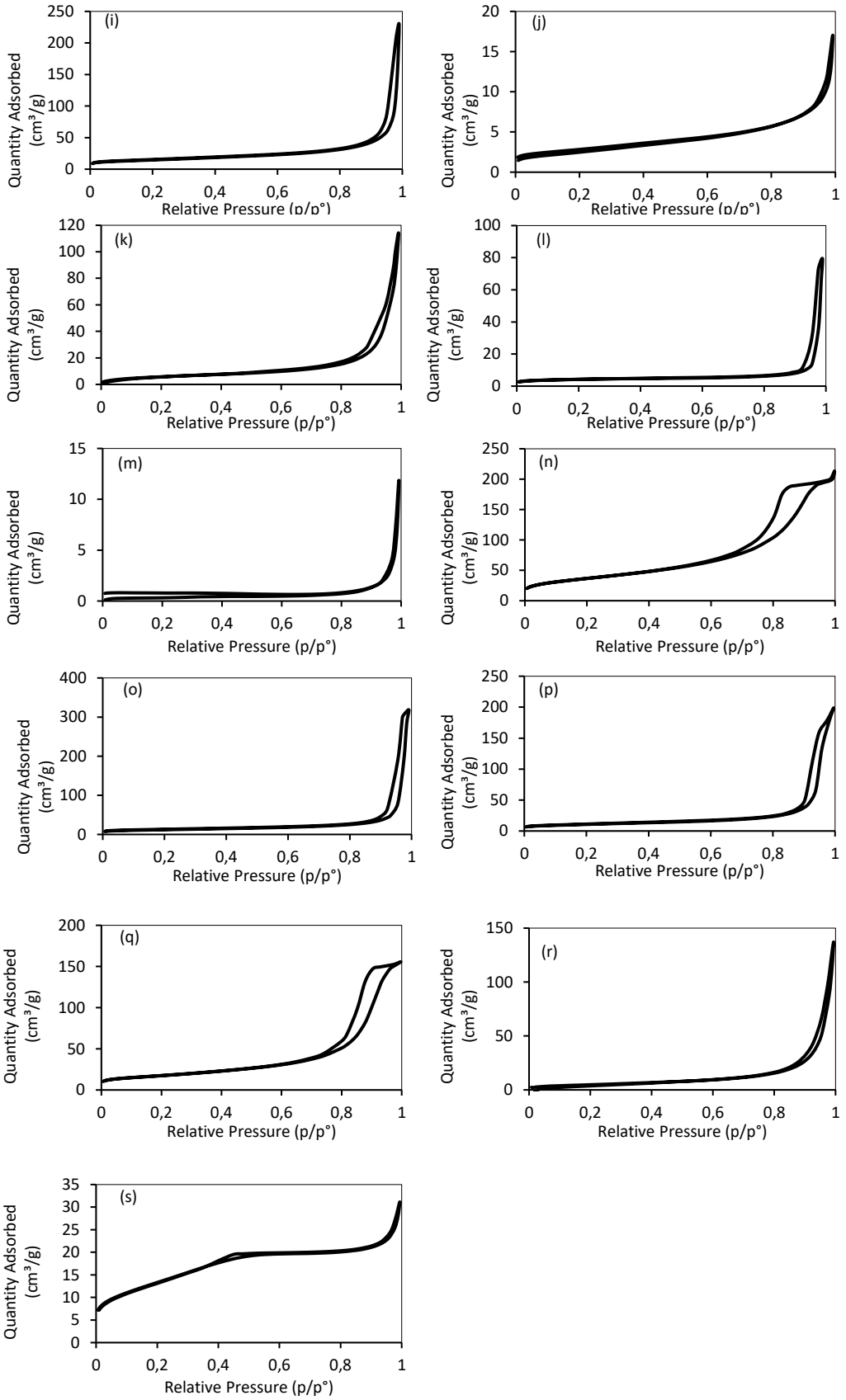

Fig S3: Nitrogen physisorption of the as synthetized (a) ZnO, (c) CoO, (e) NiO, (f) Cu_2O, (g)MnO, (h) Fe_3O_4, (i) MnO_2, (j) Mn_2O_3, (k) Mn_3O_4, (l) VO_2, (m) V_2O_5, (n) Fe_2O_3, (o) Co_3O_4, (p) Cr_2O_3, (q) CuO, (r) Sc_2O_3 and (s) TiO_2 nanoparticles and pore size distribution calculated via Horvath-Kawazoe method for (b) ZnO, and (d) CoO

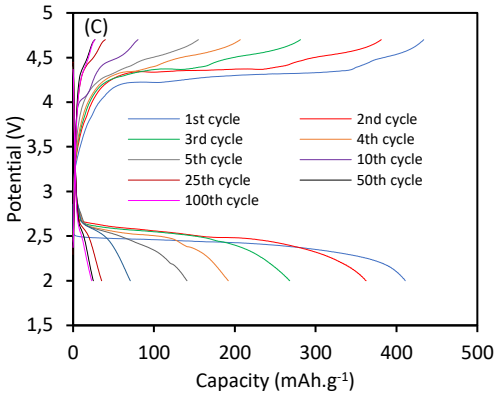
(C)
Potential (V)
Capacity (mAh.g-1)
1st cycle
2nd cycle
3rd cycle
4th cycle
5th cycle
10th cycle
25th cycle
50th cycle
100th cycle

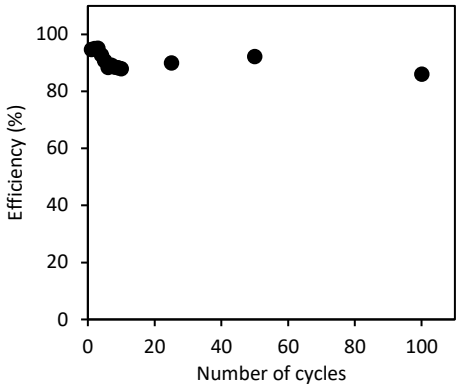
Efficiency (%)
Number of cycles

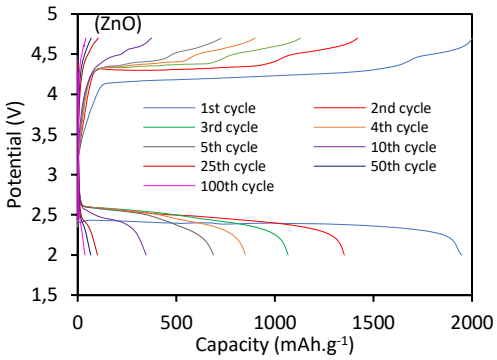
(ZnO)
Potential (V)
Capacity (mAh.g-1)
1st cycle
2nd cycle
3rd cycle
4th cycle
5th cycle
10th cycle
25th cycle
50th cycle
100th cycle

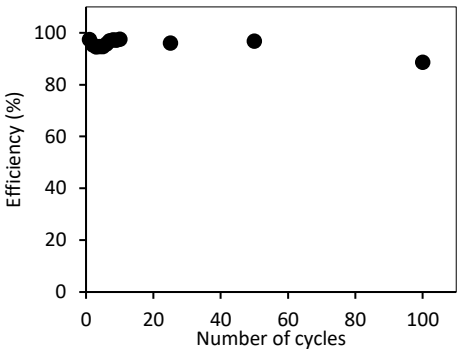
Efficiency (%)
Number of cycles

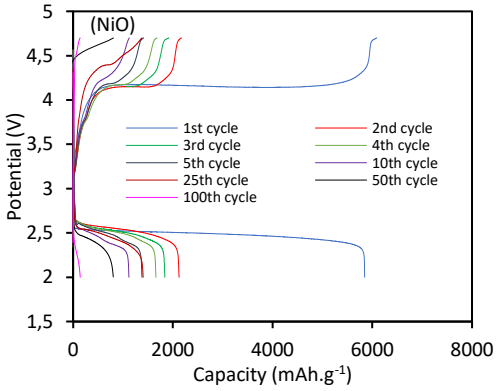
(NiO)
Potential (V)
Capacity (mAh.g-1)
1st cycle
2nd cycle
3rd cycle
4th cycle
5th cycle
10th cycle
25th cycle
50th cycle
100th cycle

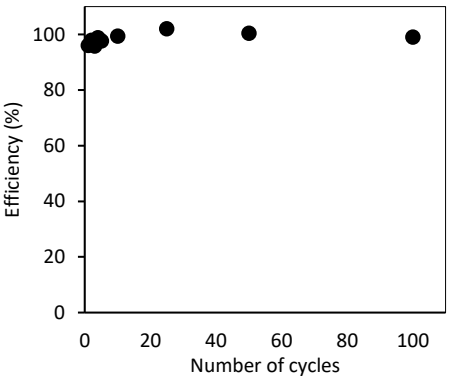
Efficiency (%)
Number of cycles

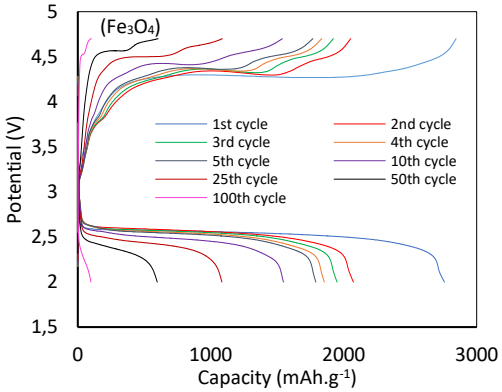
(Fe3O4)
Potential (V)
Capacity (mAh.g-1)
1st cycle
2nd cycle
3rd cycle
4th cycle
5th cycle
10th cycle
25th cycle
50th cycle
100th cycle

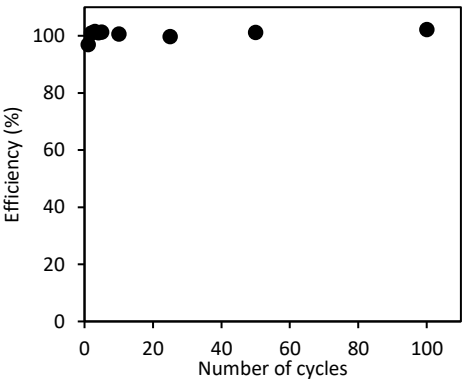
Efficiency (%)
Number of cycles

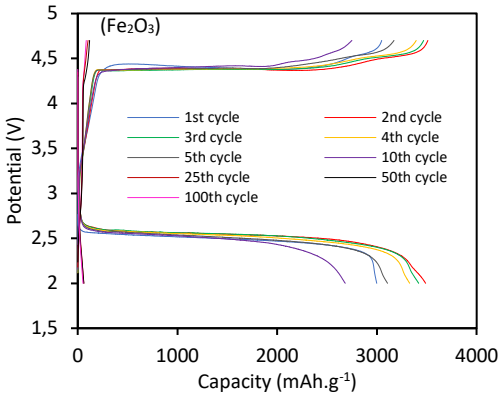
(Fe2O3)
Potential (V)
Capacity (mAh.g-1)
1st cycle
2nd cycle
3rd cycle
4th cycle
5th cycle
10th cycle
25th cycle
50th cycle
100th cycle

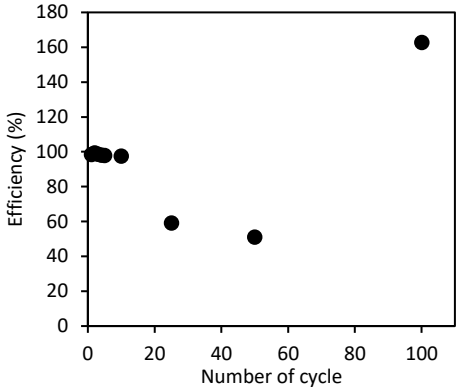
Efficiency (%)
Number of cycle

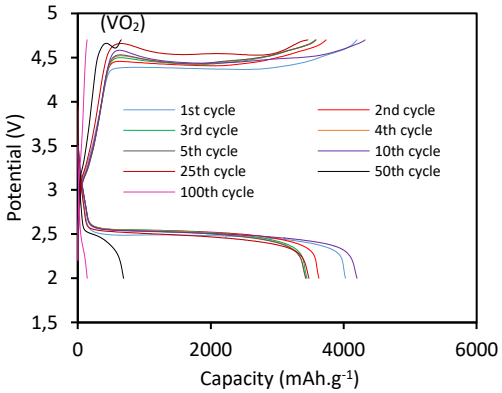
(VO2)
Potential (V)
Capacity (mAh.g-1)
1st cycle
2nd cycle
3rd cycle
4th cycle
5th cycle
10th cycle
25th cycle
50th cycle
100th cycle

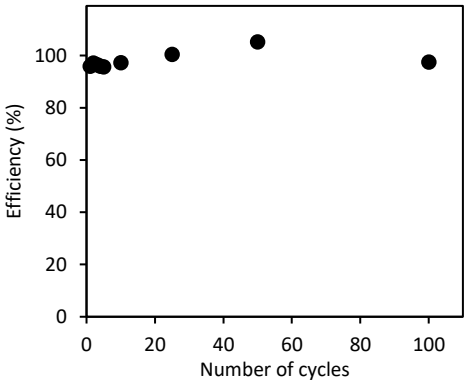
Efficiency (%)
Number of cycles

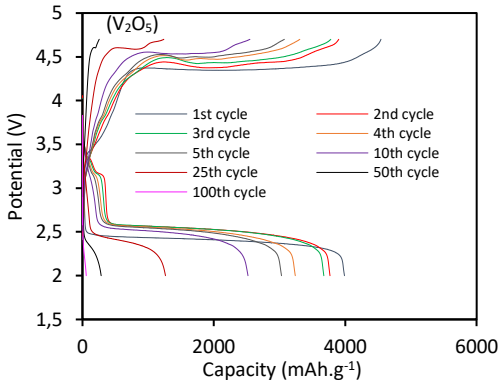
(V2O5)
Potential (V)
Capacity (mAh.g-1)
1st cycle
2nd cycle
3rd cycle
4th cycle
5th cycle
10th cycle
25th cycle
50th cycle
100th cycle

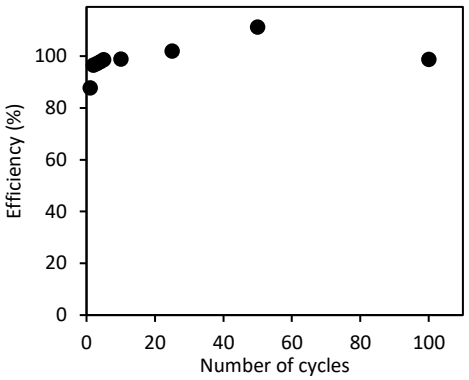
Efficiency (%)
Number of cycles

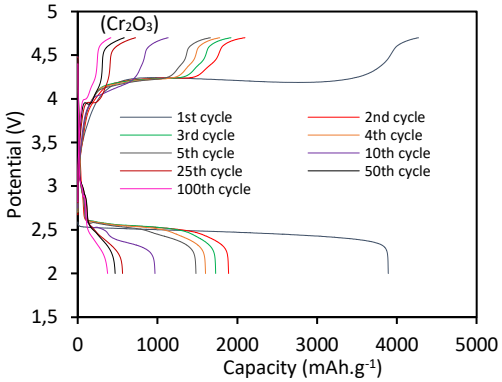
(Cr2O3)
Potential (V)
Capacity (mAh.g-1)
1st cycle
2nd cycle
3rd cycle
4th cycle
5th cycle
10th cycle
25th cycle
50th cycle
100th cycle

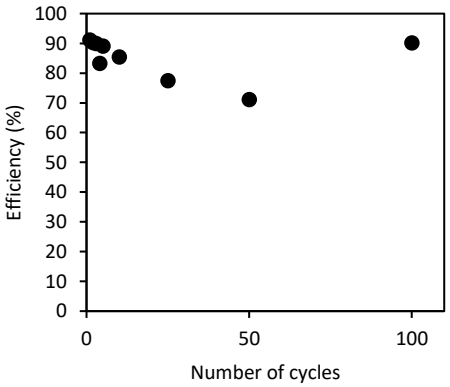
Efficiency (%)
Number of cycles

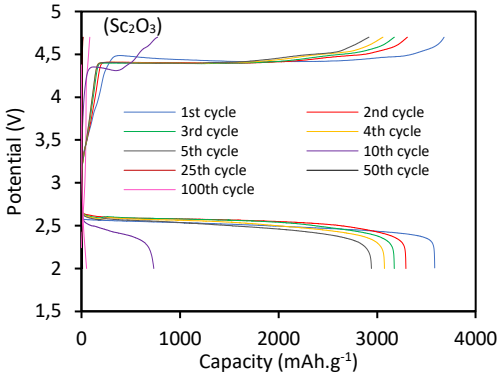
(Sc_2O_3)
Potential (V)
Capacity (mAh.g^{-1})
1st cycle
2nd cycle
3rd cycle
4th cycle
5th cycle
10th cycle
25th cycle
50th cycle
100th cycle

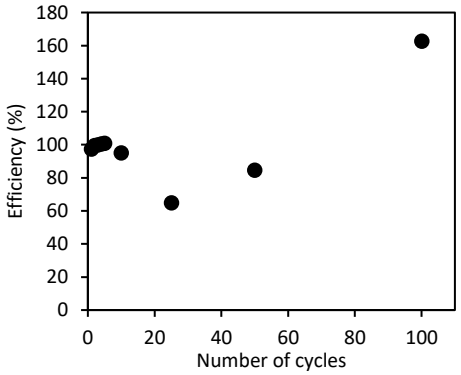
Efficiency (%)
Number of cycles

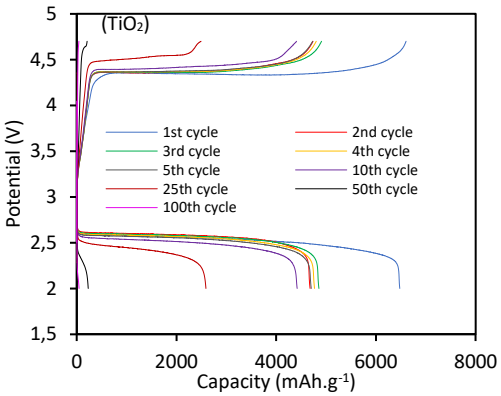
(TiO_2)
Potential (V)
Capacity (mAh.g^{-1})
1st cycle
2nd cycle
3rd cycle
4th cycle
5th cycle
10th cycle
25th cycle
50th cycle
100th cycle

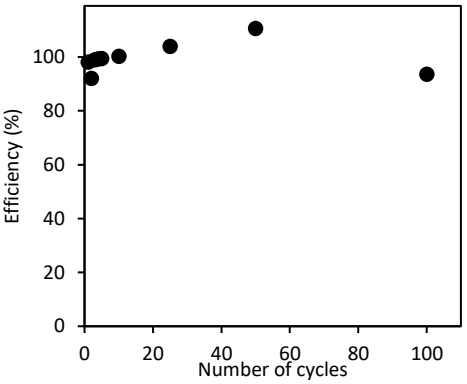
Efficiency (%)
Number of cycles

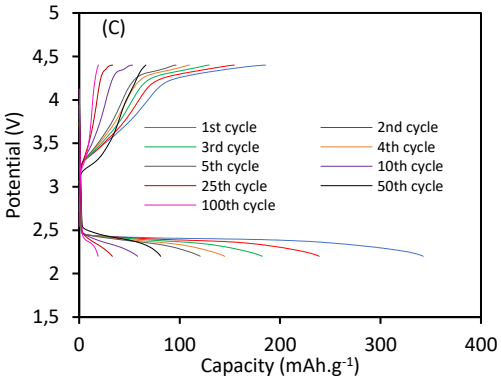
(C)
Potential (V)
Capacity (mAh.g^{-1})
1st cycle
2nd cycle
3rd cycle
4th cycle
5th cycle
10th cycle
25th cycle
50th cycle
100th cycle

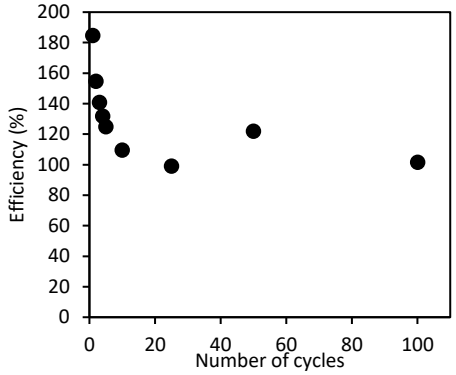
Efficiency (%)
Number of cycles

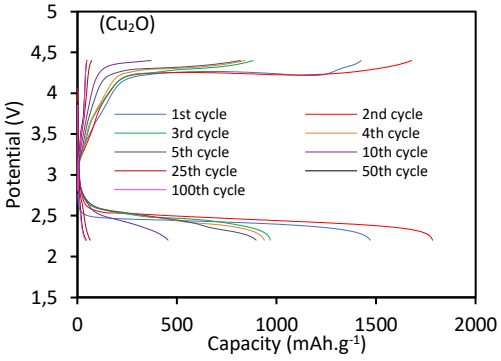
(Cu_2O)
Potential (V)
Capacity (mAh.g^{-1})
1st cycle
2nd cycle
3rd cycle
4th cycle
5th cycle
10th cycle
25th cycle
50th cycle
100th cycle

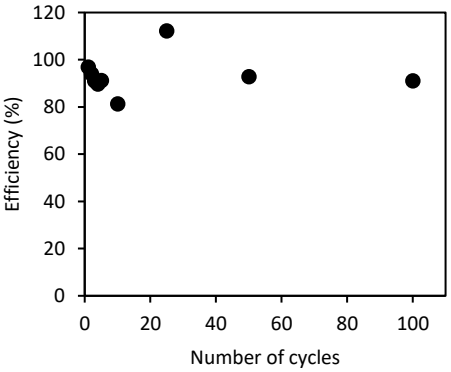
Efficiency (%)
Number of cycles

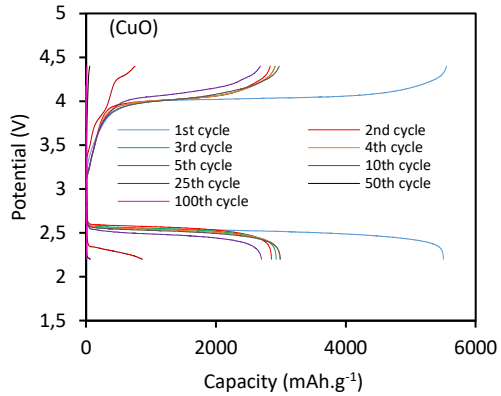
(CuO)
Potential (V)
Capacity (mAh.g-1)
1st cycle
2nd cycle
3rd cycle
4th cycle
5th cycle
10th cycle
25th cycle
50th cycle
100th cycle

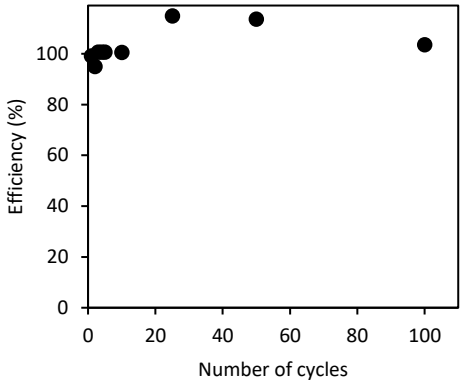
Efficiency (%)
Number of cycles

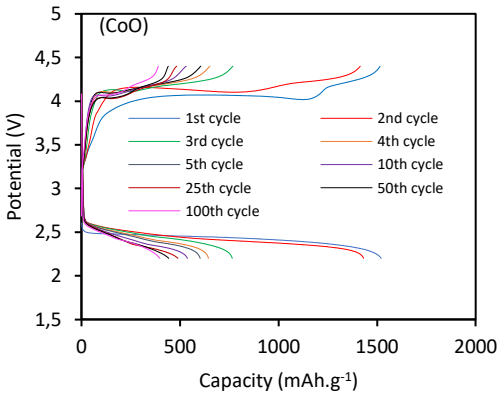
(CoO)
Potential (V)
Capacity (mAh.g-1)
1st cycle
2nd cycle
3rd cycle
4th cycle
5th cycle
10th cycle
25th cycle
50th cycle
100th cycle

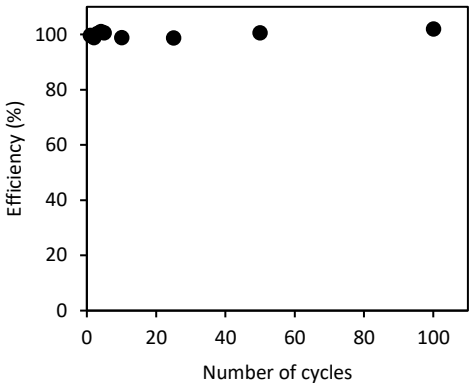
Efficiency (%)
Number of cycles

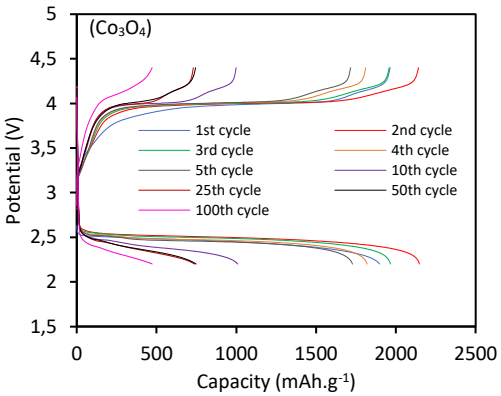
(Co3O4)
Potential (V)
Capacity (mAh.g-1)
1st cycle
2nd cycle
3rd cycle
4th cycle
5th cycle
10th cycle
25th cycle
50th cycle
100th cycle

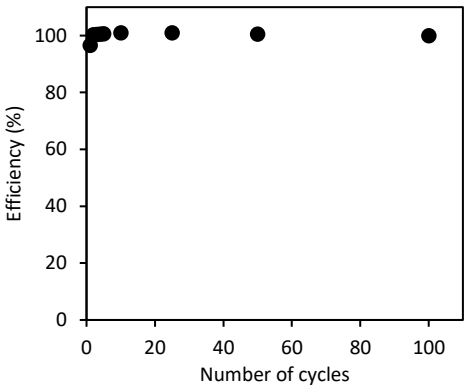
Efficiency (%)
Number of cycles

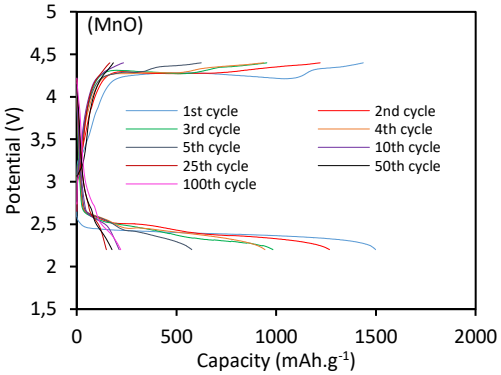
(MnO)
Potential (V)
Capacity (mAh.g-1)
1st cycle
2nd cycle
3rd cycle
4th cycle
5th cycle
10th cycle
25th cycle
50th cycle
100th cycle

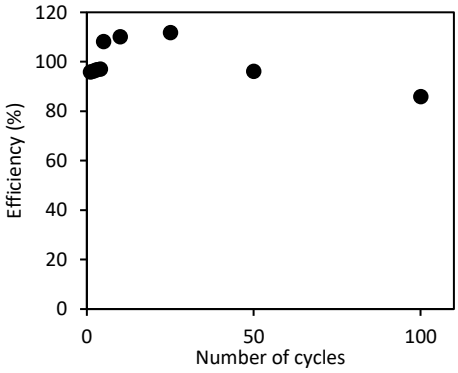
Efficiency (%)
Number of cycles

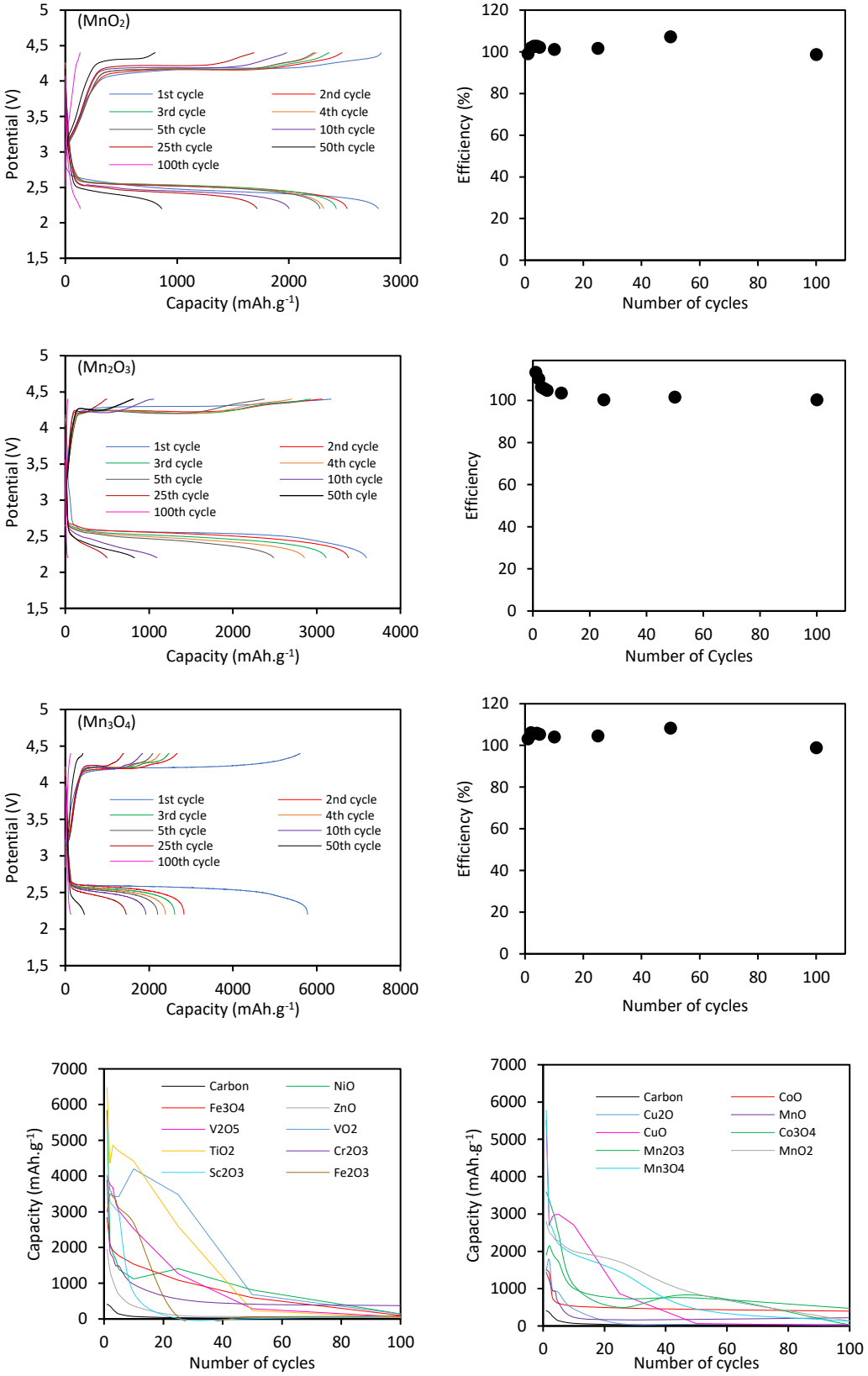

Fig S4: Cycling profile over 100 cycles and the associated efficiency within a 2.0 - 4.7 V voltage windows for C, ZnO, NiO, Fe_3O_4, Fe_2O_3, VO_2, V_2O_5, Cr_2O_3, Sc_2O_3, TiO_2, and within a 2.2 – 4.4 V windows voltage for C, Cu_2O, CuO, CoO, Co_3O_4, MnO, MnO_2, Mn_2O_3, Mn_3O_4 and the evolution of their respective capacities

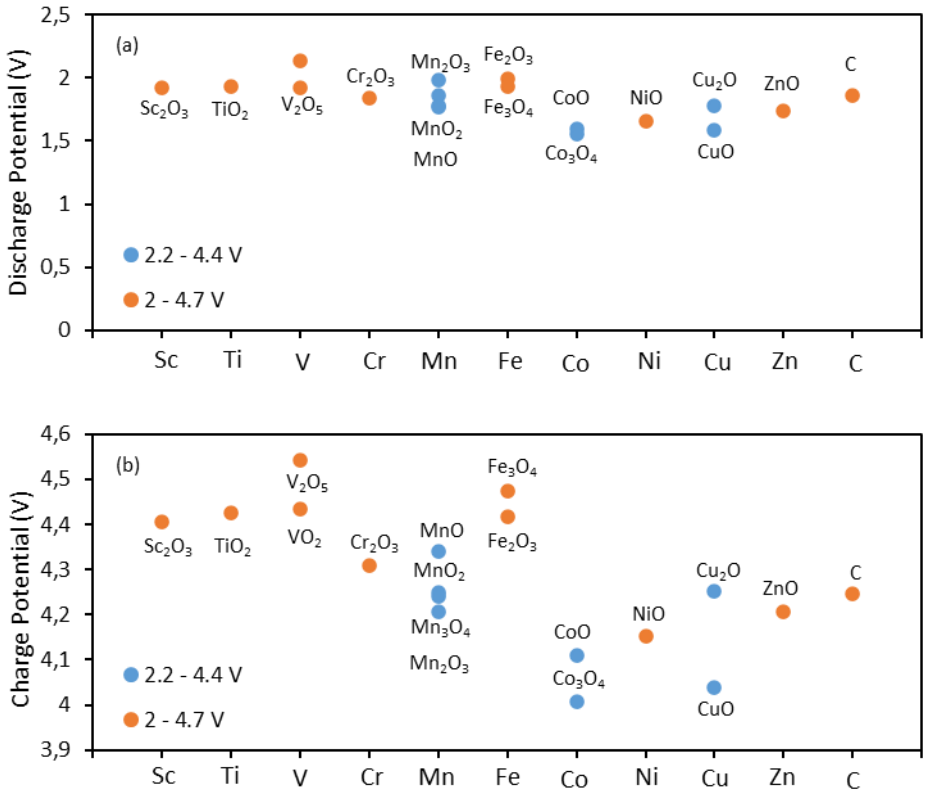

Fig S5: (a) charge and (b) discharge potential plateau for all metal oxides at 150 mA.g^{-1} within a 2-4.7 V or 2.2-4.4 V voltage window

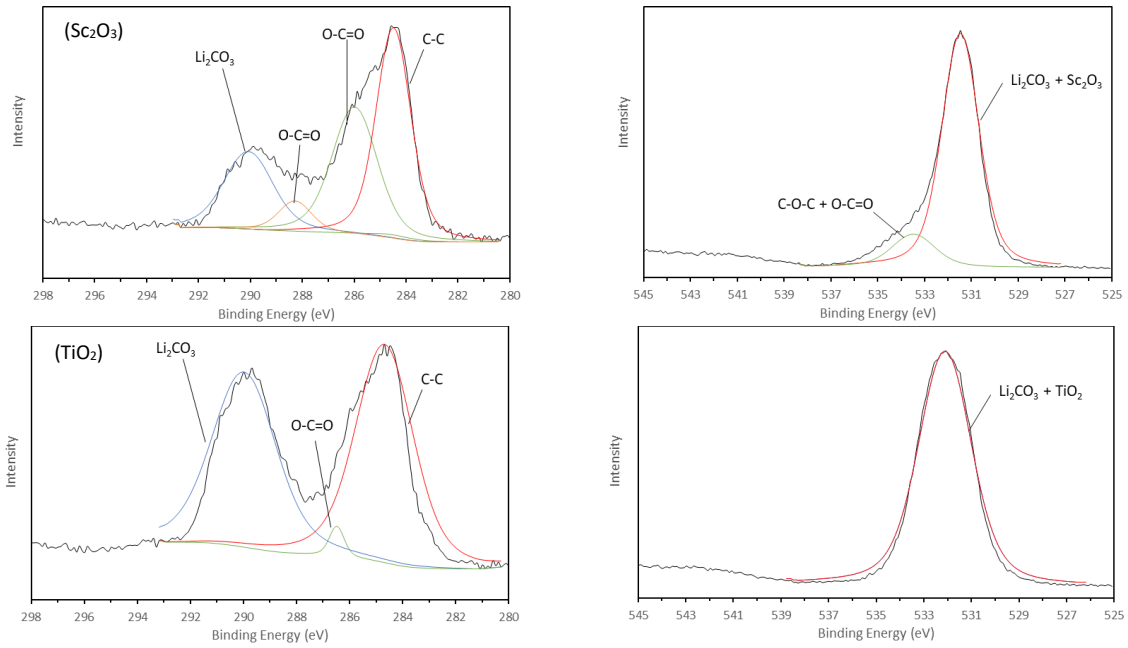

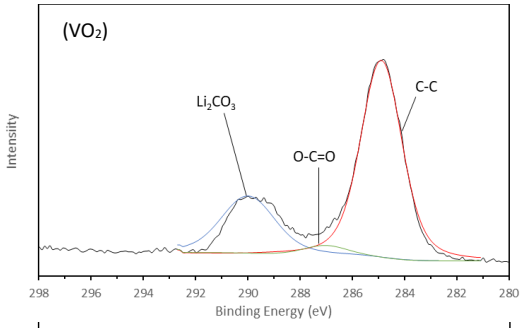
(VO2)
Li2CO3
O-C=O
C-C
Intensity
298 296 294 292 290 288 286 284 282 280
Binding Energy (eV)

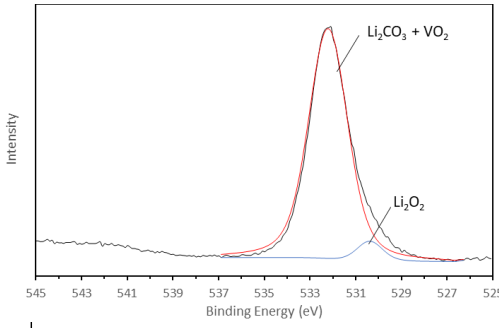
Li2CO3 + VO2
Li2O2
Intensity
545 543 541 539 537 535 533 531 529 527 525
Binding Energy (eV)

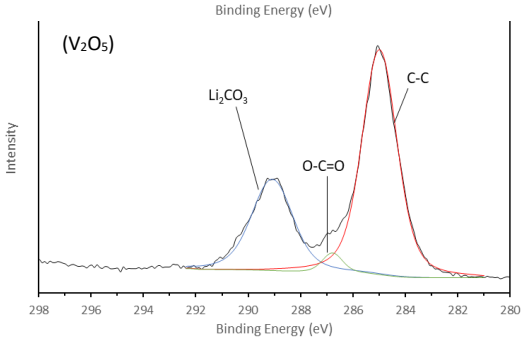
(V2O5)
Li2CO3
O-C=O
C-C
Intensity
298 296 294 292 290 288 286 284 282 280
Binding Energy (eV)

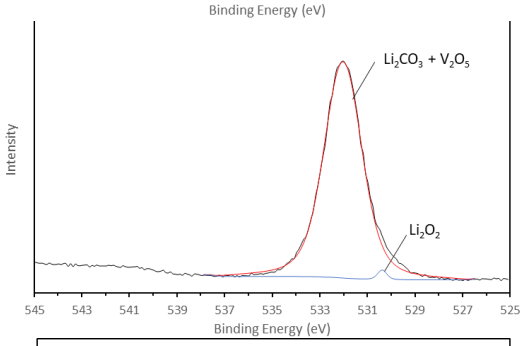
Li2CO3 + V2O5
Li2O2
Intensity
545 543 541 539 537 535 533 531 529 527 525
Binding Energy (eV)

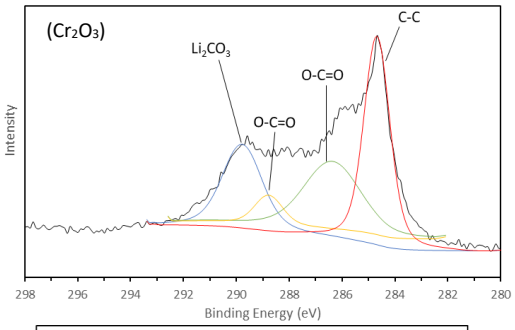
(Cr2O3)
Li2CO3
O-C=O
O-C=O
C-C
Intensity
298 296 294 292 290 288 286 284 282 280
Binding Energy (eV)

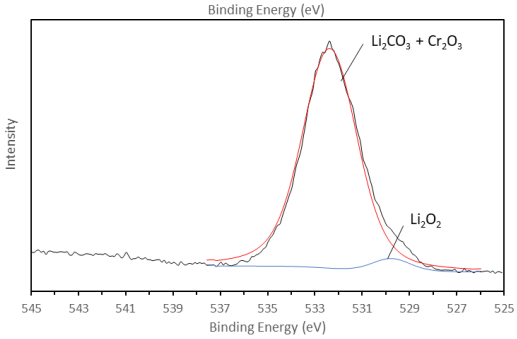
Li2CO3 + Cr2O3
Li2O2
Intensity
545 543 541 539 537 535 533 531 529 527 525
Binding Energy (eV)

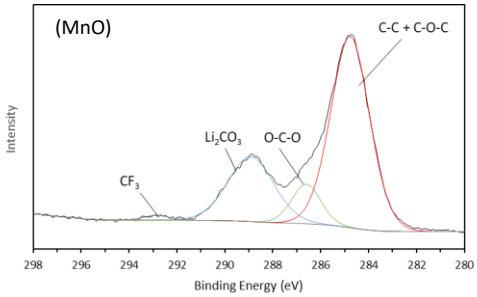
(MnO)
C-C + C-O-C
Li2CO3
O-C-O
CF3
Intensity
298 296 294 292 290 288 286 284 282 280
Binding Energy (eV)

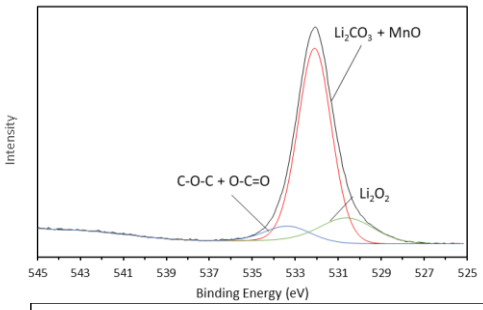
Li2CO3 + MnO
C-O-C + O-C=O
Li2O2
Intensity
545 543 541 539 537 535 533 531 529 527 525
Binding Energy (eV)

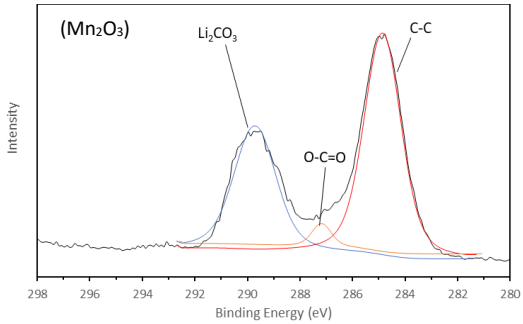
(Mn2O3)
Li2CO3
O-C=O
C-C
Intensity
298 296 294 292 290 288 286 284 282 280
Binding Energy (eV)

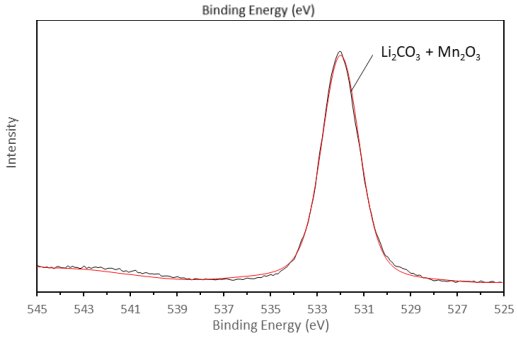
Li2CO3 + Mn2O3
Intensity
545 543 541 539 537 535 533 531 529 527 525
Binding Energy (eV)

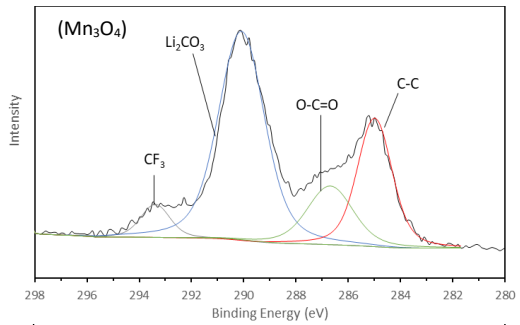
(Mn3O4)
Li2CO3
CF3
O-C=O
C-C
Intensity
298 296 294 292 290 288 286 284 282 280
Binding Energy (eV)

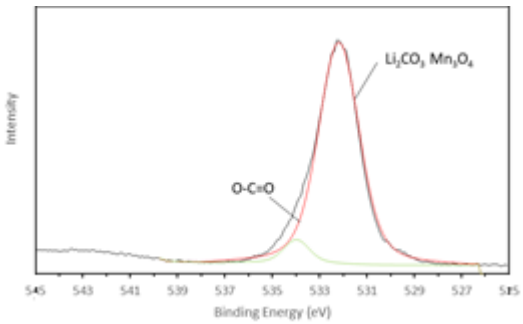
Li2CO3, Mn3O4
O-C=O
Intensity
545 543 541 539 537 535 533 531 529 527 525
Binding Energy (eV)

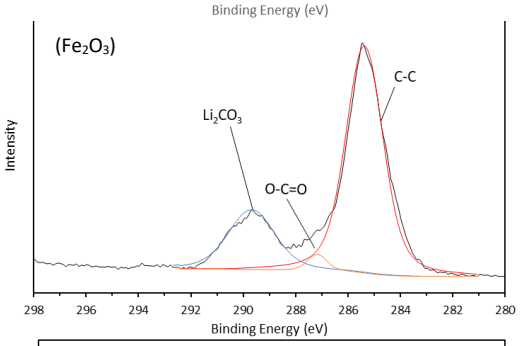
(Fe2O3)
Li2CO3
O-C=O
C-C
Intensity
298 296 294 292 290 288 286 284 282 280
Binding Energy (eV)

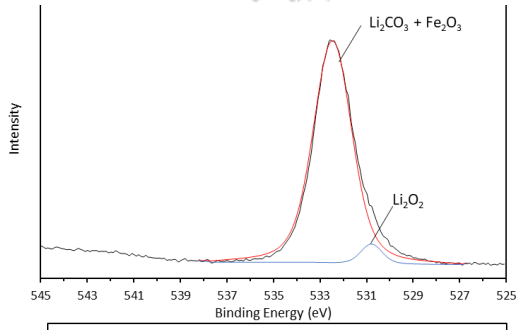
Li2CO3 + Fe2O3
Li2O2
Intensity
545 543 541 539 537 535 533 531 529 527 525
Binding Energy (eV)

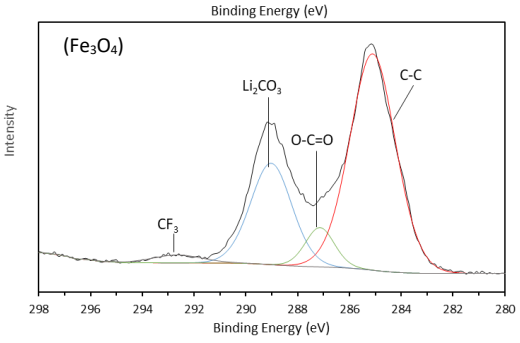
(Fe3O4)
Li2CO3
O-C=O
C-C
CF3
Intensity
298 296 294 292 290 288 286 284 282 280
Binding Energy (eV)

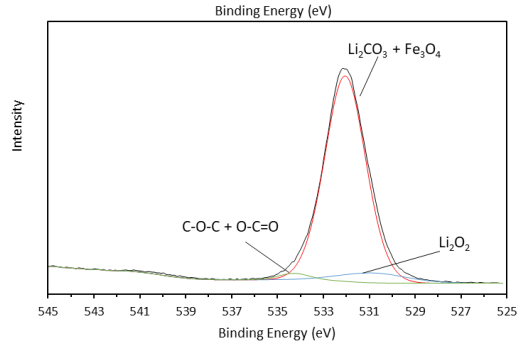
Li2CO3 + Fe3O4
C-O-C + O-C=O
Li2O2
Intensity
545 543 541 539 537 535 533 531 529 527 525
Binding Energy (eV)

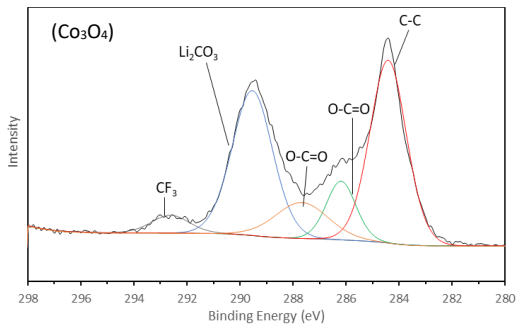
(Co3O4)
Li2CO3
O-C=O
O-C=O
C-C
CF3
Intensity
298 296 294 292 290 288 286 284 282 280
Binding Energy (eV)

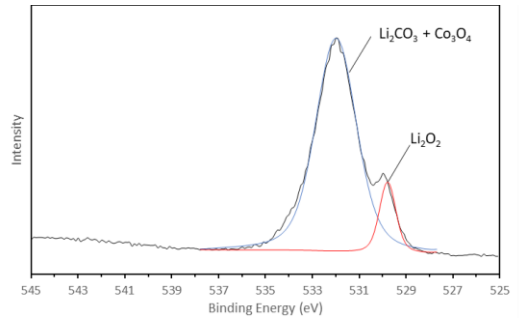
Li2CO3 + Co3O4
Li2O2
Intensity
545 543 541 539 537 535 533 531 529 527 525
Binding Energy (eV)

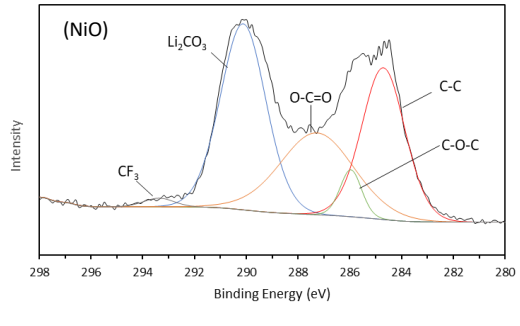
(NiO)
Li2CO3
O-C=O
C-C
C-O-C
CF3
Intensity
298 296 294 292 290 288 286 284 282 280
Binding Energy (eV)

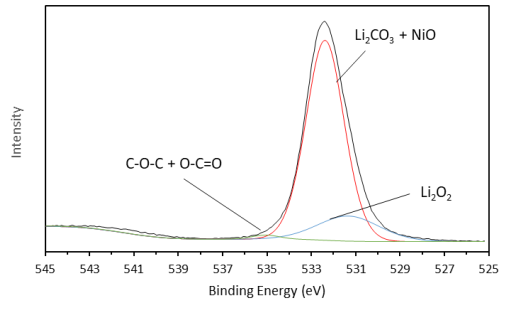
Li2CO3 + NiO
C-O-C + O-C=O
Li2O2
Intensity
545 543 541 539 537 535 533 531 529 527 525
Binding Energy (eV)

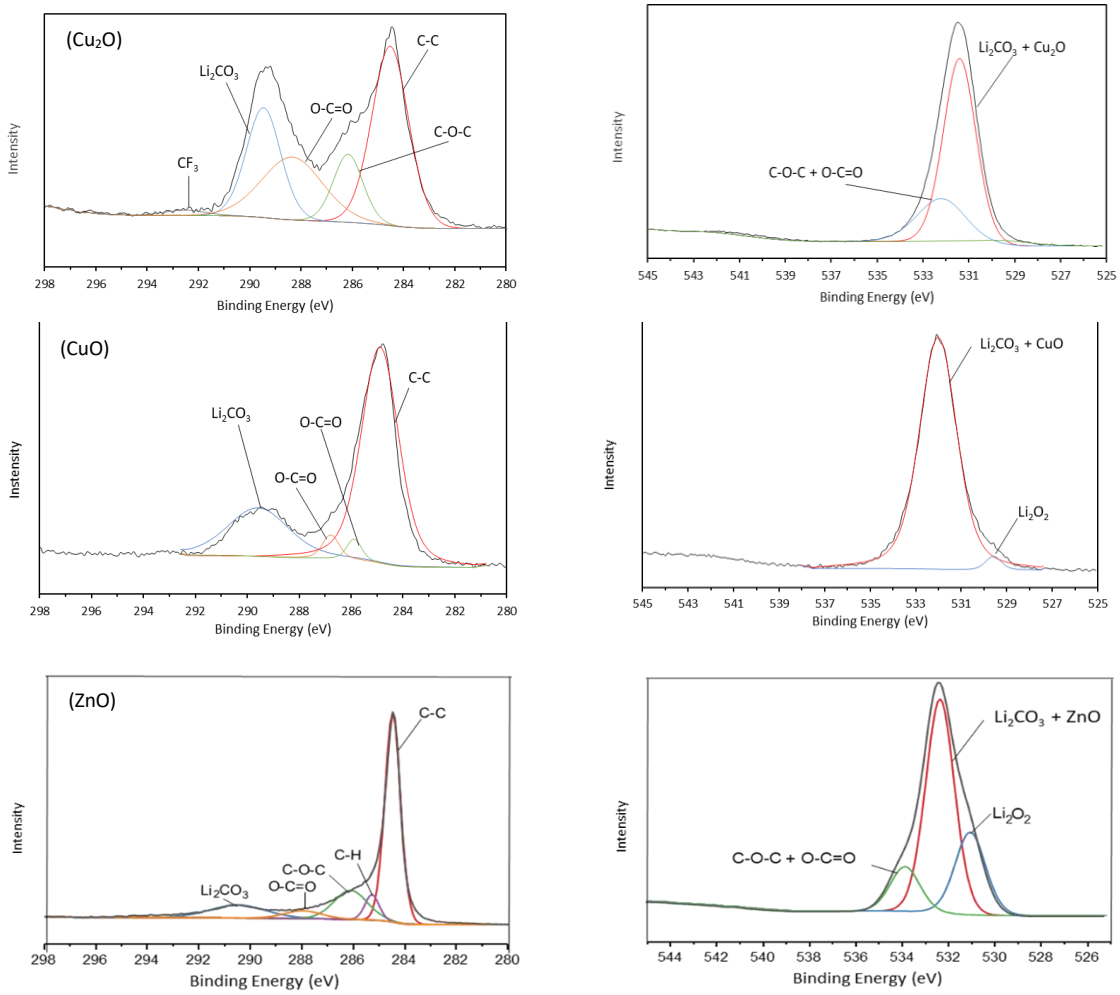

Figure S6: C1s (left) and O1s (right) XPS spectra of Sc_2O_3, TiO_2, VO_2, V_2O_5, Cr_2O_3, MnO, Mn_2O_3, Mn_3O_4, Fe_2O_3, Fe_3O_4, Co_3O_4, NiO, Cu_2O, CuO, and ZnO obtained after 100 cycles at 150 $mA.g^{-1}$

Chapter 5: Carbon free MCo_2O_4 (M = Mn, Ni, Zn) Nano-grass-like cathode: toward the Garden of Eden of the Li-O_2 battery?

Abstract:

The development of an oxygen electrode containing a stable, low-cost catalyst, allowing high electrochemical performance to be achieved, is a major challenge in view of current energy and environmental constraints. In this study, a carbon-free, three-dimensional network structured material composed of MCo_2O_4 (M = Mn, Ni, Zn) nanowires grown on Ni foam were synthesized via a hydrothermal method followed by a heat treatment. The specific network structure, when applied as cathode for lithium-oxygen battery, enables the surface of the nanowires to be highly accessible to reactants and facilitates the transport of electrons during the charge/discharge processes. The battery made with the $MnCo_2O_4$ electrode has the best performance. This work suggests the potential of carbon-free $MnCo_2O_4$@Ni as oxygen-electrodes for lithium-oxygen batteries. it reaches a maximum capacity of 2110.8 $mAh.g^{-1}$ and can perform seven cycles when the capacity is limited to 1000 $mAh.g^{-1}$. This work suggests the great potential of the carbon-free MCo_2O_4@Ni (M = Mn, Ni, Zn) as oxygen electrodes for lithium–oxygen batteries.

Introduction

Energy issues are one of the biggest challenges of the 21st century. The decreasing accessibility of fossil fuels, and political environmental regulations such as the "Paris Agreements" are pushing to limit the production of greenhouse gases to use alternative energy from renewable sources, more respectful of the environment. [1,2] As a result, there is a growing need and interest in safe, reliable high-energy density storage systems for wireless device applications and for storing energy produced by renewable and intermittent energy sources.

Among these systems lithium-ion batteries standing out for their electrochemical characteristics attract increasing attention and are widely used. However, the rapid growth of all-electric, energy-hungry systems is driving the development of new batteries with higher specific energies. A second generation of batteries called metal-air batteries, especially lithium-air batteries, are gaining more and more attention and are increasingly being developed. Their highly theoretical specific energy of 3505 $Wh.kg^{-1}$ which is 10 times higher than that of commercially available lithium-ion batteries puts them in the position of outsiders.[3]

The most commonly employed configuration for lithium-oxygen batteries includes a non-aqueous electrolyte. In this system, during discharge the oxygen is reduced and reacts with the lithium cation Li^+ to form the insoluble compound Li_2O_2. During charge, the previously formed Li_2O_2 decomposes through oxidation to give back lithium cations and oxygen. The reaction can be summarised as follows: $2Li + O_2 \leftrightarrow Li_2O_2$. Such reactions provide high storage capacity and high energy density.[4]

Unfortunately, these high-potential batteries are subject to many limitations. The most current ones are its short life cycle and low energy density. [5] As the cathode is the site of the oxidation and reduction reactions of lithium peroxide, it is important to look for the best parameters in order to reach high capacity, power density, high round-trip efficiency and long cycling life. The two main parameters which need to be controlled are the morphology and the composition. A suitable morphology will optimise the formation of lithium peroxide on the electrode surface. The greater the formation of lithium peroxide, the greater the capacity. The oxidation and reduction reaction of lithium peroxide take place in the cathode. The addition of materials that are stable and accelerate the kinetics of the oxygen reduction reaction (ORR) and the oxygen evolution reaction (OER) during the charge/discharge processes will reduce the overvoltage and limit possible degradation.

Carbon has already been widely used as a cathode material due to their availability, price, weight, large specific surface area and conductivity. [6-9] However, carbon cathode material has strong drawbacks as it is not stable for voltages exceeding 3.5V, that results in the formation of lithium carbonate which leads to severe charge/discharge polarisation. [10] Moreover, lithium carbonate formed during the discharge is insoluble, and thus could not be totally removed during the charge and will clog the cathode. As a result, current density could be reduced by ten to one hundred times, leading to a severe increase of the overpotential, with a consequent decrease in the battery performance.[11] A study performed by Yashina et al. [12] investigate the reactivity of carbon as cathode material in lithium-oxygen batteries, using in situ ambient pressure XPS experiments. They showed that superoxide radicals formed by oxygen reduction promoted nucleophilic addition or electron transfer leading to epoxy-groups on carbon which then are transformed into carbonates. They also demonstrated that carbon

double bonds or aromatic systems activated by the oxygen superoxide and associated defects boosted the carbonate formation.

Precious metals such as Pt, Pd, Ru, Au, Ir and their oxides have been studied as catalysts to stabilise carbon electrodes and increase battery performance and has demonstrated that they promote the reversible formation/decomposition of Li_2O_2 and thus improve charging and cycling performance.[13-16] However, the high cost of noble metals limits their use in cathode material. Metal oxides have also been widely used as catalysts and have the advantage of being less expensive and have shown an improvement in the electrochemical properties and consequently in the general properties of the battery.[17] These catalysts have proven their high effectiveness, allowing a better understanding on the relationship between their physicochemical properties and their electrochemical performances as cathode materials in Li-O_2 batteries. However, the prevention of the formation of lithium carbonate from carbon still remains a great challenge.

The shape of the catalytic converter will also be a key parameter, as the microstructure of the catalyst will largely influence the performance of the battery.[18] Mass transfer at gas-liquid-solid interfaces and low electrode kinetics can lead to an increase in an overpotential and a drop in battery capacity and cyclability. It is therefore necessary to create a specific structure to optimise the slow kinetics of the oxygen reduction reaction and the oxygen evolution reaction.[19,20] Lee et al.[21] evaluated different shapes of carbon-free cobalt oxide cathodes for lithium–oxygen batteries. They synthetised the electrodes via an electrodeposition–conversion process and obtain three main morphologies: nanosheet, nanoneedle, and nanoflower. Experimental capacity reached 1127 $mAh.g^{-1}$ for the nanosheet 1930 $mAh.g^{-1}$ for the nanoflower and 2280 $mAh.g^{-1}$ for the nanoneedle demonstrating that nanoneedle possess a significant advantage over other types of structures.

In this study, we present a carbon-free electrode design based on the spinel structure to overcome the carbon-induced problems of Li-O_2 battery cathodes. The structure chosen for this study is the AB_2O_4 spinel structure and will be mainly based on MCo_2O_4 (M = Mn, Ni, Zn) cobaltite metals. The choice of these materials is justified by their good catalytic activity and good conductivity.[21-28] $NiCo_2O_4$, for instance, is already well known for its bifunctional electrocatalytic activities toward ORR and oxygen evolution reaction (OER) and has been widely used in supercapacitors, Li-ion batteries and recently in Li-S and Na-air batteries.[21-28] Carbon free, porous nano-grass-like MCo_2O_4 (M = Mn, Ni, Zn) nanowire arrays were directly grown on nickel foam using a facile hydrothermal method and were used as oxygen electrodes to investigate the influence of their compositions and morphologies on the performance of the battery. The $MnCo_2O_4$@Ni electrode has the best performance, it reaches a maximum capacity of 2110.8 $mAh.g^{-1}$ and can perform seven cycles when the capacity is limited to 1000 $mAh.g^{-1}$. This performance is explained by the three-dimensional network structure and the catalytic activity of the material on the OER/ORR.

Results and Discussions

MCo_2O_4 (M=Ni, Mn, Zn) synthesis

The detailed synthesis of spinel is reported in the experimental part. A schematic overview of the electrode fabrication process is shown in Figure 1.

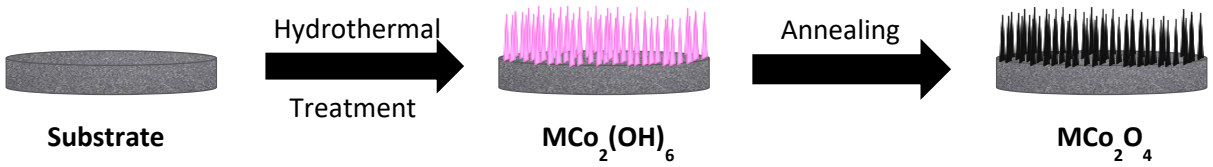

Figure 1: Schematic illustration of the synthesis of the MCo_2O_4 cathodes.

Under hydrothermal conditions, the pH is adjusted by the amount of urea added to the medium. The hydrolysis of the urea allows the growth of a very dense nanowire array of $MCo_2(OH)_6$ precursor to grow in grass form on the nickel foam. Their annealing under air enables the formation of the final spinel structure to be obtained. The following equations describe the synthesis mechanism:

$$CO(NH_2)_2 + H_2O \rightarrow 2NH_3 + CO_2 \quad (1.1)$$

$$NH_3 + H_2O \rightarrow NH_4^+ + OH^- \quad (1.2)$$

$$M^{2+} + 2\ Co^{2+} + 6\ OH^- \rightarrow MCo_2(OH)_6 \quad (1.3)$$

$$MCo_2(OH)_6 + 0.5\ O_2 \rightarrow MCo_2O_4 + 3\ H_2O \quad (1.4)$$

It should be noted that all the nanowires were formed on the surface of the nickel foam by the addition of NH_4F during the synthesis. F^- provided by NH_4F can activate the initial nucleation, improving the adhesion of the substrate to the precursor and facilitate growth. [29]

NiO and Co_3O_4 nanowires array on Ni foam were also prepared as reference samples.

Crystalline phase and morphology

The crystalline phase of the MCo_2O_4 (M=Ni, Mn, Zn), and two reference samples NiO and Co_3O_4 was analysed by XRD and the diffractograms are shown in Figure 2 and Figure S1. All of the diffraction peaks can be indexed in those of the reference JCPDS files. All materials have a spinel crystalline structure while NiO adopts a NaCl type structure. It is worth noting that a small amount of ZnO is present in the $ZnCo_2O_4$ sample. The impurity ZnO can come from the high reactivity of zinc in basic solution leading to the formation of zinc hydroxide which after annealing forms zinc oxide.[17]

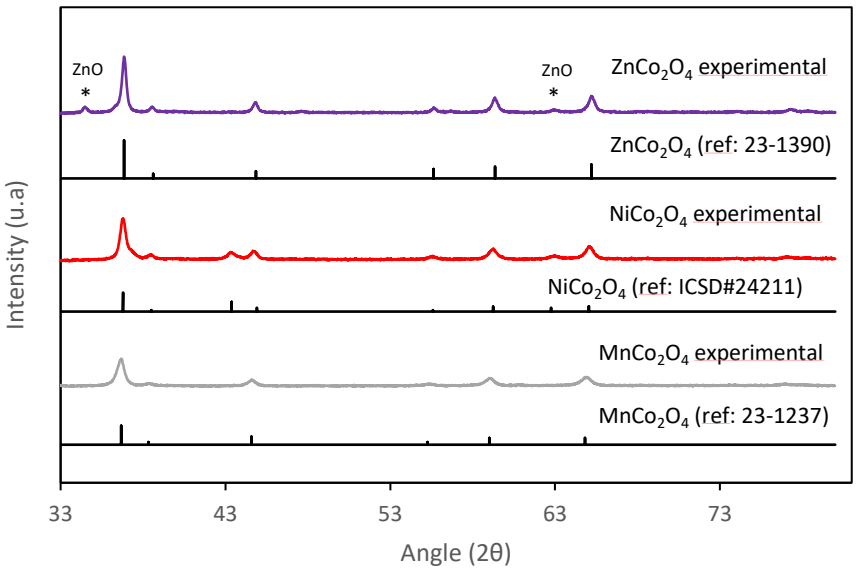

Figure 2 : Powder X-ray diffraction pattern of the as synthesized $NiCo_2O_4$, $MnCo_2O_4$, and $ZnCo_2O_4$, with their references.

The morphology of MCo_2O_4 (M=Ni, Mn, Zn), NiO and Co_3O_4 on the nickel foam was analysed by SEM and is shown in Figure 3 and Figure S2. All electrodes present a well dense nanowire arrays, where the nanowires grow vertically and uniformly on the surface of the nickel foam. However, some differences can be observed between the samples. The nickel oxide-based nanowire array has the smallest length of nanowire. $ZnCo_2O_4$ nanowire array with the thinnest and longest nanowire. This specific shape leads to a superior entanglement of the nanowire. Co_3O_4, $NiCo_2O_4$ and $MnCo_2O_4$ have the same nanowire shape. In terms of size, the Co_3O_4 nanowire is the tallest, followed by $MnCo_2O_4$ and $NiCo_2O_4$.

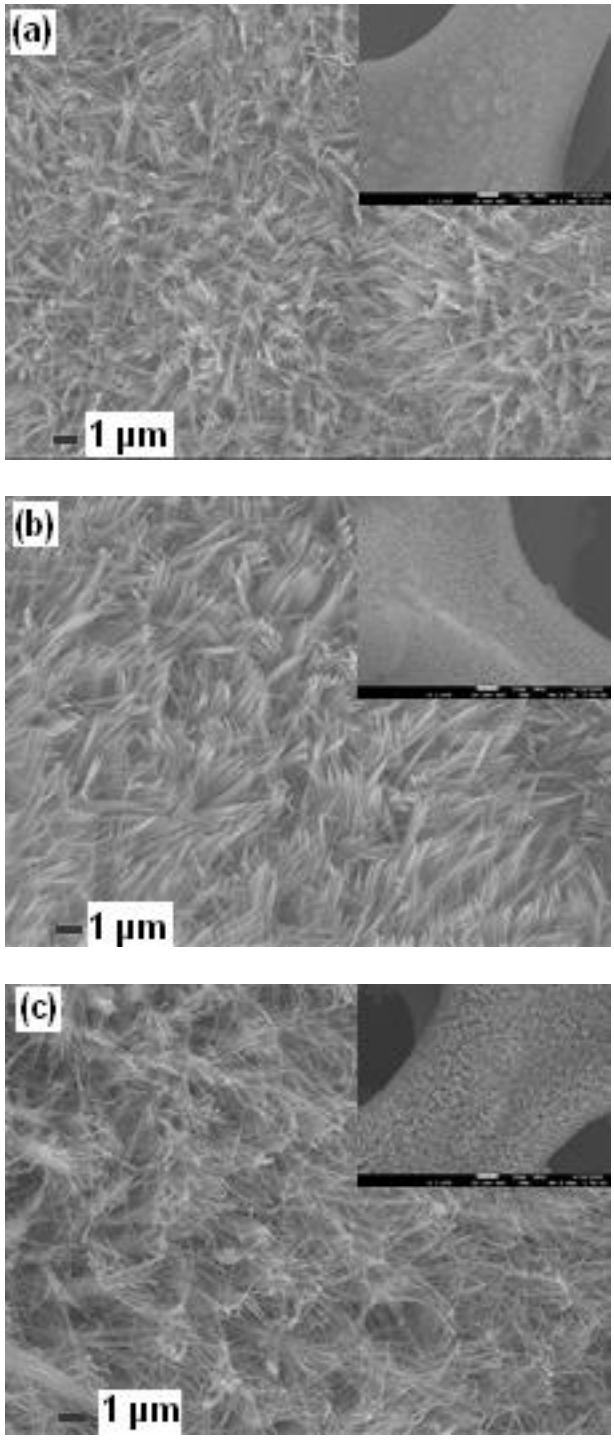

***Figure 3:* SEM micrographs demonstrating morphology of the as synthetized (a) $NiCo_2O_4$, (b) $MnCo_2O_4$, (c) $ZnCo_2O_4$ on nickel foam**

Transmission electron microscopy was used to study the morphology of the nanoparticles. Micrographs are presented in Figure 4 and Figure S3. It shows that all the samples are made up of rod assemblies to give a kebab shape. These rods are formed by a succession of nanoparticles having an elongated shape and connected by their vertices. NiO has the smallest rods (77 nm), followed by $MnCo_2O_4$ (246 nm), $ZnCo_2O_4$ (420 nm), Co_3O_4 (875 nm) and $NiCo_2O_4$ (973 nm). A nitrogen physisorption analysis has been carried out to determine the specific surface area and the pore size distribution and

are available in the supplementary information (Figure S4). The specific surface area is 16, 34, 19, 39, 19 $m^2.g^{-1}$ for Co_3O_4, NiO, $NiCo_2O_4$, $MnCo_2O_4$ and $ZnCo_2O_4$ respectively. The average pore size is 0.97 nm for Co_3O_4, NiO, $MnCo_2O_4$ and $ZnCo_2O_4$ and 0.95 nm for $NiCo_2O_4$. The average crystallite size, average pore size and specific surface area for each material is summarised in Table 1.

Table 1 : Summary of the length, width, specific surface area and average pore size of all nanoparticles.

Material	Length Nanoparticles size (nm)	Width Nanoparticles size (nm)	Specific surface area ($m^2.g^{-1}$)	Average pore size (nm)
Co_3O_4	875	47	16	0.97
NiO	77	31	34	0.97
$NiCo_2O_4$	973	33	19	0.95
$MnCo_2O_4$	246	23	39	0.97
$ZnCo_2O_4$	420	21	19	0.97

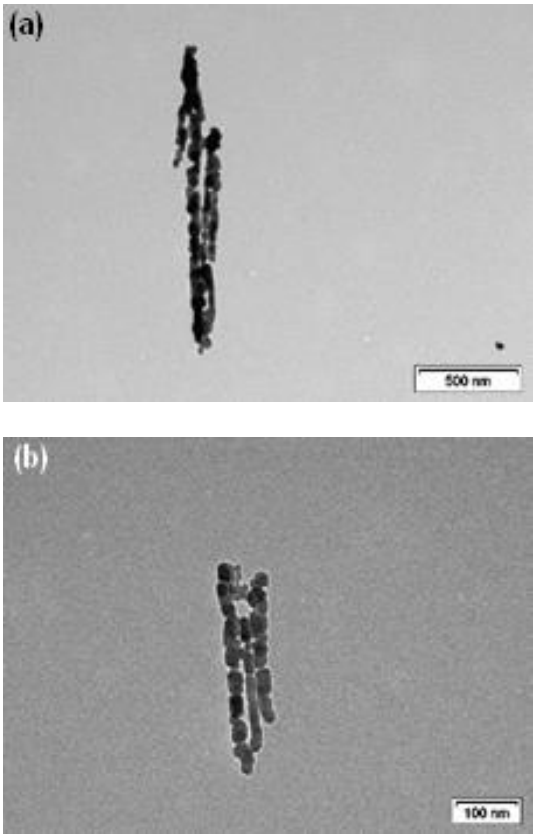

Figure 4 : Bright-field TEM micrographs demonstrating morphology and particle size of the as synthetized (a) $NiCo_2O_4$, (b) $MnCo_2O_4$, (c) $ZnCo_2O_4$.

Electrochemical studies

The catalytic activity of all nanowire arrays on OER/ORR process was examined by cyclic voltammetry (CV). The results obtained are reported in Figure 5 and Figure S5. All cyclic voltammograms appear similarity. The higher the current, the more electrons are transferred per oxygen molecule and the higher the reaction kinetics. It displays one reduction peak corresponding to the ORR (formation of Li_2O_2) and two oxidation peaks related to the OER (decomposition of Li_2O_2). The first peak at ~3.3 V can be attributed to the decomposition of nonstoichiometric $Li_{2-x}O_2$, and the second peak at ~3.96 V indicates the decomposition of dense Li_2O_2 film.[30-31] Over the first five cycles, the $MnCo_2O_4$ electrode shows the highest ORR/OER current density and largest integration areas during the cathodic and anodic scans, indicating that the $MnCo_2O_4$ cathode has the best electrocatalytic activity over other electrodes (Figure 5b). On the contrary, NiO cathode exhibits the lowest ORR/OER current and the smallest integration areas reflecting its low electrocatalytic activity (Figure S5b). $NiCo_2O_4$, $ZnCo_2O_4$, and Co_3O_4, have an initial oxidation current of about 0.0006 A and a reduction current of 0.0006 A for $NiCo_2O_4$ and Co_3O_4 and 0.0004V for $ZnCo_2O_4$. Over the five cycles the potential decreases, reflecting a decrease in electron transfer. This decrease in current may be due to the creation of insolent species on the cathode surface, preventing electrode flow.

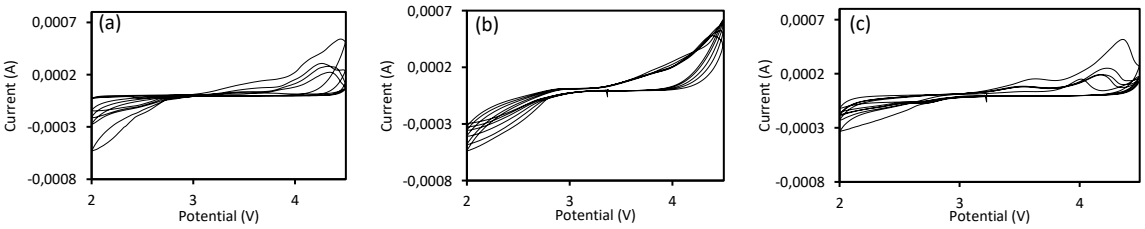

Figure 5: Cyclic voltammograms obtained from, (a) $NiCo_2O_4$, (b) $MnCo_2O_4$, and (c) $ZnCo_2O_4$ nanowire arrays electrodes in lithium-oxygen battery application.

The EIS analysis results for each electrode is shown in Figure 6. The Nyquist plots can be divided into two parts: the semicircle in the high frequency region is associated to the charge transfer resistance and the line in the low frequency region is related to the ion diffusion in the electrodes. Higher charge-transfer resistance leads to slower charge-transfer kinetics. The charge-transfer resistance has been

calculated. $NiCo_2O_4$, $ZnCo_2O_4$, Co_3O_4 and NiO electrodes have the smallest semicircle, which means that they have the lowest charge transfer resistance (311, 346, 425 and 642 ohms, respectively). This lower charge transfer resistance may reflect the good conductivity of the compounds but also their low catalytic activity leading to the formation of a small amount of insulating Li_2O_2. $MnCo_2O_4$ electrode has the highest charge transfer resistance (2229 ohms) which can express its low conductivity and/or high catalytic efficiency to the ORR leading to the formation of a thick layer of insulating Li_2O_2 that impedes the electron flow.

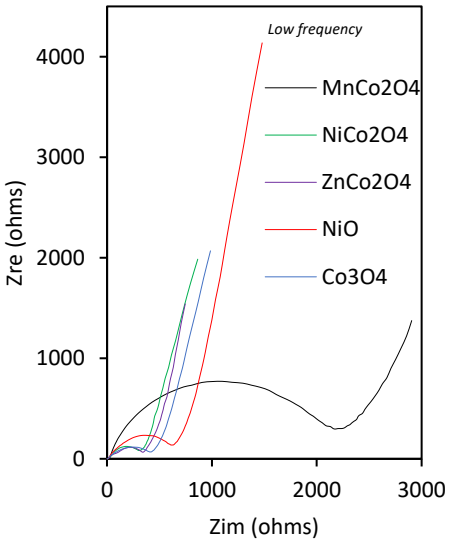

Figure 6: Experimental Nyquist plot for Co_3O_4, NiO, $NiCo_2O_4$, $MnCo_2O_4$, and $ZnCo_2O_4$ electrodes in lithium-oxygen batteries.

The performance of batteries built with Co_3O_4, NiO or MCo_2O_4 (M=Ni, Mn, Zn) cathodes has been evaluated via charge-discharge cycles within a cut-off voltage window of 2.3 to 4.3 V. The applied voltage was determined according to the protocol of Park et al [30] who demonstrated that to achieve optimal deposition and dissolution of lithium peroxide on the nanowires, a voltage of 0.1 $mA.cm^{-2}$ must be applied during charging and 0.3 $mA.cm^{-2}$ during discharge. This higher voltage compensates for a higher surface-charge density, which is electrochemically more active on the top of the nanowire array than on the bottom. This difference in surface-charge density results, at low discharge rate, in the formation of crystalline Li_2O_2 at the top of the nanowires, which blocks the access to the bottom of the nanowires and can even clump or break them. At higher discharge rate, Li_2O_2 precipitates at the top region of the nanowire, forming a film of smaller and less crystalline discharge products. The film deposited at the top of the film allows the lower part of the nanotube network to be usable and form Li_2O_2. The phenomenon is illustrated in Figure 7.

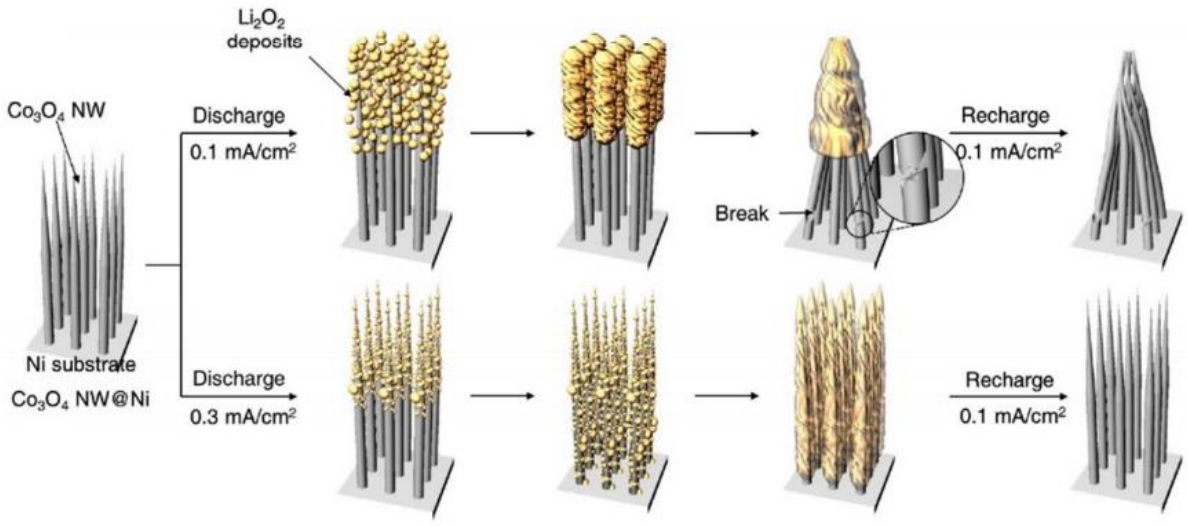

Figure 7: A schematic illustration of the structural evolution of the Co_3O_4 NW array with the low and high discharge rates. [31]

The first hundred full discharge and charge profiles are shown in Figure 8, and the associated efficiency in Figure S6. The first cycle capacity reached with NiO, Co_3O_4, $NiCo_2O_4$, $ZnCo_2O_4$, $MnCo_2O_4$ are 30.1, 400.4, 61.5, 766.4 and 2110.8 $mAh.g^{-1}$ respectively. The NiO electrode has the lowest capacity. This poor performance can be explained by the low catalytic activity on the OER and ORR observed during cyclic voltammetry, but also by its charge transfer resistance probably due to the resistivity of NiO. The $NiCo_2O_4$ electrode also exhibits a low capacity. This result is surprising as the electrode has similar characteristics to the Co_3O_4 electrode regarding morphology, catalytic activity on the OER/ORR and internal resistance, while its capacity obtained is 6.5 times lower. The good capacity reached by $ZnCo_2O_4$ can be explained by its catalytic properties according to the OER/ORR, by its low internal resistance but also by its morphology. In fact, $ZnCo_2O_4$ nano-grass electrode have the thinnest nano-needles, thus potentially allowing more lithium peroxide to be deposited. The highest capacity is achieved with the $MnCo_2O_4$ electrode. This result agrees with the results obtained by CV. The high resistance observed by EIS could be explained by the formation of a thick layer of insulating lithium peroxide.

From the second cycle, the capacities of all cathodes sharply decrease. The only electrode that retains a good capacity in spite of its high decrease is the $MnCo_2O_4$ cathode. The slower decrease in capacity is consistent with the results obtained in CV. The catalytic activity on the OER remains constant compared to the other electrodes, whose activity significantly decreases.

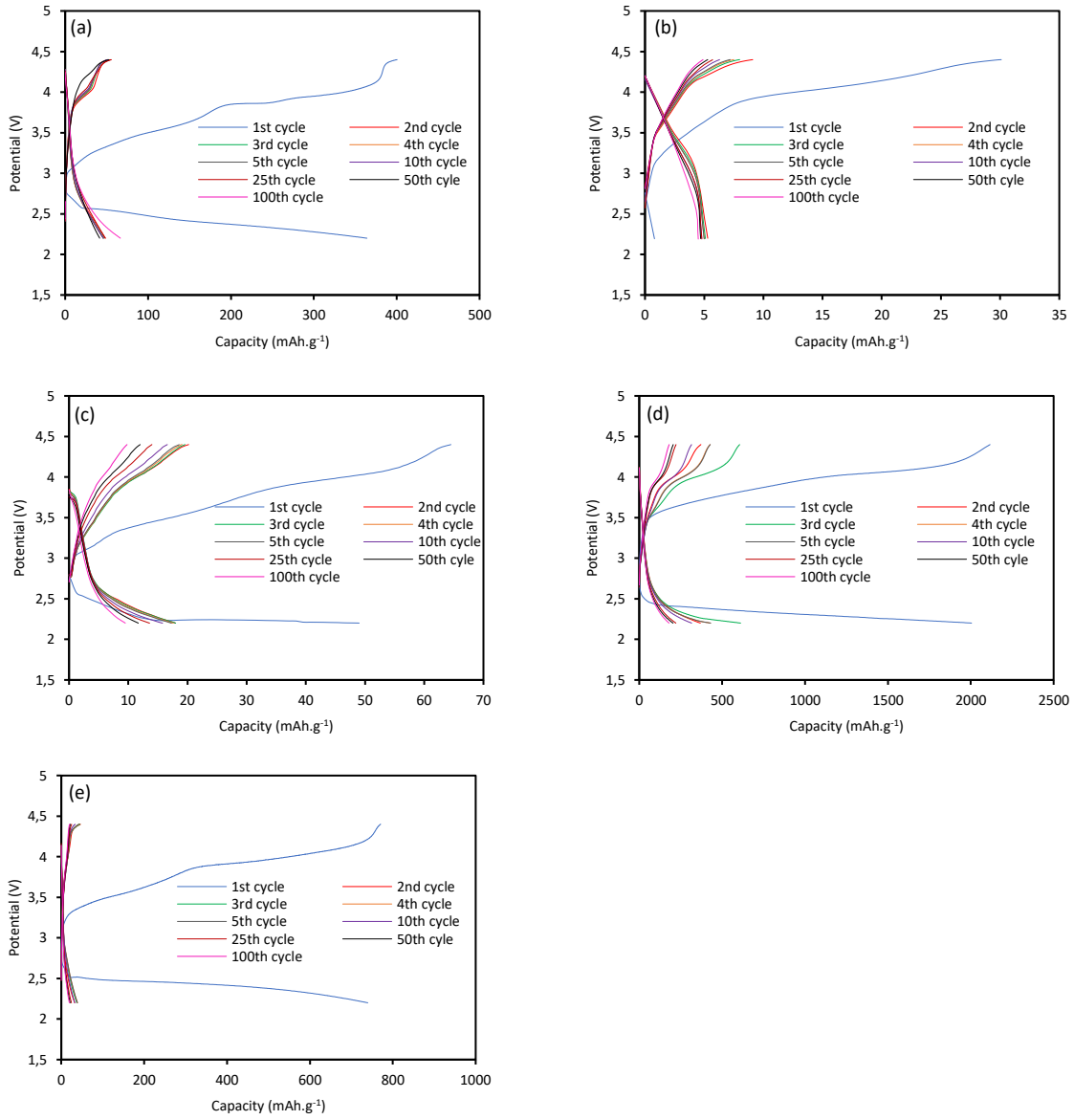

Figure 8 : Cycling profile over 100 cycles within a 2.2 - 4.4 V voltage windows for (a) Co_3O_4, (b) NiO, (c) $NiCo_2O_4$, (d) $MnCo_2O_4$, and (e) $ZnCo_2O_4$ electrode in lithium-oxygen batteries.

The cycling performance of the NiO, Co_3O_4, and MCo_2O_4 (M=Ni, Mn, Zn) nanowire cathodes were further examined with a limited capacity of 1000 mAh.g^{-1}. The full charge/discharge cycling profiles are shown in Figure 9. The NiO-based electrode did not reach the limit capacity of 1000mAh.g^{-1}, which is consistent with the results previously obtained. This electrode has a low catalytic activity on the OER/ORR, making it unsuitable for Li-O_2 battery applications. Cells made with, $NiCo_2O_4$, Co_3O_4, $ZnCo_2O_4$, and $MnCo_2O_4$ reached 2, 2, 3, and 7 cycles respectively. The $MnCo_2O_4$ electrode achieves the highest number of cycles. This data is consistent with the obtained results, which show that this cathode has the highest catalytic activity according to EOR/ORR and allows the highest capacity to be achieved in a limited window potential. However, the number of cycles reached is low and does not meet the desired expectations for Li-O_2 batteries.

The charge profiles highlight two plateaus. The potential values of the two plates match the values found in CV and are ~3.3 V and ~4.0 V. The first plateau can be attributed to the decomposition of nonstoichiometric $Li_{2-x}O_2$, and the second one refers to the decomposition of dense Li_2O_2 film. All

cathodes have a maximum charge potential less than or equal to 4.0 V reflecting their good catalytic activity on the OER. However, the charge potential of the MCo_2O_4 based electrode is above 4 V from the third cycle and for a capacity higher than 850 mAh.g^{-1}. The discharge potential decreases drastically from the second cycle onwards for all electrodes indicating a low catalytic activity of the materials for ORR.

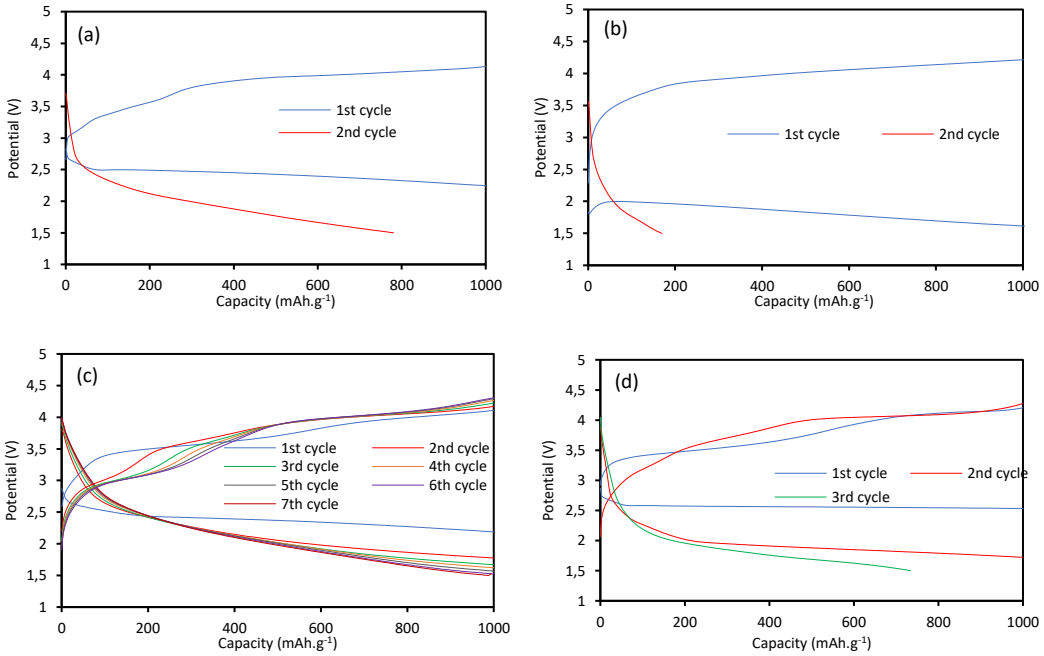

Figure 9 : Cycling performances of Li-O_2 batteries made with (a) Co_3O_4, (b) $NiCo_2O_4$, (c) $MnCo_2O_4$, and (d) $ZnCo_2O_4$ electrode at a fixed capacity of 1000 mAh.g^{-1}

XPS analyses were carried out in order to evaluate the consequences of the potential drop during discharge. C1s and O1s spectra of each MCo_2O_4 (M=Ni, Mn, Zn) nanowire cathode and their respective deconvolutions are shown in Figure 10.

The XPS spectra of all cathodes show peaks corresponding to carbonate (≈ 292 eV), O-C=O (≈ 288 eV) and C-O-C (≈ 286 eV) bonds. The presence of these species confirms that degradation has taken place during the cycles. The appearance of C-C bonds and the increased peak air between the species for the $MnCo_2O_4$ electrode means that more degradation has occurred. Figure 10 b,d,e show the C1s XPS spectrum of MCo_2O_4 (M=Ni, Mn, Zn) nanowire cathodes, in which the fitting peak at ~ 529 eV is typical of metal–oxygen bonds, whereas the peak at ~ 532 eV is ascribed to oxygen defects with low oxygen coordination sites. The absence of the peak at 534 eV, corresponding to carbonates, could mean that degradation is minimal in these batteries. Consequently, the decrease in battery performance with MCo_2O_4 (M=Ni, Mn, Zn) cathodes could be mainly due to the low catalytic activity of the materials on the ORR, leading to a slight deposit of Li_2O_2.

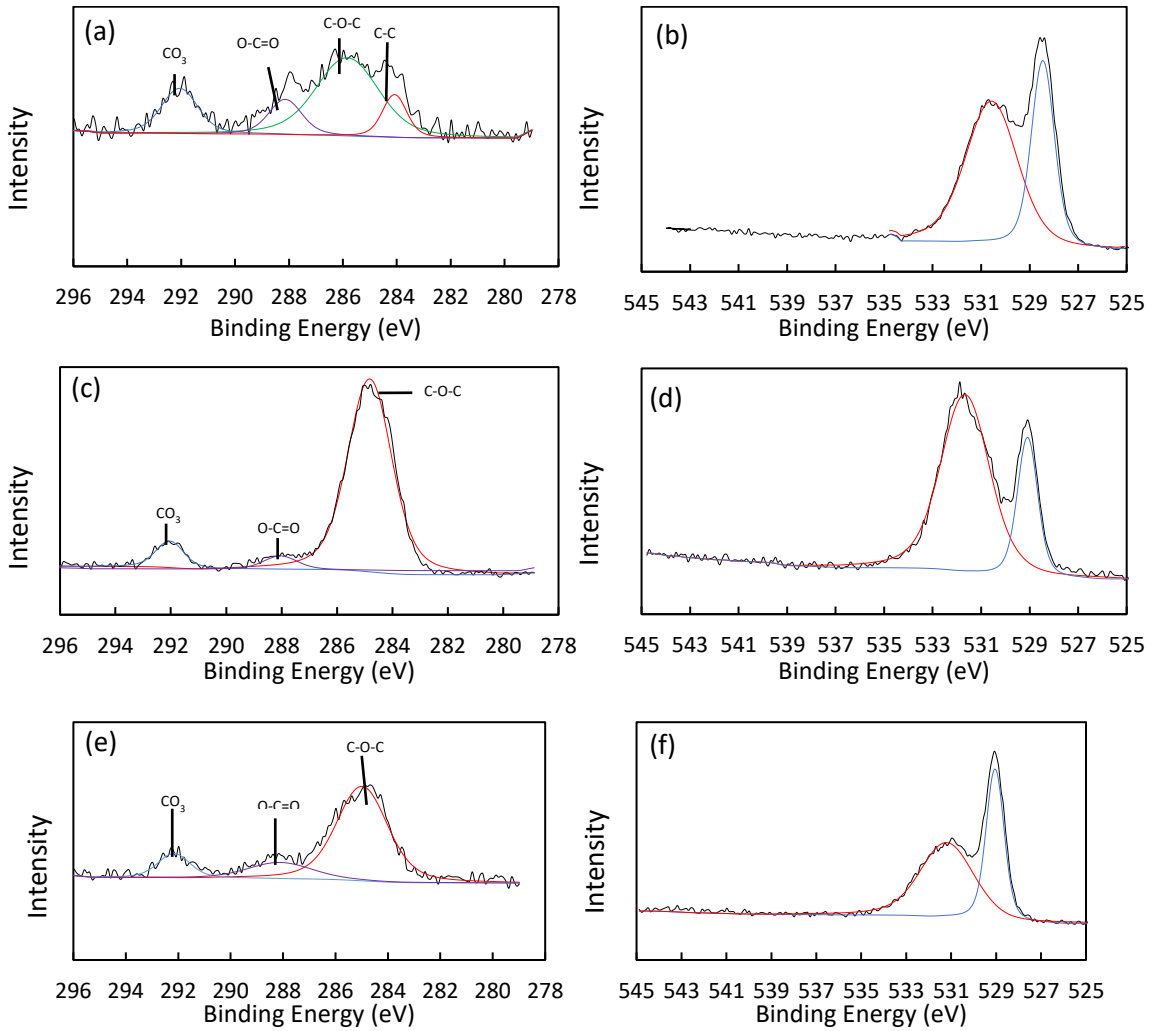

Figure 10 : C1s and O1s XPS spectra of (a,b)) $MnCo_2O_4$, (c,d) $NiCo_2O_4$, (e,f) $ZnCo_2O_4$, obtained after 100 cycles.

Conclusion

MCo_2O_4 (M=Ni, Mn, Zn) nanowire grown in situ on the nickel foam were successfully synthetised using a facile hydrothermal process followed by a calcination treatment, and were directly served as carbon-free cathode for Li-O_2 batteries.

This unique three-dimensional network structure of these electrodes facilitates electronic transmission between the nanowire and the nickel foam. It also allows easier diffusion of ions and oxygen, ensuring a faster electrochemical reaction. The homogeneous distribution of the nanowires on the support and the large open spaces between them would promise an abundant deposit of Li_2O_2.

This study shows that it is possible to control the synthesis of spinel-based nanowires on nickel foam to produce carbon-free cathode catalysts with good OER catalytic performance. As a cathode for Li-O_2 batteries, the MCo_2O_4 (M=Ni, Mn, Zn) exhibits good catalytic activity on the oxygen evolution reaction. However, a low catalytic activity on the ORR leads to a strong decrease of the discharge potential during cycles leading to low cyclability. The battery made with the $MnCo_2O_4$ electrode has the best performance, it reaches a maximum capacity of 2110.8 $mAh.g^{-1}$ and can perform seven cycles when the capacity is limited to 1000 $mAh.g^{-1}$. This performance could be improved by coupling MCo_2O_4 (M=Ni, Mn, Zn) with another material with good catalytic activity on the ORR.

A perspective to this study could be the use of oxides containing three 3d metals. A parallel with the lithium manganese cobalt oxides (NCM) currently used in lithium oxygen batteries can be drawn. The first step would be to delithiate the material in order to use it directly as a cathode. In this context Solmaz et al[33] have used a manganese cobalt oxides electrode in lithium metal-ion batteries and have shown an initial capacity of 1000 $mAh.g^{-1}$ and 330 $mAh.g^{-1}$ after 100 cycles. These results are encouraging and it would be worthwhile trying to use this type of electrode in lithium-oxygen batteries in the future.

Experimental

Cobalt (II) nitrate hexahydrate [$Co(NO_3)_2$. 6 H_2O, >98%, Roth], Nickel (II) nitrate hexahydrate [$Ni(NO_3)_2$. 6 H_2O, >99%, Roth], Manganese (II) nitrate tetrahydrate [$Mn(NO_3)_2$. 4 H_2O, >98%, Roth], Zinc nitrate hexahydrate [$Zn(NO_3)_2$. 6 H_2O, >98%, Roth], Ammonium fluoride [NH_4F, 98+%, ACS reagent, ACROS Organics], Urea [CH_4N_2O, 99%, ACROS Organics], Acetone (Fischer, > 95%), Hydrochloric Acid (Fisher, 37%), and ethanol (≥96%, VWR), were used as purchased.

MCo_2O_4 (M = Mn, Ni, Zn) electrodes synthesis

A nickel foam disc with a surface area of 1.32 cm² was used as a current collector and was pre-treated to remove possible surface oxides and grease. The foam was immersed in several successive baths (acetone, HCl 3M, H_2O, and ethanol) under sonication for 15 minutes each and then dried overnight at 60°C. The prepared nickel foam was then placed in Teflon-lined stainless-steel autoclaves. 1.4 mmol of metal (Mn, Ni, Zn) nitrates and 2.8 mmol of cobalt nitrate were dispersed in a solution made of 40 mL of deionized water and 7.2 mL of ethanol. Once solubilised, 2.9 mmol NH_4F and 8.7 mmol urea were added, the precursor solutions were stirred for 15 minutes and then transferred into the autoclaves where the prepared nickel foam was placed and kept at 120 °C for 9 h. After cooling to room temperature naturally, the electrodes were washed, under sonication, in three successive baths of distilled water followed by one made of ethanol and then dried at 80 °C for 12 h. After drying, the electrode undergoes a heat treatment at 550°C for 3.5 hours to obtain the desired MCo_2O_4 (M = Mn, Ni, Zn).

For comparative purposes, two metal oxides, Co_3O_4 and NiO, have been synthesized according to the above protocol. The only difference is an autoclave reaction time of 24 hours instead of 9 hours for nickel oxide.

Materials characterisation

X-ray diffractograms of the samples were recorded on a PANalytical X'Pert Pro diffractometer equipped with a direct optical positioning goniometric system and stuffed with a PIXcel 1D detector. The anode is made of copper and the emitted radiation correspond to the Kα ray (λ = 1.54184 Å). A 45 kV voltage and 30 mA current supply x-ray tubes. Diffractograms were record under room temperature, in 2θ configuration, with a step of 0.016711° each 24 seconds. Data were analysed using Data Collector and HighScore Plus software.

TEM micrographs were obtained using a TEM Tecnai 10 microscope composed of a LaB6 electron gun, an OSIS Magaview III camera, and configured in imaging mode with an accelerating voltage of 80 kV.

SEM micrographs were obtained using a Field Emission SEM JEOL 7500-F microscope configured in SEI mode with an accelerating voltage of 20 kV.

X-Ray photoelectron spectroscopy was used to analyse the chemical composition of the discharge products after cycling test. The spectroscope is an Escalab 250 Xi from Thermo Scientific, made of a magnesium anode (Kα ray, hv=1253.6Ev). The experiments were performed at room temperature and under reduced pressure.

Nitrogen physisorption analyses were done using an ASAP 2420 from Micromeritics. The samples were degassed overnight at 150 °C before the measurement. The pore size distribution for the porous nanoparticles was calculated via Horvath-Kawazoe method and specific surface area via Brunauer-Emmett-Teller (BET) method.

Electrochemical measurements

Homemade Li-O_2 cells were designed following Swagelok cells structure. The cell was made of an electrolyte consisting of 1M lithium bis(trifluoromethanesulfonyl)imide (LITFSI, ≥99% Sigma-Aldrich) in 1,2-Dimethoxyethane (DME, 99+%, Alfa Aesar), a lithium foil, used as reference and counter electrode, the as prepared O_2 –electrode used as cathode, and a glass fiber separator. The cell was assembled in an argon-filled glove box where moisture and oxygen concentrations were less than 1 ppm. The pbtained batteries were put under high purity oxygen flux (99.999%) for several seconds, they were then maintained under an O_2 atmosphere at a pressure of 1 atm for 10 hours before the electrochemical measurements were performed.

The galvanostatic discharge-charge tests were performed using a LANHE CT2001A multi-channel battery tester with a voltage between 2.2 and 4.4V and at a current rate of 0.1mA.cm^{-1} for the charge and 0.3 mA.cm^{-1} for the discharge. The specific capacities obtained were normalized by the material weight grafted onto the cathode.

Electrochemical impedance spectroscopy (EIS) and cyclic voltammetry was performed using a Princeton Applied Research, VersaSTAT 3, potentiostat/galvanostat. Galvanostatic charge and discharge tests were carried out between 2 and 4.5V (vs LI/LI^+), with a scanning rate of 0.1 mV.s^{-1}. Impedance response was collected after the first discharge by applying a constant AC voltage of 5mV, with 15 points per decade, and a scanning frequency between 0.01 and 100000 Hz.

Bibliography

1 Q. Ding, S.I. Khattak, M. Ahmad, *Sustainable Production and Consumption*, 2021, **27**, 254–268.

2 M.W. Jones, R.M. Andrew, G.P. Peters, G. Janssens-Maenhout, A.J. De-Gol, P. Ciais, P.K. Patra, F. Chevallier, and C. Le Quéré, *Scitific data*, 2021, **8**, 2.

3 P.G. Bruce, L.J. Hardwick, K.M. Abraham, *MRS Bull*, 2011, **36**, 506–512.

4 P. G. Bruce, S. A. Freunberger, L. J. Hardwick and J.-M. Tarascon*, Nat. Mater*, 2012, **11**, 19–29.

5 W.J. Kwak, D. Sharon, D. Aurbach et al, *Chem. Rev, 2020*, **120**, 6626–6683.

6 Ogasawara.T, Débart.A, Holzapfel.M, Novàk.P, Bruce.P.G, *J Am Chem Soc*, 2006**, 128**, 1390–1393.

7 M. Song, X. Du, Y. Chen, L. Zhang, D. Zhu, Y. Chen, *Materials Reasearch Bulletin*, 2015, **68**, 75-79.

8 B.D. McCloskey, A. Speidel, R. Scheffler, D.C. Miller, V. Viswanathan, J.S. Hummelshøj, J.K Nørskov, A.C. Luntz, *J. Phys. Chem. Lett*, 2012, **3**, 997.

9 J.H. Kim, H.S. Woo, W.K. Kim, K.H. Ryu, D.W. Kim, *ACS Appl. Mater. Inter*, 2016, **8**, 32300–32306.

10 M.M. OttakamThotiyl, S.A. Freunberger, Z. Peng, P.G. Bruce, *J.Am.Chem.Soc*, 2013, **135**, 494–500.

11 A. Torayev, S. Engelke, Z. Su, et al. *J. Phys. Chem C*, 2021, **125**, 9, 4955-4967.

12 D.M. Itkis, D.A. Semenenko, E.Y. Kataev, A.I. Belova, V.S. Neudachina, A.P. Sirotina, M. Hävecker, D. Teschner, A. Knop-Gericke, P. Dudin, A. Barinov, E.A. Goodilin, Y. Shao-Horn, L.V. Yashina, *Nano Lett*, 2013, **13**, 4697−4701.

13 Y.C. Lu, H.A. Gasteiger, Y. Shao-Horn, *J. Am. Chem. Soc,* 2011, **133**, 47, 19048-19051.

14 N.A. Galiote, U. Ulissi, S. Passerini, F. Huguenin, *J. Phys. Chem. C*, 2018, **122**, 15826−15834.

15 F. Wu, Y. Xing, X. Zeng, Y. Yuan, X. Zhang, R. Shahbazian-Yassar, J. Wen, D.J. Miller, L. Li, R. Chan, J. Lu, K. Amine, *Adv. Funct. Mater*, 2016, **26**, 7626–7633.

16 Z. Peng, S. A. Freunberger, Y. Chen and P. G. Bruce, *Science*, 2012, **337**, 563.

17 Tan.P, Shyy.W, Wu.M.C, Huang.Y.Y, Zhao.T.S, *Journal of Power Sources*, 2016, **326**, 303–312.

18 M. Kim, E. Yoo, W.S. Ahn, S.E. Shim, *Journal of Power Sources*, 2018, **389**, 20–27.

19 Z. Luo, Y. Zhao, J. Guo, K. Luo, *Materials Review*, 2015, **29**, 20.

20 Y.Y. Huang, Y.Q. Wang, C. Tang, J. Wang, Q. Zhang, Y.B. Wang, J.T. Zhang, *Adv. Mater*, 2019, **31**, 17.

21 A. Riaz, K.N. Jung, W. Chang, S.B. Lee, T.H. Lim, S.J. Park, R.H. Song, S. Yoon, K.H. Shin, J.W. Lee, *Chem. Commun*, 2013, **49**, 5984.

22 L. Kumar, M. Chauhan, P.K. Boruah, M.R. Das, S.A. Hashli, and S. Deka, *ACS Appl. Energy Mater,* 2020, **3**, 7, 6793–6804.

23 K.B. Jang, K.R. Park, K.M. Kim, S.Mhin et al, *Applied Surface Science*, 2021, **545**, 148927.

24 D. Zhang, Y. liu, L. Wu, L. Fang, W. Qin, *Journal of Solid State Chemistry*, 2021, **295**, 121903.

25 S. Abualela et al, *J. Phys.: Conf. Ser*, 2020, **1707**, 012006.

26 S. Chen, P. Gao, D. Zhang et al, *Journal of Alloys and Compounds*, 2020, **860**, 158346.

27 R. Packiaraj et al, *Journal of Energy Storage*, 2021, **34**, 102029.

28 E. Faktorovich-Simon, A. Natan, E. Peled, D. Golodnitsky, *Frontiers in Materials*, 2019, **6**, 249.

29 Chen.Y, Qu.B, Hu.L, Xu.Z, Li.Q and Wang.T, *Nanoscale*, 2013,**5**, 9812-9820

30 A.W.M. Al-Ogaili, T. Cetinkaya, S. Pakseresht, H. Akbulut, *Journal of Alloys and Compounds*, 2021, **854**, 157293

31 Y.C. Lu, Y. Shao-Horn, *J. Phys. Chem. Lett*, 2013, **4**, 93−99

32 H. Lee, Y.J. Kim, D.J. Lee, J. Song, Y.M. Lee, H.T. Kim, J.K. Park, *J.Mater.Chem.A*, 2014, **2**, 11891

33 R. Solmaz, B. Deniz Karahan, O. Keles, *Journal of Applied Electrochemistry*, 2020, **50**, 1079–1089

Figure Table

Figure 1: Schematic illustration of the synthesis of the MCo_2O_4 cathodes. 173
Figure 2 : Powder X-ray diffraction pattern of the as synthesized $NiCo_2O_4$, $MnCo_2O_4$, and $ZnCo_2O_4$, with their references. 174
Figure 3: SEM micrographs demonstrating morphology of the as synthetized (a) $NiCo_2O_4$, (b) $MnCo_2O_4$, (c) $ZnCo_2O_4$ on nickel foam 175
Figure 4 : Bright-field TEM micrographs demonstrating morphology and particle size of the as synthetized (a) $NiCo_2O_4$, (b) $MnCo_2O_4$, (c) $ZnCo_2O_4$. 177
Figure 5: Cyclic voltammograms obtained from, (a) $NiCo_2O_4$, (b) $MnCo_2O_4$, and (c) $ZnCo_2O_4$ nanowire arrays electrodes in lithium-oxygen battery application. 177
Figure 6: Experimental Nyquist plot for Co_3O_4, NiO, $NiCo_2O_4$, $MnCo_2O_4$, and $ZnCo_2O_4$ electrodes in lithium-oxygen batteries. 178
Figure 7: A schematic illustration of the structural evolution of the Co_3O_4 NW array with the low and high discharge rates. [31] 179
Figure 8 : Cycling profile over 100 cycles within a 2.2 - 4.4 V voltage windows for (a) Co_3O_4, (b) NiO, (c) $NiCo_2O_4$, (d) $MnCo_2O_4$, and (e) $ZnCo_2O_4$ electrode in lithium-oxygen batteries. 180
Figure 9 : Cycling performances of Li-O_2 batteries made with (a) Co_3O_4, (b) $NiCo_2O_4$, (c) $MnCo_2O_4$, and (d) $ZnCo_2O_4$ electrode at a fixed capacity of 1000 mAh.g^{-1} 181
Figure 10 : C1s and O1s XPS spectra of (a,b)) $MnCo_2O_4$, (c,d) $NiCo_2O_4$, (e,f) $ZnCo_2O_4$, obtained after 100 cycles. 182

Table 1 : Summary of the length, width, specific surface area and average pore size of all nanoparticles. 176

Supplementary Information

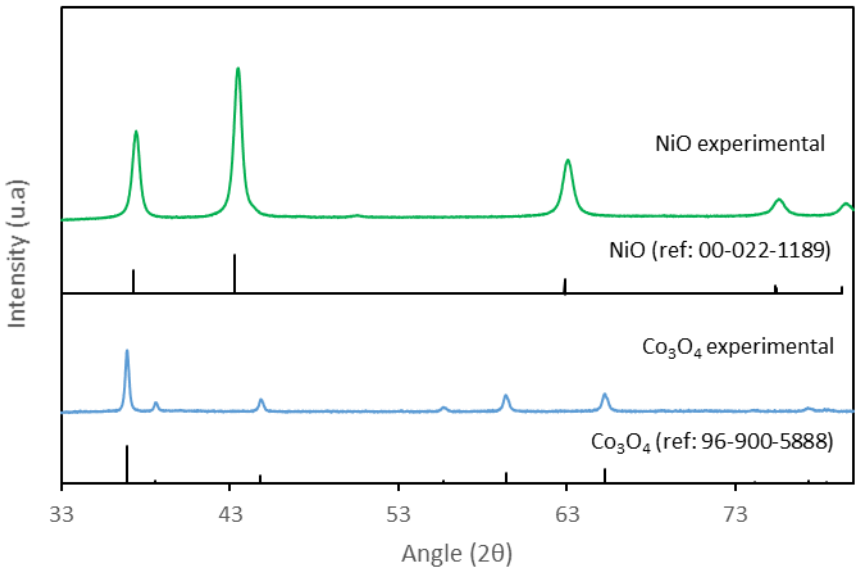

Figure S1: Powder X-ray diffraction pattern of the as synthesized NiO, and Co_3O_4 with their references.

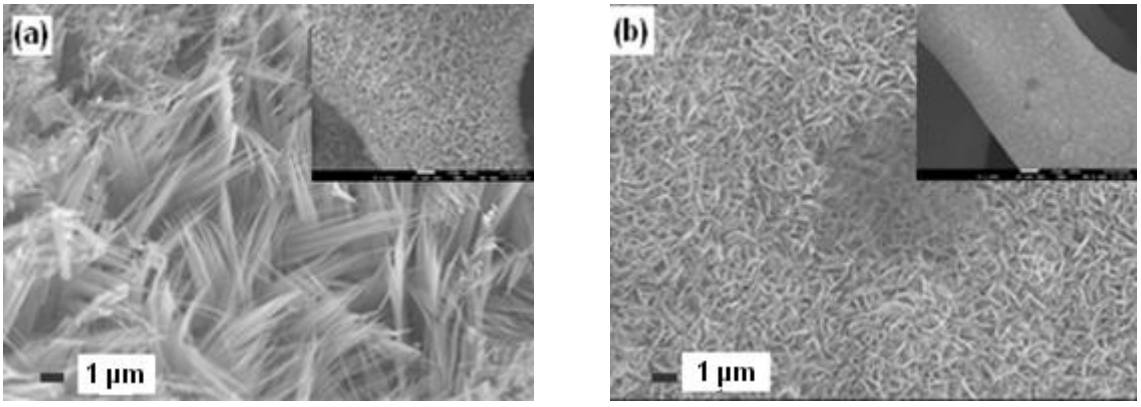

Figure S2: SEM micrographs demonstrating morphology of the as synthetized (a) Co_3O_4, (b) NiO

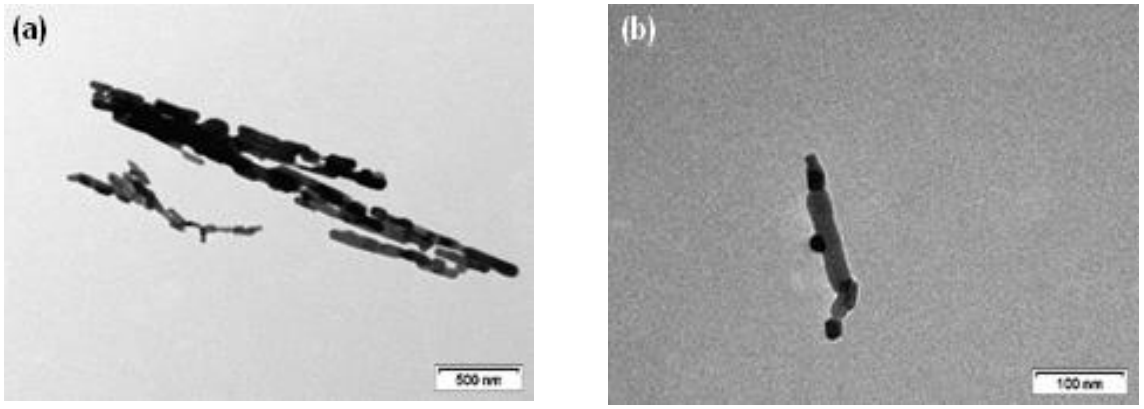

Figure S3: Bright-field TEM micrographs demonstrating morphology and particle size of the as synthetized (a) Co_3O_4, (b) NiO

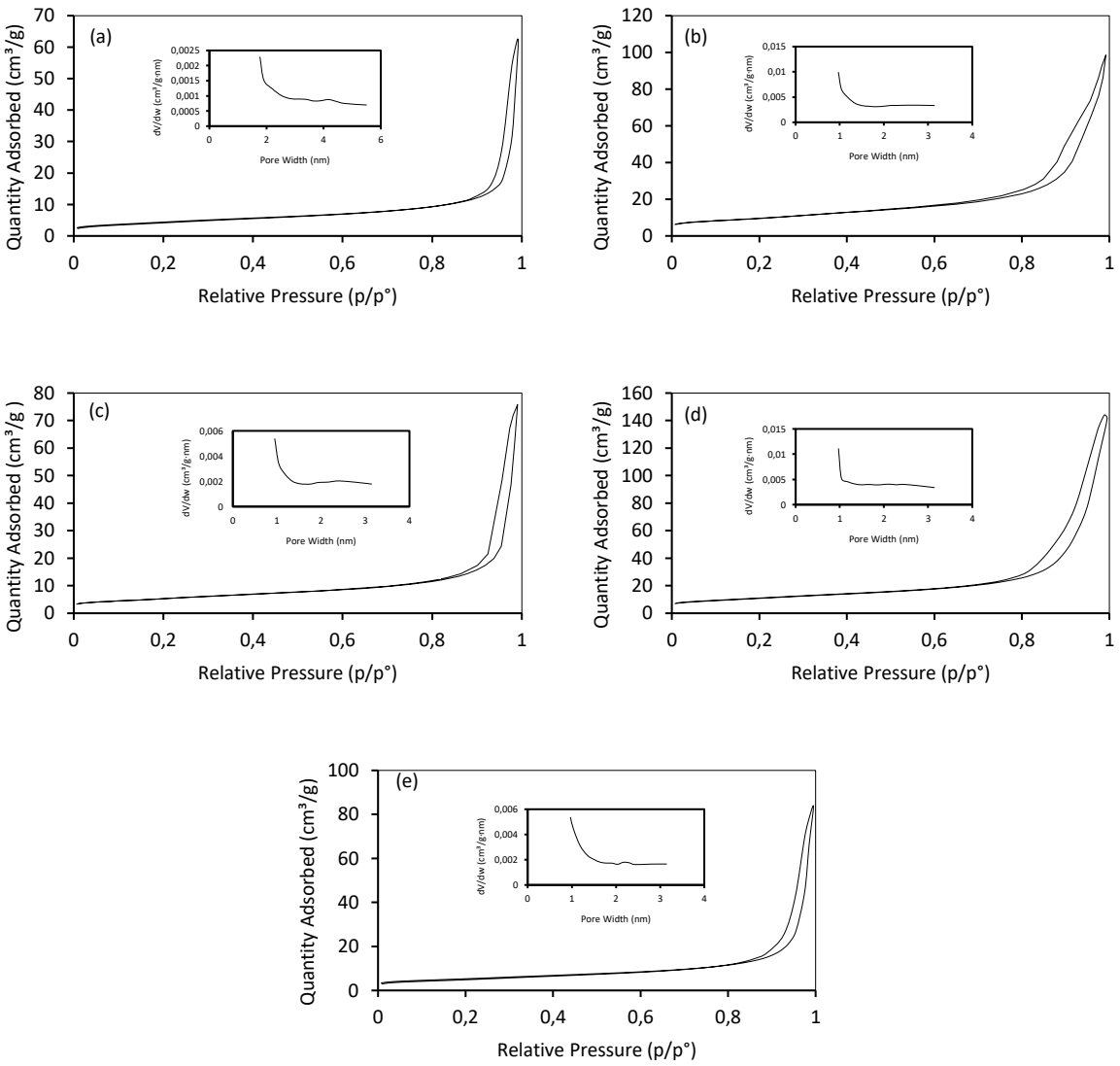

Figure S4: Nitrogen physisorption and pore size distribution of the as synthetized (a) Co_3O_4, (b) NiO, (c) $NiCo_2O_4$, (d) $MnCo_2O_4$, (e) $ZnCo_2O_4$.

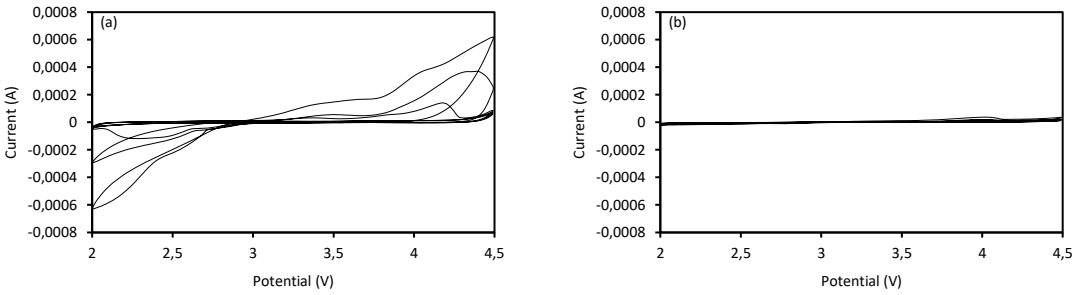

Figure S5: Cyclic voltammograms obtained from (a) Co_3O_4, (b) NiO, nanowire arrays electrodes in lithium-oxygen battery application.

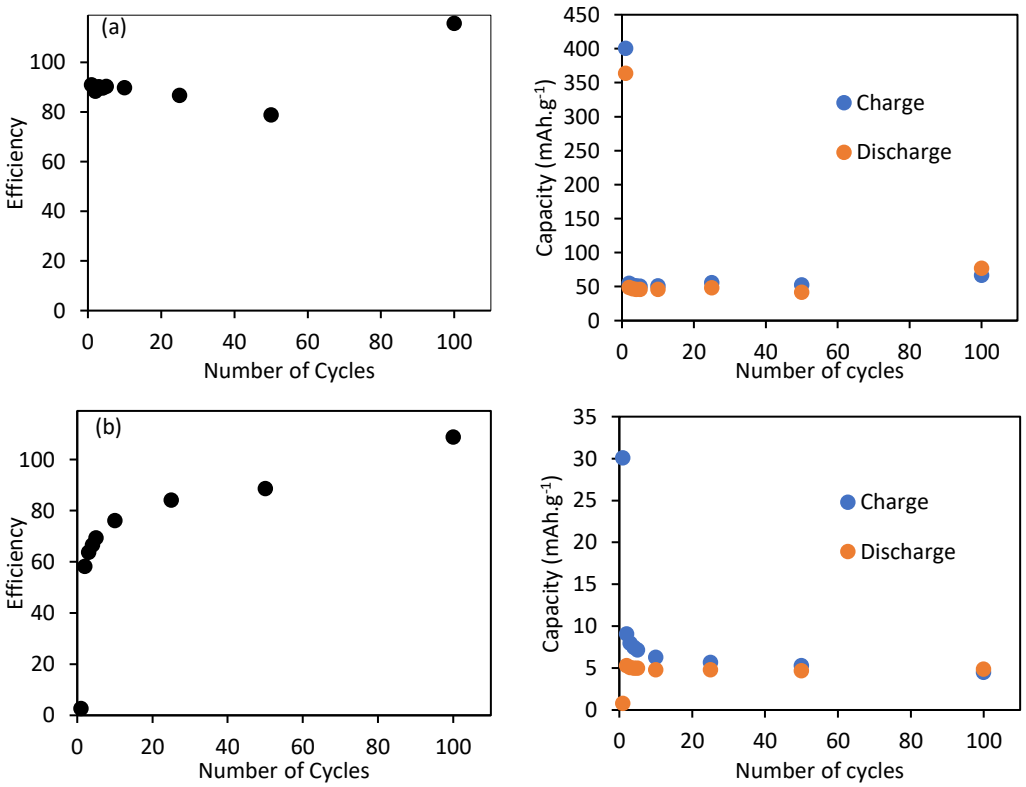

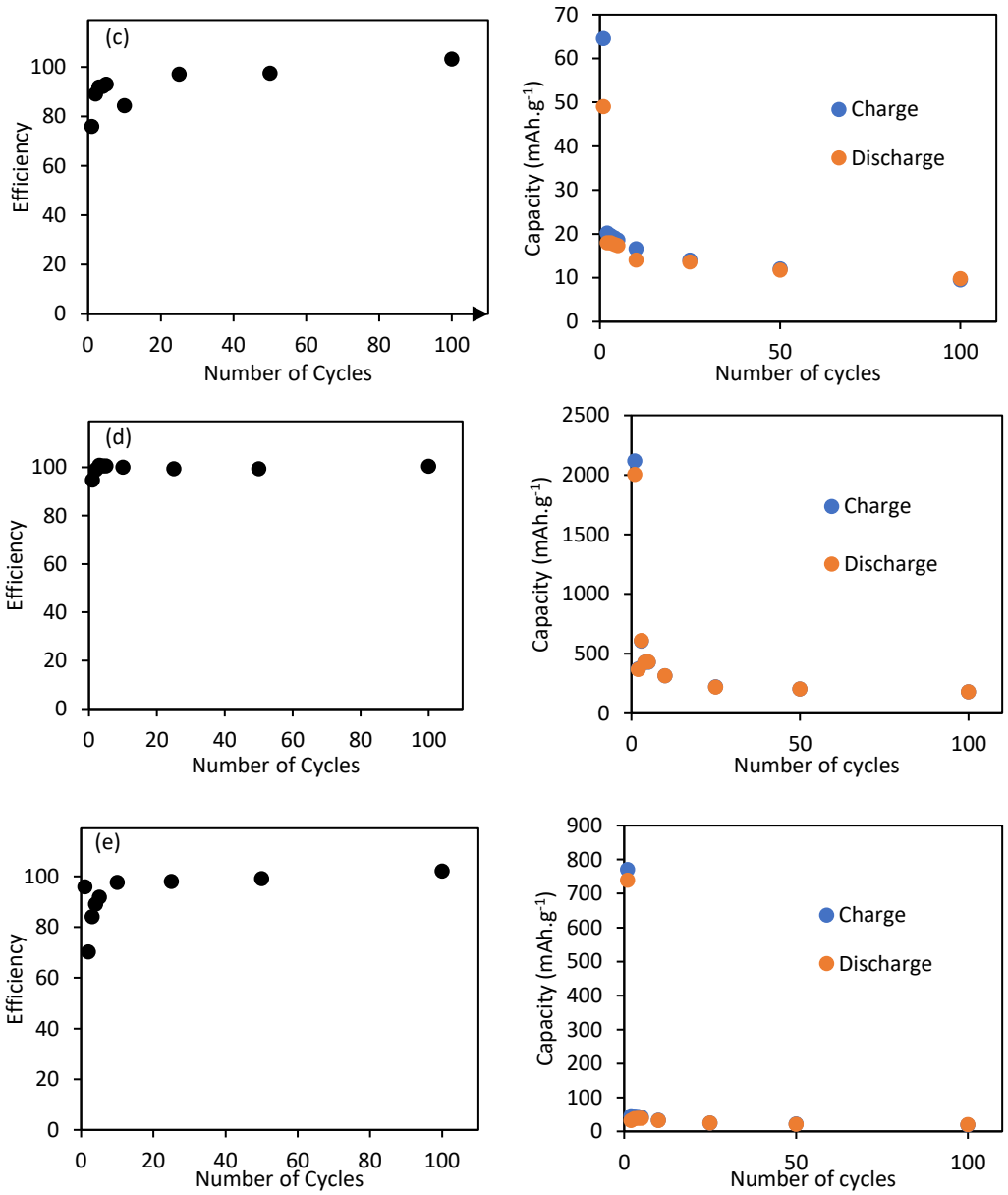

Figure S6: Li-O_2 battery capacity evolution over 100 cycles (left) and the associated efficiency (right) within a 2.2 - 4.4 V voltage windows for (a) Co_3O_4, (b) NiO, (c) $NiCo_2O_4$, (d) $MnCo_2O_4$, (e) $ZnCo_2O_4$ cathode

Part III – Conclusion and outlook

Chapter 6 – General conclusion and outlook

The main objective of this PhD was to design cathode materials for lithium-oxygen battery applications. The results are summarized into three chapters.

The first chapter focused on the relationship between the structure of the cathodes and the resulting electrochemical performances of lithium-oxygen batteries. Cathodes with a network of interconnected macro-meso-micro pores following Murray's law design was synthesized. Three materials have been developed, one based on zinc oxide nanoparticles alone and the others combined with carbon nanoparticles and have been tested as cathodes in Li-O_2 batteries. The zinc oxide hierarchical macro-meso-micro porous material alone did not provide convincing results due to its high brittleness and lack of conductivity. The hierarchical porous structure assembled with carbon nanoparticles and carbon nanotubes led to an increase in capacity on the first cycle of 110% (2236 mAh.g^{-1}) and 42% (957 mAh.g^{-1}) respectively compared to a carbon slurry-based cathode. This increase of performances is explained by the presence of a hierarchical porosity leading to an increase in the specific surface area and greater diffusion of reagents improving the formation of lithium peroxide and leading to a higher capacity. However, the reactivity of the carbon leads to the formation of lithium carbonates passivating the cathode, increasing the overpotential and leading to the degradation of the system.

The next step in this project was the addition of materials with catalytic activity on the OER/ORR to reduce the overpotential in order to preserve the degradation within the battery. 3d metal oxides (MOx) have been used as catalysts in Super P carbon cathodes in lithium-oxygen batteries. For the first time, a comprehensive and comparative study on all of the 3d metal oxides was realised. MOx cathodes promote the catalytic activities of OER and ORR processes and lead to a decrease of the overpotential, and an increase of the specific capacity. The MOx electrodes also demonstrated significant improvement in the round-trip efficiency and specific capacity over the pure carbon cathode. Among the most significant improvements, it has been shown that the use of Co_3O_4 electrode reduces overpotential to 1.464 V, TiO_2 increases capacity to 6448 mAh.g^{-1} and Mn_3O_4 increases the number of cycles at 500 mAh.g^{-1} to 417 cycles. The effect of the oxidation state of a same metal on their performance in Li-O_2 battery has been deeply studied. This first comprehensive leads to important information on the understanding of OER and ORR behaviour of all these 3d metal oxides and will be the good guideline for the selection of the optimal cathode materials for advanced Li-O_2 batteries. However, previously observed degradations are still present in this system configuration and reduce performance during charge/discharge cycles. The main side reaction product formed is lithium carbonate. In order to minimise its generation, the next step of the study was to create carbon-free cathodes.

In order to obtain carbon-free cathodes, MCo_2O_4 (M=Ni, Mn, Zn) dense nanowire array was grown on a nickel foam using a facile hydrothermal process followed by a calcination treatment. Spinel nanowire has been selected because they combine a morphology allowing an optimal deposition of lithium peroxide and possess a good catalytic activity on the OER allowing an optimised dissolution during charging. Experimentally, the MCo_2O_4 (M=Ni, Mn, Zn) exhibits good catalytic activity on the oxygen evolution reaction. The battery made with the $MnCo_2O_4$ electrode has the best performance, it reaches a maximum capacity of 2110.8 mAh.g^{-1} and can perform seven cycles when the capacity is limited to 1000 mAh.g^{-1}. However, a low catalytic activity on the ORR leads to a strong decrease of the discharge potential leading to low cyclability. This performance could be improved by coupling MCo_2O_4 (M=Ni, Mn, Zn) with another material with a good catalytic activity on the ORR.

To conclude, this manuscript has shown that several approaches can be considered to optimise the cathodes and improve the battery performance. Firstly, the morphology of the cathode must be judiciously selected in order to optimise the deposition of Li_2O_2 during discharge. The second optimization path is to modify the composition of the cathode materials in order to improve the catalytic activities on the OER and ORR. This improvement of the catalytic processes will allow an optimal formation and degradation of the Li_2O_2 leading to an enhancement of the battery overpotential, preserving the potential degradation.

In the future, it will be essential to better understand the mechanisms that occur within Li-O_2 batteries during charge and discharge. To do this, two axes can be explored. The first would be to analyse the gas flow at the exit of the battery during the cycles by a Gas Chromatography-Mass Spectrometry (GCMS) connected to a high precision manometer. This analysis could provide a better understanding of the interactions between the cathode surface and the oxygen. The second would be to follow the evolution of the products formed during the charge/discharge cycles. An in situ XPS analysis could give very interesting results.

For cathodes, a possible approach following our work would be to create a hierarchical porous carbon network and to coat it homogeneously with metal oxides. The coating methods could be either by chemical vapor deposition (CVD) or by immersion followed by calcination under air of precursor salt.

More concretely, our study could be completed by modifying the electrolyte. The electrolyte used throughout this study is of its most common composition. The performance obtained could be significantly improved by changing the solvent or by adding additives such as redox mediators.

ANNEXES

1) X-ray diffraction (XRD)

1.1) Principle

X-ray diffraction is a non-destructive characterization technique based on the diffraction phenomenon that results from an interaction between an electromagnetic wave and a crystalline structure. There are two main kinds of X-ray diffraction methods: one performed on a single crystal and the other on a powder. A powder is defined as a random organisation of several crystallite. The analysis of single crystal allows to find the crystalline structure, and the powder the identification of the phases. Typically, a monochromatic X-ray wave, with a wavelength λ, and an angle of incidence θ, will interact with a crystalline structure composed of several grid planes (hkl) spaced at a distance d. The interactions between the planes and the X-ray wave will be alternately constructive or destructive with respect to the direction in space (Fig.1), and will induce variations in the intensity of the photon flux. These changes in intensity as a function of the direction in space are the basis of the diffraction phenomenon. The directions of the constructive interferences can be determinate by the Bragg's law:

$$2d_{hkl} \sin\theta = n\,\lambda \text{ (n: integer)} \qquad \text{(A.1)}$$

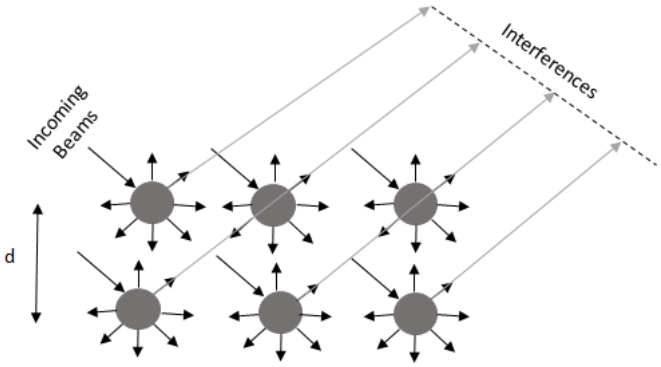

Figure 1: Scheme of the diffraction phenomenon

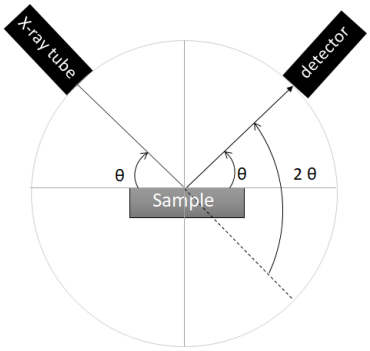

Figure 2: scheme of a θ -2 θ XRD diffractometer configuration

Usually a diffractometer consists of an X-ray tube, Soller slits, a monochromator and a detector. Several configurations are possible; the most common is the Brag-Brantano. Two angle configurations are available: θ-θ where the sample remains fixed and the detector and tube move simultaneously at an angle θ, and 2θ-θ where the tube remains fixed and the detector and the sample move respectively at an angle θ and 2θ (Fig.2).

1.2) Measuring conditions

Sample diffractograms were recorded on a PANalytical X'Pert Pro diffractometer equipped with a direct optical positioning goniometric system and equipped with a PIXcel 1D detector. The anode is made of copper and the emitted radiation corresponds to the Kα ray (λ = 1.54184 Å). A 45 kV voltage and 30 mA current supply x-ray tubes. The diffractograms were recorded at room temperature, between 5° and 80° in 2θ configuration, with a step of 0.016711° each 24 seconds. Data were recorded and analysed using Data Collector and HighScore Plus software.

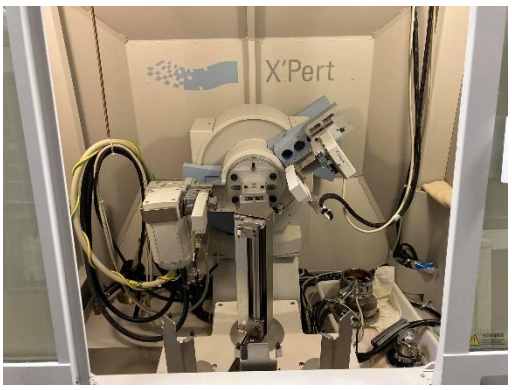

Figure 3: Photograph of the DRX diffractometer

1.3) Data treatments

The main application of X-ray powder diffraction is the identification of crystalline phases. Moreover, a qualitative study can be carried out if the material is composed of several phases. By searching the position and intensity of the peaks and comparing them with a database, the phases can be identified.

The first step is an automatic search for peaks using software that corrects the background noise, smoothes the curve and removes the $K_{\alpha 2}$ radiation from the copper. Once the signal is corrected, the software adjusts the position of the peaks. The next step compares the diffractograms obtained with a database (COD or ICDD files). The software identifies the different species thanks to the positions of the most intense peaks, and gives the characteristics of the recognised phases.

1.4) Size of the crystallites

The approximative size of the crystallites can be found using XRD diffractograms and the Scherrer equation (A.2). The equation links the Full-Width Half-Maximum (FWHM) of the diffractograms peaks to the size of the crystallites. However, this equation cannot be used to determine crystallite sizes higher than 100 nm.

$$T = \frac{K\lambda}{\Delta(2\theta)cos\theta} \quad \text{(A.2)}$$

$\Delta(2\theta)$ correspond to the FWHM of the Bragg peaks

T is the size of the crystallite

K is a dimensionless shape factor

2) Fourier Transform Infrared Spectroscopy (FTIR)

2.1) Principle

Infrared spectroscopy is the study of electromagnetic radiation scattered, absorbed or diffused by molecules. It provides information on the structure of molecules and particularly on the nature of the bond. Experimentally, when IR rays pass through a sample, some of them are absorbed and others are transmitted. If the order of the wavelength of the incident beam is close to the vibrational energy of the molecule, it will absorb some of the radiation and induce a decrease in intensity. The resulting signal represents the molecular fingerprint of the molecule, then a Fourier transform converts the output of the detector into an interpretable spectrum. Each molecule has a different spectrum and is explained by the different forces within the molecules, and by the different masses and electronegativity of the atoms. The identification of a compound can be done by spectrum analysis.

The IR spectrum link a transmittance for each wavelength. The transmittance is the ratio of the incoming intensity to the transmitted intensity. This relation is $T = \frac{I}{I0}$ and represent the fraction of the light intensity, that goes through the powder. It can be related to the absorbance thanks to this relation: A = -log(T). In this thesis, this method is used to detect the presence of impurity in compounds.

2.2) Measuring conditions

Experimentally, the analyses were performed between 500 and 4000 cm^{-1} with a Perkin Elmer Spectrum 65 FT IR Spectrometer. The sample was placed directly onto the powder carrier and the results were processed using Spectrum 10 spectroscopy software from PerkinElmer.

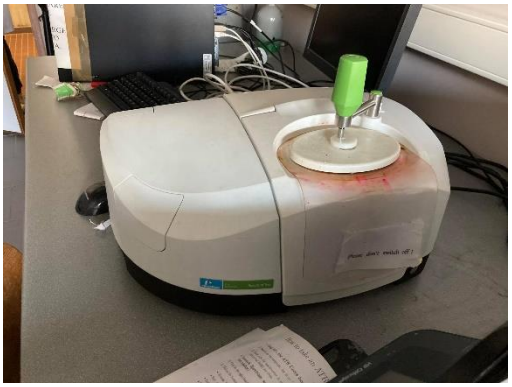

Figure 4: Photograph of the FTIR spectrophotometer

3) Transmission Electron Microscopy (TEM)

3.1) Principle

The transmission electron microscope is a device used for a qualitative study of the nanoparticles. It is based on the electrons diffraction. The Figure 5 shows the schematic diagram of the TEM principle; it consists of an electron gun, a nitrogen cooling system, a vacuum pump, an optical column containing magnetic lenses, a sample holder and an electron detector. Experimentally, the electron gun produces an electron beam and a system of magnetic lenses deflect or focuses the beam onto the sample. The diffracted image can be seen on a fluorescent screen or detected with a CCD camera. Two modes are available: diffraction and image. The first one, uses the wave behaviour of electrons. When they hit the crystalized nanoparticles, the main electron beam is diffracted into several smaller ones and is recombined through magnetic lenses to form a diffracted pattern. For the second, the electron beam passes through the sample, depending on its properties such as thickness, nature, or density, the electrons will be more or less absorbed. By placing a detector in this plane, an image of the irradiated area can be observed by transparency. In these studies, only the image mode was used, giving information on the structure, size, and shape of the particles.

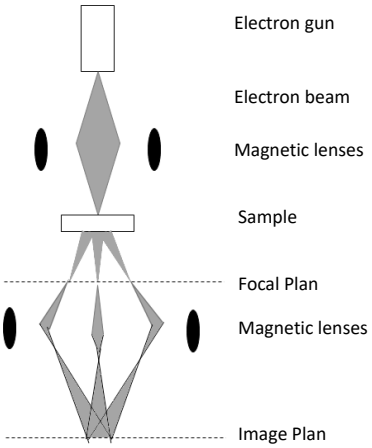

Figure 5: scheme of a TEM configuration

3.2) Samples Preparation and measuring conditions

The samples need to be very thin, as the electrons have to pass through it, their thickness must be on an average of few nanometers. In this study, only nanoparticles were studied under this microscope. First, nanoparticles are suspended in ethanol and then drop cast on a copper carbon coated grid for analysis. The samples were analyzed using a Tecnai 10 TEM microscope composed of a LaB_6 electron gun, an OSIS Magaview III camera, and used in imaging mode with an accelerating voltage of 80 kV.

Figure 6: Photograph of a Tecnai 10 microscope

4) Scanning Electron Microscopy (SEM)

4.1) Principle

The main use of a scanning electron microscope is to observe the morphology, especially the microstructure and texture of compounds. Figure 7 shows the schematic diagram of a SEM. An electron gun, some apertures, condenser lenses, a stigmator, deflection coils and a sample holder make up the microscope. Then a detector collects the signals to display the image.

In practise, an electron gun creates an electron beam with a specific kinetic energy and scans the surface of the sample. The beam interacts with the surface causing a dissipation of kinetic energy and leads to the creation of several signals from several types of electrons.

- Secondary electrons: Torn from matter by incident or backscattered electrons, their energies are small. The main use of this kind of electrons is in the production of SEM images, especially to show morphology and topography.
- Backscattered electrons: Their energies are close to that of the incident electron. Their main use is to illustrate compositional contrasts in multiphase samples. The brightness of the sample varies according to the heaviness of the atom. This phenomenon is often referenced as chemical contrast.
- Diffracted backscattered electrons: used to determine crystal structure, and the orientations of minerals.
- Auger electrons: Got a low energy, used for elementary surface analyses

- Photons X: used for elemental analysis (EDS) and continuous X-rays
- Visible light (Visible Photon): they are at the origin of the cathodoluminescence phenomenon. It is based on a complex function of composition, lattice structure and superimposed strain or damage on the structure of the material.

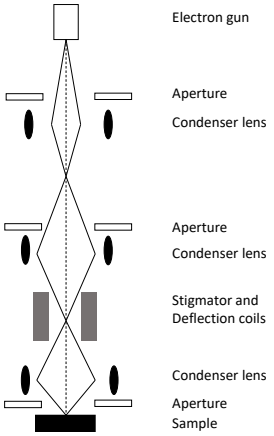

Figure 7: scheme of the SEM configuration

4.2) Samples Preparation

A Jeol JSM-7500F Field Emission Scanning Electron Microscope analysed the sample. This microscope is a field emission one, it allowed to obtain the same resolution as a traditional microscope (with a filament as electron source) but with a lower voltage of 7-9 kV instead of 20-40kV. Moreover, the "charge effects" are considerably reduced. The detector was configured to detect secondary and backscattered electrons. It will provide information on morphology and chemical contrast. Regarding the sample preparation and to reduce the charge effects, the samples were metalized with gold before being observed.

Figure 8 : Photograph of a Jeol JSM-7500F microscope

5) X-ray Photoelectron spectroscopy (XPS)

5.1) Principle

X-Ray photoelectron spectrometry is a none destructive surface analysis method. It can perform analyses at depth from 1 to 5 or 10 nm maximum depending on the model. It gauge the photoelectron spectra induced by X-ray photons. The device is made of an X-ray source, an irradiation chamber, an ion gun, a charge neutralizer, pumps, an electron analyzer and a detector. A simplified scheme of the apparatus is shown below (Fig.9).

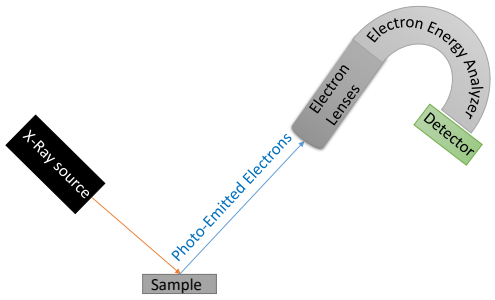

Figure 9: Scheme representing an XPS device

In practise, a sample is subjected to X-ray radiation with a well-defined wavelength, and emits a photoelectron. Photoelectrons have specific energies proper to each element; thanks to this property, it is possible to determine the composition of the sample. To perform a qualitative analysis; the element must have a concentration higher than 0.1%, whereas a quantitative analysis can be performed if 5% of the element is present. The specificity of X-ray Photoelectron spectroscopy is that the ejected electrons are core electrons. These electrons have a specific and constant kinetic energy. As a result, the atom become an ion.

The photoemission obeys to conservation energy's law. The kinetic energy is measured and each incident X-photon has the same energy. When the X-photon interact with the atom, one part of his energy will be used to break the bind between the nucleus and the electron, and the other part will be transfer to the electron as kinetic energy. The equation written below calculate the kinetic energy.

$$E_K = E_B - h\nu$$

h: Planck constant (J.s)

v: Radiation frequency (s^{-1})

E_B: Binding energy (J)

E_K: Kinetic energy (J)

Unfortunately, this equation is not complete and can not completely describe the energy's transfer in this phenomenon. To do so, the Fermi level need to be considered, and the equation become:

$$E_K = h\nu - \varphi - E_B^F$$

φ: Work function (J)

E_B^F: Binding energy relative to Fermi level (J)

The analysis of the emitted core electron gives an information of the nature of the element whereas the oxidation state is given by the shifts of XPS peaks. These shifts come from the energy variations between the valence shell. All these characteristics are resume in the scheme below (Fig.10).

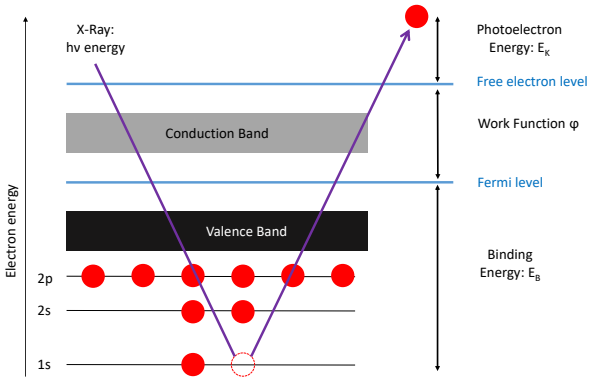

Figure 10: Physic principle of XPS

5.2) Measuring conditions

X-Ray photoelectron spectroscopy were performed to characterize the discharge products on the electrode. The spectroscope is an Escalab 250 Xi from Thermo Scientific, made of a magnesium anode (Kα ray, hν=1253.6Ev). The experiments have been performed at room temperature and under reduced pressure. The samples were prepared in a glove box filled with argon and transferred to the spectrometer in an airtight plastic bag due to the lack of a transport module.

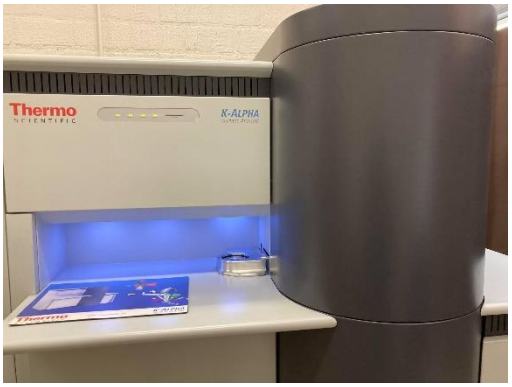

Figure 11: Photograph of the XPS spectrophotometer

6) Porosity measurement

6.1) Principle

In these studies, the determination of the specific surface characterises the contact area between the electrolyte and the cathode. Indeed, an increase in the surface leads to a higher lithium-ion transfer and to better capacity. The experiments were made on powder, and the unity of the specific surface area is in $m^2.g^{-1}$.

The specific surface area is determined by physical adsorption of nitrogen on the surface of the sample and by calculating the amount of adsorbate gas to form a monolayer. This phenomenon occurs, when the surface is exposed a gas close to his condensation point. The temperature of the experiment is the one of liquid nitrogen. In addition, the gas is linked to the surface thanks to Van der Wall's interactions.

Consequently, the vapor quantity adsorbed at the solid surface depend of three main factors: the temperature, the pressure, and the interactions between the gas and the surface. The temperature being fixed, the adsorbed gas volume depends only of the pressure, and absorption isotherms V=f(P) could be drawn. The specific surface area can be determined directly thanks to these isotherms via two kind of measurements: the multi-point and the single measurements.

6.2) Multi-point measurements

In this method, data will be treated according to the Brunauer, Emmett and Teller (BET) adsorption isotherm equation.

$$\frac{1}{V_a(\frac{P_0}{P}-1)} = \frac{C-1}{V_m C} * \frac{P}{P_0} + \frac{1}{V_m C}$$

P: pressure of absorbed gas in equilibrium with the surface (Pa)

P_0: saturated pressure of adsorbate gas (Pa)

V_a: gas volume adsorbate in STP conditions (cm^3)

V_m: volume of the monolayer adsorbed at the surface in STP conditions (cm^3)

C: constant related to the adsorption enthalpy between the gas and the surface.

To measure the specific surface area, at least 3 points are recorded for a relative pressure (P/P_0) from 0.05 to 0.3. This interval is chosen because the isotherm should tend to a linear line. Regarding to the equation, the slope correspond to $\frac{(C-1)}{V_m C}$ and the intercept to $\frac{1}{V_m C}$. Thanks to these data, V_m is calculated as $\frac{1}{(slope+intercept)}$, and C as $\frac{slope}{intercept}+1$.

Once the calculation of V_m done, the specific surface area (S_{BET}) can be determinate thanks to the equation wrote below:

$$S_{BET} = \frac{V_m N_A A_N}{V_0}$$

S_{BET}: specific surface area ($m^2.g^{-1}$)

N_A: Avogadro number ($6.0221 * 10^{23}$ mol^{-1})

V_0: molar volume of the gas in STP conditions

A_N: occupancy area by a nitrogen molecule

6.3) Single point measurement

Usually, three points are needed to calculate the specific surface area, but if the BET straight line goes through the origin, it can be resume in one point. Consequently, the constant 1/C approached zero. The point chosen for the measure is the 0.3 relative pressure as it gave the best match comparing to the multi-point method. By this method, the equation for calculating V_m become:

$$V_m = V_a(1 - \frac{P}{P_0})$$

The single-point method could be used indirectly for a series of very similar powder samples of a given material for which the material constant C is assumed invariant.

6.4) Samples Preparation and measuring conditions

The analysis was done via an ASAP 2420 from Micromeritics, in a multi point configuration. The samples were degassed under vacuum at 150°C for eight hours before being analysed with nitrogen.

After degassing, the samples are immersed in a Dewar filled with liquid nitrogen. The surface adsorbs the nitrogen, and its concentration in the atmosphere decreases. The samples are then removed from the dewar vessel, the temperature rise and the adsorbed nitrogen is released. This difference of nitrogen in the atmosphere is recorded and transcribed on several graphs (Isotherm, Adsorption/Desorption: dV/dw dV/dlog(w) dA/dw dA/dlog(w) Pore Volume ...).

For the studies, the analyses consist in measuring the volume V of nitrogen adsorbed after put a defined amount of nitrogen. The specific surface area is determined after 10 measurements between the linear adsorption ranges from 0.05 to 0.3 for P/P0. Using V the volume of adsorbed nitrogen, the volume Vm is calculated using software according to the BET equation, and the total surface area of the sample is found. The surface area is then divided by the mass of the sample and gives the specific surface area.

Figure 12: Photograph of the physisorption device

7) Accumulator design

Swagelok cells were designed during this thesis to test the synthesized cathodes. Figure 1 shows a schematic of the Swagelok cell used in the tests. It consists of two 316L stainless steel disks with the following components in their centres: a lithium disk, an electrolyte-impregnated fiberglass separator, the cathode, a perforated steel plate, and a spacer. The two steel discs are separated by a nylon disc to isolate them and prevent short circuits. Nitrile O-rings are placed on each side of this nylon disc to ensure gas tightness inside the assembly. Nylon pieces are also used to insulate the screws, holding the steel discs together. In order to ensure the connection between the cell and the analysis terminal two screws are embedded in the steel discs.

In order to put the accumulator under oxygen the upper disc was drilled and valves were installed. A needle valve is used for the oxygen input to the system, while a simple valve is used for the oxygen output. After the system has been purged for 15 seconds, a balloon filled with O_2 (6N) is attached to the inlet valve before opening it. The outlet valve remains closed at all times after purging.

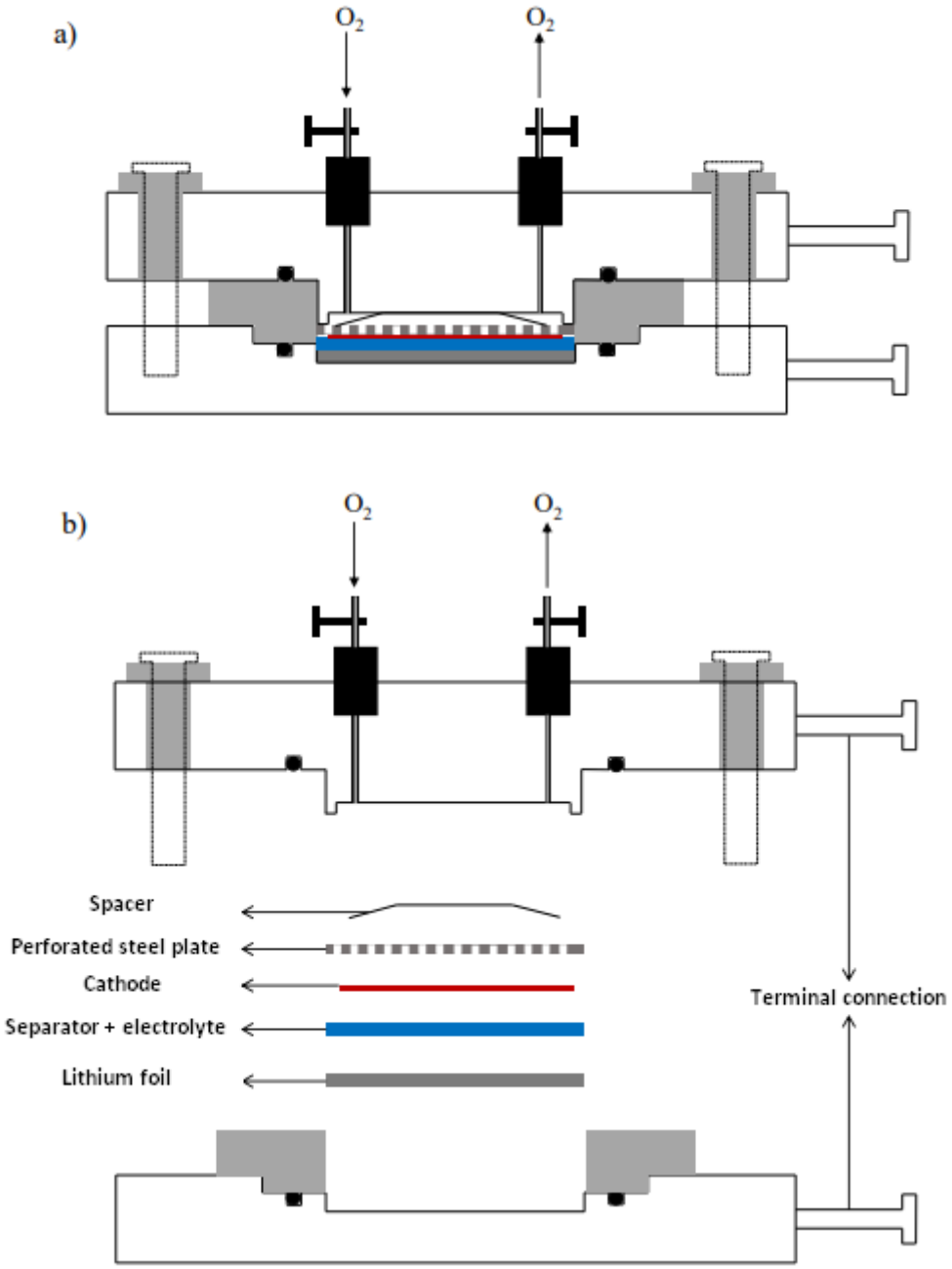

Figure 13: Cross sectional views (a) compact and (b) exploded of the homemade Swagelok cell assembly used for cathode